Structure and Bonding 141
Series Editor: D.M.P. Mingos

Andrew Bocarsly
D. Michael P. Mingos *Editors*

Fuel Cells and Hydrogen Storage

Springer

141
Structure and Bonding

Series Editor: D. M. P. Mingos

For further volumes:
http://www.springer.com/series/430

Structure and Bonding

Series Editor: D. M. P. Mingos

Recently Published and Forthcoming Volumes

Fuel Cells and Hydrogen Storage
Volume Editors: Andrew Bocarsly, D. M. P. Mingos
Vol. 141, 2011

Zintl Ions
Principles and Recent Developments
Volume Editor: Thomas F. Fässler
Vol. 140, 2011

Zintl Phases
Principles and Recent Developments
Volume Editor: Thomas F. Fässler
Vol. 139, 2011

Inorganic 3D Structures
Volume Editor: Angel Vegas
Vol. 138, 2011

Molecular Catalysis of Rare-Earth Elements
Volume Editor: Peter W. Roesky
Vol. 137, 2010

Metal-Metal Bonding
Volume Editor: Gerard Parkin
Vol. 136, 2010

Functional Phthalocyanine Molecular Materials
Volume Editor: Jianzhuang Jiang
Vol. 135, 2010

Data Mining in Crystallography
Volume Editors: Hofmann, D. W. M., Kuleshova, L. N.
Vol. 134, 2010

Controlled Assembly and Modification of Inorganic Systems
Volume Editor: Wu, X.- T.
Vol. 133, 2009

Molecular Networks
Volume Editor: Hosseini, M. W.
Vol. 132, 2009

Molecular Thermodynamics of Complex Systems
Volume Editors: Lu, X., Hu, Y.
Vol. 131, 2009

Contemporary Metal Boron Chemistry I
Volume Editors: Marder, T. B., Lin, Z.
Vol. 130, 2008

Recognition of Anions
Volume Editor: Vilar, R.
Vol. 129, 2008

Liquid Crystalline Functional Assemblies and Their Supramolecular Structures
Volume Editor: Kato, T.
Vol. 128, 2008

Organometallic and Coordination Chemistry of the Actinides
Volume Editor: Albrecht-Schmitt, T. E.
Vol. 127, 2008

Halogen Bonding
Fundamentals and Applications
Volume Editors: Metrangolo, P., Resnati, G.
Vol. 126, 2008

High Energy Density Materials
Volume Editor: Klapötke, T. H.
Vol. 125, 2007

Ferro- and Antiferroelectricity
Volume Editors: Dalal, N. S., Bussmann-Holder, A.
Vol. 124, 2007

Photofunctional Transition Metal Complexes
Volume Editor: V. W. W. Yam
Vol. 123, 2007

Single-Molecule Magnets and Related Phenomena
Volume Editor: Winpenny, R.
Vol. 122, 2006

Fuel Cells and Hydrogen Storage

Volume Editors:
Andrew Bocarsly · D. Michael P. Mingos

With contributions by

H.D. Abruña · J. Benziger · A. Bocarsly · M.J. Cheah · A.M. Herring · J.L. Horan · M.T. Kelly · P. Majsztrik · S. Sachdeva · B. Satterfield · S.C. Singhal · J.A. Turner · H. Wang · Q. Zhao · X.-D. Zhou

Springer

Editors
Andrew Bocarsly
Departments of Chemistry
and Chemical Engineering
Princeton University
Princeton, NJ, USA
bocarsly@princeton.edu

D. Michael P. Mingos
Inorganic Chemistry Laboratory
Oxford University
South Parks Road
Oxford OX1 3QR, UK
michael.mingos@st-edmund-hall.oxford.ac.uk

ISSN 0081-5993 e-ISSN 1616-8550
ISBN 978-3-642-21779-1 e-ISBN 978-3-642-21780-7
DOI 10.1007/978-3-642-21780-7
Springer Heidelberg Dordrecht London New York

Library of Congress Control Number: 2011934252

Cover design: eStudio Calamar, Berlin/Figueres, Spain

Printed on acid-free paper

Springer is part of Springer Science+Business Media (www.springer.com)

Series Editor

Prof. D. Michael P. Mingos

Principal
St. Edmund Hall
Oxford OX1 4AR, UK
michael.mingos@st-edmund-hall.oxford.ac.uk

Volume Editors

Andrew Bocarsly

Departments of Chemistry
and Chemical Engineering
Princeton University
Princeton, NJ, USA
bocarsly@princeton.edu

D. Michael P. Mingos

Inorganic Chemistry Laboratory
Oxford University
South Parks Road
Oxford OX1 3QR, UK
michael.mingos@st-edmund-hall.oxford.ac.uk

Editorial Board

Prof. Jean-Pierre Sauvage

Faculté de Chimie
Laboratoires de Chimie
Organo-Minérale
Université Louis Pasteur
4, rue Blaise Pascal
67070 Strasbourg Cedex, France
sauvage@chimie.u-strasbg.fr

Structure and Bonding
Also Available Electronically

Structure and Bonding is included in Springer's eBook package *Chemistry and Materials Science*. If a library does not opt for the whole package the book series may be bought on a subscription basis. Also, all back volumes are available electronically.

For all customers who have a standing order to the print version of *Structure and Bonding*, we offer the electronic version via SpringerLink free of charge.

If you do not have access, you can still view the table of contents of each volume and the abstract of each article by going to the SpringerLink homepage, clicking on "Chemistry and Materials Science," under Subject Collection, then "Book Series," under Content Type and finally by selecting *Structure and Bonding*.

You will find information about the

– Editorial Board
– Aims and Scope
– Instructions for Authors
– Sample Contribution

at springer.com using the search function by typing in *Structure and Bonding*.

Color figures are published in full color in the electronic version on SpringerLink.

Aims and Scope

The series *Structure and Bonding* publishes critical reviews on topics of research concerned with chemical structure and bonding. The scope of the series spans the entire Periodic Table and addresses structure and bonding issues associated with all of the elements. It also focuses attention on new and developing areas of modern structural and theoretical chemistry such as nanostructures, molecular electronics, designed molecular solids, surfaces, metal clusters and supramolecular structures. Physical and spectroscopic techniques used to determine, examine and model structures fall within the purview of *Structure and Bonding* to the extent that the focus

is on the scientific results obtained and not on specialist information concerning the techniques themselves. Issues associated with the development of bonding models and generalizations that illuminate the reactivity pathways and rates of chemical processes are also relevant.

The individual volumes in the series are thematic. The goal of each volume is to give the reader, whether at a university or in industry, a comprehensive overview of an area where new insights are emerging that are of interest to a larger scientific audience. Thus each review within the volume critically surveys one aspect of that topic and places it within the context of the volume as a whole. The most significant developments of the last 5 to 10 years should be presented using selected examples to illustrate the principles discussed. A description of the physical basis of the experimental techniques that have been used to provide the primary data may also be appropriate, if it has not been covered in detail elsewhere. The coverage need not be exhaustive in data, but should rather be conceptual, concentrating on the new principles being developed that will allow the reader, who is not a specialist in the area covered, to understand the data presented. Discussion of possible future research directions in the area is welcomed.

Review articles for the individual volumes are invited by the volume editors.

In references *Structure and Bonding* is abbreviated *Struct Bond* and is cited as a journal.

Impact Factor in 2009: 4.152; Section “Chemistry, Inorganic & Nuclear”:
Rank 2 of 43; Section “Chemistry, Physical”: Rank 7 of 113

Preface

A fuel cell is a device which converts the chemical energy stored in fuels, such as hydrocarbons, alcohols or hydrogen, into electricity by way of a series of electrochemical-chemical reactions. Since no direct combustion processes are involved, fuel cell efficiencies are not governed by theoretical Carnot efficiencies and electrical work is converted from a substantial fraction of the enthalpy associated with the electrochemical oxidation of the fuel into water and carbon dioxide. Fuel cells are characterized by their electrolyte material; the solid oxide fuel cell (SOFC) has a solid oxide or ceramic electrolyte. Besides having high efficiencies, these fuel cells have long-term stabilities, fuel flexibility, low emissions and relatively low running costs. Their major disadvantage is their high operating temperatures, which results in longer start-up times and mechanical and chemical compatibility issues. Proton exchange membrane fuel cells (PEMFCs) conduct positive hydrogen ions (protons) through a polymer electrolyte from the anode to the cathode, whereas the SOFCs use a solid oxide electrolyte to conduct negative oxygen ions from the cathode to the anode. SOFCs have a wide variety of applications particularly as auxiliary power units in vehicles with outputs from 100 W to 2 MW. Their high operating temperatures make SOFCs suitable candidates for application with heat engine energy recovery devices.

This volume brings together recent developments in the science and technology of fuel cells. Chapter 1 by Xiao-Dong Zhou and Subhas Singhal describes recent developments in the solid state materials used in SOFCs and emphasises the simultaneous improvements in their activities (their system performance), and their durability (stability of their performance). These improvements are based primarily on the structures and bonding characteristics of SOFC components. The role of local structural effects and chemical bonding in the electrochemical performance of the new materials is discussed in detail. Chapter 2 by Hongsen Wang and Hector Abruña provides new insights into the direct alcohol fuel cell related anode electrocatalysis. This work relies heavily on the use of quantitative differential electrochemical mass spectrometry (DEMS) for studying the mechanism of methanol electro-oxidation on platinum and platinum/ruthenium catalysts. The application of this technique to the electro-oxidation of ethanol and acetaldehyde on metal

nano-particle catalysts is also discussed. The studies have also shed new light on the mechanism of dissociative adsorption and electro-oxidation of ethanol, acetaldehyde and ethylene glycol. In Chap. 3, Jay Benziger, Andrew Bocarsly, May Jean Cheah, Paul Majsztrik Barclay Satterfield and Qiao Zhao describe the mechanical and transport properties of Naflon. Naflon is an ionomer that has a hydrophobic tetrafluoroethylene (TFE) backbone and perfluoroalkyl ether side chains terminated with hydrophilic sulphonate acid groups. It has been used as a polymer electrolyte membrane (PEM) since the early 1990s. It is more robust than hydrocarbon membranes in fuel cells and the acid form has high proton conductivity. This chapter describes recent studies tracing the effect of water absorption changes on the mechanical and transport properties of Naflon. The unusually large changes in properties are indicative of microstructural changes induced by water absorption. Water absorption is thought to cause clustering of hydrophilic sulphonic groups and water within a hydrophobic PTFE matrix. The hydrophilic domains form a network which facilitates transport and creates physical cross links that stiffen Naflon. Sonny Sachdeva, John Turner, James Horan and Andrew Herring describe the use of heteropolyacids (HPAs) in proton exchange fuel cells in Chap. 4. In this chapter, the fundamental aspects of proton conduction in HPAs are introduced and liquid-based HPA fuel cells are reviewed. Four types of composite proton exchange membranes containing HPAs are identified.

In recent years, hydrogen gas has been promoted as a potential environmentally friendly fuel. Michael Kelly in Chap. 5 reviews the scientific and technical issues associated with generating hydrogen from non-fossil fuel sources and addresses the storage problems associated with this fuel. Whilst molecular hydrogen has the highest energy per unit weight of any known compound, it has a poor energy content per unit volume. Liquefaction of hydrogen results in a substantial volume reduction, but it suffers from the disadvantages of employing a fuel at 20K in a 300K environment. Therefore, hydrogen production and storage represents a complementary problem to the fuel cell scientific and technology issues discussed in the earlier chapters. Taken together, we hope that these chapters provide a timely summary of some exciting developments in hydrogen storage and the utilization of fuel cells for energy generation.

Princeton University
Oxford University
April 2011

Andrew Bocarsly
D. Michael P. Mingos

Contents

Struct Bond (2011) 141: 1–32
DOI: 10.1007/430_2011_42

Published online: 24 May 2011

Structure and Bonding: Solid Oxide Fuel Cells

Xiao-Dong Zhou and Subhash C. Singhal

Abstract Recent materials development for solid oxide fuel cells (SOFCs) has been driven by the recognition of simultaneous improvement over the activity (e.g., system performance) and durability (e.g., stability of the performance). Structure and bonding of SOFC components and devices lie at the heart of the viable approaches to achieve these improvements. We will start this paper with a brief illustration of structure and bonding in SOFCs, followed by detailed analysis on the role of local structure and chemical bonding on the electrochemical performance and performance stability of SOFCs.

Keywords Components · Performance · Solid oxide fuel cells · Stability · Structure

Contents

X.-D. Zhou (✉) and S.C. Singhal
Pacific Northwest National Laboratory, Richland, WA 99352, USA
e-mail: zhox@cec.sc.edu

1 Introduction

A solid oxide fuel cell (SOFC) is an energy conversion device that converts the chemical energy stored in fuels (such as hydrogen or methane) into electricity through a series of electrochemical reactions, and no combustion process is involved. As a result, fuel cell efficiencies are not limited by theoretical Carnot efficiencies since the electrical work is directly converted from a substantial fraction of the enthalpy associated with the electrochemical oxidation of the fuel to water and/or carbon dioxide. Hence, fuel cells can deliver higher electrical conversion efficiencies when compared with traditional technologies such as coal-fired power plants and electrical generators based on internal combustion engines. In addition to high efficiency, SOFCs, when compared with other fuel cells, have two particular advantages, owing to their high-temperature operation: (1) SOFCs allow the use of a variety of fuels, ranging from hydrogen to CO to hydrocarbons, because of the use of an oxide-based anode, which serves as an active catalyst for oxidation at high temperatures, and (2) SOFCs produce a significant amount of heat, a byproduct of SOFCs, which can be used in combined heat and power (CHP) systems. The overall efficiency of a CHP may exceed 70%. In addition, the quiet, vibration-free operation of fuel cells also eliminates noise usually associated with power generation systems; and fuel cells have very low levels of SO_x and NO_x emissions.

Figure 1 illustrates a typical SOFC, which essentially consists of two porous electrodes separated by a dense, oxide ion conducting electrolyte. Oxygen gas

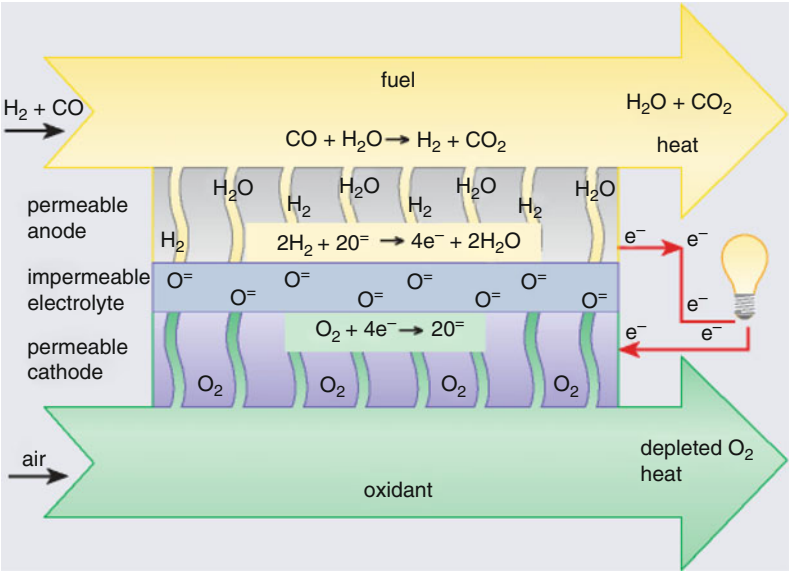

Fig. 1 Operating principle of a solid oxide fuel cell

molecules on the cathode side react with incoming electrons coming from the external circuit to form oxygen ions, which migrate through the oxide ion conducting electrolyte to the anode. At the anode, oxide ions react with H_2 or other fuels to form H_2O (and/or CO_2), liberating electrons, which flow from the anode through the external circuit to the cathode to produce electricity. Provided that both fuels and oxygen are supplied constantly, the continuous electrochemical reactions steadily generate electricity.

Quantitatively speaking, the electron motive force (EMF) of a cell is determined by the chemical potential of oxygen (i.e., oxygen activity), which is expressed by Nernst Equation:

$$\mathrm{EMF} = \Gamma \frac{RT}{4F} \ln\left(\frac{(\mathrm{pO_2})_a}{(\mathrm{pO_2})_b}\right) \tag{1}$$

where Γ is the ionic transference number (ionic conductivity/total conductivity), T is operation temperature, F is Faraday constant, $(\mathrm{pO_2})_a$ is the oxygen activity on the oxidant side, and $(\mathrm{pO_2})_b$ is the oxygen activity on the fuel side. In the case without external circuit, the EMF is corresponding to open circuit voltage (OCV). For instance, an OCV ~ 1.1 V can be calculated for an SOFC operating at 800°C with air and room-temperature-humidified H_2 are used.

Under cell operating conditions, i.e., when a current passes through it, a fingerprint characteristic of fuel cells is the relationship between voltage and current density. Figure 2 illustrates a schematic of V–I curve for a typical SOFC, which

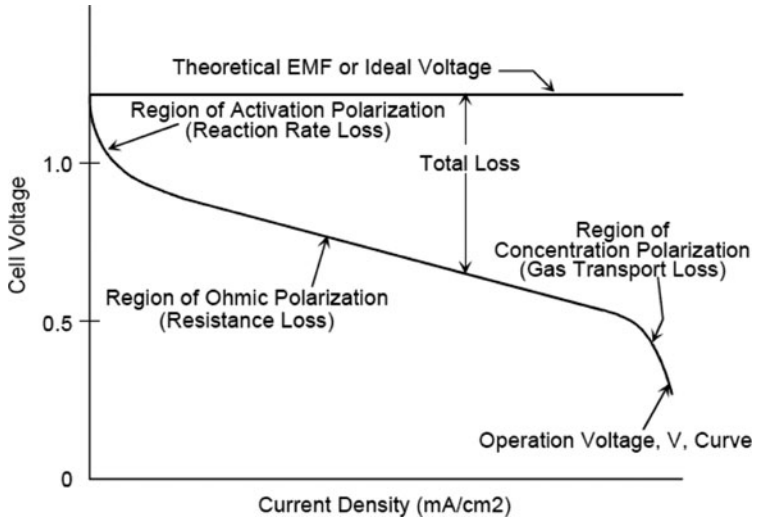

Fig. 2 Schematic V–I curve for a typical SOFC, which shows OCV, cathodic polarization loss, anodic polarization loss, and ohmic loss

represents OCV (E°), cathodic polarization loss, anodic polarization loss, and Ohmic loss. The cell voltage (V) is given by:

$$V = E^{\circ} - iR - \eta_{\mathrm{A}} - \eta_{\mathrm{F}} \tag{2}$$

where i is the current passing through the cell, R is the electrical resistance of the cell, and η_{A} and η_{F} are the polarization voltage losses associated with the air electrode (cathode) and the fuel electrode (anode), respectively. These polarizations are related to three primary elementary physical processes: gas diffusion, gas–solid interaction, and ionic migration. These processes are analyzed from the viewpoints of structure and chemical bonding. We will start from the analysis at the atomic scale, in which emphasis will be on charge exchange and transport with respect to crystal structure, local chemical bonding/ordering. Then, on the microscale, emphasis will be on gas diffusion and triple phase boundary (TPB) analysis.

2 Structure and Chemical Bonding at the Atomic Scale

2.1 Oxygen Ion Conductivity in the Electrolyte

In an SOFC as shown in Fig. 1, the electrolyte is exposed to both oxidizing (air side) and reducing species (fuel side) at high temperatures; therefore, the long-term successful SOFC operation requires that the electrolytes satisfy several strict requirements: (1) Sufficient ionic conductivity – the electrolyte materials must have an ionic transference number close to unity, i.e., the electronic conductivity in the electrolyte must be sufficiently low to provide a high energy conversion efficiency. Also, the oxide ion conductivity must be high to minimize the ohmic loss; (2) Dense structure – to produce maximum electrochemical performance, the electrolyte must be gas tight. This presents challenges in fabricating dense thin electrolyte layers using either the anode or the cathode as the supporting structure; (3) Stability – the operation of SOFCs requires the cathode and the anode to be porous for gas transport; therefore, the electrolyte is exposed to both the air and the fuel at elevated temperatures. This means that the electrolyte must be chemically stable in these environments so that it is thermally and mechanically stable during thermal cycling. This requires that the thermal expansion coefficients must match at the interfaces.

The current electrolyte material is Y stabilized ZrO_2 (YSZ), which can satisfy the aforementioned requirements, with acceptor-substituted CeO_2, B_2O_3, and (La,Sr) $(Mg,Ga)O_3$ being investigated as primary candidates. The ZrO_2, CeO_2 and Bi_2O_3 are fluorite family oxides, which have a general formula of MO_2, and for this discussion M will be either Zr or Ce or Bi. The lattice of fluorite structure is basically face center cubic (space group Fm3m), in which the cations are in eightfold coordination sites at (0, 0, 0) and oxygen ions are in fourfold coordination sites at (1/4, 1/4, 1/4) and (3/4, 3/4, 3/4). The cations reside in the tetrahedral holes

in cubic closest packing with the oxygen ions. The *fcc* lattice possesses a large open volume fraction (>35%), and as a result is capable of tolerating considerable oxygen nonstoichiometry and forming solid solution with a number of lower valence elements.

2.1.1 Local Chemistry of Oxygen Vacancies

The oxygen vacancies are created in the oxides with low-valence-element substitutions that are usually described as acceptor dopants. The oxygen ion conductivity is determined by carrier (oxygen vacancy) density and carrier mobility. It seems straightforward to design the oxygen ion conductor by increasing the oxygen vacancy concentration. This might not be valid in many cases, because other factors such as vacancy ordering, charge mobility, and compatibility with other components, must be taken into consideration. In this section, emphasis is on the local chemistry of oxygen vacancies.

Extrinsic Defects

In case of low valence element substitution to either CeO_2 or ZrO_2, the oxygen vacancy concentration, $[V_O^{\bullet\bullet}]$, is primarily determined by the acceptor concentration, then the neutrality condition is:

$$n + [A'_{Ce}] = 2[V_O^{\bullet\bullet}] \tag{3}$$

The total conductivity, σ_t, is the sum of ionic conductivity (σ_i) and electronic conductivity (σ_e):

$$\sigma_t = \sigma_i + \sigma_e \tag{4}$$

If the acceptor concentration is much larger than electron density, then oxygen vacancy concentration is constant as shown in (13). The electronic conductivity

$$\sigma_e = nq\mu = A \exp\left(\frac{-\Delta H}{2kT}\right)[pO_2]^{-1/4} q \frac{1}{T} \exp\left(-\frac{E_h}{kT}\right) \tag{5}$$

and the ionic conductivity is

$$\sigma_i = [V_O^{\bullet\bullet}] q \mu_{O^{2-}} \tag{6}$$

It is known that acceptor-doped CeO_2 (e.g., Gd doped CeO_2 – GDC) can be reduced at a very low oxygen partial pressure. Table 1 is a list of P^*O_2 (atm) for various dopant levels, y, in $Ce_{1-y}Gd_yO_{1-y/2}$ at different temperatures. P^*O_2

Table 1 P^*O_2 (atm) for various dopant levels, y, in $Ce_{1-y}Gd_yO_{1-y/2}$ at different temperatures [1]

y	Temperature (°C)			
	700	750	800	850
0.1	1.3×10^{-17}	2.53×10^{-16}	2.43×10^{-15}	3.56×10^{-14}
0.2	1.24×10^{-19}	3.92×10^{-18}	9.2×10^{-17}	1.73×10^{-15}
0.3	3.16×10^{-19}	5.6×10^{-18}	8.5×10^{-17}	9.0×10^{-16}
0.4	9.3×10^{-19}	8.8×10^{-18}	6.3×10^{-17}	3.85×10^{-16}
0.5	1.46×10^{-16}	1.38×10^{-15}	1.12×10^{-14}	6.5×10^{-14}

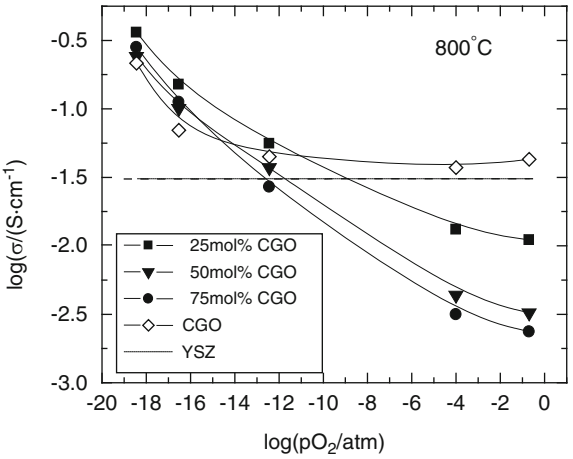

Fig. 3 A plot of log (σ) vs. log (pO_2) for CGO_x–YSZ_{1-x} ($x = 1$, 0.75, 0.5 and 0.25) solid solution measured at 800°C [4]

represents the oxygen partial pressure at which the ionic transference number of the solid solution becomes 0.5. Because the electrons have a much higher mobility (~3 orders) than oxygen ions, a transfer number of 0.5 only indicates that the electron concentration (Ce^{3+}) is about 0.1% of oxygen-vacancy concentration. On the other hand, the ionic conductivity of acceptor-doped ZrO_2 is stable against wide range of oxygen partial pressure (e.g., $\sigma_e \ll \sigma_i$).

Vacancy-Dopant Associates

An oxygen vacancy has a positive charge, whereas the acceptor dopant has a negative charge; hence, oxygen vacancy and acceptor-dopant can bond together and form a local associate. Indeed, formation of such an associate was observed in CeO_2-based oxygen ion conductors. An example of the substantial influence of vacancy-dopant associates on oxygen migration is lower conductivity in solid solutions of GDC-YSZ than those of either GDC or YSZ. Figure 3 shows the oxygen-activity dependence of the conductivity of solid solutions containing 25, 50, and 75 mol% CGO. The electronic conductive behavior of the solid solution

CGO_x–YSZ_{1-x}, which depends on oxygen activity, is somewhat surprising in that this system can still be considered as an acceptor (Y and Gd)-doped conductor. However, the flat region for log (σ) vs. log (pO_2) was not observed, which is the characteristic behavior for an acceptor-doped ionic conductor because the acceptors pin the concentration of oxygen vacancies. In the CeO_2 system, the electronic conduction is well known to be due to the redox reaction between Ce^{4+} and Ce^{3+} oxidation states, which are oxygen-activity dependent. This reaction can be expressed as $2Ce_{Ce}^{\times} + O_O^{\times} \rightarrow 1/2O_2 + V_O^{\bullet\bullet} + 2Ce'_{Ce}$ (Kröger–Vink notation) [2]. The reduction energy has been calculated to decrease when zirconia is introduced because of the formation of defect clusters, such as $(Ce'_{Zr} - V_O^{\bullet\bullet} - Ce'_{Zr})$ [3]. This type of defect cluster decreases the ionic conductivity because the oxygen ion mobility decreases due to the trapping of oxygen vacancies.

Vacancy Ordering

Stabilized Bi_2O_3 has a fluorite structure with a highly deficient oxygen sublattice, as shown in Fig. 4, which is attributed to its higher ionic conductivity compared to ZrO_2- or CeO_2-based materials [5–11]. Therefore, it is necessary to study the ionic transport in Bi_2O_3-based oxides, which can allow an understanding of the underlying physics of transport of oxide ions in a highly defective fluorite structure. Bi_2O_3-based materials exhibit a complex array of structures and properties, depending upon the dopant concentration, temperature, and atmosphere. There exists an ordering/disordering of oxygen vacancies in Bi_2O_3-based oxides, which plays a substantially important role in ionic conductivity. The order–disorder transition takes place at ~600°C in the doped Bi_2O_3 [7, 12]. The sublattice for oxygen (and oxygen vacancies) is ordered when the annealing temperature is less than the transition temperature. As a result, oxygen ion conductivity undergoes degradation as a function of time. Transmission electron microscopy and neutron diffraction [13] results indicated that the vacancy ordering takes place along $\langle 111 \rangle$, which is similar to the YSZ system [12, 14]. Therefore, the ordering of oxygen vacancies in $\langle 111 \rangle$ might be common to fluorite oxides at high-vacancy concentrations.

2.1.2 Mobility and Enthalpy for the Migration of Oxygen Ions

The mobility can be seen as the ability of defects to transport over the energy barrier, which is expressed as:

$$\mu = \frac{Aqva_0^2}{kT} \exp\left(\frac{\Delta S_m T - \Delta H_m}{kT}\right) \tag{7}$$

where A is a constant, v is the defect vibrational frequency (s^{-1}), a_0 is the distance between two equivalent sites (m), k is the Boltzmann constant (1.38×10^{-23} J/K),

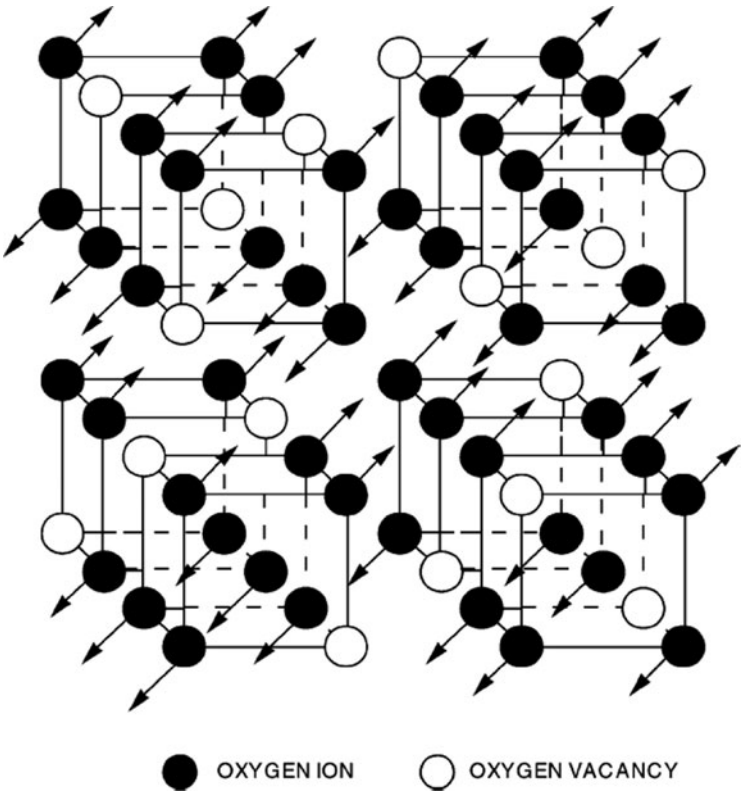

Fig. 4 Model of ordered structure showing both occupancy ordering (*filled* vs. *vacant*) and positional ordering [7]

T is the temperature (K), and ΔS_m (J/K) the entropy and ΔH_m (J) the enthalpy of ionic motion.

Oxygen ion conductivity can be improved by tailoring the parameters in (7) to subsequently increase the mobility. For instance, oxygen ion mobility in doped ZrO_2 is found to be dependent on the atomic number, ion radius, and concentration of the dopants. Additionally, the microstructural features, such as dopant segregation and grain boundary impurities play a role in the magnitude of the overall ionic conductivity. The maximum ionic conductivity in doped ZrO_2 is observed when the concentration of acceptor-type dopant(s) is close to the minimum necessary to completely stabilize the cubic fluorite-type phase. Further additions decrease the ionic conductivity due to increasing association of the oxygen vacancies and dopant cations into complex defects of low mobility. The effect of dopant concentration increases with increasing difference between the host and dopant cation radii. Figure 5 illustrates a plot of ionic conductivity and diffusion enthalpies as a function of the ionic radius of dopant cations to ZrO_2. The ionic radius for Zr^{4+} is 0.84 Å when coordination number is 8; it is 0.87 Å for Sc^{3+} and 1.109 for Y^{3+}.

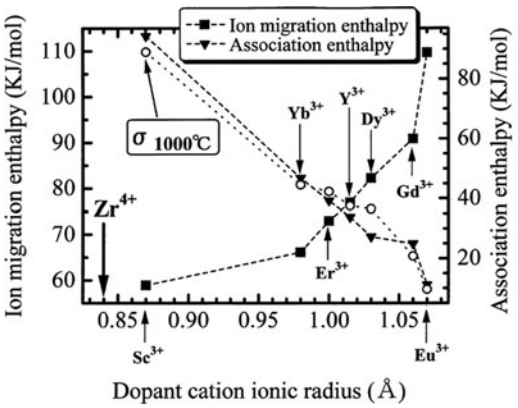

Fig. 5 Ionic conductivity and diffusion enthalpies as a function of the ionic radius of dopant cations to ZrO_2 [15]

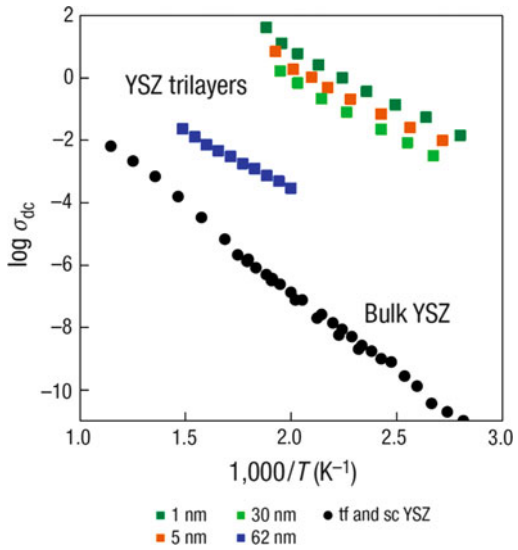

Fig. 6 Ionic conductivity (S/cm) of the trilayers STO/YSZ/STO versus inverse temperature. The thickness range of the YSZ layer is 1–62 nm. Also included are the data for a single crystal (sc) of YSZ and a thin film (tf), 700 nm thick, with the same nominal composition [16]

Sc-doped zirconia, therefore, is a promising candidate due to its conductivity similar to doped CeO_2. However, the cost and known aging of Sc-doped ZrO_2 present challenges in using this material for commercial SOFCs.

Recently, Garcia-Barriocanal et al. reported colossal increase in conductivity in a superlattice structure [16, 17], which consists of alternating $SrTiO_3$ and YSZ layers. The conductivity was found to be dependent upon the thickness of YSZ layers, thus the interfaces between $SrTiO_3$ and YSZ (Fig. 6). In addition, they observed a decrease in the temperature dependence of ionic conductivity, indicating that oxygen ions migrate more easily in the interfaces than in the bulk lattice [e.g., greater a_0 and ν in (7)]. Moreover, the epitaxial growth of thin films creates a 7% tensile strain in YSZ thin films, which may subsequently result in more defects in YSZ, accompanied by larger open space in ZrO_2 lattice.

2.2 Electrochemical Reactions in the Cathode

The electrochemical performance of the cathode is determined by the rate of reduction of oxygen molecules on the cathode surface and the transport of oxygen ions through the cell. It is known that oxygen reduction requires transfer of four electrons, thus it represents a limiting step that lowers the efficiency of a practical fuel cell. Hence, understanding these reactions and finding strategies for circumventing these limitations are important in developing new and more practical SOFCs. In the search for new cathode materials, two important physical properties are critical to the oxygen reduction in SOFCs, the surface exchange coefficient (k) and the diffusion coefficient (D), both of which are strongly correlated with defect chemistry of the cathode.

2.2.1 Basic Defect Chemistry

The defect chemistry of oxides has been studied for several decades, particularly in the ternary compounds (ABO_3), also known as the perovskite family of oxides. Perovskite type oxides are of great interest in energy conversion devices because of their unique local bonding and chemical structures: (1) site occupancy is determined mainly by ionic size; so the site location of a particular cation is fairly certain; (2) electronic conductivity (σ) is determined by the B site ion and ionic conductivity results from the motion of oxygen vacancies; (3) the oxygen octahedron (BO_6) is a rigid unit, which can twist or bend or tolerate loss of oxygen. Thus, this family of oxides has been tailored to be used as dielectrics, mixed ionic and electronic conductors, superionic conductors, and superconductors. Defect chemistry is the most important technique involved in gaining an understanding of the mass and charge transfer properties because it determines the defect type, density, defect associations and carrier mobility.

The occupants of ABO_3 at A site can be $A_A^{\times}$, V'''_A and Sr'_A (for simplicity, assume Sr is the low valence element substituting at the A site). The occupants at the B site are $B_B^{\times}$, B'_B, $B_B^{\bullet}$ and V'''_B, where $B_B^{\times}$ indicates a majority of B cations are in valence of 3+, B'_B represents that some B site cations are in 2+ state and $B_B^{\bullet}$ shows some B site cations are in 4+ valence state. The oxygen site can have two types of occupants, $V_O^{\bullet\bullet}$ and $O_O^{\times}$. Details on these notations can be found from [2, 18, 19].

The main defect reaction for generation of oxygen ion vacancies is

$$2B_B^{\bullet} + O_O^{x} \rightarrow \frac{1}{2} O_2 + 2B_B^{\times} + V_O^{\bullet\bullet} \tag{8}$$

$$K_{V_O^{\bullet\bullet}} = \frac{P_{O_2}^{1/2}[B_B^{\times}]^2[V_O^{\bullet\bullet}]}{[B_B^{\bullet}]^2[O_O^{\times}]} \tag{9}$$

For the compounds in this study, i.e., ABO_3, we emphasize the regime where the cation vacancies are minor, thus the electroneutrality condition becomes:

$$p = [\mathrm{Sr}'_{\mathrm{La}}] - 2[\mathrm{V}_{\mathrm{O}}^{\bullet\bullet}] + n \tag{10}$$

Three assumptions must be made to analytically solve the equations:

1. Assume that the positive hole is the higher valence transition metal ion, $\mathrm{B}_{\mathrm{B}}^{\bullet}$; and negative electron is the lower valence ion, B'_{B}, thus

$$\left[\mathrm{B}_{\mathrm{B}}^{\bullet}\right] = [\mathrm{h}^{\bullet}] = p \quad \text{and} \quad [\mathrm{B}'_{\mathrm{B}}] = [\mathrm{e}'] = n \tag{11}$$

2. Assume electron population (n) is much smaller than hole population (p), thus

$$n \ll p \tag{12}$$

Therefore, the equality $\left[\mathrm{B}_{\mathrm{B}}^{\bullet}\right] + [\mathrm{B}'_{\mathrm{B}}] + \left[\mathrm{B}_{\mathrm{B}}^{\times}\right] = 1$ becomes $\left[\mathrm{B}_{\mathrm{B}}^{\bullet}\right] + \left[\mathrm{B}_{\mathrm{B}}^{\times}\right] = 1$

3. Assume that oxygen ion vacancy concentration is much smaller than the lattice oxygen concentration,

$$[\mathrm{V}_{\mathrm{O}}^{\bullet\bullet}] \ll [\mathrm{O}_{\mathrm{O}}^{\times}] \tag{13}$$

Based on these three assumptions, (9) can be simplified as:

$$K_{\mathrm{V}_{\mathrm{O}}^{\bullet\bullet}} = \frac{P_{\mathrm{O}_2}^{1/2}[1-p]^2([\mathrm{Sr}'_{\mathrm{La}}] - p)/2}{p^2 \times 3} \tag{14}$$

which can be rearranged to yield

$$6K_{\mathrm{V}_{\mathrm{O}}^{\bullet\bullet}} P_{\mathrm{O}_2}^{-1/2} = \frac{[1-p]^2([\mathrm{Sr}'_{\mathrm{La}}] - p)}{p^2} \tag{15}$$

The temperature dependent of (14) is given by

$$\begin{aligned} K_{\mathrm{V}_{\mathrm{O}}^{\bullet\bullet}} &= \exp\left(-\frac{\Delta G_{\mathrm{f}}}{kT}\right) = \exp\left(-\frac{\Delta H_{\mathrm{f}} - T\Delta S_{\mathrm{f}}}{kT}\right) \\ &= \exp\left(\frac{\Delta S_{\mathrm{f}}}{k}\right)\exp\left(-\frac{\Delta H_{\mathrm{f}}}{kT}\right) \end{aligned} \tag{16}$$

An analytical solution for p in (14) can be achieved as a function of oxygen activity and $K_{\mathrm{V}_{\mathrm{O}}^{\bullet\bullet}}$, where $K_{\mathrm{V}_{\mathrm{O}}^{\bullet\bullet}}$ is a function of temperature. At a specific temperature, $K_{\mathrm{V}_{\mathrm{O}}^{\bullet\bullet}}$ is a constant and can be simulated by plotting σ vs. PO_2.

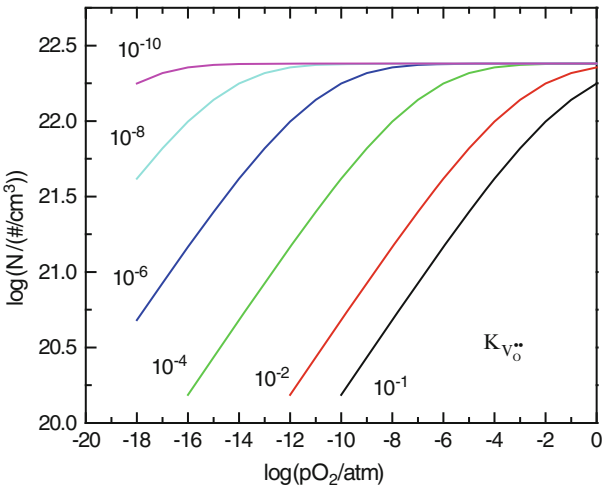

Fig. 7 A plot of carrier concentration as a function of oxygen activity with various $K_{V_O^{\bullet\bullet}}$ values, calculated from global solution 2

Figure 7 illustrates the influence of $K_{V_O^{\bullet\bullet}}$ on the carrier concentration as a function of oxygen activity. As can be seen, the carrier concentration exhibits a flat region when $K_{V_O^{\bullet\bullet}}$ is relatively small. With increasing $K_{V_O^{\bullet\bullet}}$, this flat region shifts to higher oxygen activity region n disappears. This behavior is similar to that shown in electrical conductivity vs. log (pO_2) (Fig. 8). The reaction constants for redox reaction in (14) for chromites, manganites and ferrites can be obtained by simulating conductivity data vs. oxygen activity. The carrier concentration (p) for determining conductivity is the analytical solution to (14). An assumption that the carrier mobility is only a function of temperature is valid in the region where oxygen vacancy concentration is rather low. Figure 8 shows a comparison between $La_{0.70}Ca_{0.30}CrO_3$ [20], $La_{0.70}Sr_{0.30}MnO_3$ [21], and $La_{0.75}Sr_{0.25}FeO_3$ [22], where the reaction constants are listed.

2.2.2 High Temperature Cathode

The overall oxygen reduction reaction is the reverse reaction of (8), as:

$$\frac{1}{2}O_2 + 2B_B^{\times} + V_O^{\bullet\bullet} \rightarrow 2B_B^{\bullet} + O_O^{x}. \tag{17}$$

From (17), it is apparent that a good cathode must satisfy the following requirements: high electronic conductivity, high activity for oxygen reduction, porous structures and high ionic conductivity. In addition, the cathode has to maintain a stable chemical composition at high temperatures in air or oxygen; and have a thermal expansion coefficient compatible with the SOFC electrolyte.

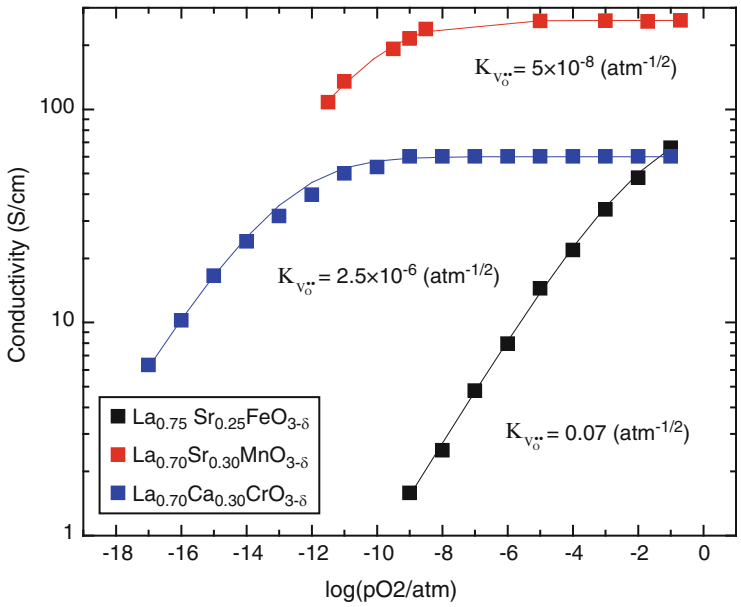

Fig. 8 A plot of simulated conductivity as a function of oxygen activity for three types of perovskites, from which $K_{V_O^{\bullet\bullet}}$ can be achieved

In earlier tubular SOFC design, a thick electrolyte (~100 μm) was used, which necessitated a high operation temperature (>900°C) to minimize the ohmic loss. At elevated temperatures, lanthanum manganite ($LaMnO_3$), which, when substituted with low valence elements, such as Ca or Sr, has a superior p type electronic conduction due to formation of large amount of Mn^{4+}. Moreover, doped $LaMnO_3$ possesses adequate electrocatalytic activity, a reasonable thermal expansion match to YSZ, and stability in the SOFC cathode operating environment. At the cathode operation conditions, doped $LaMnO_3$ has oxygen excess, or precisely speaking, has cation vacancies because one unit cell of $LaMnO_3$ can only accommodate as many as 3 oxygen ions. Therefore, the oxygen ionic conductivity is relatively low in Sr-doped $LaMnO_3$ (LSM), on the order of 10^{-7} S/cm at 800°C [23–25]. Furthermore, the reactivity and interdiffusion studies between doped lanthanum manganite and yttria-stabilized zirconia (YSZ) electrolyte have shown any interactions between these two materials up to 1,000°C to be minimal, thus LSM-YSZ composite is expected to have a reasonably chemical stability and compatibility [26–29]. The mechanical stability and compatibility can be provided by control over the thermal expansion coefficient to avoid delamination between the cathode and the electrolyte [30].

Electrochemical impedance spectroscopy (EIS) and second ion mass spectroscopy (SIMS) were used to investigate the mechanisms of oxygen reduction on LSM surfaces. EIS with microelectrodes was employed at the Max Plant Institute to investigate the rate-limiting process with LSM on YSZ. They found the corresponding electrode resistance was approximately proportional to the inverse

electrode area. Furthermore, strong electrode-thickness dependence was observed in 60 different microelectrodes, which showed that the electrode polarization resistance scales varies almost linearly with thickness. This is a strong indication in favor of a bulk path determining the oxygen reduction rate, with transport of oxide ions in LSM being the rate-determining step. In the case of cathodic bias (−300 mV), the electrode polarization resistance was also proportional to the inverse of the electrode area, hence it is a bulk-transport limited process. If the anodic bias was applied (+300 mV), the polarization resistance was proportional to the electrode diameter, indicating a surface path limited process. It is the great advantage of such microelectrode measurements that they yield quantitative parameters for both bulk and surface paths. These data can then be used to simulate the weight of each path for porous cathodes. In addition to microelectrodes, SIMS can provide mechanistic information on the reduction of oxygen on cathode surfaces by using isotopic ^{17}O or ^{18}O as the sources and mapping isotopic oxygen [31–34]. From SIMS studies, inhomogeneous ^{18}O tracer distribution was found underneath the YSZ/LSM boundary, indicating the existence of particularly active spots. These observations are in accordance with the results obtained from the microelectrode measurements discussed above. The two complementary experiments thus yield an improved understanding of the oxygen reduction kinetics at LSM cathodes.

2.2.3 Reduction on LSCF: Role of Oxygen Vacancies

From the previous discussion, we know that oxygen vacancies are generated upon increasing temperature. It can be expected that oxygen vacancy concentration is extremely low at relatively low temperatures (~ room temperature) for the compounds shown in Fig. 8, therefore conductivity should increase with increasing temperature because of their increasing mobility. At elevated temperature, the total carrier numbers will decrease because of the increasing oxygen vacancy concentration (14), i.e., increasing temperature. Mobility, however, continuously increases with increasing temperature. Hence, a maximum conductivity at a specific temperature is expected due to an increasing mobility and decreasing carrier concentration. Figure 9 shows a plot of conductivity vs. temperature for various p-type conductors. A shift of the temperature corresponding to the maximum conductivity is observed in the order T_{LSCr} (~1,200°C) [35] > T_{LSM} (~900°C) [36] > T_{LSF} (~600°C) > T_{LSCo} (~550°C) [37, 38] > T_{LSFCu} (~400°C) [39]. As discussed previously, this maximum in conductivity represents the temperature at which the oxygen vacancy concentration starts to influence the carrier concentration. It does not mean that the oxygen vacancy concentration is negligible at this temperature, but on the contrary, the influence of oxygen vacancy concentration on total carrier concentration is negligible below this temperature and the concentration of oxygen vacancies is so small that their contribution to transport processes becomes minimal.

Initial studies on the electrical conductivities of ferrite materials have shown that oxygen vacancies play an important role in the electrochemical and catalytic

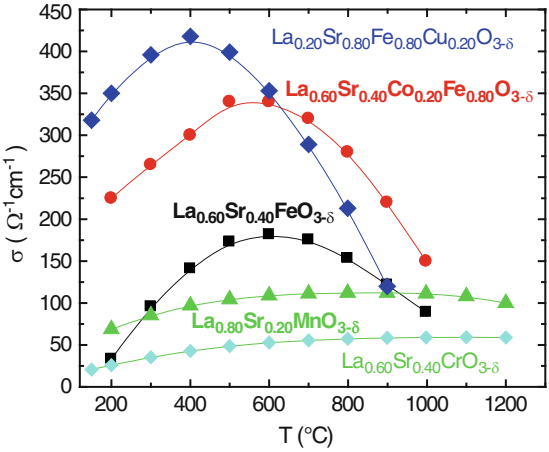

Fig. 9 A plot of conductivity measured in air as a function of temperature for five types of perovskites

properties that are commonly related to the electronic structure. Therefore, it is important to study the atomic structures of ferrite materials. For example, the overlap of transition metal and oxygen orbitals plays a dominant role in determining properties such as the generation of oxygen vacancies, holes, and the spin states of the transition metals. Research on low temperature cathode materials continuously draws attention to SOFC developments in and it is a challenge to simultaneously meet the requirements of fast electrochemical reduction of O_2 and fast oxide ion diffusion, around 600°C. Shao and Haile recently reported that $Ba_{0.5}Sr_{0.5}Co_{0.8}Fe_{0.2}O_3$ (BSCF) a proven oxygen separation membrane material, possessed an excellent cathode performance around 600°C (~1 W/cm^2) [40]. They attributed the improved cathode performance to fast oxide ion transport. Although the thermal expansion of BSCF might be fairly high, the material itself is of particular interest in the use as a component in low temperature SOFC cathode.

2.2.4 Materials Microstructure and Modeling

A large group of chemical compositions has been investigated as potential candidates for IT SOFC cathode materials. A recent article by Skinner has provided an overview of the progress of perovskite type oxides for the SOFC cathode, with an emphasis on the role of chemical compositions [41]. On the contrary, microstructure plays a major role in the cathode function as well. This is particularly true when the composite cathode, which shows a better performance compared to a single composition cathode, is used. Several authors have shown that electrode microstructure and transport properties have a profound effect on polarization. Tanner et al. [42] have shown that polarization resistance (R_p) depends upon the grain size, d, of the ionic conductor in the composite electrode and the volume fraction porosity, which was further derived as in (1) by considering the monolayer gas adsorption. A similar relation has been proposed as [43]:

$$R_{\text{chem}} = A\frac{1}{T}\sqrt{\frac{\tau}{(1-\varepsilon)aC_{\text{O}}^2 D^* k}} \tag{18}$$

where R_{chem}: chemical reaction induced R; D^*: oxygen self-diffusion coefficient ($\text{cm}^2\ \text{s}^{-1}$); k: oxygen surface exchange coefficient ($\text{cm}\ \text{s}^{-1}$); C_{O}: concentration ($\text{mol}\ \text{cm}^{-3}$) τ: tortuosity; ε: fractional porosity; a: surface area/unit volume. This equation explicitly shows the resistance induced by chemical reaction between the cathode and the electrolyte as a function of microstructure and reaction parameters, which can reveal some criteria for the search of the new cathode materials.

2.2.5 Chromium Poisoning

Metallic interconnects are Cr_2O_3-forming alloys that have compatible thermal expansion coefficients with other SOFC components. The reason for choosing alloys that develop Cr_2O_3 is because Cr_2O_3 has the best combination of slow growth rate and sufficient conductivity. Unfortunately, Cr_2O_3 gives out Cr-containing volatile species that deposit on electrolyte and electrode surfaces and interfaces [44], which leads to rapid deterioration of the cathode's oxygen reduction reaction rate, and thus to a significant decline in cell performance [45]. Volatilization of Cr_2O_3 was studied several decades ago by Caplan and Cohen [46–48], who showed that Cr_2O_3 was volatile only in an oxidizing atmosphere and that moisture significantly increased the rate of evaporation. In dry oxygen, the main volatile species is CrO_3, but this reaction has a high activation energy; therefore, is not much of a concern for SOFCs that operate at intermediate temperatures (ITs) between 650 and 800°C. With the presence of moisture, many gaseous Cr hydroxyl compounds are present, such as $CrO_2(OH)$, $Cr_2(OH)_3$, and $CrO_2(OH)_2$ [49]. The thermodynamics of the gaseous phase Cr species was reported by Ebbinghaus in 1993 [50]; the data were published for three gaseous Cr oxides and 12 gaseous Cr oxyhydroxides, as a function of temperature, oxygen activity and water vapor activity. Among them, $CrO_2(OH)_2$ is the most abundant and it also has the lowest activation energy.

Cr poisoning of the cathode in SOFCs has been studied for many years, particularly by groups in Germany [51–56]. The well-accepted conclusions are (1) Cr poisoning is a major contributor to cell degradation, particularly for long-term operations (2) the mechanism of Cr poisoning is not clear, although reactions of the cathode with $CrO_2(OH)_2$ are considered the likely cause. Badwal et al. [45] observed the formation of Cr containing spinel layers between the electrolyte and the cathode for cells with a high Cr containing interconnect (~95%) that had been operated at relatively high temperatures (~800°C). They concluded that Cr volatile species could compete with the oxygen reduction reaction, as:

$$2\text{CrO}_2(\text{OH})_2(\text{g}) + 6\text{e}' = \text{Cr}_2\text{O}_3 + 2\text{H}_2\text{O}\,(\text{g}) + 3\text{O}^{2-} \tag{19}$$

which can lead to the deposition of Cr species at the electrode/electrolyte interface. This has the effect of seriously degrading the cathode performance by decreasing

the three-phase electrode/electrolyte/gas boundary area, changing the surface electrochemistry of the electrode and blocking active sites for the oxygen reduction reaction. Results from PNNL and ANL showed that cells with ferritic steel interconnects degraded much faster at 700°C than that at 800°C, in particular with the presence of H_2O in the cathode gas. A more interesting reported result was that Cr poisoning was significantly faster using (La,Sr)FeO_3 (LSF) cathodes than with (La,Sr)MnO_3 (LSM). Both of these experiments were performed in single cell testing.

While this is of concern, the impact of this phenomenon on commercial SOFC stacks is unclear. At lower operating temperatures, Cr volatility from the oxide scales grown on metallic alloy interconnects is a problem, but not all Cr-containing oxides liberate volatile Cr species at the same rate, so appropriate tailoring of the scale chemistry may be helpful. If necessary, other mitigation strategies could be employed, involving, for example, a reduction in Cr vapor pressure and flux during stack operation and/or the development of Cr-tolerant cathode materials. Possible approaches include use of suitable surface layers on alloy interconnects to reduce Cr evaporation; La-chromites, Mn-chromite and non-Cr-containing oxides such as $(Mn,Co)_3O_4$ can reduce Cr flux during the operation of cell or stack. Such layers could potentially be applied either in a separate fabrication step (e.g., thermal spray) or grown in-situ through suitable modification of the alloy bulk or surface. Another approach is the gettering of Cr vapor present in the gas phase before it makes its way to the cathode/electrolyte interface [57]. Alloys protected from corrosion by a chromia scale and $LaCrO_3$-based perovskites are used as materials for the interconnect of SOFCs. The chromium vaporization of these materials was studied by thermochemical modeling. Partial pressures of the vaporizing species were determined for different O_2 and H_2O concentrations in the oxidizing gas. $CrO_2(OH)_2(g)$ and $CrO_3(g)$ are the most abundant species in air with and without humidity, respectively. The potential of the Cr-containing vapor species for the degradation of the electrical properties of an SOFC was analyzed by thermodynamic computations. The electrochemical reduction of the Cr-containing vapor species at the cathode/electrolyte/gas phase boundary can lead to polarization losses [56].

2.3 *Fuel/Anode Interaction*

The anode must be an excellent catalyst for the oxidation of fuel (H_2, CO), stable in the reducing environment of the fuel, electronically conducting, and must have sufficient porosity to allow the transport of the fuel to and the transport of the products of fuel oxidation away from the electrolyte/anode interface where the fuel oxidation reaction takes place [58]. The reaction taking place on the anode side is that of the fuels, such as hydrogen, which react with oxide ions that are delivered from the electrolyte. Electrons are the reaction product, accompanied by the formation of water:

$$H_2 + O^{2-} \rightarrow H_2O + 2e^- \tag{20}$$

Hence, the anode must be catalytically active to oxidize the fuel and electronically conductive to transport electrons. The other requirements include matching of thermal expansion coefficients of the electrolyte and the interconnect; integrity of porosity for gas permeation; chemical stability with the electrolyte and the interconnect; and applicability to use with versatile fuels and impurities (such as sulfur). In addition, cost-effectiveness is always a factor in commercialization processes.

2.3.1 Ni-YSZ Anode Materials

During the early stage of SOFC development, the anode materials were precious metals (such as Pt and Au) and transition metals (such as Fe and Ni), primarily because of their catalytic activity. These anode candidates, however, cannot meet the stringent aforementioned requirements for the anode in SOFC. For instance, Ni is found to be an excellent catalyst; however, it possesses a high thermal expansion coefficient (13.4×10^{-6}/°C), and exhibits a coarsening of microstructure due to metal aggregation through grain growth. YSZ was discovered to constrain Ni aggregation [59, 60]. The YSZ prevents sintering of the nickel particles, decreases the effective thermal expansion coefficient bringing it closer to that of the electrolyte, and provides better adhesion of the anode with the electrolyte. In the Ni/YSZ cermet anode, nickel has the dual roles of catalyst for hydrogen oxidation and electrical current conductor. In addition to being an excellent catalyst for the oxidation of hydrogen, nickel is also highly active for the steam reforming of methane [61]. This catalytic property is exploited in so-called internal reforming SOFCs that can operate on fuels composed of mixtures of methane and water. Although nickel is an excellent hydrogen oxidation and methane-steam-reforming catalyst, it also catalyzes the formation of carbon from hydrocarbons under reducing conditions. Unless sufficient amounts of steam are present along with the hydrocarbon to remove carbon from the nickel surface, the anode may be destroyed. As a result, even when using methane as the fuel, relatively high steam-to-carbon ratios are needed to suppress this deleterious reaction. Unfortunately, due to the high catalytic activity of nickel for hydrocarbon cracking, this approach does not work for higher hydrocarbons, and it is generally not possible to operate nickel-based anodes on higher hydrocarbon-containing fuels without pre-reforming with steam or oxygen.

One approach to overcoming the limitations of nickel anodes, which has met with some success, is to augment the oxidation activity of Ni/YSZ cermets through the addition of an oxide-based oxidation catalyst. For example, stable operation on dry methane has been reported at 650°C in an SOFC using an yttria-doped ceria interlayer between the YSZ electrolyte and the Ni/YSZ cermet anode [61]. Ceria is a well-known oxidation catalyst, and might be expected to increase the activity of the anode for the electrochemical oxidation of methane. This approach still requires, however, that the operating temperature be maintained below 700°C to suppress carbon deposition reactions that take place on nickel.

2.3.2 Morphology and Microstructure of Ni-YSZ Anode

Patterned Ni stripe electrodes were prepared on the surface of YSZ electrolyte to elucidate the reaction mechanism of SOFC anode in H_2/H_2O environments. Ni stripes provide well which have well-defined length and morphology of the gas/nickel/YSZ triplet phase boundary. The rate of anodic reaction was found to be essentially determined by the reaction of H_2 and the adsorbed oxygen on the nickel surface [62, 63]. The relations between anode morphology and electrochemical performance of Ni/YSZ anodes were reported in anode supports with various particle sizes. The active thickness of the fine cermet anode is demonstrated to be about 10 μm and is believed to relate to the conductivity of the YSZ network. In the temperature range 850–1,000°C, polarization resistance exhibits an apparent activation energy, which increases with coarseness of the anode. Physical transport limitations are suggested as possible causes for the observed anode polarization [64]. Issues with Ni-based anodes are redox tolerance, sulfur poisoning, and carbon deposition in hydrocarbon fuels. Nickel is easily oxidized above 500°C. The presence of sulfur or sulfur-containing compounds in the fuel leads to degradation of anode performance even when the S content is less than 5 ppm. The nickel anode is not stable in the presence of hydrocarbons due to hydrocarbon cracking, which results from the propensity of Ni to catalyze carbon formation. The case is even worse when liquid fuel is used. Additionally, carbon deposition was reported to take place even when carbon was not the thermodynamically preferred product [60].

2.3.3 Other Anode Materials

A unique aspect of the anode in SOFCs is that one can utilize the high operation temperature (>600°C) for endothermic reforming. Ideally, gasoline, diesel or even soot can be used as the fuel, provided that there exists a suitable material that can function as an active catalyst, as well as an active anode. This places significant challenges and opportunities to the chemical engineers and materials scientists. Current advances in the SOFC anode technologies include the development of improved nickel-zirconia composites, a Cu/ceria anode for direct oxidation of hydrocarbons, and ceramic anode. Copper/ceria composite was used as the SOFC anode for the direct oxidation of hydrocarbon fuels. Unlike Ni, Cu is not an active catalyst for the carbon formation. The addition of CeO_2 provides active catalytic sites. A mixture of Cu–CeO_2–YSZ was developed by Gorte et al. [65, 66]. In addition, Cu-based anodes possess sulfur tolerance and relatively low sintering temperature for an anode. The development of ceramic anodes is of particular interest, particularly in building an "all ceramic cell". Doped perovskite compounds, (La,Sr)TiO_3, (La,Sr)CrO_3 are used with addition of CeO_2 as the anodes [67, 68]. Very recently, Zhan and Barnett used a catalytic layer of Ru-CeO_2/CeO_2-ZrO_2/Ru-CeO_2 on top of the conventional Ni-based anode [69]. The catalytic layer allows internal reforming of iso-octane without coking and yielded stable power densities of 0.3–0.6 W/cm^2. The idea of using bi-layer anode is of particular

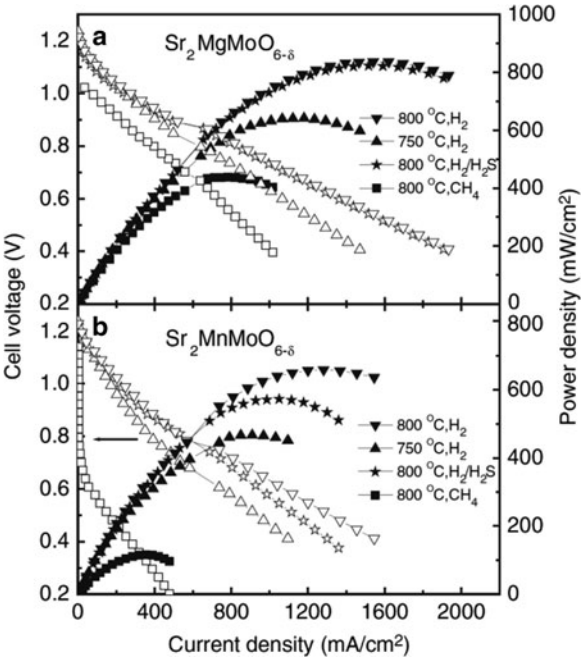

Fig. 10 Cell voltage and power density vs. current density for the single cells with $SrCo_{0.8}Fe_{0.2}O_3$ as the cathode and with anodes of (**a**) with $Sr_2MgMoO_{6-\delta}$ and (**b**) $Sr_2MnMoO_{6-\delta}$ in H_2, H_2/H_2S, and CH_4 at 750 and 800°C. Cell voltages are represented by *open symbols*, and power densities by *closed symbols* [71]

interest, albeit the catalytic layer used by Zhan and Barnett possessed lower gas permeation in the anode and higher electronic resistance. On the contrary, ceramic oxides offer more possibilities in terms of catalytic, electrochemical and mechanical properties, and sulfur tolerance [70], which warrants extensive studies. For instance, Goodenough's group reported the double perovskites, $Sr_2Mg_{1-x}Mn_xMo_{6-\delta}$, which was found to meet the requirements for tolerance to sulfur with long-term stability (Fig. 10); moreover, the double perovskites showed good electrochemical performance in hydrogen and methane [71].

3 Structure and Chemical Bonding at the Micrometer Scale

3.1 Gas Diffusion Requirement

In an operating SOFCs, gases (air or fuel) diffuse through the porous electrodes to reach electrode/electrolyte interfaces. The gas diffusion rate must be fast enough to minimize the diffusion loss. Three primary processes are involved with gas diffusion in porous electrodes: ordinary diffusion, Knudsen diffusion, and surface diffusion. The surface diffusion is negligible at elevated temperatures (e.g., 600–800°C). The question remains as to whether ordinary diffusion or Knudsen diffusion is the limiting step of the diffusion process. The answer resides in the pore

size in the media. If the pore size is larger than the mean free path of the gas molecule at a given temperature, the ordinary diffusion is the predominant mechanism. On the contrary, the Knudsen diffusion is governing when the pore size is smaller than the mean free path. Assuming the cell works at 600°C and using Fuller's equation, the ordinary diffusion coefficient of oxygen in air at 600°C is 1.28 cm^2/sec, which is in good agreement with the published data shown in Fig. 11 (Zhang, personal communication).

The Knudsen diffusion coefficient (D_k) is determined by the pore radius (r), temperature (K), and gas molecular weight (M):

$$D_k = 9700\, r\, (T/M)^{0.5} \tag{21}$$

Hence, at 600°C, when the pore size is ~0.5 μm, Knudsen diffusion coefficient of O_2 is equal to the ordinary diffusion coefficient. When the pore size is less than 0.5 μm, the molecular oxygen diffusion is limited by the collisions between molecular oxygen and pore walls; therefore, accompanied by high diffusion resistance. To minimize the diffusion resistance, larger pore size is desirable to ensure that the Knudsen diffusion coefficient be greater than the ordinary diffusion coefficient. In other words, the pore size must be larger than 5 μm to avoid pore walls to inhibit the oxygen diffusion along the pore channels to the three-phase boundary area.

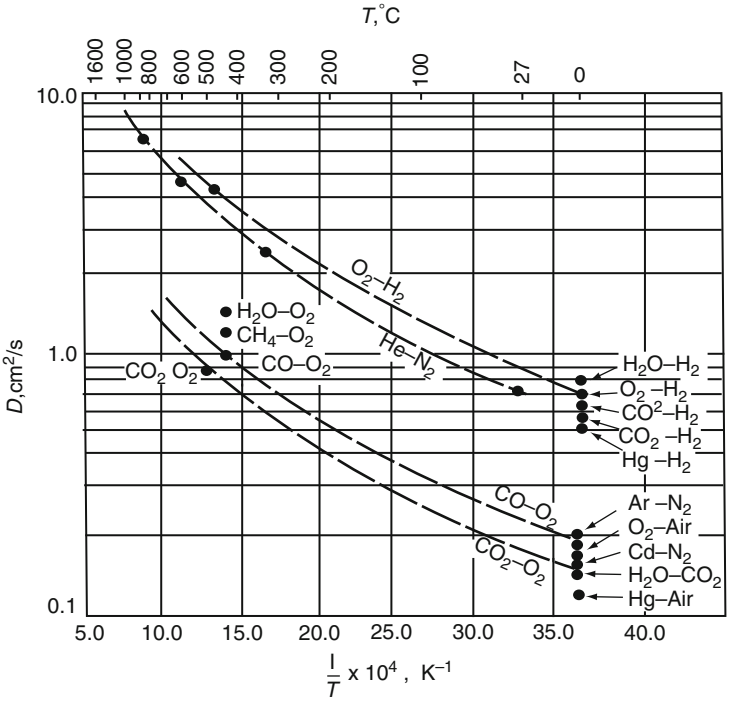

Fig. 11 Diffusion coefficients in gas mixtures

3.2 Triple Phase Boundary

In LSM-based cathode, the concept of TPB plays a crucial role in understanding oxygen reduction mechanisms and the kinetics (i.e., the exchange current density) when LSM is used as the cathode. TPB is the location where electronic conductor (phase I), ionic conductor (phase II), and gas (phase III) meet. As mentioned above, the ionic conductivity is relatively low in LSM, it is generally assumed that the (electrode) surface path dominates the reaction rate of the cathodic reaction. Therefore, a large TPB length, as is realized in composites consisting of electrode and electrolyte particles, is expected to be favorable, and, in fact, composite cathodes are successfully applied in SOFCs [72, 73]. The relationship between the overpotential and the TPB length was investigated by constructing a model, indicating the effective thickness of it was observed to be less than 20 μm [74].

To gain insights into mechanisms governing the cathodic oxygen reduction and incorporation reaction, patterned dense microelectrodes were employed by several groups to investigate the role of geometry on the cathodic polarization resistance of LSM and Pt on YSZ [25, 75–77]. Virkar and his colleagues [76, 77] showed charge transfer resistance is inversely proportional to TPB length, hence proportional to grain size by using sputtering LSM or Pt cathode. Dense YSZ disk (~3.5 mm) electrolyte was sintered at 1,500°C and the surface was polished to a 1 μm finish. Micro-photolithography was used to prepare masks for deposition of LSM of nearly 0.5 μm thickness by radiofrequency sputtering. The as-sputtered LSM electrodes were designed to have identical active areas (electrode–electrolyte interface), but with different TPB length (l_{TPB}). The half cell reaction, i.e., oxygen reduction, was then studied by measuring impedance spectra as a function of oxygen partial pressure and temperature. They found that area specific charge-transfer resistance, R-ct, varied inversely with l_{TPB}. While the charge-transfer resistance is inversely proportional to l_{TPB}, consistent with the charge-transfer reaction occurring mainly at the TPB, at 800°C some transport through LSM also appears to occur.

3.3 Sealant

Within the SOFC stack, an effective seal must have a thermal expansion coefficient which matches the fuel cell components, it must be electrically insulating and must be thermochemically stable under the operating conditions of the stack. The seal should exhibit no deleterious interfacial reactions with other cell components, should be stable under both the high temperature oxidizing and reducing operational conditions, should be created at a low enough temperature to avoid damaging cell components (under 850°C for some materials), and should not migrate or flow from the designated sealing region during sealing or cell operation. In addition, the sealing system should be able to withstand thermal cycling between the operational temperature and room temperature. That is, thermal stresses that develop because of

mismatches in the thermal contraction characteristics of the different SOFC materials either must be reduced to well below the failure strengths of the materials or must be relieved in some fashion.

A number of different sealing approaches are under development, including rigid, bonded seals (e.g., glass-ceramics and brazes), compliant seals (e.g., viscous glasses), and compressive seals (e.g., mica-based composites); multiple sealants may be used in any given stack design between different components [57]. Rigid seals typically rely on a glass that softens and "glues together" the adjacent stack components during stack fabrication (at a temperature above the operating temperature), but then becomes rigid and immobile, frequently due to crystallization, when cooled to the operating temperature.

Glass-based seals represent a relatively straightforward means of sealing an SOFC stack (at least initially), but the brittle nature of glasses (below the glass transition temperature) and glass-ceramics makes the seals vulnerable to crack formation (resulting from stresses related to thermal expansion mismatches with the adjacent components). As a consequence, the coefficient of thermal expansion must be similar to that of the other components. While glass compositions can be tailored to optimize their physical properties, the selection of glasses offering appropriate thermal expansion behavior is relatively narrow, and the selection is further limited by the need for the glass to have appropriate wetting behavior and viscosity at the sealing temperature. An "invert glass" was developed by Brow et al. [78], who employed a concept of ceramic-glass structure. The origin glass can be converted to a glass-ceramic by a heat treatment, which provides strong bonds to YSZ and to ferritic steels through a glass phase to achieve the hermeticity, whereas maintains the sealant integrity through the ceramic phase. Moreover, the "invert glass" possesses a chemical compatibility with the Cr-containing alloys, as indicated by little interfacial reaction between the seals and the interconnects.

4 Structure and Chemical Bonding at the Macro Scale

An aforementioned single cell generally produces voltage less than 1 V and power around 1 W/cm^2. A series of connected single cells, or stack, therefore, is needed to yield higher power. Unlike a single cell, which deals with mostly material aspects of the components, research on fuel cell stacks must consider many other issues with the object of generating maximum stable power. The design of SOFC stack must take into account the following issues: (1) electrochemical performance, which is to generate more power out of the stack; (2) structural and mechanical integrity, which allows the stack to be operated at high temperature with sufficient long duration and possible thermal cycles; (3) gas manifold, which considers supplying reactant gas to a large cell area, removing reaction products and providing gas hermeticity, and (4) ease of fabrication. The readers are encouraged to refer to the literature for more information on stack design, fueling reforming and stack modeling [79–81]. In terms of stack design, since 1960s, most development

has focused on planar and tubular design cells, each of these designs having a number of interesting variants; for example, the planar SOFC may be in the form of a circular disk fed with fuel from the central axis, or it may be in the form of a square plate fed from the edges. The tubular SOFC may be of a large diameter (>15 mm), or of much smaller diameter (<5 mm), the so-called microtubular cells. Also, the tubes may be flat and joined together to give higher power density and easily printable surfaces for depositing the electrode layers. Here, we will discuss seals, interconnect, and examples of two main generic designs of stacks.

4.1 Interconnect

The interconnects in SOFC systems provide the electrical connection between cells and ensure gas separation within the cell stack. The interconnect must be chemically, electronically and mechanically compatible with the other cell components and must be stable in both oxidizing and reducing environments. For high temperature operations (900–1,000°C), perovskite type chromites (LaCrO3 based) have been shown to be useful as interconnect materials. However, the cost associated with the fabrication of these ceramic interconnects hinders SOFC commercialization. Thus, in an effort to lower the overall cost of SOFCs, research is being done with the objective of lowering the operating temperature to an IT regime (600–800°C) so that corrosion-resistant metallic alloys can be used as the interconnect materials. The use of commercially available alloys not only offers the possibility of lower cost materials, but also may allow simpler fabrication processes than those required for the high-temperature conducting oxides. This section is focused on metallic interconnect.

The typical requirements of the interconnects include: high electronic conductivity with low ionic conductivity; chemical stability in both fuel and air; thermal expansion match to other cell components; high mechanical strength; high thermal conductivity; and chemical stability with regard to other cell components. In addition, when considering a stacking design, one must take account into ease of fabrication into various configurations.

The requirements of the interconnection are the most severe of all cell components and include: nearly 100% electronic conductivity; stability in both oxidizing and reducing atmospheres at the cell operating temperature since it is exposed to air (or oxygen) on the cathode side and fuel on the anode side; low permeability for oxygen and hydrogen to minimize direct combination of oxidant and fuel during cell operation; a thermal expansion coefficient close to that of the cathode and the electrolyte; and nonreactivity with other cell materials.

To satisfy these requirements, doped lanthanum chromite is used as the interconnection for cells intended for operation at about 1,000°C. Lanthanum chromite is a p-type conductor; its conductivity is due to small polaron hopping from room temperature to 1,400°C at oxygen pressures as low as 10^{-18} atm. The conductivity is enhanced as lower valence ions (e.g., Ca, Mg, Sr, etc.) are substituted on either the La^{3+} or the Cr^{3+} sites [82].

In cells intended for operation at lower temperatures (<800°C), it is possible to use oxidation-resistant metallic materials for the interconnection. Compared to lanthanum chromite ceramic interconnects, metallic alloys offer advantages such as improved manufacturability, significantly lower raw material and fabrication costs, and higher electrical and thermal conductivity. But to be useful for the interconnect application, the metallic alloys must satisfy additional requirements, including resistance to surface oxidation and corrosion in a dual atmosphere (simultaneous exposure to oxidizing and reducing atmospheres), thermal expansion matching to other stack components (particularly for stacks using a rigid seal design), chemical compatibility with other materials in contact with the interconnect, such as seals and cell materials, high electrical conductivity not only through the bulk material but also in in-situ-formed oxide scales, mechanical reliability and durability at the cell's operating temperature, and strong adhesion or bond strength between the as-formed oxide scale and the underlying alloy substrate. Ferritic stainless steels are the most promising candidates, owing to the fact that some alloys in this family offer a protective and conductive Cr-based oxide scale, appropriate thermal expansion behavior, ease of manufacturing and low cost. Several new ferritic stainless steels, such as Crofer22 APU, have also been developed specifically for the SOFC interconnect application. Although these alloys demonstrate improved performance over the traditional compositions, several critical issues remain. Among these are chromia scale evaporation and subsequent poisoning of cathodes; scale electrical resistivity in the long term; corrosion and spalling under interconnect exposure conditions; and compatibility with the adjacent components such as seals and electrical contact layers. As an alternative approach to developing new alloys, surface modification can result in enhanced performance. For example, electrically conductive perovskites and spinels can be applied onto metallic interconnects to minimize scale growth, electrical resistance and Cr volatility [57].

4.2 Cell Design and Power Systems

Currently, electrolyte-supported, cathode-supported, anode-supported, and metallic substrate-supported planar SOFCs are under development. In electrolyte-supported cells, the thickness of the electrolyte, typically YSZ, is 50–150 μm, making their ohmic resistance high, and such cells are suitable only for operation at ~1,000°C. In electrode-supported designs, the electrolyte thickness can be much lower, typically 5–20 μm, which decreases their ohmic resistance and makes them better suited for operation at lower temperatures. The anode (Ni/YSZ cermet) is selected as the supporting electrode, because it provides superior thermal and electrical conductivity, superior mechanical strength, and minimal chemical interaction with the electrolyte. Kim et al. [83] have reported power densities as high as 1.8 W/cm^2 at 800°C for such anode-supported SOFCs. At Pacific Northwest National Laboratory [84, 85], similar anode-supported cells have been developed using ~10 μm

thick tape cast YSZ electrolyte and ~600 μm thick tape cast Ni/YSZ anode, which are laminated together and co-sintered at about 1,350°C for 1 h. Cathode consists of either Sr-doped lanthanum manganite, LSM+YSZ, or Sr-doped lanthanum ferrite (LSF), which is applied to the electrolyte by screen printing and then sintered. Cells with LSF cathode and a $Ce_{0.8}Sm_{0.2}O_{1.9}$ interlayer between the LSF cathode and the YSZ electrolyte have shown a power density of up to 1 W/cm^2 (at 0.7 V) at 800°C with air as oxidant and a mixture of 97% H_2+3% H_2O as fuel. The performance of these cells depends to a large extent on the microstructures of the cathode and at the cathode/electrolyte interface; optimization of cathode and interlayer materials and microstructures can provide still higher and stable performance.

4.2.1 Planar SOFC Design

In the planar design, a series of cell components are configured as thin, flat plates, then electrically connected to build up desirable electrochemical performance. Shown in Fig. 12 is a generic schematic of a planar SOFC design. Planar designs offer several potential advantages, including simpler and less expensive manufacturing processes and higher power densities than tubular cells described in the next section. However, planar designs need high temperature gas-tight seals between the components in the SOFC stack; such seals are not necessary with tubular cells. These seals must prevent (or at least minimize sufficiently for acceptable performance) both leakage of fuel and oxidant gases from the stack to the outside environment, and mixing of fuel and oxidant gases within the stack; leakage of fuel leads to reduced stack efficiency (as a lower fraction of the input fuel is available for conversion to electricity), while mixing of fuel and oxidant within the stack not only reduces efficiency but can also lead to degradation of the cell

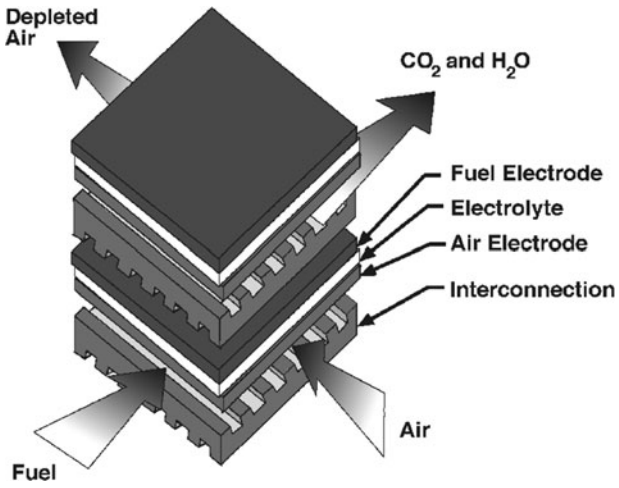

Fig. 12 Planar solid oxide fuel cell design

components owing to localized "hot spots" resulting from the heat of the combustion reactions. The seals must also offer electrical insulation to prevent shorting between cells within the stack.

The most important feature of the planar design shown in Fig. 12 may reside in the configuration of gas flow and gas manifold, which play a crucial role in minimizing the use of seals, improving fuel utilization, managing uniform distribution of temperature and current to reduce thermal stress, and improving the stability of the stack. Generally, the interconnect is ribbed on both sides to adopt cross-flow, co-flow, or counter-flow. The initial planar design SOFC configuration employed the electrolyte as the support, which required operating temperature often higher than 900°C. Advances in ceramic processing allow reproducible fabrication of thin electrolytes 10 μm by low-cost conventional ceramic processing techniques such as tape casting, tape calendaring, slurry sintering, screen printing, or by plasma spraying.

4.2.2 Tubular SOFC Design

In the tubular SOFC, as illustrated by the Siemens Westinghouse design shown in Fig. 13 [86], the cell components are deposited in the form of thin layers on a doped lanthanum manganite cathode tube [80, 87]. The cathode tube (2.2 cm diameter, 2.2 mm wall thickness, about 180 cm length) is fabricated by extrusion followed by sintering to obtain about 30–35% porosity. Up until recently, a dense YSZ electrolyte (about 40 μm thick) and a porous Ni-YSZ anode (about 100–150 μm thick) layers were deposited on this cathode tube by electrochemical vapor deposition [88]. However, since the electrochemical vapor deposition process is complex and capital-cost intensive, both of these layers are now deposited by atmospheric plasma spraying to reduce cost [86]. The doped lanthanum chromite interconnection, in the form of about 85 μm thick strip along the length of the cathode tube, is

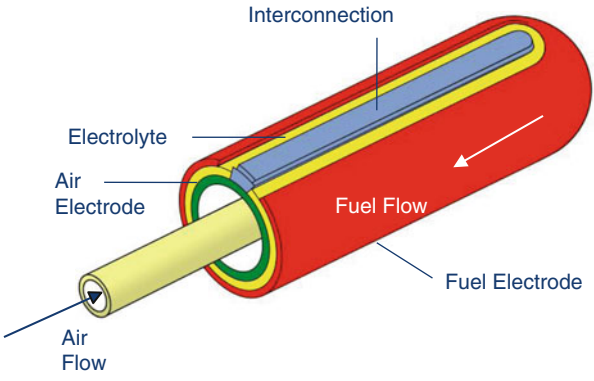

Fig. 13 Tubular solid oxide fuel cell design

also deposited by atmospheric plasma spraying followed by densification sintering to obtain a gas-tight layer [89].

The cell tube is closed at one end. For cell operation, oxidant (air or oxygen) is introduced through an alumina injector tube positioned inside the cell. The oxidant is discharged near the closed end of the cell and flows through the annular space formed by the cell and the coaxial injector tube. Fuel flows on the outside of the cell from the closed end and is electrochemically oxidized while flowing to the open end of the cell generating electricity. At the open end of the cell, the oxygen-depleted air exits the cell and is combusted with the partially depleted fuel. Typically, 50–90% of the fuel is utilized in the electrochemical cell reaction. Part of the depleted fuel is recirculated in the fuel stream and the rest combusted to preheat incoming air and/or fuel. The exhaust gas from the fuel cell is at 600–900°C depending on the operating conditions.

The single biggest advantage of tubular cells over planar cells is that they do not require any high temperature seals to isolate oxidant from the fuel, and this makes performance of tubular cell stacks very stable over long periods of times (several years). However, their areal power density is much lower (about 0.2 W/cm^2) compared to planar cells (up to 2 W/cm^2 for single cells and at least 0.5 W/cm^2 for stacks) and manufacturing cost is higher. The volumetric power density is also lower for tubular cells than for planar cells. To increase the power density and reduce the physical size and cost of tubular SOFC stacks, alternate tubular geometry cells are under development [90]. Such alternate geometry cells combine all the advantages of the tubular SOFCs, such as not requiring high temperature seals, while providing higher areal and volumetric power densities. The performance of these new design cells is much higher than that of cylindrical tubular cells, but still lower than that of anode-supported planar cells [90].

5 Summary

Both structure and chemical bonding play key roles in the electrochemical performance and stability of the SOFC – an electrochemical device which converts chemical energy of a fuel into electricity at temperatures from 500 to 1,000°C. In the ionic conductor used as the electrolyte, the ionic conductivity is related to the crystal structure, ionic radii of the cations, lattice parameter, residual strain in the material, and temperature. The bonding between the cation and oxygen ion determines the stability of ionic conductivity. Doped ZrO_2 was found to be the most stable ionic conductor against reducing environments. The electrochemical activity of both cathode and anode is determined by the local chemistry of the materials and microstructure of the electrode. Improving the mixing conduction appears to enhance the electrochemical activity accordingly. The electrical resistance of tubular SOFCs is high, and areal power density (W/cm^2) and volumetric power density (W/cm^3) low; higher power density alternate tubular geometry cells are now being conceived and developed. Planar SOFCs are capable of achieving very

high power densities, but require high temperature seals, which are a big factor in their performance stability and useful lifetime. The challenge in successfully commercializing SOFCs offering high-power densities and long-term durability requires reduction of costs associated with the cells and the balance-of-plant.

References

1. Mogensen M, Sammes NM, Tompsett GA (2000) Physical, chemical and electrochemical properties of pure and doped ceria. Solid State Ionics 129:63–94
2. Kroger FA, Vink HJ (1957) In: Seitz F, Turnbull T (eds) Solid state physics – advances in research and applications. Academic, New York
3. Balducci G, Kaspar J, Fornasiero P, Graziani M, Islam MS, Gale JD (1997) Computer simulation studies of bulk reduction and oxygen migration in CeO_2-ZrO_2 solid solutions. J Phys Chem B 101:1750–1753
4. Zhou XD, Scarfino B, Anderson HU (2004) Electrical conductivity and stability of Gd-doped ceria/Y-doped zirconia ceramics and thin films. Solid State Ionics 175:19–22
5. Azad AM, Larose S, Akbar SA (1994) Bismuth oxide-based solid electrolyte for fuel-cells. J Mater Sci 29:4135–4151
6. Sammes NM, Tompsett GA, Nafe H, Aldinger F (1999) Bismuth based oxide electrolytes – Structure and ionic conductivity. J Eur Ceram Soc 19:1801–1826
7. Wachsman ED (2004) Effect of oxygen sublattice order on conductivity in highly defective fluorite oxides. J Eur Ceram Soc 24:1281–1285
8. Wachsman ED (2002) Functionally gradient bilayer oxide membranes and electrolytes. Solid State Ionics 152:657–662
9. Jiang NX, Wachsman ED, Jung SH (2002) A higher conductivity Bi_2O_3-based electrolyte. Solid State Ionics 150:347–353
10. Wachsman ED, Boyapati S, Kaufman MJ, Jiang NX (2000) Modeling of ordered structures of phase-stabilized cubic bismuth oxides. J Am Ceram Soc 83:1964–1968
11. Wachsman ED, Ball GR, Jiang N, Stevenson DA (1992) Structural and defect studies in solid oxide electrolytes. Solid State Ionics 52:213–218
12. Bogicevic A, Wolverton C, Crosbie GM, Stechel EB (2001) Defect ordering in aliovalently doped cubic zirconia from first principles. Phys Rev B 64:014106
13. Boyapati S, Wachsman ED, Chakoumakos BC (2001) Neutron diffraction study of occupancy and positional order of oxygen ions in phase stabilized cubic bismuth oxides. Solid State Ionics 138:293–304
14. Goff JP, Hayes W, Hull S, Hutchings MT, Clausen KN (1999) Defect structure of yttria-stabilized zirconia and its influence on the ionic conductivity at elevated temperatures. Phys Rev B 59:14202
15. Arachi Y, Sakai H, Yamamoto O, Takeda Y, Imanishai N (1999) Electrical conductivity of the ZrO_2-Ln_2O_3 (Ln = lanthanides) system. Solid State Ionics 121:133–139
16. Garcia-Barriocanal J, Rivera-Calzada A, Varela M et al (2008) Colossal ionic conductivity at interfaces of epitaxial ZrO2: Y2O3/SrTiO3 heterostructures. Science 321:676–680
17. Kilner JA (2008) Ionic conductors: feel the strain. Nat Mater 7:838–839
18. Anderson HU, Zhou X-D, Dogan F (2004) Defect chemistry of mixed ionic/electronic p-type oxides. NATO Sci II Math Phys Chem 173:303–312
19. Zhou XD, Anderson HU (2005) In: Sorrell CC, Sugihara S (eds) Defect chemistry and ternary oxides. Materials for Energy Conversion Devices, CRC Press 235–259
20. Yasuda I, Hikita T (1993) Electrical conductivity and defect structure of calcium-doped lanthanum chromites. J Electrochem Soc 140:1699–1704

21. Mizusaki J, Mori N, Takai H et al (2000) Oxygen nonstoichiometry and defect equilibrium in the perovskite-type oxides $La_{1-x}Sr_xMnO_{3+d}$. Solid State Ionics 129:163–177
22. Mizusaki J, Sasamoto T, Cannon WR, Bowen HK (1983) Electronic conductivity, Seebeck coefficient, and defect structure of $La_{1-x}Sr_xFeO_3$ (x=0.1, 0.25). J Am Ceram Soc 66:247–252
23. Mizusaki J, Saito T, Tagawa H (1996) A chemical diffusion-controlled electrode reaction at the compact $La_{1-x}Sr_xMnO_3$/stabilized zirconia interface in oxygen atmospheres. J Electrochem Soc 143:3065–3073
24. De Souza RA, Kilner JA (1998) Oxygen transport in $La_{1-x}Sr_xMn_{1-y}Co_yO_{3+/-delta}$ perovskites – Part I. Oxygen tracer diffusion. Solid State Ionics 106:175–187
25. Brichzin V, Fleig J, Habermeier HU, Cristiani G, Maier J (2002) The geometry dependence of the polarization resistance of Sr-doped $LaMnO_3$ microelectrodes on yttria-stabilized zirconia. Solid State Ionics 152:499–507
26. Lau SK, Singhal SC (1985) Potential electrode/electrolyte interactions in solid oxide fuel cells. Corrosion 85:1–9
27. Yokokawa H, Sakai N, Kawada T, Dokiya M (1991) Thermodynamic analysis of reaction profiles between LaMO3 (M=Ni, Co, Mn) and ZrO2. J Electrochem Soc 138:2719–2727
28. Wiik K, Schmidt CR, Faaland S, Shamsili S, Einarsrud MA, Grande T (1999) Reactions between strontium-substituted lanthanum manganite and yttria-stabilized zirconia: I, powder samples. J Am Ceram Soc 82:721–728
29. Kleveland K, Einarsrud MA, Schmidt CR et al (1999) Reactions between strontium-substituted lanthanum manganite and yttria-stabilized zirconia: II, diffusion couples. J Am Ceram Soc 82:729–734
30. Clausen C, Bagger C, Bildesorensen JB, Horsewell A (1994) Microstructural and microchemical characterization of the interface between $La_{0.85}Sr_{0.15}MnO_3$ and Y_2O_3-Stabilized ZrO_2. Solid State Ionics 70:59–64
31. Horita T, Yamaji K, Sakai N et al (2002) Imaging of oxygen transport at SOFC cathode/electrolyte interfaces by a novel technique. J Power Sources 106:224–230
32. Becker JS, Westheide J, Saprykin AI, Holzbrecher H, Breuer U, Dietze HJ (1997) Mass spectrometric analysis of ceramic components for solid oxide fuel cells. Mikrochim Acta 125:153–160
33. Horita T, Yamaji K, Kato T, Sakai N, Yokokawa H (2004) Imaging of labeled gas movements at the SOFC electrode/electrolyte interfaces. Solid State Ionics 169:105–113
34. Horita T, Yamaji K, Sakai N, Yokokawa H, Kawada T, Kato T (2000) Oxygen reduction sites and diffusion paths at $La_{0.9}Sr_{0.1}MnO_{3-x}$/yttria-stabilized zirconia interface for different cathodic overvoltages by secondary-ion mass spectrometry. Solid State Ionics 127:55–65
35. Karim DP, Aldred AT (1979) Localized level hopping transport in $La(Sr)CrO_3$. Phys Rev B 20:2255–2263
36. Kuo JH, Anderson HU, Sparlin DM (1990) Oxidation reduction behavior of undoped and Sr-doped $LaMnO_3$ – defect structure, electrical conductivity, and thermoelectric power. J Solid State Chem 87:55–63
37. Tai LW, Nasrallah MM, Anderson HU, Sparlin DM, Sehlin SR (1995) Structure and electrical properties of $La_{1-x}Sr_xCo_{1-y}Fe_yO$. 1. The system $La_{0.8}Sr_{0.2}Co_{1-y}Fe_yO_3$. Solid State Ionics 76:259–271
38. Tai LW, Nasrallah MM, Anderson HU, Sparlin DM, Sehlin SR (1995) Structure and electrical properties of $La_{1-x}Sr_xCo_{1-y}Fe_yO$. 2. The system $La_{1-x}Sr_xCo_{0.8}Fe_{0.2}O_3$. Solid State Ionics 76:273–283
39. Kaus I, Anderson HU (2000) Electrical and thermal properties of $La_{0.2}Sr_{0.8}Cu_{0.1}Fe_{0.9}O_{3-delta}$ and $La_{0.2}Sr_{0.8}Cu_{0.2}Fe_{0.8}O_{3-delta}$. Solid State Ionics 129:189–200
40. Shao ZP, Haile SM (2004) A high-performance cathode for the next generation of solid-oxide fuel cells. Nature 431:170–173
41. Skinner SJ (2001) Recent advances in Perovskite-type materials for solid oxide fuel cell cathodes. Int J Inorg Mater 3:113–121

42. Tanner CW, Fung KZ, Virkar AV (1997) The effect of porous composite electrode structure on solid oxide fuel cell performance.1. Theoretical analysis. J Electrochem Soc 144:21–30
43. Adler SB, Lane JA, Steele BCH (1996) Electrode kinetics of porous mixed-conducting oxygen electrodes. J Electrochem Soc 143:3554–3564
44. Jiang SP, Zhang JP, Zheng XG (2002) A comparative investigation of chromium deposition at air electrodes of solid oxide fuel cells. J Eur Ceram Soc 22:361–373
45. Badwal SPS, Deller R, Foger K, Ramprakash Y, Zhang JP (1997) Interaction between chromia forming alloy interconnects and air electrode of solid oxide fuel cells. Solid State Ionics 99:297–310
46. Caplan D, Cohen M (1961) The volatilization of chromium oxide. J Electrochem Soc 108:438–442
47. Caplan D, Cohen M (1952) High temperature oxidation of some iron-chromium alloys. J Met 4:1057–1065
48. Caplan D, Cohen M (1952) High temperature oxidation of some iron-chromium alloys. Trans Am Inst Min Metall Eng 194:1057–1065
49. Farber M, Srivasta RD (1973) Mass-spectrometric investigation of reactions involving vanadium and chromium with potassium-seeded H_2-O_2 flames. Combust Flame 20:43–49
50. Ebbinghaus BB (1993) Thermodynamics of gas-phase chromium species – the chromium oxides, the chromium oxyhydroxides, and volatility calculations in waste incineration processes. Combust Flame 93:119–137
51. Stanislowski M, Wessel E, Hilpert K, Markus T, Singheiser L (2007) Chromium vaporization from high-temperature alloys I. Chromia-forming steels and the influence of outer oxide layers. J Electrochem Soc 154:A295–A306
52. Stanislowski M, Froitzheim J, Niewolak L et al (2007) Reduction of chromium vaporization from SOFC interconnectors by highly effective coatings. J Power Sources 164:578–589
53. Konysheva E, Penkalla H, Wessel E et al (2006) Chromium poisoning of perovskite cathodes by the ODS alloy Cr5Fe1Y(2)O(3) and the high chromium ferritic steel Crofer22APU. J Electrochem Soc 153:A765–A773
54. Peck DH, Miller M, Hilpert K (2002) Vaporization and thermodynamics of the MgO-Cr_2O_3-La_2O_3 system investigated by Knudsen effusion mass spectrometry. Solid State Ionics 147:29–40
55. Gindorf C, Singheiser L, Hilpert K (2001) Chromium vaporisation from Fe,Cr base alloys used as interconnect in fuel cells. Steel Res 72:528–533
56. Hilpert K, Das D, Miller M, Peck DH, Weiss R (1996) Chromium vapor species over solid oxide fuel cell interconnect materials and their potential for degradation processes. J Electrochem Soc 143:3642–3647
57. Stevenson JW, Singh P, Singhal SC (2005) The secrets of SOFC success. The Fuel Cell Review 2:15–21
58. Atkinson A, Barnett S, Gorte RJ et al (2004) Advanced anodes for high-temperature fuel cells. Nat Mater 3:17–27
59. Spacil HS (1970) US Patent 3,558,360
60. Jiang SP, Chan SH (2004) A review of anode materials development in solid oxide fuel cells. J Mater Sci 39:4405–4439
61. Murray EP, Tsai T, Barnett SA (1999) A direct-methane fuel cell with a ceria-based anode. Nature 400:649–651
62. Mizusaki J, Tagawa H, Saito T et al (1994) Preparation of nickel pattern electrodes on YSZ and their electrochemical properties in H_2-H_2O atmospheres. J Electrochem Soc 141: 2129–2134
63. Mizusaki J, Tagawa H, Saito T et al (1994) Kinetic-studies of the reaction at the nickel pattern electrode on Ysz in H_2-H_2O atmospheres. Solid State Ionics 70:52–58
64. Brown M, Primdahl S, Mogensen M (2000) Structure/performance relations for Ni/yttria-stabilized zirconia anodes for solid oxide fuel cells. J Electrochem Soc 147:475–485

65. Gorte RJ, Kim H, Vohs JM (2002) Novel SOFC anodes for the direct electrochemical oxidation of hydrocarbon. J Power Sources 106:10–15
66. Gorte RJ, Park S, Vohs JM, Wang CH (2000) Anodes for direct oxidation of dry hydrocarbons in a solid-oxide fuel cell. Adv Mater 12:1465–1469
67. Marina OA, Bagger C, Primdahl S, Mogensen M (1999) A solid oxide fuel cell with a gadolinia-doped ceria anode: preparation and performance. Solid State Ionics 123:199–208
68. Marina OA, Mogensen M (1999) High-temperature conversion of methane on a composite gadolinia-doped ceria-gold electrode. Appl Catal A-Gen 189:117–126
69. Zhan ZL, Barnett SA (2005) An octane-fueled olid oxide fuel cell. Science 308:844–847
70. Matsuzaki Y, Yasuda I (2000) The poisoning effect of sulfur-containing impurity gas on a SOFC anode: Part I. Dependence on temperature, time, and impurity concentration. Solid State Ionics 132:261–269
71. Huang YH, Dass RI, Xing ZL, Goodenough JB (2006) Double perovskites as anode materials for solid-oxide fuel cells. Science 312:254–257
72. Fleig J (2003) Solid oxide fuel cell cathodes: polarization mechanisms and modeling of the electrochemical performance. Ann Rev Mater Res 33:361–382
73. Adler SB (2004) Factors governing oxygen reduction in solid oxide fuel cell cathodes. Chem Rev 104:4791–4843
74. Fukunaga H, Ihara M, Sakaki K, Yamada K (1996) The relationship between overpotential and the three phase boundary length. Solid State Ionics 86–8:1179–1185
75. Brichzin V, Fleig J, Habermeier HU, Maier J (2000) Geometry dependence of cathode polarization in solid oxide fuel cells investigated by defined Sr-doped $LaMnO_3$ microelectrodes. Electrochem Solid State Lett 3:403–406
76. Radhakrishnan R, Virkar AV, Singhal SC (2005) Estimation of charge-transfer resistivity of Pt cathode on YSZ electrolyte using patterned electrodes. J Electrochem Soc 152:A927–A936
77. Radhakrishnan R, Virkar AV, Singhal SC (2005) Estimation of charge-transfer resistivity of $La_{0.8}Sr_{0.2}MnO_3$ cathode on $Y_{0.16}Zr_{0.84}O_2$ electrolyte using patterned electrodes. J Electrochem Soc 152:A210–A218
78. Brow RK, Reis ST, Benson GM (2005) US Patent Application
79. Minh NQ (1993) Ceramic fuel-cells. J Am Ceram Soc 76:563–588
80. Singhal SC (2000) Advances in solid oxide fuel cell technology. Solid State Ionics 135: 305–313
81. Singhal SC, Kendall K (2003) High temperature solid oxide fuel cells: fundamentals, design, and applications. Elsevier, Oxford, UK
82. Anderson HU (1992) Review of p-type doped perovskite materials for SOFC and other applications. Solid State Ionics 52:33–41
83. Kim JW, Virkar AV, Fung KZ, Mehta K, Singhal SC (1999) Polarization effects in intermediate temperature, anode-supported solid oxide fuel cells. J Electrochem Soc 146:69–78
84. Simner SP, Bonnett JR, Canfield NL et al (2003) Development of lanthanum ferrite SOFC cathodes. J Power Sources 113:1–10
85. Simner SP, Bonnett JF, Canfield NL, Meinhardt KD, Sprenkle VL, Stevenson JW (2002) Optimized lanthanum ferrite-based cathodes for anode-supported SOFCs. Electrochem Solid State Lett 5:A173–A175
86. DiGiuseppe G (2005) In: Singhal SC, Mizusaki J (eds) The electrochemical society proceedings series, SOFC-IX Pennington, NJ
87. Singhal SC (2000) Science and technology of solid-oxide fuel cells. MRS Bull 25:16–21
88. Pal UB, Singhal SC (1990) Electrochemical vapor-deposition of yttria-stabilized zirconia films. J Electrochem Soc 137:2937–2941
89. Kuo LJH, Vora SD, Singhal SC (1997) Plasma spraying of lanthanum chromite films for solid oxide fuel cell interconnection application. J Am Ceram Soc 80:589–593
90. Vora SD (2005) Fuel cell seminar extended abstracts. Courtesy associates, Washington, DC

Struct Bond (2011) 141: 33–83
DOI: 10.1007/430_2011_40

Published online: 7 April 2011

Electrocatalysis of Direct Alcohol Fuel Cells: Quantitative DEMS Studies

Hongsen Wang and Héctor D. Abruña

Abstract In this chapter, we present new insights in direct alcohol fuel cell-related anode electrocatalysis based on quantitative differential electrochemical mass spectrometry (DEMS) studies. First, we review the history and development of the DEMS technique, as well as the calibration method for quantification. We then discuss some contributions of quantitative DEMS to the study of the mechanism of methanol electrooxidation on Pt and PtRu model catalysts. We also discuss quantitative DEMS studies of the mechanism of dissociative adsorption and electrooxidation of ethanol and acetaldehyde at Pt, Pt_3Sn, PtRu, and PtRh nanoparticle catalysts. Finally, the mechanism of dissociative adsorption and electrooxidation of ethylene glycol and its oxidative derivatives on carbon-supported Pt, Pt_3Sn, and PtRu nanoparticle catalysts are discussed, based on quantitative DEMS results.

Keywords DEMS · Direct alcohol fuel cells · Dissociative adsorption of alcohols · Electrocatalysis · Electrooxidation of alcohols

Contents

H. Wang and H.D. Abruña (✉)
Department of Chemistry and Chemical Biology, Baker Laboratory, Cornell University, Ithaca, NY, USA
e-mail: hda1@cornell.edu

1 Introduction

Compared to polymer electrolyte membrane fuel cells that use hydrogen, direct alcohol fuel cells (DAFCs) are compact and therefore have attracted considerable attention due to their potential application as power sources for portable devices, such as cellular phones, notebook computers, and portable power supplies. Liquid fuels, such as methanol, ethanol, and ethylene glycol, have a higher volumetric energy density and better energy efficiency, and are more easily stored and transported than hydrogen. However, the development and widespread deployment of DAFCs have been hampered by: (1) slow electrode-kinetics, (2) CO and sulfur poisoning of the catalysts at low temperatures, (3) methanol crossover, and (4) high cost of the membrane and catalysts. In the case of catalysts, it is imperative to develop CO and S tolerant, more active and durable, and less expensive catalysts. To design better catalysts, we need a thorough understanding of the mechanisms and kinetics of fuel cell-related reactions. Such understanding will only come from fundamental studies.

The mechanism of methanol oxidation on Pt-based catalysts has been studied for several decades [1–14]. Complex parallel and series reaction pathways in which several adsorbed species and soluble intermediates were involved in methanol oxidation were proposed by Bagotzky et al. [2]. The in situ application of infrared spectroscopy during methanol oxidation showed that adsorbed CO is formed on the Pt surface [15]. However, other adsorbed intermediates are still not identified. Formaldehyde, formic acid, methyl formate, and dimethoxy methane have been identified as soluble intermediates [8, 10, 16–18]. The quantitative analysis of methanol oxidation products changing with various parameters can help us better understand the mechanism of methanol oxidation and identify reaction pathways. This can be achieved by online quantitative differential electrochemical mass spectrometry (DEMS), which will be discussed in Sect. 3.

It is widely recognized that, as a single component catalyst, platinum is the only element to show significant electrocatalytic activity toward methanol oxidation. The catalytic activity of platinum, however, is still much too low to consider direct methanol fuel cells (DMFCs) as practical power sources. In order to improve the

performance of DMFCs, platinum-based binary catalysts such as PtRu [3, 5, 13, 19–21], PtSn [22–24], and PtMo [25–27] have been examined for electrocatalytic activity toward the oxidation of methanol. PtRu binary catalysts, in particular, have proven to exhibit stable catalytic activity toward methanol electrooxidation. At present, the effects on methanol oxidation of a second metal as an alloy or adlayer element on platinum have been ascribed to the following reasons: (a) Bifunctional mechanism: in PtRu alloys, Ru sites adsorb oxygen-containing species at potentials 200–300 mV lower than on the pure platinum surface, and the carbonaceous species (such as CO) adsorbed on platinum sites are preferentially oxidized by oxygen-containing species formed on neighboring Ru atoms [3, 4]. (b) Electronic effect or ligand effect: the second metal modifies the electronic nature of the surface of the base metal [4, 13]. Such an effect was observed, for example, where the Pt-CO bond strength was found to be weakened by the presence of Ru or Sn [28]. In most studies, the effects of the second element on methanol oxidation are often discussed in terms of the resulting Faradaic currents. However, the effects on product distribution are seldom studied. In this chapter, we will also review new insights of the effect of Ru adatoms on the oxidation of methanol at platinum electrodes studied by online quantitative DEMS.

Compared to methanol, ethanol possesses intrinsic advantages such as low toxicity, comparable electrochemical activity, high theoretical volumetric/mass energy density, the fact that it is a renewable fuel, and its easy production by the fermentation from sugar-containing raw materials. Therefore, direct ethanol fuel cells (DEFCs) have spurred a great deal of interest in recent years [29, 30]. However, the complete oxidation of ethanol involves 12 electrons per molecule, leading to many adsorbed intermediates and byproducts during the ethanol oxidation process [31–35]. Furthermore, ethanol oxidation to CO_2 involves the cleavage of a C–C bond, which requires a much higher activation energy than C–H bond breaking, at least for currently known electrocatalysts [36]. In order to obtain reasonable rates, at moderate overpotentials, which would make DEFCs viable, more active anode electrocatalysts are urgently needed. Although Pt-based binary or even ternary alloys (e.g., PtSn, PtRu, PtRh, PtRuSn, PtRhSn) [32, 36–41] have been used as anodes in DEFCs to improve performance, the ethanol oxidation products are still mainly acetaldehyde and acetic acid [36, 39, 42]. The efficiency for ethanol oxidation can also be improved by optimization of the reaction parameters and conditions, e.g., by operating under conditions where the formation of poisoning reaction intermediates or the loss of volatile reaction intermediates is minimized. Strategies to achieve these goals require a thorough mechanistic and kinetic understanding of the processes proceeding during electrocatalytic ethanol oxidation, especially the rate-limiting step(s). In this chapter, quantitative DEMS studies on the mechanism of ethanol and acetaldehyde oxidation on Pt-based nanoparticle catalysts will also be reviewed. This will include a detailed analysis of the reaction pathways and a quantitative knowledge of the kinetics of the most important elementary reaction steps contributing to the total reaction process.

Ethylene glycol has a high boiling point and comparable electrochemical activity to methanol and ethanol, and thus is another alternative potential fuel for direct

fuel cells. Therefore, the electrochemical oxidation of ethylene glycol (EG) has attracted increasing interest over the past years. These previous studies have shown that in addition to the complete oxidation product, CO_2, EG electrooxidation leads to a number of partly oxidized byproducts. For example, glycolaldehyde, glyoxal, glycolic acid, glyoxylic acid, and oxalic acid as well as formaldehyde and formic acid have been identified by chromatographic analysis [43–46]. In addition, adsorbed CO has been detected, by in situ IR measurements, as a stable adsorbate [47–49]. Details of the reaction mechanism and the influence of the specific reaction conditions and parameters on the EG oxidation behavior, however, are much less known. Therefore, we have also systematically studied the electrooxidation of EG and its oxidative derivatives at real fuel cell catalysts by quantitative DEMS. The contribution of quantitative DEMS to the understanding of the mechanism of EG oxidation on Pt-based nanoparticle catalysts will be also reviewed.

Quantitative DEMS is a very powerful method to study the oxidation mechanisms of small organic molecules (SOMs) and the kinetics of related elementary reaction steps. DEMS allows online detection of gaseous and volatile products during electrochemical reactions, especially SOM oxidation, and analysis of organic adsorbates. When combined with suitable electrochemical cells and techniques, DEMS can provide quantitative information about gaseous and volatile products of electrochemical reactions and organic adsorbates. DEMS is a very sensitive analytical technique with a detection limit of ~0.1 nmol, and can analyze and even quantify submonolayer amount of organic adsorbates [50]. In the following sections, we will first briefly describe the history and development of the DEMS technique, and DEMS cell types, in which the use of a dual thin-layer flow cell will be emphasized. We will then focus on the use of DEMS, with the dual thin-layer flow cell, to comprehensively study the mechanism and kinetics of electrooxidation of alcohol molecules (methanol, ethanol, ethylene glycol, and its oxidative derivatives) under continuous reaction and continuous flow conditions on Pt and Pt-based bimetallic catalysts. We will first analyze the adsorbed poisoning species formed during molecule decomposition, and the saturated coverage of adsorbate and even their formation rate by detecting desorption products by DEMS. We will then discuss the product distribution (or current efficiency for product generation) of SOM oxidation in solution under controlled mass transport, as well as reductive products, which are calculated based on the DEMS measurements after proper calibration of the corresponding mass signals. Based on these results, a mechanism of SOM oxidation on Pt-based catalysts will be presented.

2 Differential Electrochemical Mass Spectrometry

In situ (or online) mass spectrometric detection of volatile electrochemical reaction products began in the early seventies, when Bruckenstein and Gadde used a porous non-wetting electrode for the coupling of an electrochemical cell to a mass spectrometer [51]. However, their system could only detect the integrated mass

spectrometric current following the closing off of the vacuum system from the pump. The technique was later improved by Wolter and Heitbaum [52, 53], so that the time constant was sufficiently short to allow the real-time online detection of volatile electrochemical reaction products during cyclic voltammetry and potential step amperometry. With proper design of the vacuum system and using turbomolecular pumps, product formation rates could be measured. To distinguish this technique from Bruckenstein's integrating approach, it was called "differential electrochemical mass spectrometry" (DEMS).

2.1 DEMS Setup

The DEMS vacuum system is shown in Fig. 1 and consists of two differentially pumped chambers and a quadrupole mass spectrometer. The ionization chamber and analysis chamber are pumped by two turbomolecular pumps, respectively, which are backed by diaphragm pumps or rotary vane pumps. The quadrupole mass spectrometer is located in the analysis chamber. The time constant of the mass spectrometer is typically in the millisecond regime. The electrochemical cell is connected to the ionization vacuum chamber via a valve at position 3 (see Fig. 1).

2.2 DEMS Cell Types

In order to detect, via mass spectrometry, volatile species that are generated at an electrode surface, they have to be transferred from the electrolyte phase to vacuum. To accomplish this, a membrane (e.g., a porous Teflon membrane), which separates

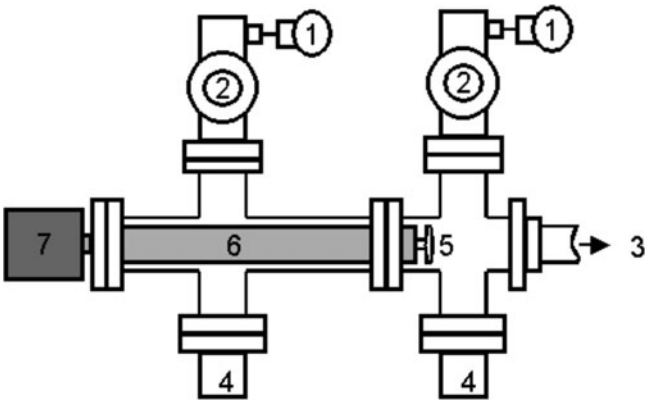

Fig. 1 The vacuum system of DEMS setup. *1* prepumps; *2* turbomolecular pumps; *3* connection to the electrochemical cell; *4* ion gauges; *5* ion source; *6* quadrupole rods; *7* electronic controller and detector

the electrolyte from vacuum, but is permeable to volatiles, is required. In addition, species need to be transferred from the electrode surface to this interface in a short time. For a fast introduction of species to the membrane, either the electrode has to be placed very close to the membrane, so that transport by diffusion is sufficiently fast, or proper convection has to be used. Several electrodes and cell types have been designed to achieve this goal. In the classical approach, the electrocatalyst layer, e.g., Pt, is sputter-deposited onto the porous Teflon membrane or a metallic lacquer containing small metallic particles is painted onto the Teflon membrane. This membrane, which is mechanically supported by a stainless steel frit, serves as the working electrode and the interface between the electrolyte and vacuum. A typical cell for these electrodes has been described in [54]. This type of DEMS cell has a very high collection efficiency, and the response time for the electrochemical reaction was determined to be about 0.1 s. However, the mass transport is not well defined, and a bulk electrode cannot be used with this cell.

In order to be able to detect volatile products of electrochemical reactions on bulk electrodes, e.g., single crystal electrodes, Baltruschat and coworkers developed a thin-layer DEMS cell [55, 56]. The bulk electrode, with a diameter of 1 cm, is separated from the porous Teflon membrane by a ~100-μm-thick Teflon gasket with an inner diameter of 6 mm. Volatile species generated at the electrode surface diffuse to the Teflon membrane within 2 s. Two capillaries positioned at opposite sides serve as electrolyte inlet and outlet and as connections to the reference and counter electrodes, respectively. This cell can be used for both the desorption experiments under stopped flow conditions and the measurement of product formation rates under continuous flow. However, under conditions of continuous electrolyte flow, the collection efficiency is very low, because a considerable amount of the products is transported out of the thin-layer volume before diffusing to the Teflon membrane. In order to increase the collection efficiency under continuous electrolyte flow, Baltruschat and coworkers later designed a dual thin-layer flow cell shown in Fig. 2. The construction of this cell has been described in detail in [10, 50, 54, 57]. This DEMS cell is made of Kel-F or titanium. There are two compartments – the upper one for electrochemical reactions and the lower one for mass spectrometric detection, which are connected through four or six capillaries. In the upper compartment, the working electrode is placed against a ~100-μm-thick Teflon gasket with an inner diameter of 6 mm. This leaves an exposed area of 0.28 cm^2 and results in an electrolyte volume of ~3 μL. In the lower compartment, a porous Teflon membrane (Gore-Tex), supported on a stainless steel frit serving as the interface between the electrolyte and vacuum, is pressed against a ~50–100-μm-thick Teflon gasket with an inner diameter of 6 or 12 mm. The Gore-Tex Teflon membrane had a mean thickness of 50 μm, a mean pore size of 0.02 μm, and a porosity of 50%. Two Pt wires at the inlet and outlet of the thin-layer cell, connected through an external resistance (0.1–3 MΩ), are used as counter electrodes. A reversible hydrogen electrode (RHE), connected to the outlet of the DEMS cell through the Teflon capillary, serves as the reference electrode. The electrolyte flow is controlled by a syringe pump or a peristaltic pump (flow rate about 5–30 μL/s), which ensures a fast transport of the species formed at the electrode to the mass

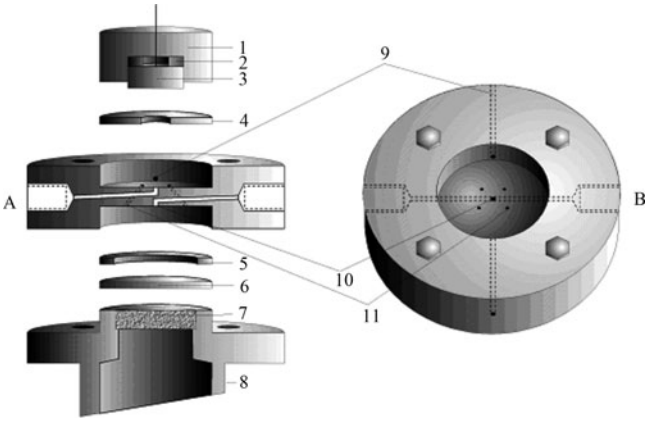

Fig. 2 The dual thin-layer flow cell for DEMS. *1* Kel-F support; *2* Kalrex gasket; *3* electrode; *4* Teflon gasket; *5* Teflon gasket; *6* porous Teflon membrane; *7* stainless steel frit; *8* stainless steel connection to MS; *9* capillaries for Ar; *10* inlet–outlet capillaries; *11* connecting capillaries . (A) Side view of the cell; (B) top view of the cell. Reprinted from Ref. [50] with permission from Elsevier

spectrometric compartment, where the volatile products are evaporated through a porous Teflon membrane into the MS vacuum system (time constant, ca. 1–2 s). In the following experiments, this type of cell was used.

2.3 Electrode Preparation

Thin film Pt/C, Pt_3Sn/C, and PtRu/C (20 wt% metal, E-TEK Inc.) electrodes for DEMS studies were prepared by pipetting and drying, in the center of a mirror-polished glassy carbon disk (Sigradur G from Hochtemperatur Werkstoffe GmbH, 9 mm in diameter), 20 μL of an aqueous catalyst suspension (2 mg/ml), leading to metal loading of 28 μg/cm^2, followed by 20 μL of an aqueous (5%) Nafion solution. The catalyst thin film had a diameter of ca. 6 mm and a geometric surface area of 0.283 cm^2. The preparation of unsupported PtRu and PtRh nanoparticle catalyst electrodes followed the same procedure; however, a higher metal loading of 140 μg/cm^2 was used.

Single crystal Pt(111) and Pt(332) electrodes were prepared by Clavillier's method which involved annealing them in a hydrogen flame for 1 min and then cooling down in an argon atmosphere for 4 min.

Ru-modified smooth polycrystalline platinum was prepared by deposition of Ru from a 5×10^{-3} M $RuCl_3$ in 0.5 M H_2SO_4 solution at different potentials from 0.3 to 0.8 V for 5 min (the corresponding coverage of Ru varied between 0.7 and 0.1 monolayers). The actual Ru coverage on the polycrystalline platinum was determined using the method of Watanabe and Motoo [3, 58]. Ru-modified Pt(111) and Pt(332) electrodes were prepared by deposition of Ru from a 5×10^{-3} M $RuCl_3$ in 0.1 M H_2SO_4 solution at 0.6 V for 5 min (the coverage of Ru was about 0.25) [58].

Sn was deposited on Pt(111) and Pt(332) electrodes at 0.6 V(RHE) for 3 min from a 1×10^{-4} M $SnSO_4$ + 0.5 M H_2SO_4 solution. The resulting coverage was ca. 25%, as determined by the suppression of the H_{upd} charge [59].

2.4 Calibration of the DEMS Setup

For quantitative detection of CO_2 formation during SOM oxidation, a calibration experiment involving adsorbed CO, CO bulk, or formic acid oxidation needs to be carried out to obtain the calibration constant K^*. In the case of stripping of adsorbed CO from a polycrystalline Pt electrode, the integrated electrochemical current includes a non-Faradaic component due to anion adsorption and a shift of the point of zero charge after CO_{ads} oxidation, which amounts to ~15–25% of the oxidation charge. Therefore, correction of integrated electrochemical current is required [53, 60, 61]. The best options for calibration are bulk CO oxidation or formic acid oxidation.

For methanol, formaldehyde, and ethylene glycol oxidation, the mass to charge ratio $m/z = 44$ can be used to monitor CO_2 formation because these fuels, and the volatile intermediate products formed during their oxidation, do not have a fragment with $m/z = 44$. The calibration constant $K^*(44)$ for CO_2 can be calculated from bulk CO or formic acid oxidation experiments as follows:

$$K^*(44) = 2\,Q_{MS}(44)/Q_F \quad \text{from cyclic voltammetry,} \tag{1}$$

$$K^*(44) = 2\,I_{MS}(44)/I_F \quad \text{from potential step amperometry,} \tag{2}$$

where Q_F is the Faradaic charge corresponding to the oxidation of CO or formic acid to CO_2, $Q_{MS}(44)$ is the integrated mass spectrometric current of CO_2 at $m/z = 44$, and 2 is the number of electrons for CO or formic acid oxidation to CO_2. I_F is the Faradaic current corresponding to the oxidation of CO or formic acid to CO_2, $I_{MS}(44)$ is the mass spectrometric current of CO_2 at $m/z = 44$.

For ethanol and acetaldehyde oxidation, the mass to charge ratio $m/z = 22$ (doubly charged CO_2) should be used to monitor CO_2 formation, because these fuels or the volatile intermediate products formed during their oxidation have a fragment with $m/z = 44$. The calibration constant $K^*(22)$ for CO_2 can be calculated from bulk CO or formic acid oxidation experiments as follows:

$$K^*(22) = 2\,Q_{MS}(22)/Q_F \quad \text{from cyclic voltammetry,} \tag{3}$$

$$K^*(22) = 2\,I_{MS}(22)/I_F \quad \text{from potential step amperometry,} \tag{4}$$

where $Q_{MS}(22)$ is the integrated mass spectrometric current of CO_2 at $m/z = 22$ and $I_{MS}(22)$ is the mass spectrometric current of CO_2 at $m/z = 22$.

The average current efficiency for CO_2 generation (η_Q) can be obtained by integrating the cyclic voltammogram (CV) (Q_F) and corresponding mass spectrometric cyclic voltammogram (MSCV) of CO_2 at $m/z = 44$ or 22 (Q_{MS}) in one potential sweep cycle:

$$\eta_Q = (z\,Q_{MS}/K^*)/Q_F, \tag{5}$$

where z is the number of electrons required for fuel oxidation to CO_2 (z = 6, 6, 5 and 5 for methanol, ethanol, acetaldehyde and ethylene glycol oxidation, respectively)

Similarly, the current efficiency for CO_2 generation (η_I) at a constant potential can be determined from the Faradaic current (I_F) and the mass spectrometric current (I_{MS}).

$$\eta_I = (z\,I_{MS}/K^*)/I_F. \tag{6}$$

To quantify the amount of acetaldehyde formed during ethanol oxidation, a calibration experiment involving selective oxidation of ethanol to acetaldehyde is required to obtain the calibration constant $K^*(29)$. At a Au electrode at high potential (1.6 V) and high concentration of ethanol (>0.5 M), the current efficiency for acetaldehyde formation during ethanol oxidation is about 90% [62]:

$$K^*(29) = 2 \times I_{MS}/(I_F \times 0.9). \tag{7}$$

Similarly, at high concentration, ethanol oxidation on a smooth polycrystalline platinum electrode also generates mainly acetaldehyde, which can also be used to calibrate the DEMS setup for acetaldehyde [33].

The average current efficiency of acetaldehyde formation (η_Q) or current efficiency (η_I) during ethanol oxidation can be calculated using the following equation:

$$\eta_Q(CH_3CHO) = 2Q_{MS}/[K^*(29) \cdot Q_F] \text{ or } \eta_I(CH_3CHO) = 2I_{MS}/[K^*(29) \cdot I_F]. \tag{8}$$

Acetic acid formation cannot be directly detected via DEMS due to its low vapor pressure, while ethyl acetate formation can be detected (through the $m/z = 61$ fragment) at high ($\geq$ 0.5 M) ethanol concentrations. Therefore, acetic acid yields are determined indirectly by calculating the difference between the measured Faradaic current and the partial currents for ethanol oxidation to CO_2 and acetaldehyde. This calculation is based on the assumption that only three reaction products, namely CO_2, acetaldehyde, and acetic acid, are formed during ethanol oxidation.

The individual product yields (W_i) are calculated from the corresponding current efficiencies (η_i) through

$$W_i = (\eta_i/n_i)/\sum_i (\eta_i/n_i), \tag{9}$$

where n_i is the number of electrons involved in the oxidation of ethanol to the corresponding product (2 per acetaldehyde, 4 per acetic acid, and 6 per CO_2 molecule formation).

3 Mechanism of Methanol Electrooxidation

3.1 Dissociative Adsorption of Methanol on Pt, PtRu, and PtSn Model Catalysts

Methanol decomposition on Pt and Pt alloys catalysts has been extensively and intensively studied due to its importance for understanding the mechanism of methanol electrooxidation [4, 13, 15, 63, 64]. Due to the successful application of in situ infrared spectroscopy for studying electrode surfaces, CO has been identified as the main product of methanol adsorption [15]. However, it is problematic to determine methanol adsorbate coverage on an electrode surface by infrared spectroscopy due to the nonlinear relationship between IR intensity and CO coverage. Similarly, determining the coverage of methanol adsorbate by electrochemical oxidation is complicated by the unknown non-Faradaic charge due to anion adsorption before and after adsorbate stripping [53, 60, 61]. However, the coverage of methanol adsorbate can be quantitatively determined through the amount of CO_2 formed during the complete oxidation of methanol adsorbate, which can be measured by DEMS. Here we will describe a methodology to determine methanol adsorbate coverage at different potentials by DEMS [13, 64]. For example, the saturation coverage of methanol adsorbate on smooth polycrystalline platinum (pc-Pt) and Ru-modified pc-Pt at different adsorption potentials was determined by a method involving adsorption and subsequent oxidative stripping: (1) at +0.05 V the supporting electrolyte (0.5 M H_2SO_4) was replaced by 0.1 M methanol + 0.5 M H_2SO_4 solution; (2) under solution flow condition (e.g., 5 μL/s), the potential was stepped to a more positive potential, methanol was adsorbed for 2 min, and then the potential was stepped back to +0.05 V; (3) after replacing the solution with supporting electrolyte under potential control, which takes around 5 min, the potential was swept in the anodic direction, and the cyclic voltammogram (CV) and corresponding MSCV of CO_2 at $m/z = 44$ were recorded simultaneously. It must be noted that +0.05 V was chosen because at this potential methanol adsorption does not take place [19], and methanol adsorbate cannot be desorbed either [65]. An adsorption time of 2 min was chosen to obtain a saturation coverage [66]. As an example, Fig. 3 shows the DEMS results for the oxidative stripping of methanol adsorbate on pc-Pt and Ru-modified pc-Pt (pc-Pt/Ru; $\Theta_{Ru} \approx 0.35$) formed at 0.4 V. It is clear that the oxidation of methanol adsorbate on pc-Pt/Ru starts at 0.4 V, i.e., 150 mV more negative than on pc-Pt, and that the oxidative peak on pc-Pt/Ru is negatively shifted by over 100 mV. Therefore, it is evident that Ru modification of Pt catalyzes the oxidation of methanol adsorbate. Both the electron number for methanol adsorbate oxidation to CO_2 being ca. 2 and IR

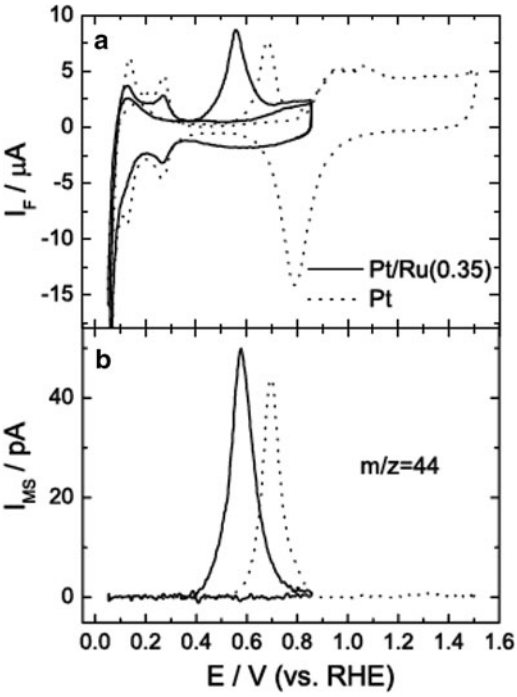

Fig. 3 Simultaneously recorded CVs (**a**) and MSCVs of CO_2 at $m/z = 44$ (**b**) for the oxidation of methanol adsorbate on smooth polycrystalline platinum (pc-Pt) and Ru-modified pc-Pt ($\Theta_{Ru} \approx 0.35$) in 0.5 M H_2SO_4 solution. Scan rate: 10 mV/s. Electrolyte flow rate: 5 μL/s. Methanol was adsorbed from 0.1 M methanol + 0.5 M H_2SO_4 at +0.4 V for 2 min

measurements [15] indicate that methanol adsorbate is adsorbed CO. Moreover, more CO_2 is formed from the oxidation of adsorbate on pc-Pt/Ru than that on pc-Pt, i.e., a higher coverage of methanol adsorbate was achieved on pc-Pt/Ru than on pc-Pt, suggesting that a low coverage of Ru can promote methanol decomposition to form CO_{ads}. From the integrated mass spectrometric current for CO_2 in the MSCV and K^*, the coverage of methanol adsorbate can be determined by the following equation: $\Theta_{CO} = (Q_{MS}(44)/K^*)/Q_H^0$, where Θ_{CO} is the coverage of methanol adsorbate (defined as the number of methanol adsorbate molecules per surface platinum atom), $Q_{MS}(44)$ is the integrated mass spectrometric current of CO_2, K^* is the calibration constant, and Q_H^0 is the charge related to the saturated adsorption of hydrogen on a clean pc-Pt in 0.5 M H_2SO_4 solution, which is obtained by integrating the hydrogen desorption current in the CV between +0.07 and +0.35 V (Q_H): $Q_H^0 = Q_H/0.77$ [67]. The dependence of methanol adsorbate coverage on adsorption potential is presented in Fig. 4a. The coverage of methanol adsorbate on pc-Pt initially increases with increasing adsorption potential for potential values below 0.6 V, and then decreases for potentials higher than 0.6 V due to oxidation of the methanol adsorbate. The maximum coverage, $\Theta_{CO} \approx 0.3$, is achieved at potentials around 0.55 V, where methanol adsorbate starts to oxidize. This could suggest that methanol dissociation to CO needs three neighboring Pt sites (ensemble size). Ru modification of Pt leads to a higher coverage of methanol adsorbate in the low potential region, likely due to electronic effects, and lower coverage in the high potential region due to

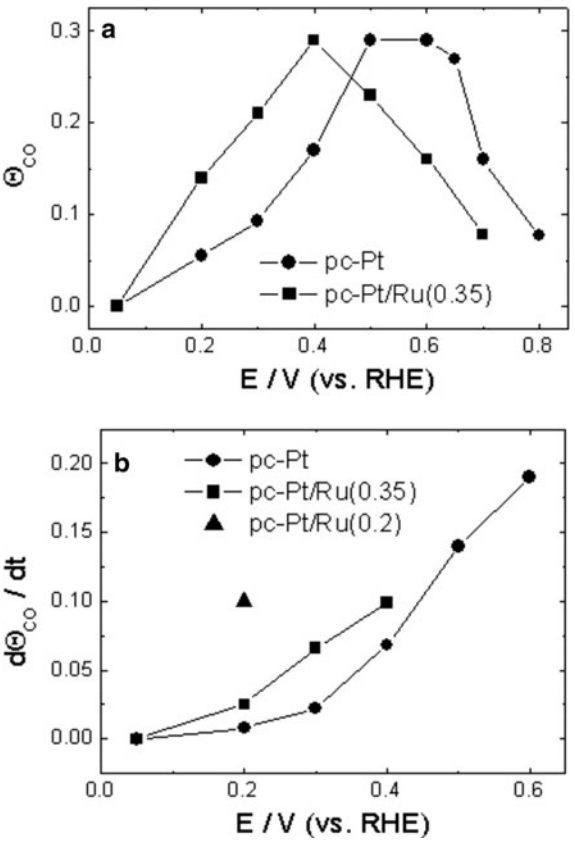

Fig. 4 (**a**) The saturated coverage of methanol adsorbate (CO_{ads}) on smooth polycrystalline platinum (pc-Pt) and Ru-modified pc-Pt ($\Theta_{Ru} \approx 0.35$) vs. adsorption potentials. (**b**) The adsorption rate on pc-Pt, Ru-modified pc-Pt ($\Theta_{Ru} \approx 0.35$), and Ru-modified pc-Pt ($\Theta_{Ru} \approx 0.2$) vs. adsorption potentials. The methanol is dissociatively adsorbed from 0.1 M methanol + 0.5 M H_2SO_4 at different adsorption potentials [64]

the bifunctional mechanism. The maximum coverage of methanol adsorbate on pc-Pt/Ru ($\Theta_{Ru} \approx 0.35$) is negatively shifted, by about 150 mV, to +0.4 V, compared to +0.55 V for pc-Pt.

In order to measure the rate of methanol dissociative adsorption, the adsorption time was reduced to 1 s with all other experimental details being as described earlier. The coverage of methanol adsorbate for an adsorption time of 1 s is plotted vs. the adsorption potential in Fig. 4b. For pc-Pt and pc-Pt/Ru, the adsorption rate of methanol increased with increasing adsorption potential over the range studied. Moreover, a smaller coverage of Ru significantly enhanced the rate of methanol adsorption, since as seen in the figure, the rate was higher for a Ru coverage of about 0.2 (pc-Pt/Ru; $\Theta_{Ru} \approx 0.2$) when compared to a Ru coverage of about 0.35 (pc-Pt/Ru; $\Theta_{Ru} \approx 0.35$).

Similarly, on Ru-modified Pt(111) and Pt(332) surfaces, methanol decomposition to form CO_{ads} is also enhanced at low potentials. For example, the coverage of methanol adsorbate formed at +0.35 V on Pt(111)/Ru and Pt(332)/Ru is much higher than on pure Pt(111) and Pt(332) (Table 1). However, Sn modification of

Table 1 Coverage of methanol adsorbate formed at 0.35 V on different electrodes [13]

Electrode	Pt(111)	Pt(111)/Ru	Pt(111)/Sn	Pt(332)	Pt(332)/Ru	Pt(332)/Sn
Coverage	0.09	0.30	0.05	0.15	0.30	0.08

The coverage of methanol adsorbate means the number of methanol adsorbate molecules per surface platinum atom. The coverage of Ru and Sn is about 25%

Pt(111) and Pt(332) suppresses methanol decomposition (Table 1). Although Sn adatoms can catalyze the oxidation of adsorbed CO, they suppress methanol decomposition to form adsorbed CO due to the third body effect. Table 1 also indicates that Pt(111) is not favorable for methanol decomposition, while steps or defects can facilitate methanol decomposition [13].

3.2 Methanol Bulk Electrooxidation on Pt Model Catalysts

As mentioned earlier, the mechanism of methanol oxidation has been widely studied for several decades due to its potential application in DMFCs. However, the mechanism is still not fully understood. Methanol oxidation on Pt and Pt-based catalysts proceeds via a complex reaction mechanism, involving several parallel and series reaction pathways [2, 4, 13]. As a result, methanol electrooxidation leads to some incompletely oxidized intermediates. The existence of complex reaction pathways and resulting adsorbed and soluble intermediates presents difficulties in studying the mechanism of methanol oxidation by pure electrochemical methods. In situ infrared spectroscopy can help monitor methanol decomposition and oxidation of adsorbed residues (CO_{ads}) and establish whether adsorption of methanol or removal of CO_{ads} is the rate-determining process. Unfortunately, in situ infrared spectroscopy cannot detect soluble intermediates and especially cannot quantify the products. Quantitative online DEMS can be used to achieve this goal. Although chromatography and fluorescence methods have been used to quantify the intermediates, they are not online (in situ) methods and can only provide information about the products formed during long-time electrolysis. In this section, we will focus on the application of quantitative DEMS, combined with the dual thin-layer flow cell, in elucidating the mechanism of methanol oxidation on Pt and PtRu catalysts.

Figure 5 presents DEMS results for the oxidation of methanol on smooth polycrystalline platinum. Figure 5a shows the cyclic voltammogram (CV), which is similar to CVs obtained in traditional electrochemical cells. Figure 5b corresponds to CO_2 formation, which is monitored at $m/z = 44$, while Fig. 5c presents the formation of methyl formate, which is detected at $m/z = 60$. We find that at an electrolyte flow rate of 5 μL/s, the average current efficiency for CO_2 formation in a single potential cycle is only ca. 28%, and for methyl formate is about 0.5%. This suggests that over 70% of the Faradaic current results in other intermediates (likely formaldehyde and formic acid). Unfortunately, formaldehyde and formic acid in

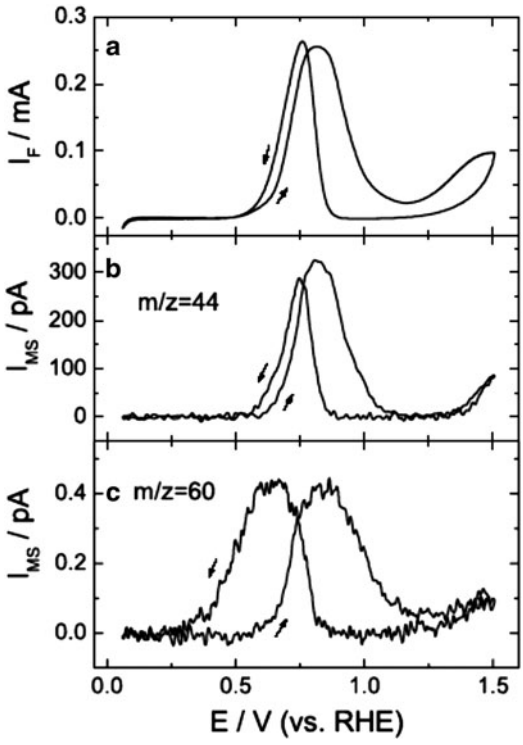

Fig. 5 Simultaneously recorded CV (**a**), MSCV of CO_2 at $m/z = 44$ (**b**), and MSCV of methyl formate at $m/z = 60$ (**c**) on smooth polycrystalline platinum in 0.1 M methanol + 0.5 M H_2SO_4 solution. Scan rate: 10 mV/s. Electrolyte flow rate: 5 μL/s [10]

water are not sufficiently volatile to be directly detected by DEMS. The effect of methanol concentration on CO_2 formation is presented on the left-hand panel of Fig. 6. In the low potential region, CO_2 formation is independent of methanol concentration, while the Faradaic current increases with an increase in methanol concentration. This means that the formation of soluble intermediates (formaldehyde, formic acid, and methyl formate) increases with increasing methanol concentration, as indicated by the decrease in the average current efficiency for CO_2 formation with methanol concentration (see Fig. 7). Comparison of these results to methanol adsorbate oxidation (Fig. 6, right-hand panel) indicates that CO_2 formation onsets at the potential where methanol adsorbate oxidation starts. In addition, the CO_2 signals for both adsorbate and bulk oxidation are almost the same in the low potential region (<0.65 V), suggesting that CO_2 formation originates from the oxidation of methanol adsorbate. However, the Faradaic current for bulk oxidation is much higher than that for adsorbate oxidation, indicating that large amounts of intermediates are simultaneously generated. The independence of CO_2 formation on methanol concentration can be explained by the fact that CO_2 comes from the oxidation of methanol adsorbate (CO_{ads}), so that the oxidation of CO_{ads} controls the CO_2 formation rate. However, at high potentials (>0.65 V), CO_2 formation increases with increasing methanol concentration, since in this case CO_{ads}

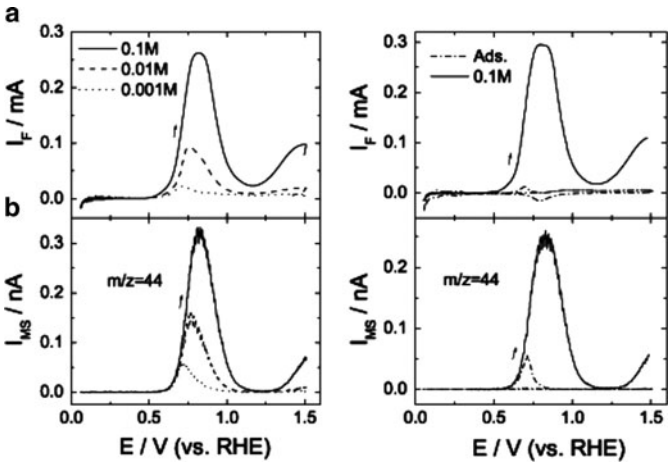

Fig. 6 (*Left-hand panel*) Simultaneously recorded CVs (**a**) and MSCVs of CO_2 at $m/z = 44$ (**b**) during methanol bulk oxidation at smooth polycrystalline platinum (pc-Pt) in different concentrations of methanol solutions with 0.5 M H_2SO_4, *solid lines* – 0.1 M, *dashed lines* – 0.01 M, *dotted lines* – 0.001 M. Only positive-going scans are shown. (*Right-hand panel*) Simultaneously recorded CV (**a**) and MSCV (**b**) of CO_2 for methanol adsorbate oxidation at pc-Pt in 0.5 M H_2SO_4 (*dashed dotted lines*). For comparison, methanol bulk oxidation in 0.1 M methanol + 0.5 M H_2SO_4 (*solid lines*) is also shown. Scan rate: 10 mV/s. Electrolyte flow rate: 5 μL/s [11]

oxidation becomes so fast that methanol decomposition to form CO_{ads} is the rate-determining step. For example, at 1.5 V, the CO_2 intensity is proportional to methanol concentration.

The facts that CO_2 comes from the oxidation of adsorbed CO, and that large amounts of soluble intermediates are also generated during methanol oxidation on platinum, suggest that the mechanism of methanol oxidation on platinum can be simply formulated as follows:

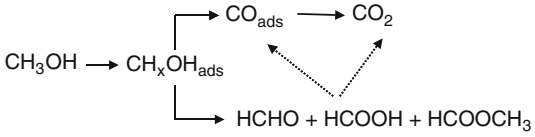

In one pathway, methanol is decomposed to form adsorbed CO, which can be further oxidized to CO_2 at potentials higher than 0.5 V. In others, methanol is oxidized to formaldehyde, formic acid, and methyl formate. These soluble intermediates can be further oxidized to CO_2 under some conditions. The extent of further oxidation of the soluble intermediates depends on convection (flow rate), electrode surface roughness and catalyst loading.

The effect of convection on CO_2 formation during methanol oxidation can be conveniently studied with the dual thin-layer flow cell in conjunction with DEMS, and is shown in Fig. 7. In the low potential region, the current efficiency of CO_2 is independent of solution flow rate [10], also suggesting that in this case CO_2

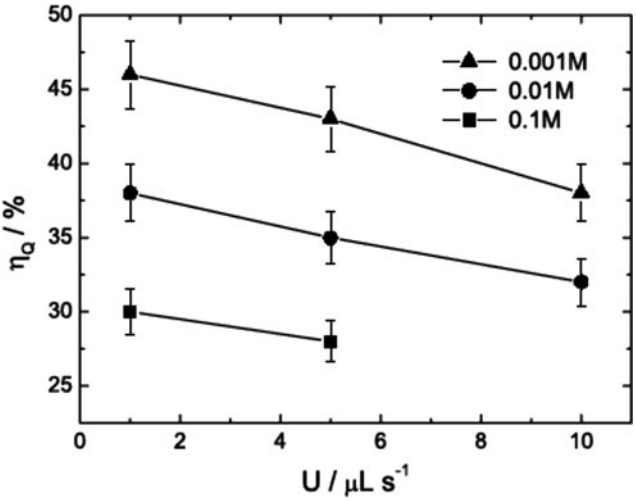

Fig. 7 Dependence of average current efficiency for CO_2 (η_Q) on solution flow rate (U) and methanol concentration. η_Q is calculated from one potential cycle between 0.05 and 1.5 V [10]

formation comes from the oxidation of adsorbed CO, and that soluble intermediates are able to diffuse away from the electrode surface thus providing little contribution to CO_2 formation. However, in the high potential region, at low methanol concentration and low solution flow rate, the intermediates have a higher probability of being further oxidized to CO_2, as indicated by the fact that the average current efficiency for CO_2 formation increases with a decrease in the solution flow rate (Fig. 7). If we use a high surface area Pt electrode, e.g., thick nanoparticle Pt catalyst layer, the soluble intermediates can stay in the pores of the catalyst layer (i.e., longer "residence time") and thus have a higher probability of being further oxidized to CO_2 before being washed away by convection. Therefore, a higher current efficiency for CO_2 formation is observed on nanoparticle Pt catalyst electrodes with high metal loading [11].

From cyclic voltammetry, only the average current efficiency of CO_2 formation in a potential cycle can be determined. To investigate the influence of potential on the current efficiency of CO_2, a series of potential step experiments were carried out on smooth polycrystalline platinum. The potential was stepped from +0.05 V to increasingly more positive potentials. The Faradaic current and corresponding current efficiency for CO_2 generation after a 2 min reaction time are shown in Fig. 8. On a smooth polycrystalline platinum electrode, the oxidation rate of methanol increases with increasing potentials over the potential region of $\leq$0.8 V, and the current efficiency of CO_2 also increases from ca. 20% to 32% when the potential is increased from +0.6 to +0.8 V. This suggests that at higher potentials the formation of CO_2 is enhanced over intermediate formation through either promotion of the pathway via CO_{ads} or acceleration of the further oxidation of intermediates, or both.

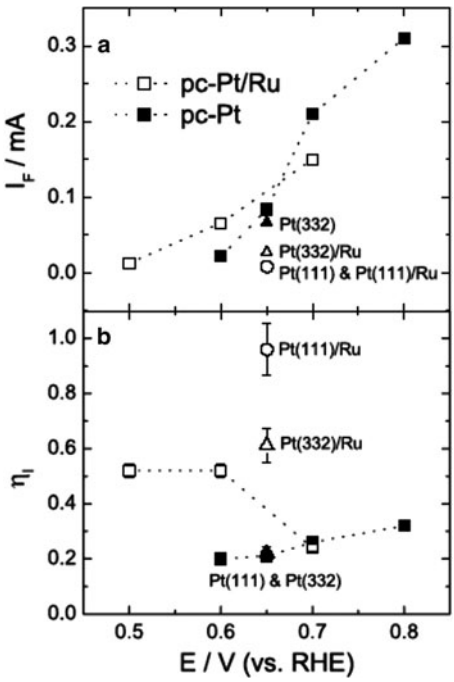

Fig. 8 Potential dependence of the Faradaic current and the current efficiency of CO_2 generation for methanol oxidation on smooth polycrystalline platinum (pc-Pt) and Ru-modified pc-Pt ($\Theta_{Ru} \approx 0.35$) in 0.1 M methanol + 0.5 M H_2SO_4. The values for Pt(111), Pt (332), and Ru-modified Pt (111) and Pt(332) ($\Theta_{Ru} \approx 0.25$) are also included [64]

Adsorbed anions can affect the reactivity of electrocatalysts toward methanol oxidation. While perchloric acid is considered a non-adsorbing electrolyte, sulfate/bisulfate anions in sulfuric acid solution can be strongly adsorbed on the platinum surface, thus inhibiting methanol adsorption, leading to a diminution of the oxidation rate of methanol. In perchloric acid solution, the Faradaic current of methanol oxidation and the rate of CO_2 and methyl formate formation are over two times that in the sulfuric acid solution. However, the current efficiency of CO_2 generation remains nearly the same, i.e., ca. 30% for the average current efficiency in one cycle and ca. 20% for the current efficiency at 0.6 V [13]. This result indicates that anion adsorption simultaneously hinders two parallel reaction pathways but does not significantly alter the overall efficiency for CO_2 generation and product distribution for methanol oxidation on a platinum electrode surface. This finding is in agreement with that obtained by Iwasita et al. based on HPLC analysis [68]. They found that on polycrystalline platinum, the yield of CO_2, HCOOH, and HCHO varied only slightly for sulfuric acid and perchloric acid solutions.

Methanol electrooxidation is a surface structure sensitive reaction [69–74]. Of the three basal planes of platinum, Pt(110) has been found to be the most active. Pt(111) has been shown to be the least reactive toward methanol decomposition, and the rate of methanol oxidation increases with increasing step density on Pt(111) surfaces. To determine the effect of steps of monocrystalline Pt surfaces on the product distribution during methanol oxidation, Pt(111) and Pt(332) single crystals

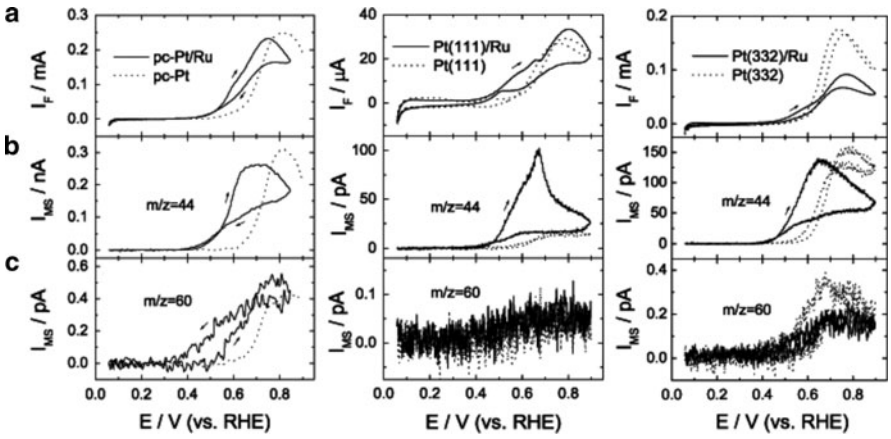

Fig. 9 Simultaneously recorded CVs (**a**) and MSCVs of CO_2 at $m/z = 44$ (**b**) and $m/z = 60$ (**c**) on pc-Pt, Pt(111), Pt(332), pc-Pt/Ru ($\Theta_{Ru} \approx 0.35$), Pt(111)/Ru, and Pt(332)/Ru ($\Theta_{Ru} \approx 0.25$) electrodes in 0.1 M methanol + 0.5 M H_2SO_4 solution. Scan rate: 10 mV/s. Electrolyte flow rate: 5 μL/s. *Arrows* indicate the direction of potential sweep [11, 13]

were studied by DEMS. Figure 9 (middle and right-hand panels, dotted lines) shows CVs and the corresponding MSCVs of CO_2, at $m/z = 44$, and methyl formate, at $m/z = 60$, for methanol oxidation on Pt(111) and Pt(332) in 0.1 M methanol + 0.5 M H_2SO_4 solutions. The Faradaic current and the CO_2 and methyl formate signals on Pt(332) are about six times those on Pt(111). This clearly indicates that the step sites are much more active toward methanol oxidation than terrace sites. The calculated average current efficiencies for CO_2 and methyl formate on Pt(111) are only 20 ± 2% and ca. 0.5%, respectively; while for Pt(332) they are 27 ± 3% and ca. 0.7%, respectively. Therefore, the presence of steps on the Pt(111) vicinal surface can only modestly enhance the complete oxidation of methanol to CO_2. The potential step amperometry results (Fig. 8) are similar to the results from cyclic voltammetry, i.e., Pt(332) exhibits a higher oxidative current than Pt(111). At +0.65 V, the current efficiencies for CO_2 are 21 ± 2% for Pt(111) and 22 ± 2% for Pt(332). Methanol oxidation seems to occur at the defect sites of Pt(111), which usually possesses terraces that are 200–500 atoms wide, and on well-prepared Pt (111) surfaces, methanol oxidation is significantly inhibited. The finding that the current efficiency of CO_2 generation is independent of step density implies that the increase in step density only leads to an increase in the active sites, but does not influence the product distribution, similar to an increase in the apparent area of the electrode surface. In general, an increase in step density of Pt electrode surfaces can enhance methanol oxidation. However, the current efficiencies of CO_2 generation do not exhibit an appreciable difference for smooth polycrystalline platinum, Pt (111), and Pt(332) electrodes. The step or defect sites appear to simultaneously enhance the two parallel pathways of methanol oxidation.

3.3 Methanol Bulk Electrooxidation on PtRu Model Catalysts

The catalytic mechanism of PtRu has been extensively studied due to the fact that it is the best electrocatalyst for methanol oxidation so far, and its catalytic activity has been assumed to be attributed to the bifunctional mechanism and/or electronic effects, although the optimal Pt:Ru ratio is still controversial. In this section, we will review some new insights in the catalytic mechanism of PtRu, achieved by quantitative DEMS studies.

CVs and the corresponding MSCVs of CO_2 at $m/z = 44$ and methyl formate at $m/z = 60$ on Ru-modified smooth polycrystalline Pt, Pt(111), and Pt(332) in 0.1 M methanol + 0.5 M H_2SO_4 solution are shown in Fig. 9 (solid lines). In the positive-going scan, the Faradaic current and the formation of CO_2 on all Ru-modified Pt surfaces start at ca. 0.4 V (Fig. 9b), i.e., over 100 mV more negative than on pure Pt surfaces. A small peak or shoulder around +0.65 V in CVs is paralleled by the maximum for CO_2 formation, as indicated by the ion peak of $m/z = 44$ (Fig. 9b). The main peak at around +0.8 V, which is followed by the ion peak of $m/z = 60$ (Fig. 9c), should mainly correspond to the formation of intermediates (formaldehyde, formic acid, and methyl formate). Of particular note, the formation of CO_2 increases dramatically on Pt(111)/Ru when compared to Pt(111). This can be explained by the fact that Ru can not only promote methanol decomposition to form adsorbed CO, due to electronic effects, but also catalyze the oxidation of adsorbed CO through the bifunctional mechanism (see Sect. 3.1). At potentials higher than +0.65 V, the formation of CO_2 is suppressed due to the oxidation of Ru to form inactive Ru oxide, although the Faradaic current and resulting intermediates formation still increase for potentials up to +0.75 V. In the case of Pt(332)/Ru, the maximum Faradaic current and corresponding formation of CO_2 and methyl formate are markedly suppressed due to the blocking of step sites by the inactive Ru oxide. This also suggests that steps are active sites for both reaction pathways of methanol oxidation.

To eliminate the effect of adsorbed CO formed from methanol dissociation on the bulk oxidation of methanol, potential step amperometric experiments on Ru-modified smooth polycrystalline Pt, Pt(111), and Pt(332) have been carried out. The effect of potential on the steady-state currents and current efficiencies for CO_2 formation are shown in Fig. 8. For methanol oxidation on Ru-modified smooth polycrystalline Pt (pc-Pt/Ru), the Faradaic current monotonically increases from +0.5 to +0.7 V. The current efficiency for CO_2 is much higher than that on pc-Pt for potentials of $\leq$0.65 V, i.e., ca. 52% vs. $\leq$20%; however, it decreases for potentials higher than +0.65 V, again due to the formation of inactive Ru oxide. For example, at +0.7 V, the current efficiency for CO_2 generation for pc-Pt/Ru is similar to that on pc-Pt. At +0.65 V, the Faradaic current is a bit smaller on Pt(111)/Ru than on Pt(111), while the formation of CO_2 increases markedly and the current efficiency of CO_2 reaches about 100%, compared to 21% on Pt(111). Compared to Pt(332), the Faradaic current is significantly reduced on Pt(332)/Ru at +0.65 V due to the blockage of step sites by Ru adatoms. However, the formation of CO_2 increases somewhat and the current efficiency of CO_2 reaches about 61%, compared to 22%

on Pt(332). This, again, suggests that in the low potential region ($\leq$ 0.65 V), Ru modification of Pt surfaces can promote the complete oxidation of methanol to CO_2.

While it is generally accepted that PtRu catalysts are the most active for methanol electrooxidation, the optimal Pt:Ru ratio is still not definitely established. Early on, Watanabe and Motoo reported that PtRu, with an Ru content of 0.5, exhibited the highest activity toward methanol oxidation, and assumed that the bifunctional mechanism played a dominant role in the enhancement [3]. Later, considering that methanol decomposition to CO requires three neighboring Pt atoms, Gasteiger et al. proposed a different model for the catalytic effect of Ru on methanol oxidation, in which a surface structure consisting of one Ru atom neighboring three Pt sites represented the optimal geometry for methanol oxidation [5]. According to this, an optimal alloy surface composition of $\approx$10 at.% Ru for the electrooxidation of methanol was predicted. However, numerous experimental results did not support such a prediction. Iudice De Souza et al. found that at room temperature, a Pt/Ru ($\Theta_{Ru} = 0.25$) layer electrodeposited on gold substrates had the highest activity for methanol oxidation [75]. Iwasita et al. studied the electrooxidation of methanol on Pt(111)/Ru electrodes with different Ru coverages and found that the maximum in the electrocatalytic activity was observed for Ru coverages between 10% and 40% [21]. Kolb et al. [76] examined the electrocatalytic behavior of three preferentially oriented "Pt(111)", "Pt(110)", and "Pt(100)" surfaces modified by Ru submonolayers toward methanol oxidation, and found that the enhancement factor depended on the surface crystallography and the Ru coverage. They reported that the optimal Ru coverage at room temperature was 30–40% of a monolayer for all three surfaces, and that the electrocatalytic activity at optimal Ru coverage decreased in the following order: "Pt(111)" > "Pt(110)" > Pt(111) > "Pt(100)". Jusys et al. found that unsupported PtRu alloy nanoparticle with 15 at.% Ru exhibited the highest activity [77]. Recently, Lamy et al. reported that carbon-supported PtRu with 20 at.% Ru was the most active catalyst toward methanol oxidation, and that a simple mixture of Pt and Ru nanoparticles supported on Vulcan was superior to Vulcan-supported PtRu alloy catalysts [78]. Thus, it seems that the optimal ratio of Ru/Pt varies with the different preparation of PtRu electrodes, i.e., co-deposition, ad-atom, alloy, and mixture of Pt and Ru nanoparticles. From these results, it appears that the Ru distribution and segregation on the surface play key roles in determining the optimal Ru/Pt ratio.

In general, to balance the decomposition of methanol to CO and further oxidation to CO_2 requires the consideration of some key factors. In Gasteiger's model [5], it is assumed that methanol oxidation proceeds only via adsorbed CO, and that the dissociative adsorption of methanol is the rate-determining step for methanol oxidation on PtRu electrodes. The electronic effect of Ru on methanol adsorption was not considered. In fact, at low potentials, a low Ru content can promote methanol decomposition to form adsorbed CO, and the oxidation of methanol adsorbates could also control the oxidation of methanol on PtRu electrodes.

Ru can promote the oxidation of adsorbed CO on Pt, but also block the Pt surface, which seems to be unfavorable for CO_{ads} formation from methanol

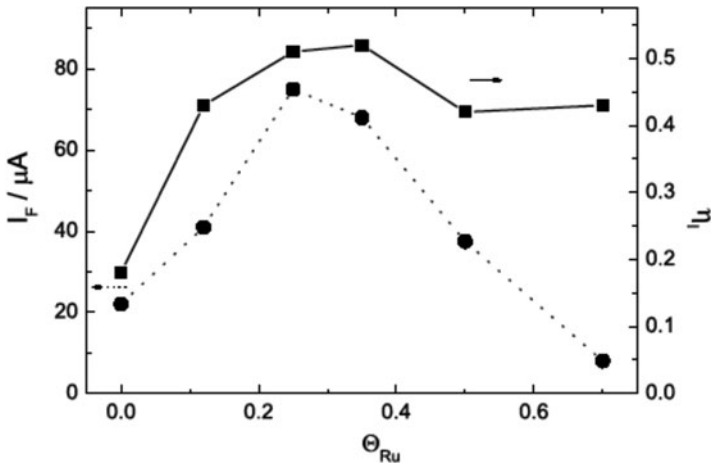

Fig. 10 The steady-state Faradaic current (I_F) and the current efficiencies for CO_2 formation (η_I) during methanol oxidation on Ru-modified pc-Pt at +0.6 V in 0.1 M methanol + 0.5 M H_2SO_4 vs. Ru coverage

decomposition without considering the electronic effect of Ru, since methanol adsorption does not occur on pure Ru at room temperature [5]. As a result, on PtRu catalysts, there would be a competition between the formation rate of adsorbed CO and the rate of oxidative removal (to CO_2), which would depend on Ru coverage. However, on PtRu surfaces with small amounts of Ru, CO_{ads} formation from methanol decomposition is not inhibited; in fact, it is even enhanced due to electronic effects (see Sect. 3.1.). For Ru-modified pc-Pt, we found, using quantitative DEMS, that samples with a Ru coverage of ~0.3 exhibited the highest Faradaic current and largest current efficiency for CO_2 formation (Fig. 10). This is consistent with the findings by Kolb et al. [76].

Recently, we studied methanol electrooxidation on ordered intermetallic PtPb electrodes by quantitative DEMS and in situ Fourier transform infrared spectroscopy (FTIRS) [14]. It is very interesting and, to some extent, surprising that PtPb can help completely oxidize methanol to CO_2, as indicated by the very high current efficiency (about 90%), in addition to the fact that no adsorbed CO was detected on the PtPb surface. Methanol electrooxidation on PtPb seems to have a different mechanism from that on Pt and PtRu: methanol can be directly oxidized to CO_2 without forming adsorbed CO.

4 Mechanism of Ethanol and Acetaldehyde Electrooxidation

Ethanol electrooxidation to carbon dioxide requires splitting of a C–C bond, which is not present in methanol. The cleavage of the C–C bond plays a key role in the electrooxidation of ethanol and determines the energy efficiency of fuels.

The difficulty of breaking the C–C bond (especially at low temperatures) at all known electrocatalysts leads to the formation of large amounts of acetaldehyde and acetic acid during ethanol electrooxidation, which clearly limits DEFC performance. Improvement of the performance of DEFCs will require a deep and detailed understanding of the mechanisms of the electrocatalytic reactions involved, which will help design better catalysts to selectively and completely oxidize ethanol to CO_2.

4.1 Dissociative Adsorption of Ethanol and Acetaldehyde on Pt-Based Nanoparticle Catalysts

To completely oxidize ethanol to CO_2, the dissociative adsorption of ethanol is the first key process, and thus has been studied for over 20 years [31, 34, 79–82]. In this section, we will discuss the dissociative adsorption of ethanol (and also acetaldehyde, since it is a major intermediate in the oxidation of ethanol) on Pt-based nanoparticle catalysts, and the identification of the resulting adsorbates/intermediates on the basis of DEMS results.

4.1.1 Decomposition Behavior of Ethanol and Acetaldehyde on Pt/C

The adsorption of ethanol or acetaldehyde was performed by connecting two electrolyte supply bottles to the common inlet of the dual thin-layer flow cell; one with supporting electrolyte, and the other with a solution containing the respective adsorbing species (0.1 M solution of ethanol or acetaldehyde) to ensure a constant rate of mass transport to the electrode during adsorption [34].

Figure 11 shows the initial 30 s of Faradaic current transients after the introduction of ethanol or acetaldehyde solutions, i.e., after switching from the pure supporting electrolyte to ethanol or acetaldehyde-containing solutions. At +0.06 V, the oxidative adsorption of ethanol is completely suppressed due to the blocking of the Pt surface by underpotentially deposited hydrogen, similar to methanol and ethylene glycol adsorption (see Sects. 3 and 5). At potentials higher than +0.06 V, the anodic current upon the introduction of ethanol suggests that oxidative adsorption of ethanol occurs. The signal increases steeply upon introduction of the electrolyte, passes through a maximum, and then decays. The anodic peak current gradually increases with the adsorption potential.

For acetaldehyde-containing solutions, the current transients exhibit much steeper and higher peak currents, suggesting a faster oxidative adsorption of acetaldehyde on the Pt/C catalyst compared to ethanol. This can be rationalized by a stronger adsorption of molecular acetaldehyde due to interactions between the metal substrate and the carbonyl group, which even allows acetaldehyde to adsorb on the H_{ads}-covered Pt surface via displacement. The potential dependence

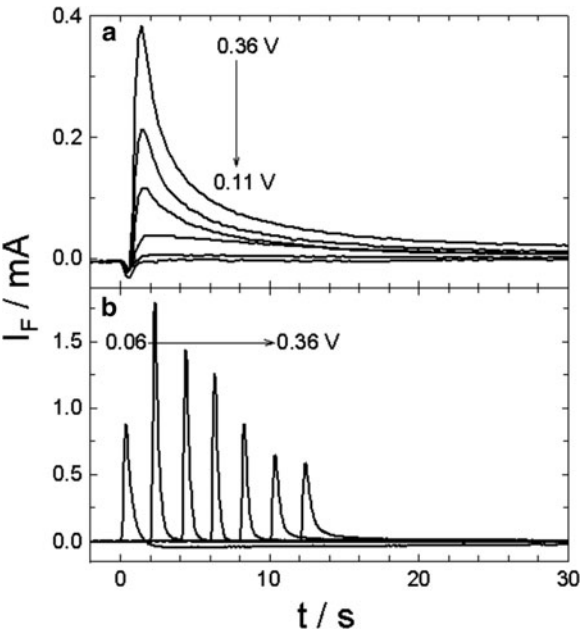

Fig. 11 Chronoamperometric Faradaic transients for the adsorption of ethanol (**a**), acetaldehyde (**b**) on Pt/C (E-TEK) catalyst at different, constant potentials between +0.06 and +0.36 V (E_{ads} is increased in steps of 50 mV). For adsorption, the electrolyte was switched at $t = 0$ from the supporting electrolyte to solutions containing 0.1 M ethanol or acetaldehyde. The current transients of acetaldehyde adsorption (**b**) are progressively shifted by 2 s for clarity [34]

of the current transients differs significantly from that observed for ethanol adsorption. First of all, the initial maximum current increases when changing the adsorption potential from +0.06 to +0.11 V, but then decreases steadily. Next, at the most negative adsorption potential of +0.06 V, the transient rapidly switches from an anodic current to a cathodic current, indicating a continuous reduction reaction, which is attributed to the bulk reduction of acetaldehyde to form ethane [83].

4.1.2 Oxidation and Reduction of Ethanol Adsorbate on Pt/C

After the adsorption of ethanol or acetaldehyde at a series of constant potentials for 10 min in 0.1 M ethanol (or acetaldehyde) + 0.5 M H_2SO_4 solution, the remaining ethanol or acetaldehyde in solution was removed by exchanging the solution with pure 0.5 M H_2SO_4 solution and extensive rinsing with that electrolyte. Later, the potential was scanned positively to oxidize the adsorbate. Both the electrochemical signal and mass spectrometric signal of CO_2, at $m/z = 44$, were simultaneously recorded. Figure 12 presents the simultaneously recorded CVs and MSCVs of CO_2 at $m/z = 44$ for the oxidation of ethanol adsorbate, formed at three different adsorption potentials (+0.16, +0.31, and +0.46 V). In the positive-going scan, the

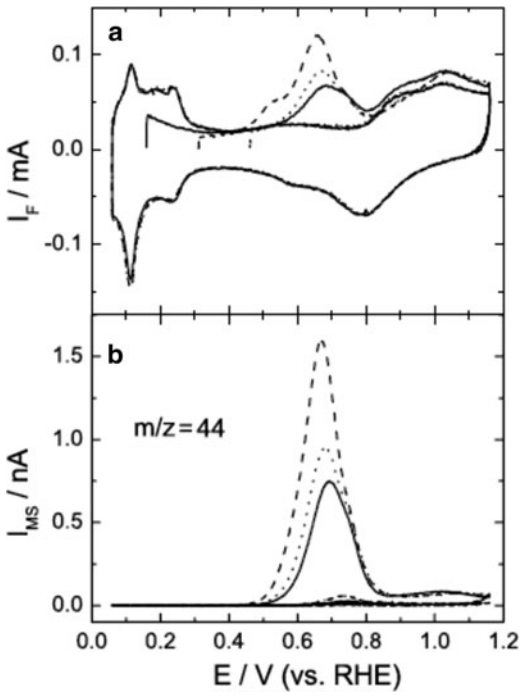

Fig. 12 Simultaneously recorded CVs (**a**) and MSCVs of CO_2 at $m/z = 44$ (**b**) for the oxidation of ethanol adsorbates formed on Pt/C (E-TEK) at different adsorption potentials. *Solid lines* – +0.16 V, *dashed lines* – +0.31 V, *dotted lines* – +0.46 V. After the adsorption of ethanol, the potential is first scanned in the positive direction. Scan rate: 10 mV/s. Electrolyte flow rate: 10 μL/s [34]

oxidation of ethanol adsorbate commences at +0.45 V and occurs in two potential regions, in a "low" potential region below +0.85 V and in a "high" potential region above +0.85 V, respectively. During the initial, positive-going scan, most of the ethanol adsorbate is oxidized to CO_2 in the lower potential region. A smaller fraction, equivalent to about 10–20% of the total CO_2 amount, is oxidized to CO_2 in the "high" potential region, together with PtO formation. If ethanol is adsorbed at around +0.3 V (between +0.2 and +0.35 V), an oxidative pre-peak is observed in the low potential region (ca. +0.5 V) during the first positive-going scan, which has no corresponding CO_2 signal. We therefore attribute it to an incomplete oxidation of adsorbates, where the reaction products remain on the surface (no other volatile species were detected). The two oxidation regions and two peaks in the low potential region suggest that different decomposition products are formed upon dissociative adsorption of ethanol. Furthermore, the adsorption potential has a pronounced influence on their relative coverages.

The relative coverage of the ethanol adsorbate, compared to that of a saturated CO adlayer on the Pt/C catalyst, calculated simply as the ratio of the mass spectrometric charge of the $m/z = 44$ peak for ethanol adsorbate oxidation to that for stripping of a saturated CO adlayer, is shown for different adsorption potentials in Fig. 13 (squares). The maximum ethanol adsorbate coverage is achieved at an adsorption potential of around +0.36 V. It is, however, only about 60% of the coverage of a saturated CO adlayer. In the hydrogen adsorption region, H_{ads}

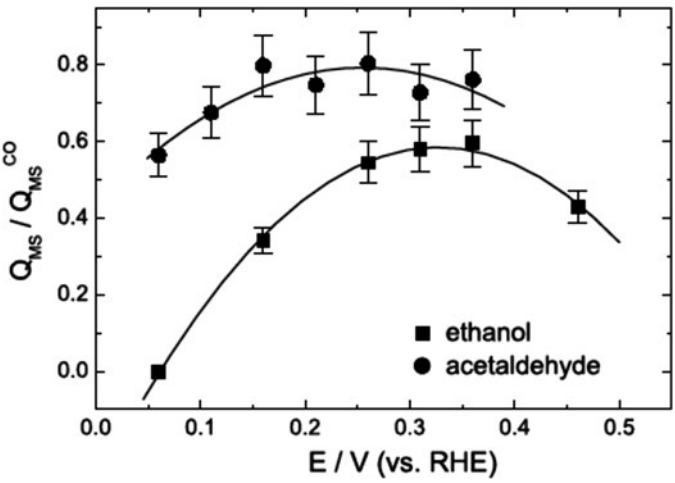

Fig. 13 Relative coverage of ethanol (*squares*) and acetaldehyde (*circles*) adsorbates on Pt/C (E-TEK) compared to that of a saturated CO adlayer for different adsorption potential [34]

increasingly inhibits the dissociative adsorption of ethanol, resulting in almost complete inhibition at +0.06 V. Similar effects were also observed for methanol and ethylene glycol adsorption (Figs. 4 and 25, respectively). For adsorption potentials above +0.45 V, a fraction of the adsorbed decomposition products is already oxidized to CO_2 during adsorption, leading to a lower coverage in the subsequent stripping experiment.

Information on the nature of the adsorbed decomposition products can be derived from the number of electrons consumed per CO_2 molecule formation in the electrooxidation reaction. The average number of electrons per CO_2 product molecule involved in the electrooxidation of the adsorbate was calculated as $n = (Q_F/Q_{MS})/(Q_F^{CO}/2Q_{MS}^{CO})$, where Q_F and Q_{MS} are the Faradaic charge and corresponding mass spectrometric charge for CO_2 generation during the oxidation of adsorbate, respectively. Q_F^{CO} and Q_{MS}^{CO} are the Faradaic charge and corresponding mass spectrometric charge of CO_2 generation during the oxidation of a saturated CO adlayer, respectively.

The calculated values for the total number of electrons (n^t) required for the oxidation of ethanol adsorbate to CO_2 in the first positive-going potential scan as well as the respective fractions in the low potential (n^l) and high potential (n^h) regions are listed in Table 2. The average number of electrons lies between 2.2 and 2.4 for n^l, except for adsorption at +0.16 V. This is close to the value of 2.0, which would be expected for CO oxidation. Our FTIR experiments have shown that adsorbed CO is formed during ethanol adsorption. The slightly higher values indicate, however, that in addition to the dominant product, CO_{ads}, other adsorbed species are also formed and oxidized in the potential range of CO oxidation as a result of ethanol adsorption on Pt/C, with their contribution depending on the adsorption potential. For the high potential region, the electron yields are much

Table 2 Number of electrons (n) required for the electrooxidation of adsorbate per CO_2 molecule

E_{ads}/V	n (±0.2)					
	Ethanol			Acetaldehyde		
	n^t	n^l	n^h	n^t	n^l	n^h
0.06				2.6	2.1	6.0
0.11				2.5	2.2	6.2
0.16	3.3	2.8	5.9	2.0	1.9	5.8
0.21				2.1	2.0	4.4[a]
0.26	2.5	2.4	3.4[a]	2.1	2.0	3.5[a]
0.31	2.4	2.3	3.8[a]	2.5	2.4	3.2[a]
0.36	2.3	2.2	3.0[a]	2.3	2.2	3.0[a]
0.46	2.4	2.2	3.9[a]			

n^l number of electrons in the low potential region (<+0.85 V), n^h number of electrons in the high potential region (>+0.85 V), n^t average number of electrons in both potential regions, E_{ads} adsorption potential

[a]Larger error in the determination of electrochemical current due to uncertainties in background subtraction [34]

higher, between 3 and 6. This suggests that some non-CO adsorbed species (adsorbed hydrocarbons) lead to the high potential peak.

In order to get the further information on the nature of the adsorbed ethanol decomposition products, experiments for reductive desorption of adsorbates were carried out. In this case, after ethanol adsorption, the potential was scanned first in the negative direction, followed by a subsequent, complete cycle, and CV and the corresponding MSCVs were simultaneously recorded. As an example, DEMS data for an adsorption potential of +0.31 V are presented in Fig. 14. After ethanol adsorption at +0.31 V (black lines), in the negative-going scan, methane and ethane were detected as reductive products at $m/z = 15$ and $m/z = 30$, respectively. Although ethane fragmentation also leads to a small signal at $m/z = 15$, its contribution must be very small considering the much lower signal of ethane. In the subsequent positive-going scan, only CO_2 was detected. Compared to the stripping experiments starting with a positive-going scan (Fig. 12), the oxidative pre-peak at ca. +0.5 V becomes significantly smaller, from about 40% of the main peak to about 30%. Likewise, in the potential region above +0.85 V, the oxidation current and the amount of CO_2 formed are much lower than in the previous experiments (Fig. 12). These results suggest that the oxidative pre-peak at +0.5 V and the oxidation reaction in the "high" potential region involve oxidation of adsorbed species other than CO_{ads}, which can be reduced, in the H_{upd} region, to methane and ethane. The non-CO adsorbates are tentatively identified as CH_x and $C_2H_y(O)$ species, which result from a catalytic C–C bond dissociation (CH_x) and an intact C–C bond dissociation of ethanol on the Pt surface. Through isotopic labeling of one of the carbon atoms of ethanol, Baltruschat et al. found that the methane produced originates from the CH_3 group of the ethanol or acetaldehyde molecule [81]. Recently, adsorbed CH_x species have been identified by surface-enhanced Raman spectroscopy (SERS) [82]. If ethanol adsorption is performed at +0.66 V instead of

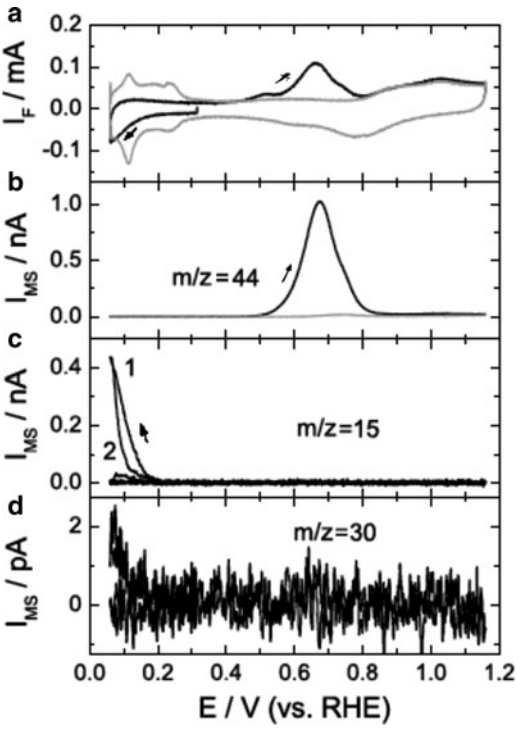

Fig. 14 Simultaneously recorded CV (**a**) and MSCVs of CO_2 at $m/z = 44$ (**b**), methane at $m/z = 15$ (**c**), and ethane at $m/z = 30$ (**d**) for the reduction and oxidation of ethanol adsorbates formed upon adsorption at +0.31 V on Pt/C (E-TEK) (*black lines*). After the adsorption of ethanol, the potential is first scanned in the negative direction. For comparison, a clean Pt/C is shown (*gray lines*). Scan rate: 10 mV/s. Electrolyte flow rate: 10 μL/s [34]

+0.31 V, where CO_{ads} can already be oxidized during adsorption, a subsequent positive-going scan (Fig. 15a, b) shows virtually no CO_2 formation in the low potential region, but similar amounts of CO_2, as observed for lower adsorption potentials, in the high potential region (>+0.85 V). The behavior in the subsequent potential cycle involves a small CO_2-formation peak (in the low potential region) in the negative-going scan and a somewhat larger peak for CO_2 formation in the second positive-going scan (not shown). As the potential is scanned negatively to +0.06 V, after the same adsorption procedure (Fig. 15c, d), methane is generated in the hydrogen adsorption (H_{upd}) region. These two experiments indicate that adsorbed CH_x species are accumulated on the Pt/C surface during ethanol oxidation at +0.66 V, while adsorbed CO is oxidized to CO_2. Although adsorbed CH_x species can be converted into CO and then further oxidized to CO_2 or directly oxidized to CO_2 in the low potential region (<+0.85 V), some adsorbed CH_x species are very difficult to oxidize, and they can only be either desorbed as methane in hydrogen region, or oxidized to CO_2 in the high potential region (>+0.85 V) [34, 81]. In general, ethanol can be decomposed to form adsorbed CO and CH_x species on platinum, while a small amount of C_2 adsorbed species are also formed. Adsorbed CH_x species are even more difficult to oxidize to CO_2, and thus accumulate on the platinum surface, resulting in poisoning of the surface. Therefore, a key

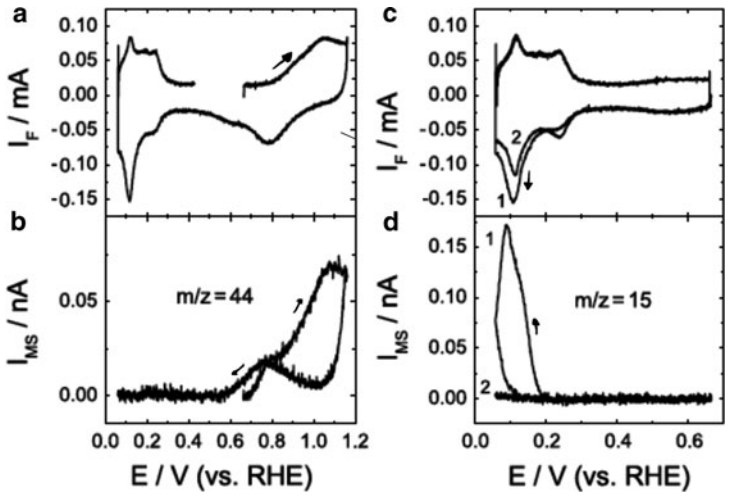

Fig. 15 (*Left-hand panel*) Simultaneously recorded CV (**a**) and MSCV of CO_2 at $m/z = 44$ (**b**) after ethanol adsorption at +0.66 V on Pt/C (E-TEK) for 10 min. The potential is first scanned in the positive direction up to +1.16 V and then cycled once between +1.16 and +0.06 V. (*Right-hand panel*) Simultaneously recorded CV (**c**) and MSCV of methane at $m/z = 15$ (**d**) after ethanol adsorption at +0.66 V for 10 min. The potential is first scanned in the negative direction to +0.06 V and then cycled once between +0.06 and +0.66 V. Scan rate: 10 mV/s. Electrolyte flow rate: 10 μL/s [34]

requirement of any anode catalyst for DEFCs is that it be able to catalyze the oxidation of $CH_{x,ads}$.

4.1.3 Oxidation and Reduction of Ethanol Adsorbate on PtRu, PtRh, and Pt_3Sn Nanoparticle Catalysts

Ethanol can also be decomposed on PtRu, PtRh, and Pt_3Sn catalysts to form CO_{ads} and $CH_{x,ads}$. After ethanol adsorption in 1 M ethanol + 0.5 M H_2SO_4 solution at +0.4 V for 15 min, the potential was first scanned negatively and then positively in ethanol-free solution, and methane ($m/z = 15$) and CO_2 ($m/z = 44$) were simultaneously recorded by mass spectrometry, as shown in Fig. 16. The positive potential limit was lowered to +0.6 or +0.7 V to avoid leaching of the less-noble component. For PtRu and PtRh (ZSW) catalysts, in the H_{upd} region, methane is formed as a reductive stripping product, while in the high potential region, the adsorbates (CO_{ads} and $CH_{x,ads}$) are oxidized to CO_2. The reductive and oxidative stripping of $CH_{x,ads}$ is difficult; hence at least six to seven cycles between +0.06 and +0.7 V are needed to remove most of the adsorbates. Compared to PtRh, a lower coverage of adsorbates is formed on PtRu, as indicated by the smaller amounts of CO_2 and methane formed during reductive and oxidative desorption, respectively. This implies that the presence of Ru inhibits C–C bond cleavage, while Rh does not. Similarly, for Pt_3Sn/C (E-TEK) methane and CO_2 are also formed as reductive and

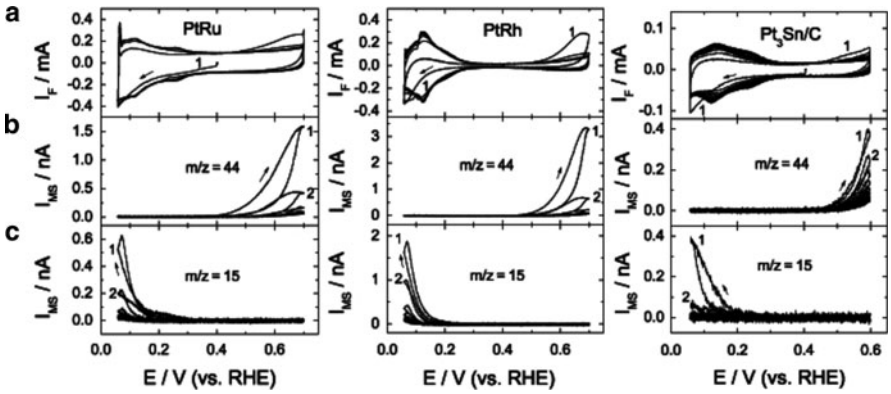

Fig. 16 Simultaneously recorded CVs (**a**) and MSCVs of CO_2 at $m/z = 44$ (**b**), and methane at $m/z = 15$ (**c**) for the reduction and oxidation of ethanol adsorbates formed upon adsorption at +0.4 V on Pt-based binary catalysts. After the adsorption of ethanol, the potential was first scanned in the negative direction. *Left-hand panel*: PtRu (ZSW, metal loading: 40 μg, particle size: 3–5 nm); *middle panel*: PtRh (ZSW, metal loading: 40 μg, particle size: 3–5 nm); *right-hand panel*: Pt_3Sn/C (DICP, metal loading: 8 μg, particle size: 2.1 nm). Scan rate: 10 mV/s. Electrolyte flow rate: 10 μL/s

oxidative stripping products, respectively. Because of the lower positive potential limit that had to be used (to mitigate leaching), over 20 scans between +0.06 and +0.6 V are needed to remove most of the adsorbates.

4.1.4 Oxidation and Reduction of Acetaldehyde Adsorbate on Pt/C

Analogous experiments were performed for the oxidative and reductive removal of the decomposition products formed during acetaldehyde adsorption. Figure 17 shows the simultaneously recorded CVs and MSCVs of CO_2 at $m/z = 44$ for the oxidation of acetaldehyde adsorbate, formed at three different adsorption potentials, with the initial scan going positive. Similar to the oxidation of ethanol adsorbate, the oxidation of acetaldehyde adsorbate starts at about +0.5 V and also exhibits two distinct potential regions. The oxidation of acetaldehyde adsorbate formed at +0.16 V produces much smaller amounts of CO_2 in the high potential region than observed for the other adsorption potentials, likely since $CH_{x,ads}$ is already desorbed by reduction. If acetaldehyde is adsorbed at +0.06 V, the oxidation current and CO_2 formation in the high potential region are increased in the positive-going scan compared to adsorption at +0.16 V. This can be explained by the presence of C_2 adsorbates, which can be generated by acetaldehyde reduction, since under these conditions, acetaldehyde can be reduced to form ethane in solution [34, 83].

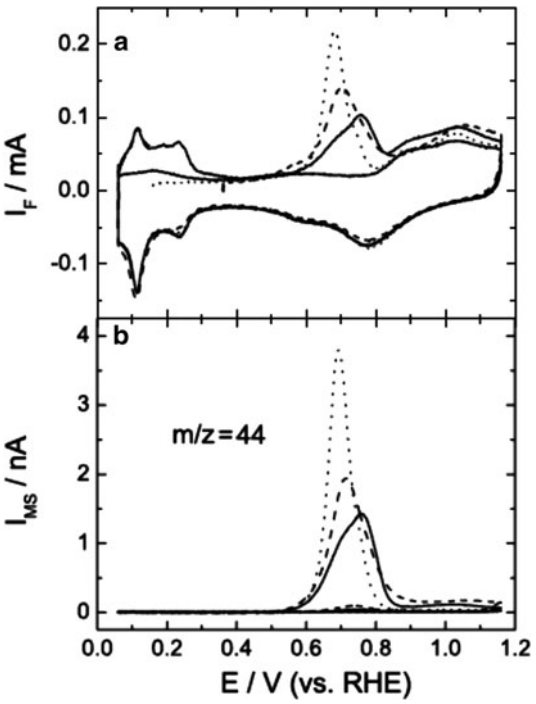

Fig. 17 Simultaneously recorded CVs (**a**) and MSCVs of CO_2 at $m/z = 44$ (**b**) for the oxidation of acetaldehyde adsorbates formed upon adsorption at different potentials: *solid lines* – +0.06 V, *dotted lines* – +0.16 V, *dashed lines* – +0.36 V in 0.1 M acetaldehyde + 0.5 M H_2SO_4. After the adsorption of acetaldehyde, the potential was first scanned in the positive direction. Scan rate: 10 mV/s. Electrolyte flow rate: 10 μL/s [34]

The acetaldehyde adsorbate coverage calculated from the mass spectrometric charge of CO_2 at $m/z = 44$ is shown in Fig. 13. Of particular note is the fact that the adsorbate coverage is significantly higher than that resulting from ethanol adsorption, with a maximum coverage of ca. 0.8 at adsorption potentials between +0.15 and +0.35 V, compared to ca. 0.6 for ethanol adsorption at around +0.3 V. H_{ads} blocking of acetaldehyde adsorption is much less pronounced than for ethanol adsorption, resulting in a relative coverage of ca. 0.6 even on an initially H_{ads}-covered surface at +0.06 V. Apparently, the dissociative adsorption of acetaldehyde is much more facile than that of ethanol, which can be explained by the higher adsorption energy of acetaldehyde than ethanol on a Pt/C surface.

The numbers of electrons per CO_2 molecule formed during acetaldehyde adsorbate oxidation in the positive-going scan are also listed in Table 2 for different adsorption potentials. Similar to ethanol adsorption, the total electron yields are generally between 2 and 2.5, but in this case we find a pronounced minimum with values of about 2 electrons per CO_2 molecule in the potential range between +0.16 and +0.26 V. In the main peak around 0.7 V, the electron yield is close to 2.0, implying that this peak results almost exclusively from oxidation of CO_{ads}. The significantly higher numbers in the high potential region above +0.85 V resemble the findings for ethanol adsorption, pointing to a similar origin; namely, the oxidation of adsorbed hydrocarbons.

Experiments for reductive desorption of acetaldehyde after adsorption at +0.16 and +0.31 V, respectively, are plotted in Fig. 18. Upon adsorption at +0.31 V (black lines), methane is the major reductive product during reductive desorption of adsorbates in the H_{ads} region (Fig. 18c), while small amounts of ethane (Fig. 18d) and acetaldehyde (Fig. 18e) were also detected. The additional signal at $m/z = 29$ around +0.7 V is assigned to the ^{13}CO or $C^{17}O$ fragments of the respective CO_2 molecule. Compared to the experiments in Fig. 17, which started with the positive-going scan, the main oxidative peak in the subsequent positive-going scan is shifted negatively, and the formation of CO_2 in the high potential region above +0.85 V almost vanishes. This can, again, be explained by the reductive desorption of the adsorbed hydrocarbon species during the negative scan, which results in a decrease of the adsorbate coverage. Analogous experiments after acetaldehyde adsorption in the H_{upd} region, at +0.16 V, did not show any methane and ethane formation during the first negative-going scan (Fig. 18, gray lines), and is very similar to adsorbed CO stripping. It is more likely that during acetaldehyde dissociative adsorption, adsorbed CH_x and/or $C_2H_y(O)$ species are already removed by the reduction to methane and ethane. Acetaldehyde desorbed in the hydrogen region suggests that

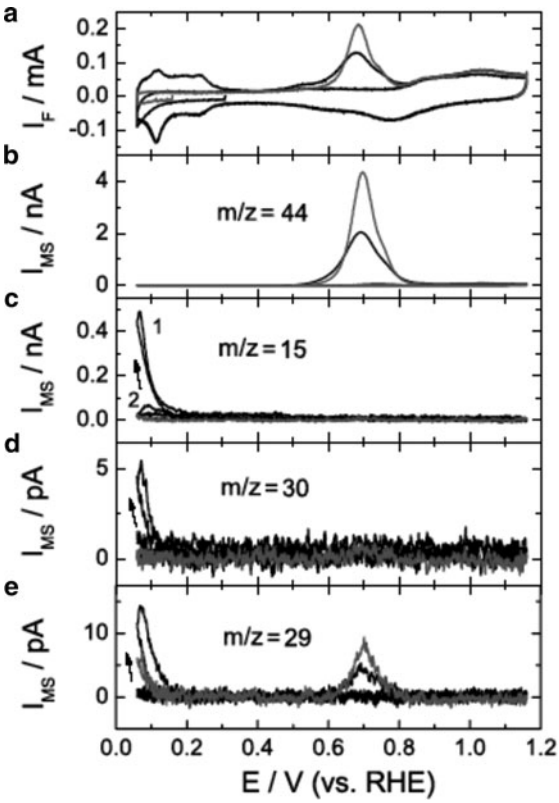

Fig. 18 Simultaneously recorded CVs (**a**) and MSCVs of CO_2 at $m/z = 44$ (**b**), methane at $m/z = 15$ (**c**), ethane at $m/z = 30$ (**d**), and acetaldehyde at $m/z = 29$ (**e**) for the reduction and oxidation of acetaldehyde adsorbates formed upon adsorption at +0.16 V (*gray lines*) and +0.31 V (*black lines*) in 0.1 M acetaldehyde + 0.5 M H_2SO_4. After the adsorption of acetaldehyde, the potential was first scanned in the negative direction [34]

acetaldehyde irreversibly adsorbs onto platinum due to its strong affinity arising from the carbonyl group.

4.2 Ethanol Bulk Electrooxidation

After reviewing ethanol and acetaldehyde dissociation on Pt-based nanoparticle catalysts, in this section we will discuss the effects of various factors, such as ethanol concentration, potential and catalyst composition on the current efficiencies, and product yields of the bulk electrooxidation of ethanol.

The CVs and corresponding MSCVs for ethanol oxidation on a Pt/C electrode in 1 M (solid lines) and 0.1 M (dotted lines) ethanol solutions containing 0.5 M H_2SO_4 are shown in Fig. 19. Ethanol bulk electrooxidation on Pt/C onsets at ca. +0.4 V and results in a peak with a shoulder on the negative side in the positive-going scan, while at higher potentials, it is hindered by PtO formation and increases again at the positive potential limit. In the negative-going scan, ethanol oxidation currents onset with PtO reduction and decrease at more negative potentials due to re-poisoning of the catalyst. As the ethanol concentration is increased, the current peaks in both scan directions shift positively. A tenfold increase in ethanol concentration results only in ca. fourfold increase in the Faradaic current (Fig. 19a).

The CO_2 formation is monitored selectively through the doubly ionized molecular ion (CO_2^{++}) at $m/z = 22$ (Fig. 19b). The onset of CO_2 formation in the positive-going scan of the steady-state voltammogram occurs at ca. +0.5 V. The fact that comparable amounts of CO_2 formed for ethanol adsorbate stripping [taking into account the ratio of $m/z = 22$ to $m/z = 44$ ion signals for CO_2 (2.8%)] and for bulk ethanol oxidation at different concentrations suggests that CO_2 formation during the positive-going scan is mostly related to the oxidation of adsorbed poisoning CO and CH_x species to CO_2, with a certain rate of re-adsorption of CO and CH_x due to C–C bond dissociation during ethanol electrooxidation, which causes some broadening of the CO_2 formation peak, compared to the stripping data. Clearly, the Faradaic current shoulder is coincident with the CO_2 formation peaks, suggesting that it originates from the oxidation of ethanol adsorbate (CO_{ads} and $CH_{x,\ ads}$), and that other products of ethanol oxidation are formed in parallel to CO_2. In the negative-going scan, the CO_2 formation rate is largely suppressed over the entire potential range, although the Faradaic current exhibits a distinct peak centered at ca. +0.6–0.7 V.

To avoid interference with CO_2 at $m/z = 44$, acetaldehyde formation can be detected selectively by the CHO^+ fragment of acetaldehyde at $m/z = 29$ during ethanol electrooxidation (Fig. 19c). The onset of acetaldehyde formation in the positive-going scan occurs at potentials positive of ca. +0.35 V, simultaneously with the onset of ethanol oxidation current. Because of the absence of CO_2 formation at potentials below +0.5 V, this suggests preferential incomplete

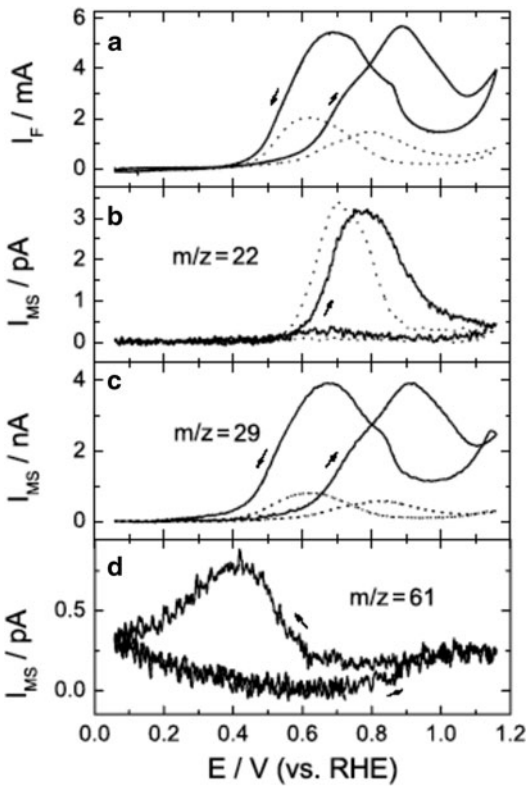

Fig. 19 Simultaneously recorded CVs (**a**) and MSCVs of CO_2 at $m/z = 22$ (**b**), acetaldehyde at $m/z = 29$ (**c**), and ethyl acetate at $m/z = 61$ (**d**) for the oxidation of ethanol on Pt/C (E-TEK) in 1 M ethanol + 0.5 M H_2SO_4 (*solid lines*) and 0.1 M ethanol + 0.5 M H_2SO_4 (*dotted lines*). Scan rate: 10 mV/s. Electrolyte flow rate: 10 μL/s. *Arrows* indicate the direction of potential scan

oxidation of ethanol at low potentials. The acetaldehyde formation follows the Faradaic current, also suggesting that the incomplete oxidation of ethanol prevails. The acetaldehyde formation rate increases by ca. sevenfold with an increase in ethanol concentration from 0.1 to 1 M, whereas the Faradaic current increases by only four times.

Due to the low volatility of acetic acid in water, no potential dependence of an ion signal at $m/z = 60$ could be detected. However, ethyl acetate (the ester derived from acetic acid and ethanol) can be detected through the $m/z = 61$ fragment at high (e.g., 1 M) ethanol concentration. The formation of ethyl acetate occurs mainly in the negative-going scan, and the delay of the signal at $m/z = 61$ seems to be due to the relatively large size of the ethyl acetate molecule and resulting low permeability through the Teflon membrane. Ethyl acetate is formed by a follow-on chemical reaction of the electrochemically formed acetic acid with ethanol. This reaction can be formulated as:

$$CH_3COOH + CH_3CH_2OH \rightleftarrows CH_3COOCH_2CH_3 + H_2O.$$

Table 3 The average current efficiency (η_i) and the average yield (W_i) of CO_2, acetaldehyde, and acetic acid for ethanol oxidation on different catalyst electrodes in one cycle of potential scan in 1 M (or 0.1 M) ethanol + 0.5 M H_2SO_4 solution (error bar for current efficiency of CO_2 and acetaldehyde: $\leq$20%)

Catalysts	Potential region (V)	η_1 (%)	η_2 (%)	η_3 (%)	W_1 (%)	W_2 (%)	W_3 (%)
Pt/C (E-TEK)	0.06–1.16	1.2	62	37	0.5	77	23
PtRu/C (E-TEK)	0.06–0.7	1.0	59	40	0.4	74	26
Pt_3Sn/C (E-TEK)	0.06–0.6	1.3	64	35	0.5	78	22
PtRh (ZSW)	0.06–0.7	5.8	42	52	2.8	60	37
Pt/C (E-TEK)#	0.06–1.16	2.7	37	60	1	55	44

η_i average current efficiency of products in one potential cycle; W_i average product yield in one potential scan. Subscripts 1, 2, and 3 indicate CO_2, acetaldehyde, and acetic acid. # means 0.1 M ethanol

In the hydrogen region, methane is also detected during ethanol bulk oxidation at $m/z = 15$ (not shown). The formation of methane is nearly independent of the concentration of ethanol, implying that it arises mainly from the reduction of strongly adsorbed CH_x species.

After calibrating the DEMS setup, the current efficiencies and product yields for acetaldehyde, acetic acid, and CO_2 formation during one complete potential cycle can be calculated, and the results are listed in Table 3. Because of the very low amount of ethyl acetate formed, it is neglected during the calculation of current efficiencies and product yields.

The quantitative DEMS results (Table 3) indicate that ethanol electrooxidation on Pt/C mainly generates intermediates (acetaldehyde and acetic acid) with CO_2 as a minor product, and the yields of acetic acid and CO_2 increase with a decrease in ethanol concentration likely due to a higher probability for further oxidation of acetaldehyde to acetic acid and CO_2.

Similar potentiodynamic measurements were also performed on Pt_3Sn/C, PtRu/C (20 wt.%, E-TEK), and PtRh (ZSW) catalysts (Fig. 20). The positive potential limit was lowered to +0.6 or +0.7 V to avoid leaching of the less-noble component. Ethanol oxidation on both Pt_3Sn/C and PtRu/C starts at around +0.3 V (Fig. 20a), which is ca. 100 mV negative of the value for Pt/C, and coincident with the onset of acetaldehyde generation (Fig. 20c). Although the onset of CO_2 formation is negatively shifted to ca. +0.4 V due to the bifunctional mechanism, the average current efficiencies for CO_2 generation are still around 1% for Pt_3Sn/C and PtRu/C catalysts, with acetaldehyde and acetic acid still being the predominant products (Table 3). Pt_3Sn/C catalysts exhibit higher current densities than PtRu/C. Higher yield of CO_2 and acetic acid is observed on PtRh relative to PtRu/C and Pt_3Sn/C catalysts. However, the onset potential is more positive, and the yield of CO_2 is still less than 3%. In addition, trace amounts of ethyl acetate are formed on these three catalysts (not shown).

Additional information on the steady-state situation during ethanol oxidation and on the effects of the applied potential were obtained from potential step experiments. Figure 21 shows the simultaneously recorded current transients (a) and mass

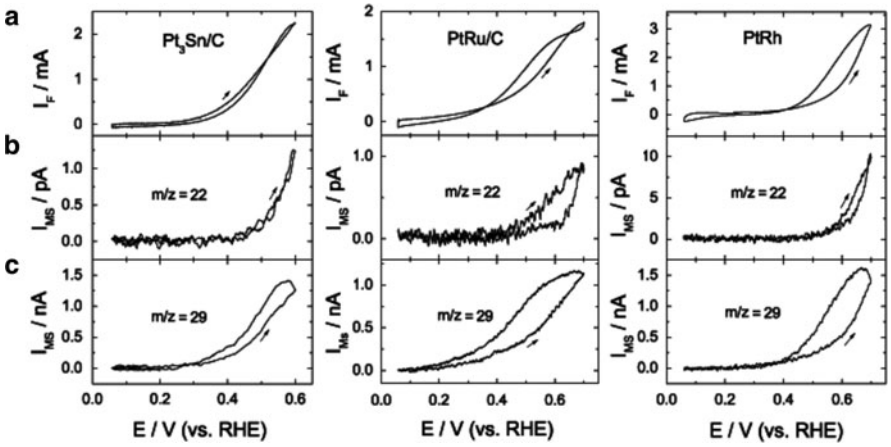

Fig. 20 Simultaneously recorded CVs (**a**) and MSCVs of CO_2 at $m/z = 22$ (**b**) and acetaldehyde at $m/z = 29$ (**c**) for the oxidation of ethanol on Pt_3Sn/C, PtRu/C (E-TEK), and PtRh (ZSW) in 1 M ethanol + 0.5 M H_2SO_4. Scan rate: 10 mV/s. Electrolyte flow rate: 10 μL/s. *Arrows* indicate the direction of potential scan

spectrometric current transients at $m/z = 22$ (b) and $m/z = 29$ (c) for the oxidation of ethanol on carbon-supported Pt, PtRu, and Pt_3Sn catalysts and unsupported PtRh catalyst in 1 M ethanol + 0.5 M H_2SO_4 after a potential step from +0.06 V to higher potentials. At the initial potential (+0.06 V), the catalyst surface should be free of ethanol adsorbate. After the potential step, resulting in the initial spike, the Faradaic current decreases with time due to the surface blockage by adsorbed poisoning species (CO_{ads} and especially $CH_{x,ads}$). The formation of CO_2 decreases more sharply than the Faradaic current and mass spectrometric current of acetaldehyde. As a result, after a reaction time of 15 min, the mass spectrometric signal of CO_2 for all the studied catalysts and potentials is negligible. The Faradaic current increases with increasing potential, and the increase in the Faradaic current leads to an increase in the formation of intermediates (acetaldehyde and acetic acid). Fifteen minutes after the potential step, the Faradaic current and mass spectrometric current were used to calculate the current efficiency and yield of CO_2, acetaldehyde, and acetic acid, which are listed in Table 4.

After 15 min following the potential step to high potentials, the yields of CO_2 are negligible for all four catalysts and all studied potentials. For Pt/C and PtRu/C catalysts, the yields of acetaldehyde and acetic acid are ca. 90% and 10%, respectively. In the case of Pt_3Sn/C catalysts, the yield of acetaldehyde decreases to 80% and the yield of acetic acid increases to 20% at +0.6 V. A higher yield of acetic acid is observed on PtRh under potentiostatic conditions, similar to the results from potentiodynamic experiments. Also under potentiostatic, steady-state conditions, ethanol oxidation largely results in incomplete oxidation to byproducts (acetaldehyde and acetic acid), while complete oxidation to CO_2 is only

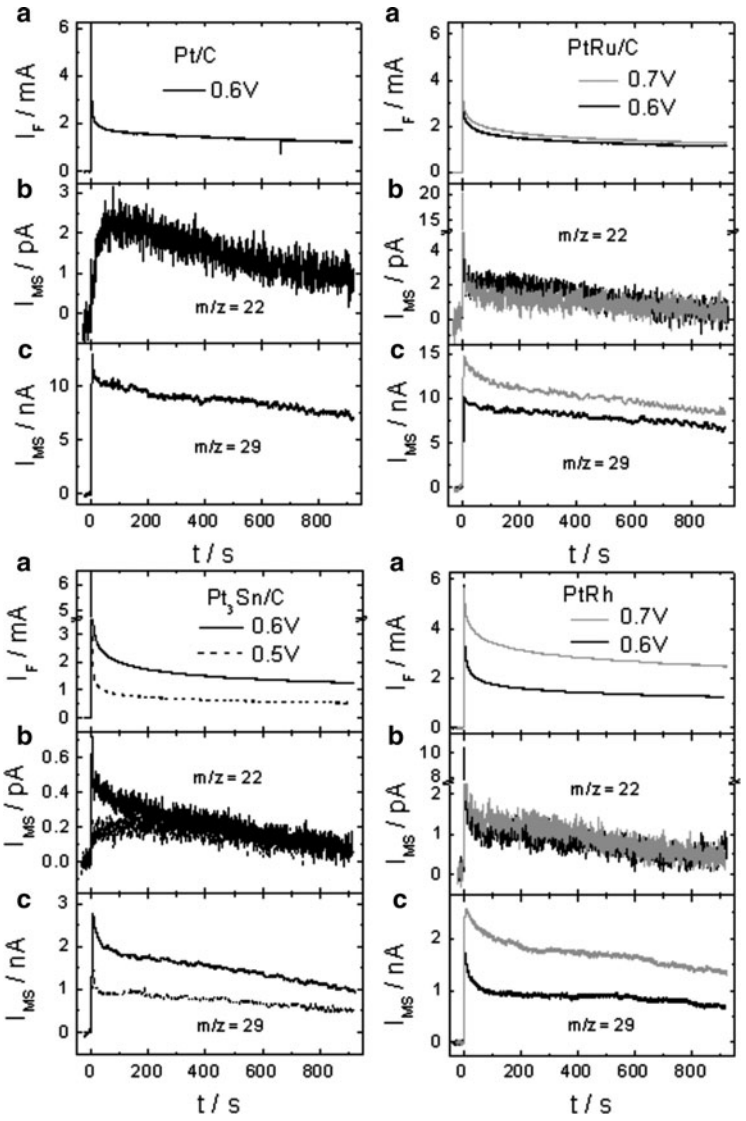

Fig. 21 Simultaneously recorded current transients (**a**) and mass spectrometric current transients of CO_2 at $m/z = 22$ (**b**) and acetaldehyde at $m/z = 29$ (**c**) for the oxidation of ethanol on Pt/C, PtRu/C, Pt_3Sn/C (E-TEK), and PtRh (ZSW) in 1 M ethanol + 0.5 M H_2SO_4 after the potential step from +0.06 V to different high potentials. Electrolyte flow rate: 10 μL/s

a minority pathway under present reaction conditions. The low yield of CO_2 is attributed to the kinetic barrier for C–C bond breaking at high potentials and oxidation of CO, and especially CH_x ad-species, at low potentials.

Table 4 Current efficiency (η_i) and the product yield (W_i) of CO_2, acetaldehyde, and acetic acid for ethanol oxidation on different catalysts at different potentials in 1 M ethanol + 0.5 M H_2SO_4 solution at the 15th minute after potential step from +0.06 V to different higher potentials (error bar for current efficiency of CO_2 and acetaldehyde: $\leq$20%)

Catalysts	*E*/*V* (RHE)	*I*/mA	η_1 (%)	η_2 (%)	η_3 (%)	W_1	W_2 (%)	W_3 (%)
Pt/C (E-TEK)	0.6	1.23	0.4	82	18	Trace	90	10
PtRu/C (E-TEK)	0.6	1.13	0.2	84	16	Trace	91	9
PtRu/C (E-TEK)	0.7	1.35	0.2	84	16	Trace	91	9
Pt_3Sn/C (E-TEK)	0.5	0.53	0.4	84	16	Trace	91	9
Pt_3Sn/C (E-TEK)	0.6	1.25	0.2	67	33	Trace	80	20
PtRh (ZSW)	0.6	1.25	0.4	39	61	Trace	56	44
PtRh (ZSW)	0.7	2.50	0.2	41	59	Trace	58	42

η_i current efficiency of products, W_i product yield. Subscripts 1, 2, and 3 indicate CO_2, acetaldehyde, and acetic acid, respectively. *E* oxidation potential, *I* Faradaic current

4.3 Acetaldehyde Bulk Oxidation

Ethanol oxidation generates large amounts of acetaldehyde, which is toxic, and leads to a considerable loss of energy efficiency. Therefore, the study of acetaldehyde oxidation is also of great interest.

The CV and the corresponding MSCV for acetaldehyde oxidation on a Pt/C electrode are shown in Fig. 22. In the positive-going scan, the oxidation of acetaldehyde starts around +0.5 V, and the CV exhibits a characteristic peak at +0.89 V with a shoulder at ca. +0.7 V. When the potential is higher than +1.0 V, the current increases again. In the negative-going scan, an oxidative peak occurs at +0.60 V with a shoulder on the right side due to the reduction of Pt oxide. The formation of CO_2 mainly occurs in the positive-going scan, corresponding to the shoulder at +0.75 V in the CV. Moreover, the amount of CO_2 formed in the positive-going scan resembles that obtained for acetaldehyde adsorbate oxidation on Pt/C, which implies that CO_2 is mainly formed via oxidation of adsorbed species resulting from decomposition of acetaldehyde at low potentials. In the negative-going scan, CO_2 formation is almost completely suppressed. The large Faradaic currents in both positive and negative scans are not correlated with CO_2 formation and hence must be due to the formation of acetic acid. Unfortunately, due to the low volatility of acetic acid in water at low concentrations, the potential-dependent signals of acetic acid cannot be observed. The average current efficiency for CO_2 formation in one potential cycle is only ca. 5%, suggesting that over 90% of the current can be attributed to acetic acid formation. The potentiostatic oxidation of acetaldehyde at +0.61 V on Pt/C also shows that the current efficiency for CO_2 formation is about 4–7%, depending on the history of the Pt/C catalyst [83].

The CVs and the corresponding MSCVs for acetaldehyde oxidation on PtRu/C and Pt_3Sn/C electrodes are presented in Fig. 23. Compared to Pt/C, PtRu/C and Pt_3Sn/C have a lower onset potential for acetaldehyde oxidation. In particular, for Pt_3Sn/C the onset potential is ca. +0.15 V, i.e., 300 mV negative of the value

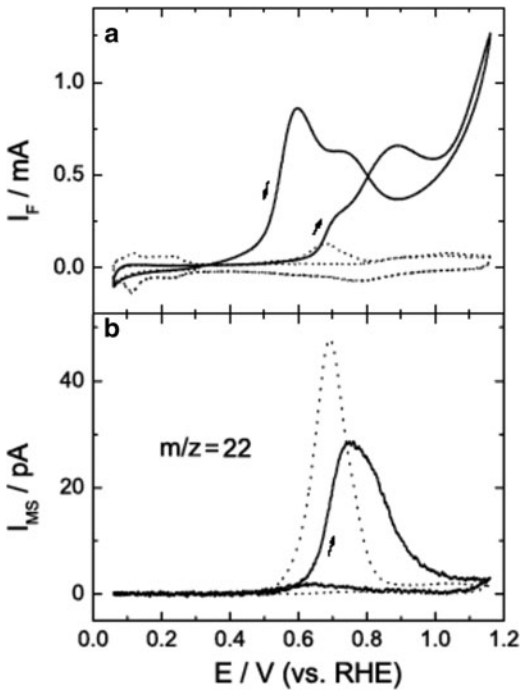

Fig. 22 Simultaneously recorded CV (**a**) and MSCV of CO_2 at $m/z = 22$ (**b**) for the oxidation of acetaldehyde in 0.1 M CH_3CHO + 0.5 M H_2SO_4 solution on a Pt/C (E-TEK) electrode (*solid lines*). For comparison, the oxidative stripping of acetaldehyde adsorbate formed at +0.31 V is also shown by *dotted lines*. Scan rate: 10 mV/s. Electrolyte flow rate: 10 μL/s [83]

for Pt/C. The formation of CO_2 starts at ca. +0.4 V, compared to +0.5 V for Pt/C. However, the average current efficiencies for CO_2 generation on PtRu/C and Pt_3Sn/C are ca. 11% and 6% in one potential scan. The potentiostatic oxidation of acetaldehyde at +0.61 V on PtRu/C and Pt_3Sn/C shows that the current efficiencies of CO_2 are even lower, about 1% and 2%, respectively [83]. Therefore, acetic acid also prevails during acetaldehyde oxidation on PtRu/C andPt_3Sn/C. The relative high yield of acetic acid during ethanol oxidation on Pt_3Sn/C can be attributed to the high activity for the further oxidation of acetaldehyde.

4.4 Dissociative Adsorption and Electrooxidation of Acetic Acid

At temperatures below 80°C, acetic acid cannot be oxidized due to its weak adsorption on platinum surfaces, as indicated by the fact that no potential-dependent CO_2 signal is observed. However, in the hydrogen adsorption region, acetic acid could be reduced to form strongly adsorbed species, likely due to the generation of acetaldehyde and its subsequent dissociation [84]. At temperatures above 80°C, acetic acid can be further oxidized to CO_2; therefore, a higher current efficiency for CO_2 can be observed [85, 86]. At 250°C, acetic acid oxidation has even faster kinetics when compared to ethanol and acetaldehyde oxidation [87].

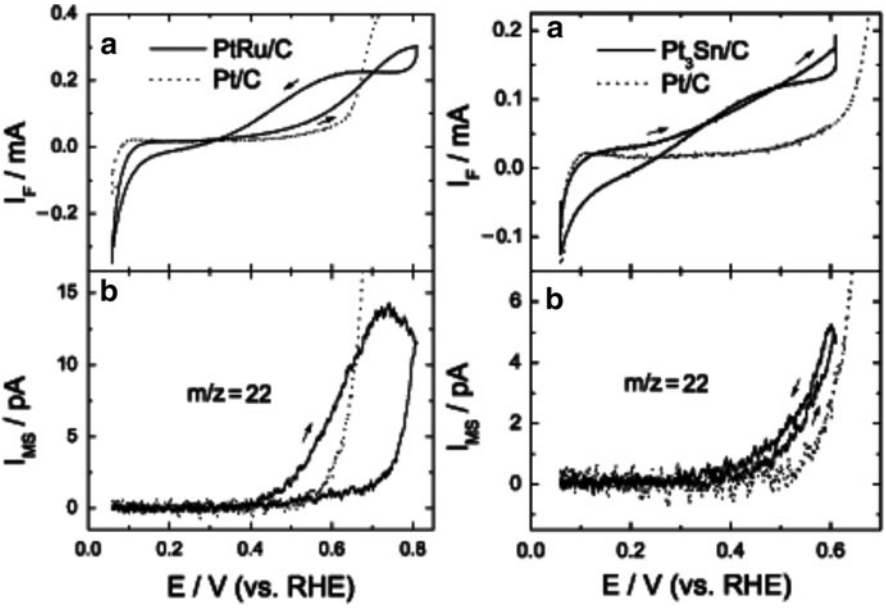

Fig. 23 Simultaneously recorded CVs (**a**) and MSCVs of CO_2 at $m/z = 22$ (**b**) for the oxidation of acetaldehyde in 0.1 M CH_3CHO + 0.5 M H_2SO_4 solution on a PtRu/C and Pt_3Sn/C (E-TEK) electrodes (*solid lines*). For comparison, Pt/C is also shown by *dotted lines*. Scan rate: 10 mV/s. Electrolyte flow rate: 10 μL/s [83]

According to these quantitative and qualitative DEMS results, the mechanism of ethanol electrooxidation under ambient conditions can be simply described as follows:

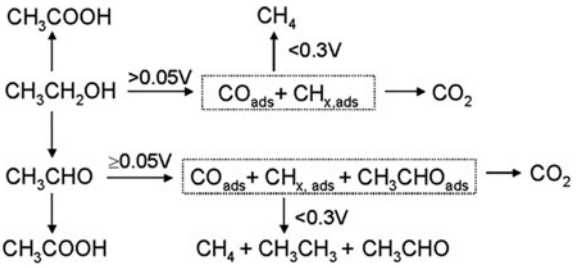

5 Mechanism of Ethylene Glycol Electrooxidation

Since both ethanol and acetaldehyde have a methyl group (CH_3-), their oxidation on Pt-based catalysts generates adsorbed CH_x species, which are even more difficult to oxidize than CO_{ads}, and strongly poison catalyst surfaces. To avoid $CH_{x,ads}$ poisoning species, ethylene glycol could represent an alternative fuel. Ethylene glycol has

two alcoholic groups, and thus its decomposition only results in adsorbed CO, with no adsorbed CH_x species [88].

5.1 *Dissociative Adsorption of Ethylene Glycol on Pt/C, PtRu/C, and Pt_3Sn/C*

The procedure for adsorption of ethylene glycol was similar to that of ethanol and acetaldehyde adsorption [88]. At +0.06 V, ethylene glycol cannot be decomposed due to surface blockage by H_{upd}, and thus no oxidative current is observed. Going to higher potentials, anodic currents are observed upon adsorption of ethylene glycol. The signal increases steeply upon introduction of the ethylene glycol-containing electrolyte, passes through a maximum, and then decays. The anodic peak current progressively increases with the adsorption potential. After a 5-min adsorption time in 0.1 M ethylene glycol + 0.5 M H_2SO_4 solution at different constant potentials, the potential was stepped to +0.06 V (since the adsorbate is only adsorbed CO, it cannot be desorbed at this potential and further adsorption is also precluded), and the electrolyte was exchanged with pure supporting electrolyte. In order to determine the amount or coverage of adsorbate, we oxidized it via cyclic voltammetry, and simultaneously recorded the mass spectrometric signal of CO_2. The amount of CO_2 formed was used to calculate the amount or coverage of adsorbate. As an example, Fig. 24 shows the CVs and corresponding MSCVs of CO_2 at $m/z = 44$ for the oxidative desorption of ethylene glycol adsorbate on Pt/C, PtRu/C, and Pt_3Sn/C electrodes. The anodic peak resembles that for the oxidation of adsorbed CO, which suggests that the ethylene glycol adsorption forms adsorbed CO. IR measurements [45, 47–49] and the calculated electron number, equaling 2, also support this conclusion. The onset potential for ethylene glycol adsorbate oxidation on Pt/C is about +0.5 V, where strongly adsorbed CO oxidation starts, and the oxidative peak

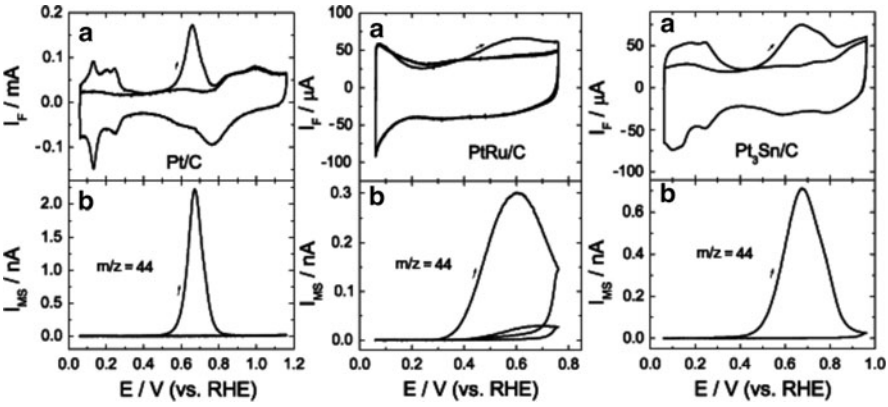

Fig. 24 Simultaneously recorded CVs (**a**) and MSCVs of CO_2 at $m/z = 44$ (**b**) for the oxidation of ethylene glycol adsorbate formed on Pt/C (E-TEK) at +0.31 V, PtRu/C (E-TEK) at +0.26 V, and Pt_3Sn/C (E-TEK) at +0.36 V. Scan rate: 10 mV/s. Electrolyte flow rate: 10 μL/s [88]

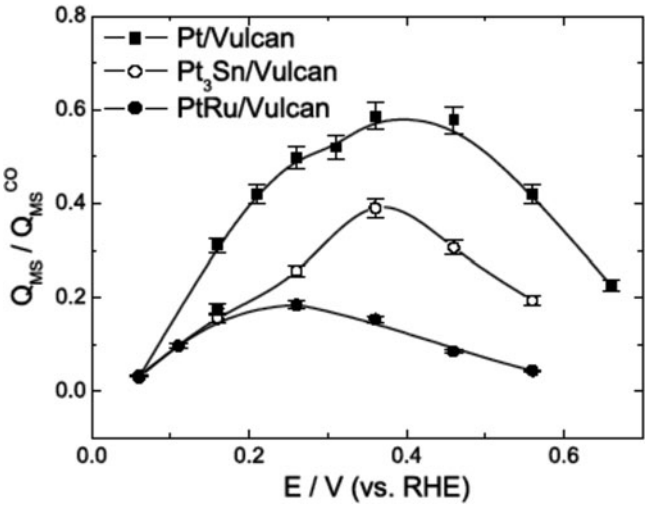

Fig. 25 Relative coverages of ethylene glycol adsorbate compared to that of a saturated CO adlayer obtained at different adsorption potentials on Pt/C, PtRu/C, and Pt_3Sn/C (E-TEK) catalyst electrodes [88]

occurs at ca. +0.67 V. For PtRu/C, the onset potential for oxidation of ethylene glycol adsorbate and the oxidative peak are negatively shifted to ca. +0.3 V and +0.6 V, respectively. Although the oxidation of ethylene glycol adsorbate onsets around +0.2 V on Pt_3Sn/C, the significant oxidation of ethylene glycol adsorbate starts around +0.4 V, and the oxidative peak occurs at the same potential as on Pt/C.

The relative coverage of ethylene glycol adsorbate compared to that of a saturated CO adlayer on the Pt/C, PtRu/C, and Pt_3Sn/C catalysts, calculated simply as the ratio of the mass spectrometric charge of the $m/z = 44$ for ethylene glycol adsorbate oxidation to that for stripping of a saturated CO adlayer, is shown for different adsorption potentials in Fig. 25. At +0.06 V, ethylene glycol cannot be decomposed to CO_{ads} due to blocking of Pt sites by H_{upd}. At more positive potentials, the coverage of ethylene glycol adsorbate increases, reaches a maximum, and then decreases with further increases in potential due to oxidative desorption at high potentials. The maximum coverages of ethylene glycol adsorbate are 0.6, 0.4, and 0.2 for Pt/C, Pt_3Sn/C, and PtRu/C, respectively. This indicates that PtRu/C and Pt_3Sn/C are not favorable for ethylene glycol dissociative adsorption at ambient temperatures when compared to Pt/C.

5.2 Ethylene Glycol Bulk Electrooxidation on Pt/C, PtRu/C, and Pt_3Sn/C

In this section, we compare ethylene glycol bulk oxidation on the three different carbon-supported Pt-based catalysts by potentiodynamic measurements and by

potentiostatic and amperometric measurements. The latter measurements, which allow us to distinguish between time and potential effects, were performed by stepping the potential from an initial value of +0.06 V to the reaction potential between +0.36 and +0.76 V. In addition to Faradaic current measurements, the CO_2 formation was monitored at $m/z = 44$ by mass spectrometry. No other volatile species were detected during ethylene glycol oxidation in these measurements.

The CVs and the corresponding MSCVs of CO_2 at $m/z = 44$ for ethylene glycol oxidation on carbon-supported Pt, PtRu, and Pt_3Sn catalyst electrodes are presented in Fig. 26. For Pt/C, the onset of ethylene glycol oxidation occurs at about +0.35 V in the positive-going scan, leading to an asymmetric peak with a maximum at +0.7 V and significant intensity in the high potential side. At the most positive potentials (E > +1.0 V), the oxidation current starts to increase again. CO_2 formation onsets at around +0.5 V, where strongly adsorbed CO oxidation starts. In the negative-going scan, an asymmetric anodic current peak is observed at +0.6 V. The related CO_2 ion current signal is much weaker than in the positive-going scan, in contrast to the higher current in the Faradaic current signal. Hence, the formation of CO_2 is much lower in the negative-going scan than in the positive-going scan. The contribution of CO_2 formation to the Faradaic current signal, which is calculated from the $m/z = 44$ signal, is of the order of a few percent (Fig. 26b, right-hand scale). This means that large amounts of intermediates are formed during ethylene glycol oxidation on Pt/C catalyst. Similarly, Horanyi et al. [43] performed constant potential electrolysis of ethylene glycol, and also found that the current efficiency for CO_2 production was about 5%, while the current efficiency for glycolaldehyde formation varied from 85% to 60% with increasing potential from +575 to +675 mV. However, no other potential-dependent products could be detected by DEMS due to the low or negligible volatility of these

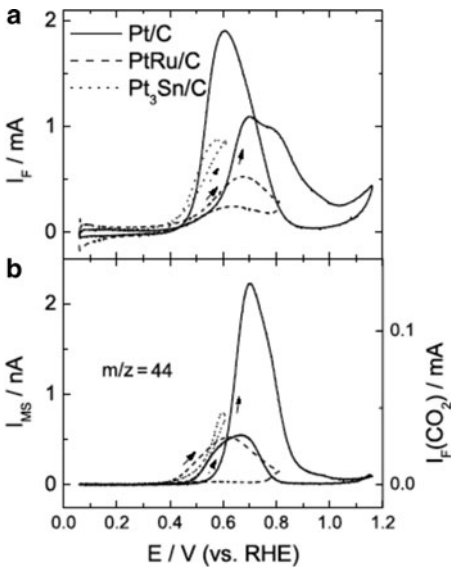

Fig. 26 Simultaneously recorded CVs (**a**) and MSCVs of CO_2 at $m/z = 44$ (**b**) on Pt/C, PtRu/C, and Pt_3Sn/C (E-TEK) catalyst electrodes in 0.1 M ethylene glycolanol + 0.5 M H_2SO_4 solution. Scan rate: 10 mV/s. Electrolyte flow rate: 10 μL/s. The right-hand scale of Fig. 26b indicates the Faradaic currents assigned to CO_2 formation [88]

intermediates. Although the bulk ethylene glycol oxidation current onsets at lower potentials and is much larger than that for adsorbate oxidation (Fig. 24), the onset potentials for CO_2 formation are about the same for the bulk oxidation and adsorbate oxidation, and the amounts of CO_2 formed are also comparable in the lower oxidation potential range (<+0.85 V) [88]. Moreover, similar to methanol oxidation, in the low potential region, CO_2 formation is independent of ethylene glycol concentration, while the Faradaic current increases with increasing concentration of ethylene glycol [89]. These facts suggest that during ethylene glycol oxidation, CO_2 is generated from the oxidation of CO_{ads} formed from ethylene glycol decomposition. Therefore, ethylene glycol electrooxidation on platinum also proceeds via a dual pathway reaction mechanism, which involves the successive oxidation of the functional groups (–OH groups) without cleavage of the C–C bond in the one reaction pathway, and C–C bond breaking with subsequent formation and oxidation of CO_{ads} to CO_2 in the second pathway.

On PtRu/C electrodes, ethylene glycol oxidation starts around +0.3 V, which is 50 mV more negative than on Pt/C. CO_2 formation starts, again, only at more positive potentials, with the onset potential being around +0.35 V. While this is more positive when compared to the Faradaic current signal, it is about 150 mV more negative than the onset for CO_2 formation on Pt/C electrodes under similar conditions, i.e., the presence of Ru can enhance both the formation of partly oxidized reaction intermediates as well as CO_2 formation. For identical catalyst loading, the peak current is, however, significantly less on PtRu/C, with 0.5 mA, as compared to about 1.1 mA on Pt/C. The loss in activity at high potentials is attributed to the oxidation of Ru. In this case, CO_2 formation occurs mainly in the positive-going scan. We observe very little CO_2 formation in the reverse scan, i.e., C–C bond breaking and CO_{ads} formation are almost completely inhibited at higher potentials, where CO oxidation would be possible. Comparison of CO_2 signals between bulk oxidation and adsorbate oxidation suggests that CO_2 formation in the positive-going scan originates from the oxidation of adsorbed CO formed at low potentials. The average current efficiency for CO_2 formation in a cyclic potential scan is ca. 6.7%. Therefore, also on the PtRu/C electrode, ethylene glycol oxidation results predominantly in C_2 byproduct formation under current reaction conditions, and C–C bond breaking and CO_2 formation represent minority pathways. These observations agree, even quantitatively, with results reported by de Lima et al., who found a CO_2 yield of 8%, from IR measurements, after a 6-min electrolysis of ethylene glycol on $Pt_{62}Ru_{38}$ [90].

For Pt_3Sn/C, the oxidation of ethylene glycol starts at around +0.3 V, which is 50 mV more negative than on Pt/C electrodes, while the onset potential for CO_2 formation is around +0.4 V, which is about 100 mV more negative than on Pt/C electrodes, and 50 mV more positive than on PtRu/C electrodes. Although the actual peak maximum was not reached because of the low potential limit, a much higher oxidative current is observed between +0.4 and +0.6 V, when compared to Pt/C and PtRu/C. The current contribution for CO_2 generation is indicated, again, by the right-hand scale in Fig. 26b. Also in this case, it is very low. The mean current efficiency for CO_2 formation, integrated over the complete potential cycle,

was around 4%. Hence, also for the Pt_3Sn/C catalyst, complete oxidation is a minority reaction pathway, and ethylene glycol oxidation results predominantly in C_2 reaction byproducts. Comparing the bulk oxidation signal with that for ethylene glycol adsorbate stripping on Pt_3Sn/C also suggests that CO_2 formation during ethylene glycol oxidation comes from the oxidation of CO_{ads} formed from ethylene glycol decomposition in the low potential region.

More information on the steady-state situation during ethylene glycol oxidation, and on the effect of the reaction potential, are obtained from potential step experiments. After a 5-min reaction time, the steady-state Faradaic currents and the corresponding mass spectrometric currents of CO_2 at $m/z = 44$ at different potentials are plotted in Fig. 27. Similar to potentiodynamic experiments, in the low potential region (<+0.6 V), PtRu/C and Pt_3Sn/C exhibit higher activity than Pt/C; in particular, Pt_3Sn/C shows the highest oxidative current. The current efficiency for CO_2 is also only several percent, and thus, also under steady-state conditions, ethylene glycol oxidation largely results in incomplete oxidation byproducts (C_2 species), with complete oxidation to CO_2 being only a minority pathway. A relatively high current efficiency for generation of CO_2 is observed on PtRu/C catalysts, when compared to Pt_3Sn/C and Pt/C, due to the high catalytic activity of PtRu toward CO oxidation. The low efficiency for CO_2 formation is attributed to the kinetic barrier for C–C bond breaking in the high potential region or slow oxidation of CO_{ads} in the low potential region as was observed for ethanol oxidation (Sect. 4).

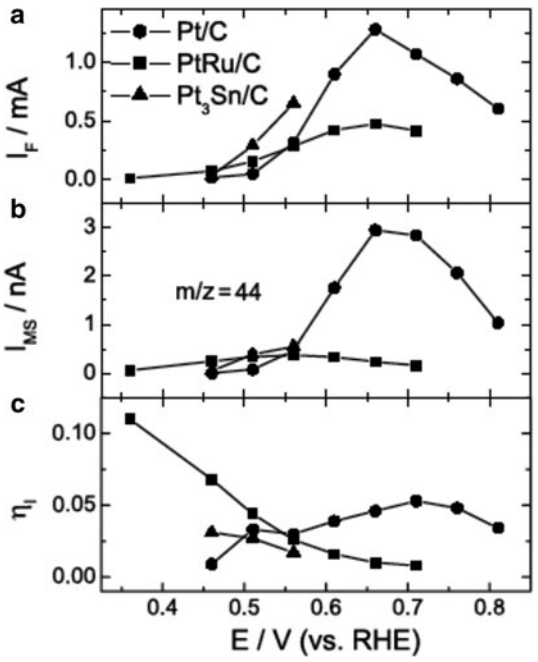

Fig. 27 Steady-state total Faradaic currents (**a**), corresponding mass spectrometric currents of CO_2 at $m/z = 44$ (**b**), and current efficiencies for CO_2 formation (**c**) as a function of the reaction potential for the different catalyst electrodes. *Black circles* – Pt/C, *black squares* – PtRu/C, black triangles – Pt_3Sn/C (E-TEK). Electrolyte flow rate: 10 μL/s [88]

5.3 *Dissociative Adsorption of Ethylene Glycol Oxidative Derivatives*

As mentioned above, ethylene glycol oxidation also generates large amounts of intermediates (e.g., glycolaldehyde, oxal, glycolic acid, glyoxylic acid, and oxalic acid). These C_2 intermediates can be further dissociatively adsorbed and oxidized to CO_2. The further oxidation of these soluble intermediates can promote the energy conversion efficiency (in a fuel cell) of ethylene glycol. Moreover, these soluble intermediates can be considered as model systems for C_2 organic substances in electrocatalysis. Therefore, the adsorption and oxidation of these soluble intermediates have also attracted a great deal of attention [43, 45, 91]. Here we just discuss glyoxylic acid dissociation on Pt/C, because it is a very good model molecule for studying dissociative adsorption due to the presence of two different functional groups: carbonyl and carboxylic. In particular, CO_2 formed during glyoxylic acid dissociation at potentials where strongly adsorbed CO cannot be oxidized to CO_2 can be detected by DEMS.

The Faradaic current responses for Pt/C electrodes at different constant potentials in the course of glyoxylic acid adsorption, upon the exchange of 0.5 M H_2SO_4 solution to 0.1 M glyoxylic acid + 0.5 M H_2SO_4 solution, are shown in Fig. 28a. The CO_2 formation was also simultaneously monitored by mass spectrometry at $m/z = 44$ in the course of adsorption (Fig. 28b).

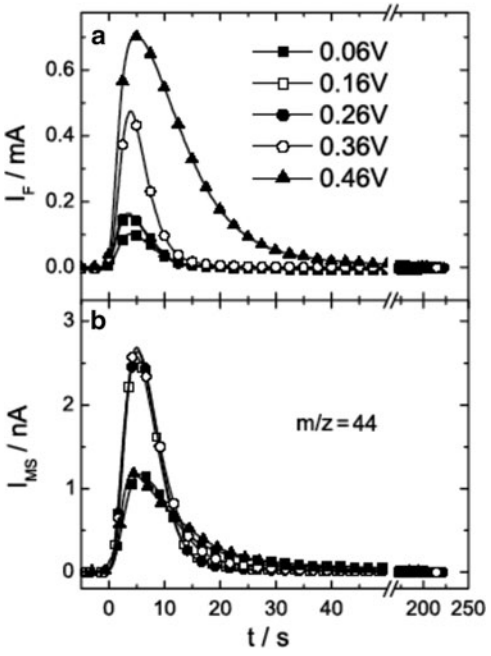

Fig. 28 Faradaic current (**a**) and corresponding mass spectrometric current of CO_2 at $m/z = 44$ (**b**) transients for the adsorption of glyoxylic acid on Pt/C (E-TEK) catalyst at different, constant potentials. For adsorption, the electrolyte was switched at $t = 0$ from the supporting electrolyte (0.5 M H_2SO_4) to one containing 0.1 M glyoxylic acid [92]

For the adsorption of glyoxylic acid, the Faradaic current transients always showed an oxidative current at all applied potentials studied (Fig. 28a). Figure 28b shows that CO_2 is formed in the course of glyoxylic acid adsorption, although in the studied potential region, adsorbed CO cannot be oxidized on the Pt catalyst due to the lack of adsorbed oxygen-containing species. With increasing adsorption potential, the adsorption current increases. However, the CO_2 formation rate increases initially, and then decreases for potentials beyond +0.36 V, suggesting that at high potentials ($>$ +0.35 V) the C–C bond cleavage is suppressed.

After adsorption for 5 min and rinsing the cell with supporting electrolyte, the adsorbate formed was stripped by anodic oxidation. Figure 29 shows simultaneously recorded CVs (Fig. 29a) and corresponding MSCVs of CO_2 at $m/z = 44$ (Fig. 29b) for the oxidative desorption of glyoxylic acid adsorbate, formed at +0.06 and +0.26 V, respectively. The anodic peaks resemble that for the oxidation of adsorbed ethylene glycol adsorbate, and the electron number per CO_2 molecule formation for the oxidative stripping of glyoxylic acid adsorbate is ca. 2. This suggests that despite the formation of CO_2 upon glyoxylic acid adsorption, the latter also leads to the formation of CO_{ads}.

It is both intriguing and important that the amount of CO_2 formed during the glyoxylic acid adsorption is nearly the same as that found during oxidative stripping of the adsorbate, allowing one to quantitatively relate the contributions of specific functional groups to individual soluble or adsorbed products formed upon

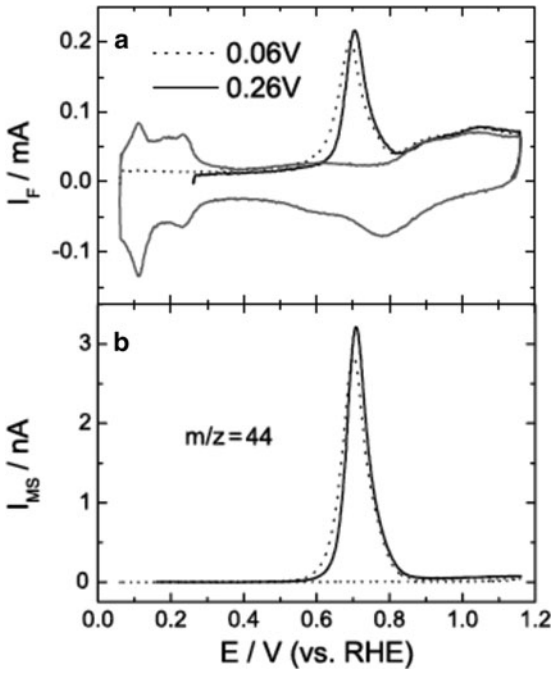

Fig. 29 Simultaneously recorded CVs (**a**) and MSCVs of CO_2 at $m/z = 44$ (**b**) for the oxidation of glyoxylic acid adsorbate formed at +0.06 and +0.26 V on Pt/C (E-TEK) catalyst electrode in 0.1 M glyoxylic acid + 0.5 M H_2SO_4 solution. *Gray solid line* indicates the base CV. Scan rate: 10 mV/s. Electrolyte flow rate: 10 μL/s [92]

adsorption. This suggests that there is C–C bond splitting during the irreversible adsorption of glyoxylic acid on platinum via the carbonyl group to form CO_{ads} as confirmed by the number of electrons per CO_2 formed in a subsequent adsorbate stripping, and the release of CO_2 from the carboxylic acid group upon adsorption.

6 Concluding Remarks

In this chapter, we have shown that online quantitative DEMS is a very sensitive and valuable technique for mechanistic studies of the oxidation of SOMs. It can detect volatile products formed in solution during the oxidation of SOMs and can also help analyze adsorbed species. Therefore, and as mentioned above, it is a very powerful tool for mechanistic studies.

Methanol electrooxidation on Pt-based catalysts proceeds via a parallel pathway mechanism. In one pathway, methanol is decomposed to form strongly adsorbed species (CO_{ads}), which can be further oxidized to CO_2 at high potentials; in others, methanol is oxidized to form formaldehyde, formic acid, and methyl formate. The extent of further oxidation of these soluble intermediates depends on convection, methanol concentration, and electrode surface roughness or catalyst loading. On smooth polycrystalline Pt, at high concentration of methanol and high flow rate, these soluble intermediates can be washed away before being further oxidized to CO_2; therefore, the current efficiency for CO_2 formation is very low (below 20%). For very rough Pt electrodes, e.g., high loading catalyst layer, these soluble intermediates stay in the pores and have a higher probability of being further oxidized to CO_2 before diffusing away. Therefore, a higher current efficiency for CO_2 formation was observed. While the formation rate of CO_2 via CO_{ads} is largely limited by the oxidation rate of CO_{ads} (in particular at low potentials), which is independent of methanol concentration, the rate of methanol oxidation via soluble intermediates increases with increasing methanol concentration. Therefore, the current efficiency for CO_2 formation decreases with increasing methanol concentration.

Ru adatoms not only promote methanol oxidation on Pt at low potentials but also increase the current efficiency for CO_2 generation. This can be explained by the facts that Ru adatoms can lower the oxidation potential of CO_{ads} on Pt, due to the bifunctional mechanism, and that low coverages of Ru adatoms can promote methanol dissociation to form CO_{ads} on Pt at low potentials, resulting from electronic effects. Therefore, Ru adatoms induce a shift from the reaction pathway via soluble intermediates to that via adsorbed CO. At potentials above +0.65 V, the current efficiency for CO_2 generation during methanol oxidation on PtRu decreases, since Ru loses its co-catalytic activity at high potentials due to the formation of inactive Ru oxide.

Ethanol electrooxidation on Pt-based catalysts also proceeds via a parallel pathway mechanism. In one pathway, ethanol is decomposed to form strongly adsorbed species (CO_{ads} and $CH_{x,ads}$, as well as trace amounts of C_2 hydrocarbon ad-species), which can be further oxidized to CO_2 at high potentials. In others,

ethanol is directly oxidized to form acetaldehyde and acetic acid without C–C bond rupture. Different from methanol and ethylene glycol, ethanol oxidation produces $CH_{x,ads}$ as poisoning species, which are even more difficult to oxidize to CO_2, and thus poison the Pt catalyst surface. The electrooxidation of ethanol on poisoned Pt-based catalysts (e.g., Pt, PtRu, Pt_3Sn and PtRh) predominantly generates acetaldehyde and acetic acid, and the amount of CO_2 formed is negligible. Addition of Ru or Sn in binary Pt catalysts lowers the onset potential for ethanol electrooxidation and the onset for CO_{ads} oxidation. It does not, however, increase the selectivity for complete oxidation to CO_2 – incomplete ethanol oxidation also prevails on these binary catalysts. For Pt_3Sn and PtRh, larger amounts of acetic acid relative to acetaldehyde are generated, likely because these two catalysts can catalyze the further oxidation of acetaldehyde.

For the practical application of DEFCs, more active anode catalysts, capable of oxidizing adsorbed CH_x species, as well as capable of splitting the C–C bond of ethanol, must be developed. Alternatively, DEFCs should be operated at elevated temperatures, since at ambient temperatures, ethanol oxidation on presently known catalysts suffers not only from a low energy density, due to incomplete ethanol oxidation, but, more importantly, also from the emission of highly undesirable toxic byproducts (acetaldehyde). Higher operating temperatures and/or electrocatalysts being more efficient for $CH_{x,ads}$ oxidation and C–C bond breaking are required to overcome these difficulties and to achieve complete oxidation of ethanol to CO_2.

Ethylene glycol electrooxidation on Pt-based catalysts also proceeds via a parallel pathway mechanism. Ethylene glycol is oxidized to CO_2 via adsorbed CO formed from C–C bond dissociation, while C_2 intermediates are also formed without C–C bond dissociation. The electrooxidation of ethylene glycol on Pt-based catalysts (e.g., Pt/C, PtRu/C, and Pt_3Sn/C) also mainly generates C_2 intermediates, and the current efficiency for CO_2 generation is still much lower than that for methanol oxidation, although it is much higher than that for ethanol oxidation. The low efficiency for CO_2 generation is attributed to the kinetic barrier for C–C bond breaking in the high potential region, or slow oxidation of CO_{ads} in the low potential region. Adsorbed CH_x species are not found during ethylene glycol decomposition. PtRu/C and Pt_3Sn/C show higher catalytic activity toward ethylene glycol oxidation than Pt/C at low potentials, and a higher current efficiency for CO_2 generation is observed on PtRu/C due to its high activity toward the oxidation adsorbed CO. A high Ru content in PtRu catalysts is not favorable for C–C bond splitting; a low Ru content PtRu catalyst should be used to increase PtRu activity.

Glyoxylic acid, a byproduct resulting from ethylene glycol oxidation, is a suitable model molecule for C_2 molecule decomposition studies. The decomposition of glyoxylic acid on Pt at low potentials generates the same amount of adsorbed CO on Pt and CO_2 in solution. This suggests that during glyoxylic acid decomposition, C–C bond cleavage occurs, where the carbonyl group is the precursor of adsorbed CO, and CO_2 originates from the carboxylic acid group.

In general, for these C_2 molecules, C–C bond splitting and successive oxidation are much slower than the oxidation of functional groups without C–C bond rupture. Therefore, the oxidation of these C_2 molecules mainly generates incompletely

oxidized C_2 intermediates, and the current efficiency for CO_2 generation reaches no more than a few percent.

Acknowledgements This work was supported by the US Department of Energy, Office of Basic Energy Sciences through grant DE-FG02-03ER46072, and by the Energy Materials Center at Cornell (EMC^2), an Energy Frontier Research Center funded by the U.S. Department of Energy, Office of Science, Office of Basic Energy Sciences under Award Number DE-SC0001086.

References

1. Gilman S (1964) J Phys Chem 68:70
2. Bagotzky VS, Vassiliev YB, Khazova OA (1977) J Electroanal Chem 81:229
3. Watanabe M, Motoo S (1975) J Electroanal Chem 60:267
4. Parsons R, VanderNoot T (1988) J Electroanal Chem 257:9
5. Gasteiger HA, Markovic N, Ross PN, Cairns EJ (1993) J Phys Chem 97:12020
6. Herrero E, Chrzanowski W, Wieckowski A (1995) J Phys Chem 99:10423
7. Vielstich W, Xia XH (1995) J Phys Chem 99:10421
8. Korzeniewski C, Childers C (1998) J Phys Chem B 102:489
9. Sriramulu S, Jarvi TD, Stuve EM (1999) J Electroanal Chem 467:132
10. Wang H, Löffler T, Baltruschat H (2001) J Appl Electrochem 31:759
11. Wang H, Wingender C, Baltruschat H, Lopez M, Reetz MT (2001) J Electroanal Chem 509:163
12. Iwasita T (2002) Electrochim Acta 47:3663
13. Wang H, Baltruschat H (2007) J Phys Chem C 111:7038
14. Wang H, Alden L, DiSalvo FJ, Abruña HD (2008) PCCP 10:3739
15. Beden B, Lamy C, Bewick A, Kunimatsu K (1981) J Electroanal Chem 121:343
16. Breiter MW (1968) Discuss Faraday Soc 45:79
17. Ota K-I, Nakagawa Y, Takahashi M (1984) J Electroanal Chem 179:179
18. Wang J, Wasmus S, Savinell RF (1995) J Electrochem Soc 142:4218
19. Krausa M, Vielstich W (1994) J Electroanal Chem 379:307
20. Chrzanowski W, Wieckowski A (1998) Langmuir 14:1967
21. Iwasita T, Hoster H, John-Anacker A, Lin WF, Vielstich W (2000) Langmuir 16:522
22. Bittins-Cattaneo B, Iwasita T (1987) J Electroanal Chem 238:151
23. Wang K, Gasteiger HA, Markovic NM, Ross PN Jr (1996) Electrochim Acta 41:2587
24. Morimoto Y, Yeager EB (1998) J Electroanal Chem 444:95
25. Kita H, Nakajima H, Shimazu K (1988) J Electroanal Chem 248:181
26. Nakajima H, Kita H (1990) Electrochim Acta 35:849
27. Samjeské G, Wang H, Löffler T, Baltruschat H (2002) Electrochim Acta 47:3681
28. Iwasita T, Nart FC, Vielstich W (1990) Ber Bunsenges Phys Chem 94:1030
29. Vigier F, Rousseau S, Coutanceau C, Leger J-M, Lamy C (2006) Top Catal 40:111
30. Antolini E (2007) J Power Sour 170:1
31. Bittins-Cattaneo B, Wilhelm S, Cattaneo E, Buschmann HW, Vielstich W (1988) Ber Bunsenges Phys Chem 92:1210
32. Schmidt VM, Ianniello R, Pastor E, Gonzalez S (1996) J Phys Chem 100:17901
33. Wang H, Jusys Z, Behm RJ (2004) J Phys Chem B 108:19413
34. Wang H, Jusys Z, Behm RJ (2004) Fuel Cells 4:113
35. Camara GA, Iwasita T (2005) J Electroanal Chem 578:315
36. Wang H, Jusys Z, Behm RJ (2006) J Power Sour 154:351
37. de Souza JPI, Queiroz SL, Bergamaski K, Gonzalez ER, Nart FC (2002) J Phys Chem 106:9825

38. Leger J-M, Rousseau S, Coutanceau C, Hahn F, Lamy C (2005) Electrochim Acta 50:5118
39. Colmenares L, Wang H, Jusys Z, Jiang L, Yan S, Sun GQ, Behm RJ (2006) Electrochim Acta 52:221
40. Wu G, Swaidan R, Cui G (2007) J Power Sour 172:180
41. Colmati F, Antolini E, Gonzalez ER (2008) J Alloys Comp 456:264
42. Wang Q, Sun GQ, Jiang LH, Xin Q, Sun SG, Jiang YX, Chen SP, Jusys Z, Behm RJ (2007) PCCP 9:2686
43. Horanyi G, Kazarinov VE, Vassiliev YB, Andreev VN (1983) J Electroanal Chem 147:263
44. Belgsir EM, Bouhier E, Yei HE, Kokoh KB, Beden B, Huser H, Leger J-M, Lamy C (1991) Electrochim Acta 36:1157
45. Wieland B, Lancaster JP, Hoaglund CS, Holota P, Tornquist WJ (1996) Langmuir 12:2594
46. Dailey A, Shin J, Korzeniewski C (1998) Electrochim Acta 44:1147
47. Hahn F, Beden B, Kadirgan F, Lamy C (1987) J Electroanal Chem 216:169
48. Leung LWH, Weaver MJ (1988) J Phys Chem 92:4019
49. Christensen PA, Hamnett A (1989) J Electroanal Chem 260:347
50. Baltruschat H (2004) J Am Soc Mass Spectrom 15:1693
51. Bruckenstein S, Gadde RR (1971) J Am Chem Soc 93:793
52. Wolter O, Heitbaum J (1984) Ber Bunsenges Phys Chem 88:2
53. Wolter O, Heitbaum J (1984) Ber Bunsenges Phys Chem 88:6
54. Baltruschat H (1999) In: Wieckowski A (ed) Interfacial electrochemistry: theory, expeiment and applications. Marcel Dekker, New York
55. Hartung T, Baltruschat H (1990) Langmuir 6:953
56. Baltruschat H, Schmiemann U (1993) Ber Bunsenges Phys Chem 97:452
57. Jusys Z, Massong H, Baltruschat H (1999) J Electrochem Soc 146:1093
58. Cramm S, Friedrich KA, Geyzers K-P, Stimming U, Vogel R (1997) Fresenius J Anal Chem 358:189
59. Massong H, Wang H, Samjeské G, Baltruschat H (2000) Electrochim Acta 46:701
60. Willsau J, Heitbaum J (1986) Electrochim Acta 31:943
61. Clavilier J, Albalat R, Gomez R, Orts JM, Feliu JM, Aldaz A (1992) J Electroanal Chem 330:489
62. Tremiliosi-Filho G, Gonzalenz ER, Motheo AJ, Belgsir EM, Leger J-M, Lamy C (1998) J Electroanal Chem 444:31
63. Iwasita T (2003) In: Vielstich W, Gasteiger HA, Lamm A (eds) Handbook of fuel cells – fundamentals, technology and applications, vol 2: electrocatalysis. Wiley, Chichester, p 603
64. Wang H, Baltruschat H (2001) In: Narayanan S, Zawodzinski T, Gottesfeld S (eds) Proc Electrochem Soc (Direct Methanol Fuel Cells), vol 4. Electrochemical Society, Pennington, p 50
65. Kunimatsu K (1990) Ber Bunsenges Phys Chem 94:1025
66. Papoutsis A, Leger JM, Lamy C (1987) J Electroanal Chem 234:315
67. Biegler T, Rand DAJ, Woods R (1971) J Electroanal Chem 29:269
68. Batista EA, Malpass GRP, Motheo AJ, Iwasita T (2004) J Electroanal Chem 571:273
69. Clavilier J, Durand R, Guinet G, Faure R (1981) J Electroanal Chem 127:281
70. Lamy C, Leger JM, Clavilier J, Parsons R (1983) J Electroanal Chem 150:71
71. Leger J-M, Lamy C (1990) Ber Bunsenges Phys Chem 94:1021
72. Cao D, Lu G-Q, Wieckowski A, Wasileski SA, Neurock M (2005) J Phys Chem B 109:11622
73. Housmans THM, Koper MTM (2003) J Phys Chem B 107:8557
74. Housmans THM, Wonders AH, Koper MTM (2006) J Phys Chem B 110:10021
75. Iudice de Souza JP, Iwasita T, Nart FC, Vielstich W (2000) J Appl Electrochem 30:43
76. El-Shafei AA, Hoyer R, Kibler LA, Kolb DM (2004) J Electrochem Soc 151:F141
77. Jusys Z, Kaiser J, Behm RJ (2002) Electrochim Acta 47:3693
78. Dubau L, Hahn F, Coutanceau C, Leger J-M, Lamy C (2003) J Electroanal Chem 554–555:407
79. Leung LWH, Chang SC, Weaver MJ (1989) J Electroanal Chem 266:317

80. Iwasita T, Pastor E (1994) Electrochim Acta 39:531
81. Schmiemann U, Müller U, Baltruschat H (1995) Electrochim Acta 40:99
82. Lai SCS, Kleyn SEF, Rosca V, Koper MTM (2008) J Phys Chem C 112:19080
83. Wang H, Jusys Z, Behm RJ (2006) J Appl Electrochem 36:1187
84. Wieckowski A, Sobrowski J, Zelenay P, Franaszczuk K (1981) Electrochim Acta 26:1111
85. Rao V, Cremers C, Stimming U, Cao L, Sun S, Yan S, Sun G, Xin Q (2007) J Electrochem Soc 154:B1138
86. Arico AS, Creti P, Antonucci PL, Antonucci V (1998) Electrochem Solid-State Lett 1:66
87. Otomo J, Nishida S, Takahashi H, Nagamoto H (2008) J Electroanal Chem 615:84
88. Wang H, Zhao Y, Jusys Z, Behm RJ (2006) J Power Sour 155:33
89. Wang H, Jusys Z, Behm RJ (2006) J Electroanal Chem 595:23
90. de Lima RB, Paganin V, Iwasita T, Vielstich W (2003) Electrochim Acta 49:85
91. Kazarinov VE, Vassiliev YB, Andreev VN, Horanyi G (1983) J Electroanal Chem 147:247
92. Wang H, Jusys Z, Behm RJ (2009) Electrochim Acta 54:6484

Struct Bond (2011) 141: 85–113
DOI: 10.1007/430_2011_41

Published online: 22 April 2011

Mechanical and Transport Properties of Nafion: Effects of Temperature and Water Activity

Jay Benziger, Andrew Bocarsly, May Jean Cheah, Paul Majsztrik, Barclay Satterfield, and Qiao Zhao

Abstract Recent studies have shown that water absorption changes the mechanical and transport properties of Nafion by orders of magnitude. The unusually large changes in properties are indicative of microstructural changes induced by water absorption. The experimental findings of changes in proton conduction, water transport, elastic modulus, and stress relaxation are highlighted and explained by microphase segregation of hydrophilic domains resulting from water absorption. Water absorption is proposed to cause clustering of hydrophilic sulfonic acid groups and water within a hydrophobic polytetrafluoroethylene matrix. The hydrophilic domains form a network that facilitates transport and create physical cross-links that stiffen Nafion. At high temperature and low water activity, the entropy of de-mixing breaks the clusters apart, causing a large drop in elastic modulus of the polymer and a large decrease in the rates of water and proton transport.

Keywords Elastic modulus · Microphase separation · Stress relaxation · Thermal transitions

Contents

J. Benziger (✉), A. Bocarsly, M.J. Cheah, P. Majsztrik, B. Satterfield, and Q. Zhao
Departments of Chemistry and Chemical Engineering, Princeton University, Princeton, NJ, USA
e-mail: benziger@princeton.edu

1 Introduction

Nafion is an ionomer that has a hydrophobic tetrafluoroethylene (TFE) backbone and perfluoro alkyl ether (PFAE) side chains terminated with hydrophilic sulfonate salt [1–4], as shown in Fig. 1. It was introduced by DuPont in 1960 and has been used in a variety of applications such as an ion-selective membrane for the Chlor-Alkali process [5, 6], a water transport membrane for humidifiers, and as a strong acid catalyst [7]. Nafion was introduced as a polymer electrolyte membrane (PEM) in fuel cells in the early 1990s [4, 8]. Compared to hydrocarbon membranes, Nafion was chemically more robust in the fuel cell and the acid form has high proton conductivity. There have been many efforts to find alternative membrane materials

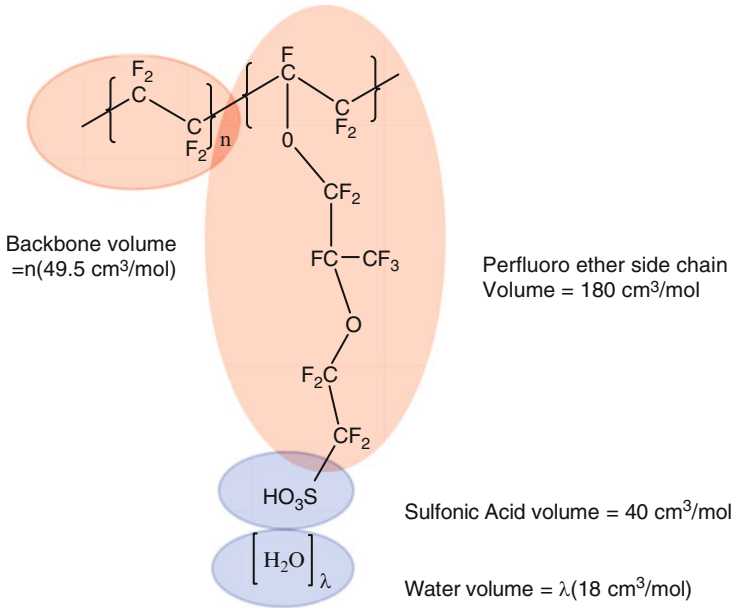

Fig. 1 Structure of Nafion

for PEM fuel cells, but Nafion remains the benchmark to which all other PEMs are compared [9–12]. Asahi Glass and Asahi Chemicals developed polymers similar to Nafion with both sulfonate salts and carboxylate salts named Flemion and Aciplex, respectively [13, 14]. Dow Chemical, 3M, and Solvay Solexis developed ionomers with similar structure to Nafion but with different variations on the length of the PFAE side chains [4].

In fuel cells, temperature (T) and water activity (a_w) change in response to the current. These changes in T and a_w can alter the transport properties of the Nafion membrane, which can in turn alter the fuel cell operation. Decreases in water activity cause the proton conductivity to decrease, which reduces the current and further reduces the water activity; this feedback mechanism can result in steady-state multiplicity in PEM fuel cells [15, 16]. Water absorption and desorption from Nafion causes it to swell and shrink, which can cause mechanical failure of the membrane and alter the interfacial contact between the membrane and the electrode [17, 18]. Choosing and controlling the operating conditions of PEM fuel cells require knowledge of the mechanical and transport properties of Nafion.

Nafion has been the subject of extensive characterization studies [1]. Its microstructure has been exhaustively studied by scattering methods, especially small angle X-ray scattering (SAXS) and small angle neutron scattering (SANS) [19–23]. Mechanical properties of Nafion as functions of temperature have been used to identify temperature-induced transitions [2, 24–27]. Transport of protons and water has also been the subject of numerous studies over the past 25 years [28–34]. However, there has been limited progress in connecting the chemical structure of Nafion to mechanical and transport properties, *especially how these properties are altered due to environmental conditions*. In this chapter, we will review recent studies of mechanical and transport properties of Nafion done under controlled conditions of water activity and temperature.

2 Chemical Structure and Synthesis of Nafion

Nafion is a random copolymer of tetrafluoroethylene (TFE) and perfluoro sulfonyl-fluoride ethyl propyl vinyl ether (PSEPVE), made by free radical polymerization. The sulfonyl fluoride terminus in the polymer is converted to the sulfonate salt by basic hydrolysis, which produces either the Na^+ or K^+ form of Nafion. Ion exchange with sulfuric acid produces the sulfonic acid form shown in Fig. 1. The copolymer ratio (x) is defined by the equivalent weight, EW $= 100x + 444$ g-polymer/mol-SO_3. Details of the monomer synthesis and subsequent conversion processes are summarized by Doyle and Rajendran [4].

Nafion films are extruded as the sulfonyl fluoride form of the polymer. They are then converted into the acid form by hydrolysis and ion exchange. The extruded hydrolyzed films are characterized using a three number code, xxy, where $xx =$ EW/100 and y is the dry film thickness in mils (1 mil $= 0.001$ in $= 25.4$ μm); thus N115 corresponds to 1100 EW Nafion, 5 mil thick (127 μm thick). The dry acid

form of Nafion (H^+-Nafion) has a density of ~2 g/cm^3; 1100 EW Nafion has a density of sulfonic acid groups of 1.82×10^{-3} mol/cm^3. The most common form of Nafion sold commercially has an equivalent weight of 1100, corresponding to $x = 6.6$. The equivalent weight can be varied by controlling the monomer ratio during synthesis. Below an EW of 800 ($x < 3.6$), Nafion forms a dispersion in water at room temperature; it loses structural integrity when in contact with liquid water and does not function as a membrane. For EW above 1,200 ($x > 7.6$), the proton conductivity of Nafion becomes too low to be useful ion transport membrane. Water content of Nafion is presented as the number of water molecules absorbed per sulfonic acid group $\left(\lambda = \frac{\#H_2O}{\#SO_3}\right)$.

Nafion films produced by extrusion, hydrolyzed and stored under ambient conditions of temperature and relative humidity (RH ~ 30–50%) are tough and flexible. They readily bend, but do not stretch easily. If the films are dried at room temperature, they become rigid and are more resistant to bending and stretching. Drying Nafion films also causes them to wrinkle or buckle. Contacting a dry Nafion film with water makes the membrane more flexible, and also causes buckling deformation of the membrane. At ambient conditions, there is no discernable difference to the touch or to the eye between the acid (H^+) and Na^+ forms of Nafion.

Extruded 1100 equivalent weight H^+-Nafion becomes more flexible when placed in liquid water. H^+-Nafion swells by ~20% in each dimension when taken from dry air and placed in liquid water for several hours, but it retains mechanical integrity when placed in liquid water for extended periods of time. Nafion also swells when placed in other polar solvents (e.g., alcohols, DMSO, acetonitrile, formamide). The amount of swelling varies, but most polar organic solvents swell Nafion more than water. Nafion swells by ~40% in each dimension when placed in ethanol at room temperature, but retains its physical integrity. Nafion "solutions" can be prepared by refluxing Nafion in ethanol or propanol. These solutions are a dispersion of nanometer-sized Nafion molecules suspended in the alcohol. Cast Nafion films may be prepared from the solubilized Nafion by solvent evaporation. There has existed some controversy about whether cast Nafion films have similar properties as extruded Nafion films. We will describe procedures for preparing cast and extruded films with identical properties. Nafion does not absorb nonpolar organic solvents to any appreciable extent. When placed in hydrocarbon solvents, Nafion does not swell or buckle.

Nafion is an electronic insulator. At low relative humidity, neither Na^+-Nafion nor H^+-Nafion has appreciable cation conductivity. However, when EW 1100 H^+-Nafion is equilibrated with 100% water vapor, it swells by ~20% in each dimension and has a high proton conductivity of ~0.1 S/cm, comparable to the conductivity of 1 M sulfuric acid. The ions in Nafion are confined within the membrane, making it easy to handle and minimally corrosive. Cation conduction through Nafion appears to require the coexistence of two distinct bi-continuous phases. PTFE and PFAE groups are hydrophobic. They constitute the majority phase of the polymer providing structural integrity. The hydrophilic sulfonate salts absorb water or other polar solvents into a hydrophilic phase permitting water and proton transport.

3 Physical State of Nafion

The literature on Nafion is filled with inconsistent and often contradictory results. Placing Nafion in a defined environment does not produce a material with well-defined properties. The mechanical and transport properties of Nafion depend on the history of the environmental conditions of temperature and water activity. Even the simplest of physical properties, such as mass and volume changes from water absorption, is inconsistent because different investigators use different sample preparation protocols. Zawodzinski et al. classified three different forms of extruded H^+-Nafion: normal (dried at 80°C), shrunken (dried at 105°C), and expanded (pretreated in boiling water and dried at room temperature) [35, 36]. They reported that the more severe the drying condition, the less water is absorbed into Nafion; they have also reported that less water is absorbed into Nafion from saturated vapor than saturated liquid [36–39]. Differences in phase equilibrium between Nafion and saturated liquid or saturated vapor appear to be contrary to thermodynamics; many investigators repeated those measurements with similar results and called this contradiction Schroeder's paradox [39–41]. It was only recently that results from Onishi et al. [40] suggested that Schroeder's paradox is an experimental artifact of the dynamics of water absorption. We have corroborated this result in our lab. We have measured the kinetics of water transport as functions of water activity and temperature. Water absorption from the vapor into Nafion is limited by interfacial transport, resulting in water absorption kinetics from the vapor being more than 10^3 times slower than water absorption from liquid water. Furthermore, polymer swelling from water absorption is limited by polymer relaxation dynamics. Satterfield and Benziger showed that the time for Nafion stress relaxation can be $>10^6$ s, much longer than accounted for by most researchers.

The time for water sorption equilibration by Nafion115 at 25°C and 60°C are illustrated in Fig. 2. Two pretreatments were compared, drying in a vacuum oven at 70°C for 2 h, or placing Nafion in boiling water for 2 h. Samples from both treatments were placed in closed containers above a solution of 0.1 M NaCl at 25°C or 60°C. The masses of the samples were checked periodically over a period of 1 month. The final water concentrations approached the same value from the different starting conditions, but it was taking more than 2,000 h to achieve equilibrium. Equilibrium was faster at 60°C than at 25°C, but even at the higher temperature final equilibrium still took more than 2,000 h.

3.1 Preparing Reproducible Samples of Nafion

Properties such as water diffusivity, tensile modulus, and proton conductivity all are dependent on water content in the Nafion membrane. Because of the slow dynamics of water equilibration with Nafion, these properties all have a history dependence that will reflect the time to which Nafion has been exposed to different

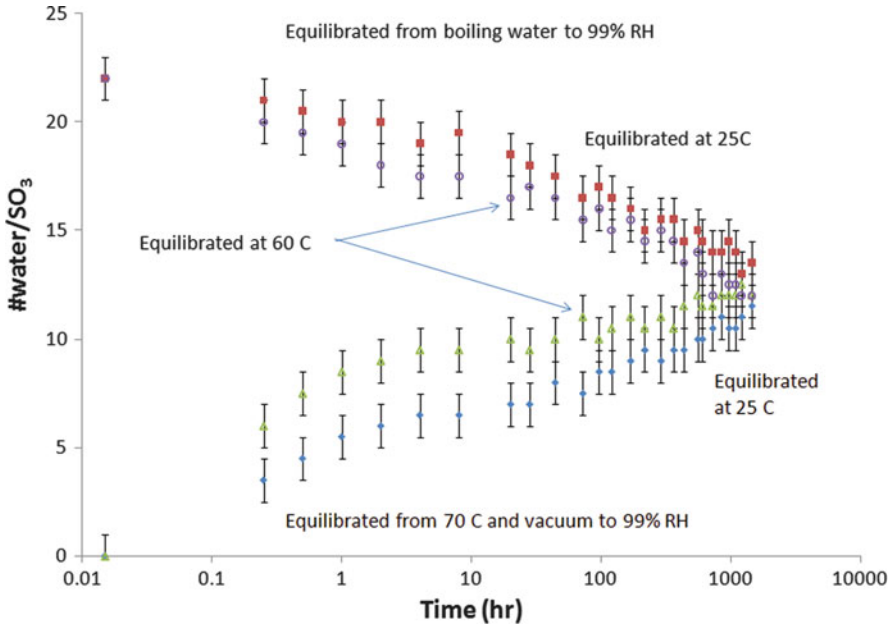

Fig. 2 Equilibration of EW 1100 H^+-Nafion with $a_w = 0.99$ water vapor at 25°C and 60°C. Samples were pretreated by either vacuum evacuation at 70°C for 2 h or boiling in deionized water for 2 h

environmental conditions. Different methods of preparing Nafion membranes have produced significant variability of the mechanical properties measured.

Our laboratory has done extensive characterization of the mechanical properties of Nafion films of different thickness as extruded films, solvent cast films, and uniaxially stressed films, and we examined many different preparation protocols [32–34, 42–47]. We arrived at the protocol listed below for producing reproducible films that showed no memory of the history of the film.

1. Anneal sample at $T \geq 80$°C in vacuum for >2 h
2. Boil in 3 wt% H_2O_2 solution for 1 h
3. Rinse sample with deionized water
4. Place membrane in boiling 1 M H_2SO_4 solution for 1 h
5. Rinse with DI water
6. Dry in vacuum oven or dry nitrogen at 80°C for 2 h

This procedure produced clear stable membranes with reproducible mechanical properties independent of past history of the film. Extruded films, solvent cast films, and uniaxially stressed films with different thickness were all converted to isotropic films with identical elastic modulus and water uptake response after this protocol. We will present results of mechanical property measurements that show why the specifics of this protocol are important. The key to reproducibility, as we shall show, is to remove all structure associated with clustering of the sulfonic acid groups in the polymer.

3.2 *Equilibrium Water Absorption into Nafion*

The equilibrium water uptake was measured as a function of water pressure at different temperatures using an isometric system [48, 49]. A PEM (e.g., Nafion) is placed in a fixed volume container and evacuated at 80°C to remove all the water from the membrane. The container is sealed and equilibrated at the desired temperature. Aliquots of water are introduced at intervals of 0.5–2 h and allowed to equilibrate with the Nafion. The pressure in the container is equal to the water pressure, and the difference between the water in the vapor and the water injected is equal to the water absorbed by the Nafion. Water sorption as a function of water activity was determined and is plotted in Fig. 3, where water activity is defined as the ratio of the partial pressure of water vapor (P_w) to the saturation water pressure (P_w^0) at the temperature of interest, $a_w = P_w/P_w^0(T)$. Water sorption curves nearly superimpose for temperatures from 30°C to 80°C; water sorption in Nafion shows the same temperature dependence as the vapor pressure of water.

The linear expansion coefficient of Nafion was also measured as a function of temperature and water activity in a dynamic creep apparatus. Samples were clamped in an environmental chamber, dried in nitrogen at 80°C for 2 h, brought to the desired temperature in dry nitrogen, and then the dry nitrogen was replaced with a humidified nitrogen stream. The change in length was recorded as a function of time; the equilibrium swelling strain was assumed to be achieved when the rate of swelling was less than 0.001/h.

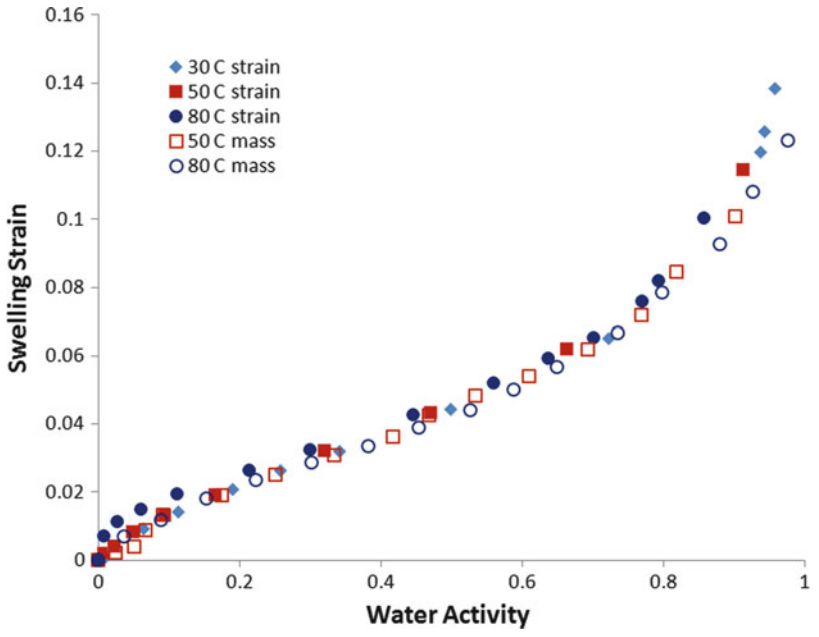

Fig. 3 Swelling strain of 1100 EW H^+-Nafion determined from strain data (ε) and from mass uptake assuming ideal mixing (ε_0)

The swelling strain for water absorption, assuming zero excess volume of mixing, can be determined from the equilibrium water absorption data. The linear expansion coefficient assuming perfect mixing and isotropic expansion, ε_0, is given by (1), where ρ_{Nafion} and ρ_{water} are densities of Nafion and water, and MW_{water} is the molecular weight of water.

$$\varepsilon_0 = \left(1 + \frac{\lambda \rho_{\text{Nafion}} \text{MW}_{\text{water}}}{\text{EW} \rho_{\text{water}}}\right)^{1/3} - 1. \tag{1}$$

The true linear expansion coefficient for water absorption, ε, is measured by experiment. The volume change of the Nafion due to water absorption assuming isotropic expansion is given by (2).

$$\frac{V}{\bar{V}} = (1+\varepsilon)^3. \tag{2}$$

The swelling strain based on ideal mixing and the real swelling strain are plotted together as functions of water activity in Fig. 3. The curves are "almost" superposable. Also there is no discernable difference in the water sorption at different temperatures at the same water activity; water sorption increases exponentially with the same temperature dependence as the water vapor pressure [e.g., P_{w} given by the Antoine equation (3)].

$$P_{\text{w}}^0 = \exp\left(10.717 - \frac{3304.8}{T - 64.85}\right)\text{bar}. \tag{3}$$

The excess volume change induced by absorption of each additional water molecule (actual swelling volume minus volume with perfect mixing), given by (4), is equal to the free volume (V_{f}) associated with water absorption normalized by the molar density of water (N_{w}).

$$\left[\frac{V_{f/\bar{V}}}{N_w}\right] = \frac{(1+\varepsilon)^3\left[(1+\varepsilon)^3 - (1+\varepsilon_0)^3\right]}{\lambda \rho_{Nafion}/EW}. \tag{4}$$

The volume fraction of water (φ_{water}) in the swollen polymer is given by (5).

$$\varphi_{\text{water}} = \frac{\left[(1+\varepsilon)^3 - 1\right]}{(1+\varepsilon)^3}. \tag{5}$$

The free volume of water per mole of water as a function of membrane water content is shown in Fig. 4.

At 80°C, the free volume decreases from 12 cm^3/mol at $\lambda = 0.5$ ($a_{\text{w}} = 0.02$) to a value of ~1.5 cm^3/mol at $\lambda = 4$ ($a_{\text{w}} = 0.5$). The free volume increases with λ to

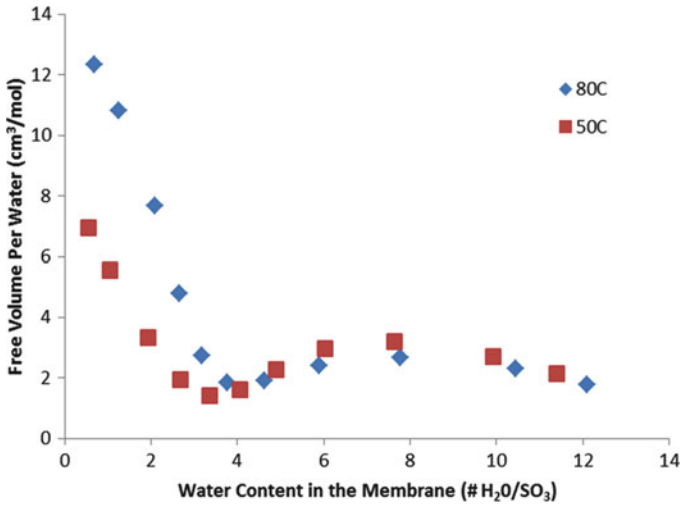

Fig. 4 Free volume of water absorption in 1100 EW H^+-Nafion as a function of water activity and temperature

~3 cm^3/mol at $\lambda = 8$ ($a_w \sim 0.8$) and then decays toward zero with further increase of water uptake. At 50°C, the free volume per water molecule decreases from ~7 cm^3/mol at $\lambda = 0.5$ to a value of 1 cm^3/mol at $\lambda = 4$. The free volume increases with λ going through a maximum at $\lambda = 8$ and then decreased toward zero. We suggest that the first transition at $\lambda = 4$ corresponds to the completion of the first hydration shell around the sulfonate group, which consists of four water molecules. Subsequent water addition is in the second hydration shell and beyond, where the interactions between water molecules are approaching the interactions of bulk water. The transition at $\lambda = 8$ might be a result of the microstructural change in the hydrophilic phase at high water activity [47].

4 Transport Properties

4.1 Proton Conductivity

Proton conductivity of Nafion has the most direct impact on fuel cell performance; hence, it has received the greatest attention. Proton conductivity measured by AC impedance concurrently with water uptake at different temperatures and water activity is shown in Fig. 5. Proton conductivity of Nafion at $T > 80°C$ increases exponentially from ~10^{-7} S/cm at $a_w = 0$ to 10^{-1} S/cm at $a_w = 1.0$. Proton conductivity at different temperatures superimpose when plotted as a function of water activity.

The proton conductivity shows a large change at low water activity, $0 < a_w < 0.2$, and then a more gradual change at high water activity, $0.2 < a_w < 1.0$.

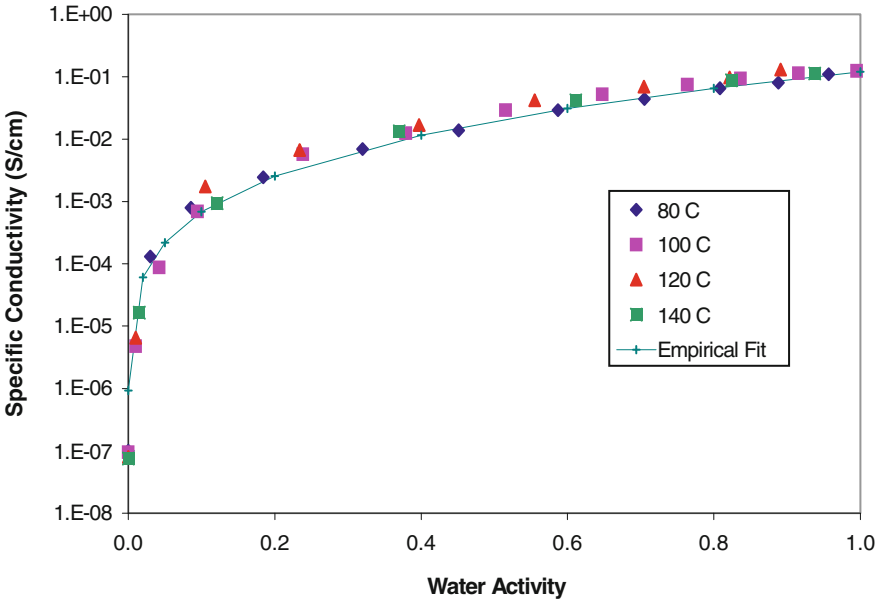

Fig. 5 Proton conductivity of Nafion as a function of water activity at different temperatures. The empirical fit to the data is given by $\sigma = 1.3 \times 10^{-7} \exp(14 a_w^{0.2})$ S/cm

The rise in conductivity results from increased connectivity of hydrophilic domains that carry the proton current as the water activity increases. At increased water activity, the hydrophilic domains are better connected (as evidenced by greater proton conductivity), and water is packed into the hydrophilic domains with less excess volume.

Proton conductivity has recently been measured using a DC measurement [50]. A membrane–electrode assembly (MEA) was prepared with a Nafion 115 membrane. Humidified hydrogen was supplied to one side of the MEA, and nitrogen gas was flowed past the other side of the MEA. The water activity of the hydrogen stream was varied. The current was measured as a function of water activity, temperature, and applied potential. Data in Fig. 6 show that the current increased with applied potential from 0 to 0.3 V and then reached a saturation value. The Nafion membrane resistance ($R = V/I$) at low applied potential decreased with increasing water activity, consistent with the AC impedance results shown in Fig. 5. The saturation current at higher voltages also increased with increasing water activity. The saturation current results from limited openings to the hydrophilic domains of the Nafion at the membrane/electrode interface. Increasing the applied potential causes the protons to move through the Nafion membrane faster, but cannot speed up proton entry at the membrane surface, resulting in the current being limited by interfacial mass transport resistance. As the water activity increases, there are more openings into the hydrophilic domains of the Nafion at the membrane interface; so the saturation

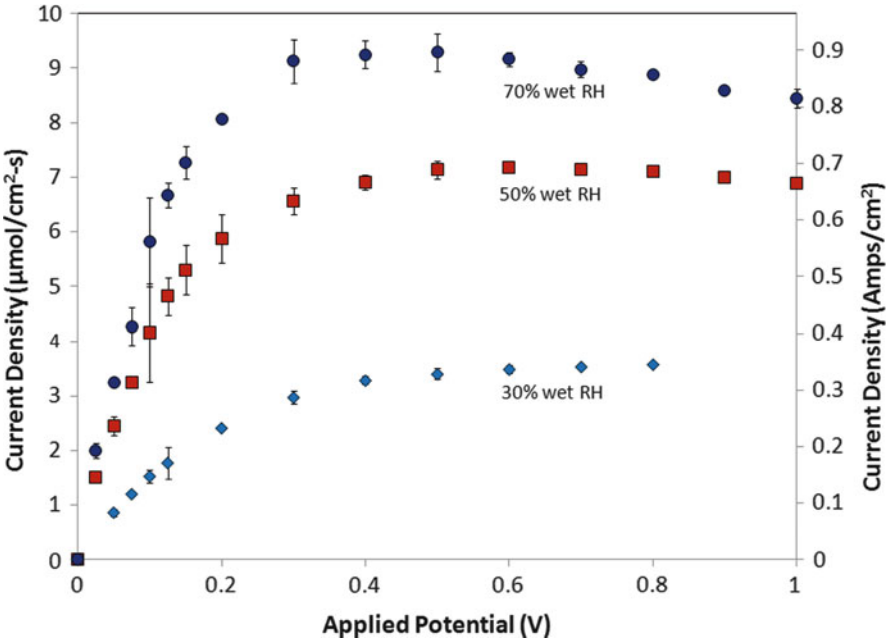

Fig. 6 Current as a function of applied potential and water activity for a Nafion 115 membrane. At low applied potential, the current is limited by the membrane resistance. At higher applied potential, the current saturates resulting from an interfacial mass transport resistance

current increases. The two resistances – interfacial transport and field-driven proton motion – in the membrane are shown schematically in Fig. 7.

The water flux across the membrane was measured concurrently with proton conductivity. The change in water flux resulting from the proton current is the electro-osmotic drag of water. The electro-osmotic drag coefficient (number of waters transported per proton) was dependent on the water activity and applied potential. It was near zero at low water activity and low applied potential, and increased to values of 0.35 at $a_w = 0.8$ and applied potential of 1 V. The results for electro-osmotic drag indicate that there is a change in the mechanism of proton transport. Protons hop by hydrogen bond rearrangement at low water activity and low applied potential; protons move as hydrated ions by vehicular transport at high water activity and high applied potential.

4.2 Water Transport

Water is made at the cathode side of the membrane in PEM fuel cells. Water is either removed with the gas flow at the cathode or it sorbs into the membrane to hydrate it. The rates of water sorption and permeation alter the water content in the Nafion membrane, which in turn controls proton transport.

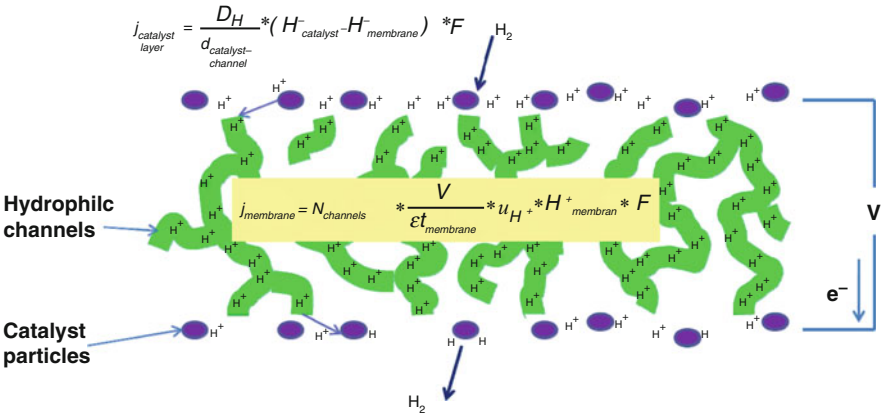

Fig. 7 Schematic of proton transport in and through Nafion membranes. Protons are generated by hydrogen oxidation on a catalyst surface. The protons move laterally in the catalyst layer (uniform potential field) until they find an opening into the hydrophilic domains of the Nafion. The protons are transported across the membrane by electric field-assisted motion. At low applied potentials, the transport across the membrane is limiting, but at high applied potentials, the proton motion is limited by diffusion in the catalyst layer to the openings of the hydrophilic domains

Water permeation through 52–254 μm EW 1100 H^+-Nafion membranes was measured from fixed water activity on one side of the membrane into a dry nitrogen stream on the other side of the membrane at temperatures from 30°C to 90°C [33]. Figure 8 shows how water activity alters the controlling resistance for water transport, which was the most important result from that study. Figure 8a shows permeation from water vapor $a_w = 0.30$ (30% RH) at different membrane thicknesses. Figure 8b shows the permeation from liquid water.

The limiting permeation rate from liquid water was almost independent on the membrane thickness, indicating that the rate-limiting step for water transport was interfacial transport at the Nafion/vapor interface. Permeation rates from $a_w = 0.30$ into dry nitrogen scaled inversely with the membrane thickness, indicating that the rate-limiting step for water transport was diffusion.

Zhao and Benziger identified three contributions to the resistance to water transport in Nafion: (1) the volume of the hydrophilic domains available for water transport; (2) the dependence of water diffusivity on the concentration of water in the hydrophilic domains; and (3) the Nafion/fluid interface [49]. They showed that at low water content in Nafion, the diffusion across the membrane is the rate-limiting step. But at high water activity, the combination of increased hydrophilic domain volume and increased connectivity of the hydrophilic domains result in a large increase in the diffusion rate across the membrane, and interfacial transport across the Nafion/vapor interface becomes the rate-limiting step.

Figure 9 shows the water self-diffusion coefficients determined with pulsed gradient spin echo NMR by Zhao and Benziger, as functions of water activity and temperature. The diffusivity increases by almost two orders of magnitude as water activity increases from near $a_w = 0.05$ to $a_w = 0.9$. The effective long-time

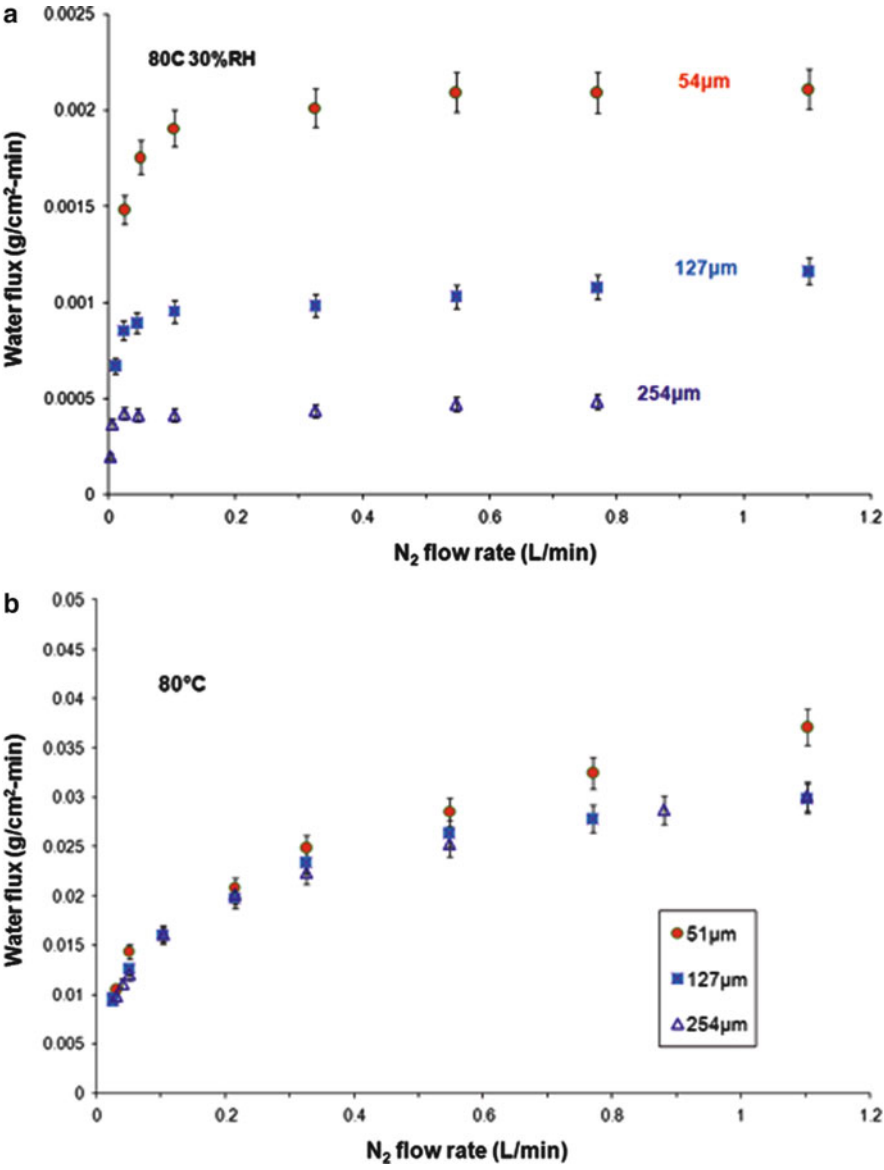

Fig. 8 (**a**) Rate of water permeation through 1100 EW H^+-Nafion at 30°C water vapor at $a_w = 0.30$ into a dry N_2 stream. The dry membrane thicknesses are shown in the graph. The permeation rate increases inversely with decreasing membrane thickness. (**b**) Rate of water permeation through 1100 EW H^+-Nafion at 80°C from liquid water into a dry N_2 stream. The dry membrane thicknesses are shown in the graph. The permeation rate changes by 20% when the membrane thickness changes by a factor of 5

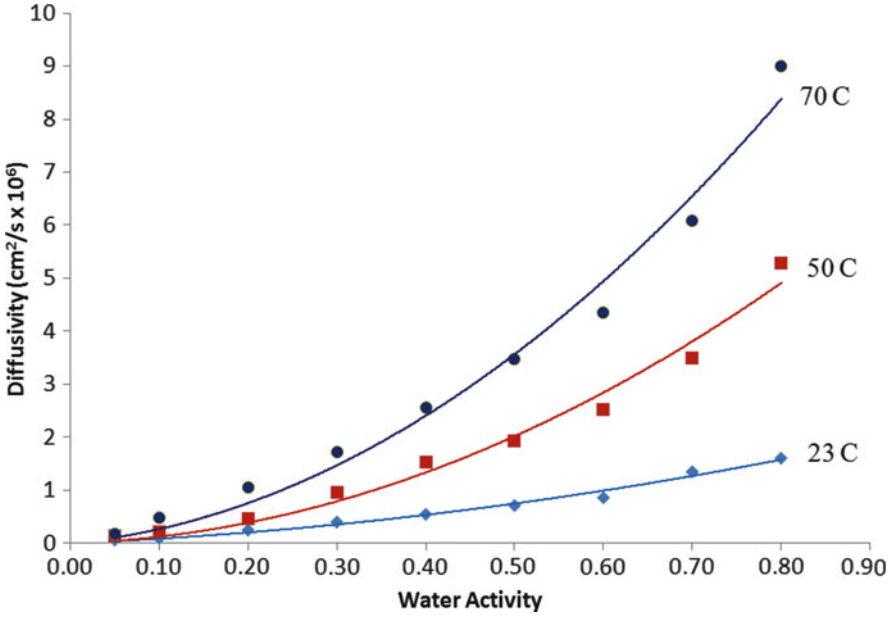

Fig. 9 Effective diffusion coefficient of water in EW 1100 Nafion as a function of water activity and temperature

diffusion coefficient for water in Nafion as a function of water activity and temperature (data in Fig. 9) was fit by (6).

$$D_{\infty} = 0.265\alpha_w{}^2 e^{\frac{-3343}{T}} \left(\mathrm{cm}^2/\mathrm{s}\right). \tag{6}$$

Zhao and Benziger were able to determine the contribution of the tortuous network for water diffusion through Nafion. They determined the effective diffusion coefficient of water with the PGSE NMR method at short delay times, where the diffusion was limited by short-range molecular interactions. They also determined diffusion coefficients at long delay times, where diffusion allowed the molecules to move through the hydrophilic domain network. The ratio of these two diffusion coefficients is the tortuosity of the hydrophilic domains, which is shown in Fig. 10. Tortuosity decreases by more than a factor of ten as water activity increases. The tortuosity follows a similar trend with water activity as the free volume of water absorption. Tortuosity, free volume, and proton conductivity are related to the evolution of the connectivity of the hydrophilic domains.

4.3 Interfacial Transport of Water

When exposing the Nafion membrane to liquid water, transport of water across the Nafion membrane was limited by interfacial transport at the membrane/vapor

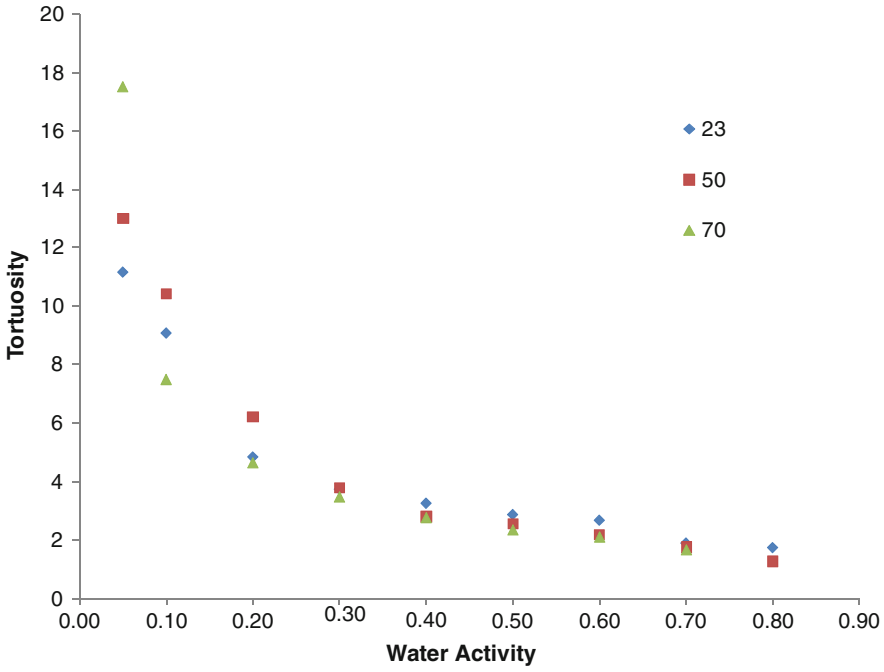

Fig. 10 Tortuosity of the hydrophilic domains for water diffusion in EW 1100 Nafion

interface as illustrated by the data in Fig. 8b. As was the case with proton transport, water must find hydrophilic domains that extend through the membrane to the vapor interface. The proton conductivity results suggested that only a limited number of hydrophilic domains extend to the vapor/membrane interface. The nature of the Nafion interface was examined by surface-wetting experiments. Goswami et al. used a Wilhelmy plate to measure the advancing and receding contact angles of water/Nafion. The advancing contact angle was $>100°$; the surface was hydrophobic similar to PTFE. The receding contact angle was ~30°, indicating that after exposure to liquid water the Nafion surface was hydrophilic. This same conclusion was reached by other investigators. Glazing-Incident SAXS studies by Bass et al. observed rearrangements of the hydrophobic chain bundles on Nafion surface to minimize surface energy when the membrane is in contact with water vapor [51]. They reported that the Nafion surface exposed to fully saturated water vapor has nearly the same hydrophobicity as a completely dry membrane. The hydrophobic surface layer at the Nafion/vapor interface is analogous to a thin film of oil on top of water; that hydrophobic film presents an interfacial transport resistance for water to enter or leave the Nafion.

Further evidence of interfacial transport limitations were provided by Satterfield and Benziger who measured water sorption/desorption rates from H^+-Nafion films 52–630 μm thick [34]. Dimensional analysis of water sorption/desorption rates as functions of a scaled time variable demonstrated that the rates of both sorption and

desorption were limited by interfacial transport. Satterfield and Benziger also suggested that sorption was limited by interfacial swelling. During water absorption, the polymer must swell to accommodate the water. The polymer swelling dynamics leads to a shrinking core during water absorption. The large difference in diffusion coefficient at high and low water content creates a shell with nearly uniform water concentration surrounding a shrinking core with low water content. Water desorption is much faster than water sorption; desorption is limited by membrane/vapor interfacial transport, but polymer swelling dynamics are not important because the polymer does not need to shrink for water to desorb.

5 Mechanical Properties of Nafion

Water absorbs into the hydrophilic domains by attractive forces of water solvating the polar sulfonate salt. The hydrophilic domains swell doing work on the surrounding hydrophobic matrix (like blowing up a balloon). Water sorption is limited by the balance between the energy of solvation and the work to swell the matrix. Mechanical properties associated with swelling are very important in determining the water content of Nafion and hence the transport properties.

Furthermore, the Nafion membrane in a fuel cell is constrained between porous electrodes. When water is absorbed, the Nafion membrane swells and flows by creep into the pores of the electrode. The interfacial contact between Nafion and the electrode will be controlled by the relaxation of stress and strain from swelling. The response of Nafion to stress and strain as a function of temperature and water activity is reported here.

5.1 Tensile Properties of Nafion

The tensile modulus of Nafion as a function of temperature and water activity as measured by Satterfield and Benziger and by Majsztrik et al. is shown in Fig. 11. Nafion, like almost all polymers, become more flexible as temperature increases. At room temperature, Nafion becomes more flexible when water is absorbed. The surprising result is that at temperatures above 70°C, the elastic modulus of Nafion at $a_w = 0.00$ was very low and the modulus increased as water activity increased. Below 40°C water sorption plasticizes Nafion, but above 50°C water sorption stiffens Nafion!

5.2 Thermal Transitions in Nafion

Several studies have examined thermal transitions for Nafion [25, 27, 52–54]. Multiple transitions have been identified from stress-strain testing, storage, and loss moduli from dynamic mechanical analysis and endotherms in differential

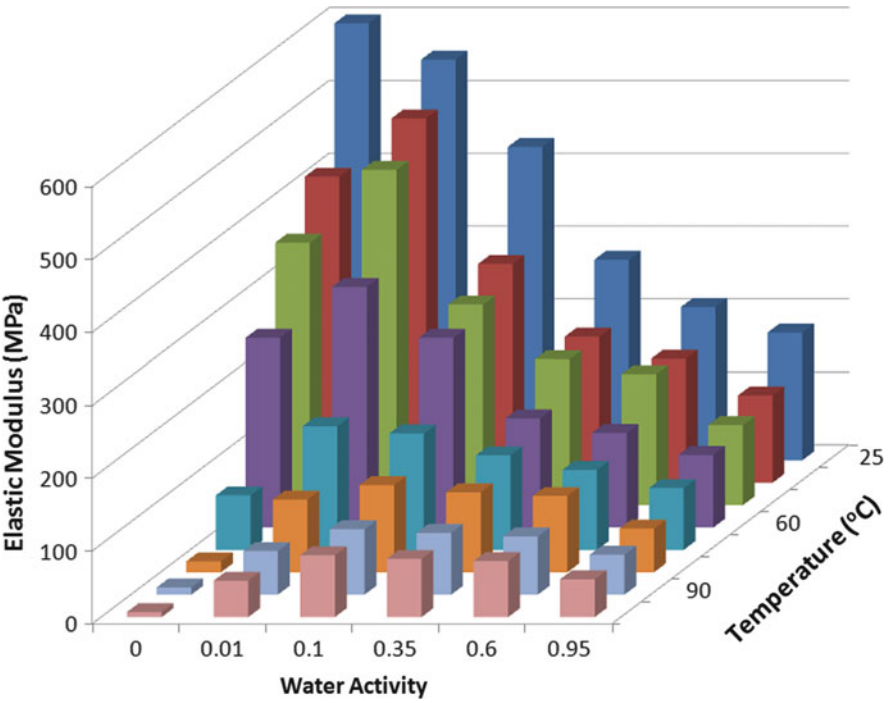

Fig. 11 Elastic modulus of 1100 EW H^+-Nafion as a function of water activity and temperature. At low temperature, the elastic modulus decreases monotonically with water activity. At temperature above 50°C the elastic modulus is low a low water activity and goes through a maximum with increasing water activity

scanning calorimetry [52, 55–60]. Under "dry conditions" (low relative humidity), H^+-Nafion shows a large decrease in elastic modulus between 70°C and 100°C; this has frequently been ascribed to a glass transition [61]. The steep decrease in elastic modulus is only observed at low water activity at $a_w < 0.01$. At higher water activity, the elastic modulus of Nafion shows a gradual decrease with increasing temperature [42, 47, 62] – no discernable transition is observed. Bauer et al. [62], Benziger and Satterfield [42], and Majsztrik et al. [47] carefully measured the elastic modulus of H^+-Nafion as a function of water activity and temperature. Below 70°C, the elastic modulus decreases monotonically with increasing water activity. Above 70°C, the elastic modulus increased with water activity and went through a maximum at $0.01 < a_w < 0.3$.

The thermal transition seen for dry Nafion at 70°C is unique to H^+-Nafion. Two other transitions have been observed with Nafion that are associated with the PTFE domains [25, 27]. Circa 200°C, there is a transition associated with crystalline ordering in the TFE phase of Nafion; there is a low temperature transition around −100°C corresponding to the glass transition temperature of amorphous PTFE.

Solute absorption in Nafion does not produce the normal plasticizing effect seen for most polymers. Water sorption plasticizes Nafion at low temperature, but

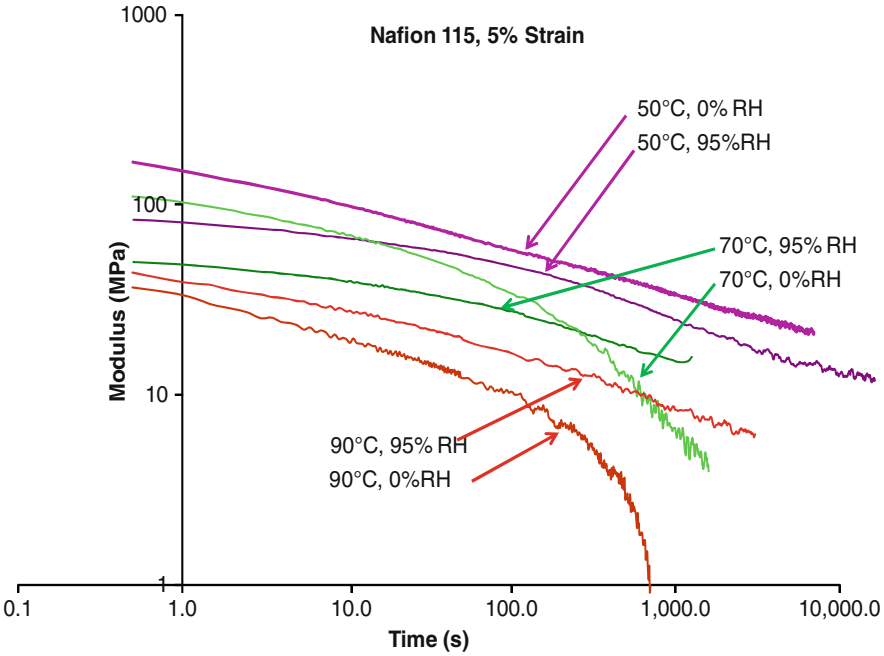

Fig. 12 Stress relaxation of Nafion at high and low water activity as a function of temperature. The relaxation rates show inverted trends with water activity at 50°C and 90°C. At 70°C, the relaxation rates cross depending on water activity

stiffens Nafion above the thermal transition temperature. This unusual behavior of solute absorption also affects the creep rate of Nafion. Majsztrik et al. reported an increase in Nafion creep rate with water activity below 50°C, but the creep rate decreases with increased water activity at temperatures above 50°C [47]. Satterfield and Benziger observed a change in stress relaxation with water activity at low and high temperature [42]. Stress relaxation data presented in Fig. 12 show that at 50°C Nafion relaxes faster at high water activity, and at 90°C Nafion relaxes faster at low water activity. A transition in the stress relaxation process between low and high water activity is observed at 70°C.

These changes in mechanical properties occur in the same range of water activity where dramatic changes in the transport of water and protons are also observed. We suggest that the changes in mechanical and transport properties are the result of microstructural changes in Nafion where the hydrophilic groups in Nafion cluster. These hydrophilic clusters provide conduction paths for water and proton diffusion. The hydrophilic clusters are connected by cross-links via the PTFE backbone as shown in Fig. 13. The cross-links stiffen the polymer. Cluster formation is reversible. The thermodynamics and kinetics of the cluster formation are driven by temperature and water activity. At high temperature and low water activity, entropy will drive the sulfonic acid groups to become randomly dispersed throughout the PTFE matrix. This results in low mechanical strength and poor conduction paths for

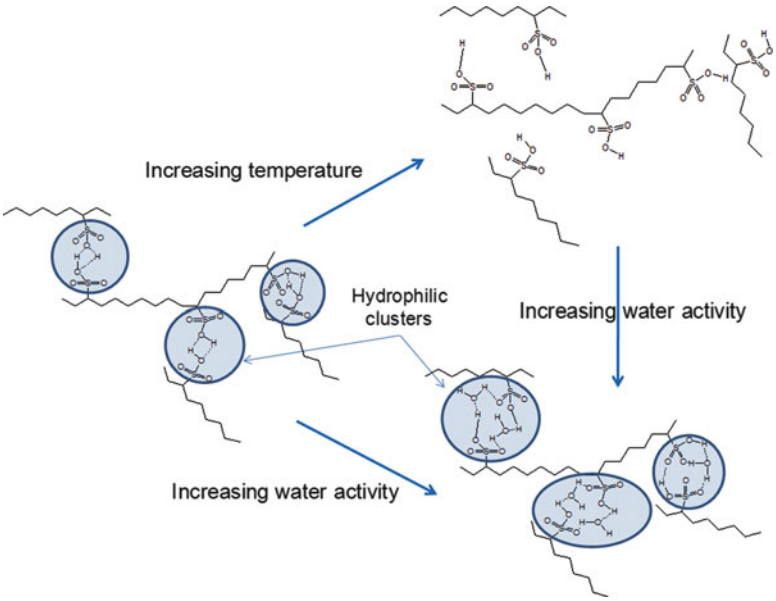

Fig. 13 Clustering of hydrophilic domains in Nafion. At low temperatures, the sulfonic acid groups cluster to reduce the repulsive interactions with the PTFE matrix. Entropy drives the sulfonic acid groups to disperse at high temperatures. Water absorption increases the fraction of hydrophilic species inducing microphase separation

water and proton transport. Sorption of water increases the volume fraction of hydrophilic species, which drives clustering of the hydrophilic domains that contain water and sulfonic acid. This stiffens the polymer and improves water and proton transport.

5.3 Water-Induced Clustering of Sulfonic Acid Groups

The combination of temperature and water absorption produces unusual mechanical and transport property changes in Nafion. We suggest that the changes in properties are the result of water and sulfonic acid groups clustering, forming connected hydrophilic domains. Two alternative mechanisms have been discussed in the literature for cluster formation. Eisenberg and Yeo suggested a clustering transition associated with microphase separation in Nafion [63]. They considered cluster formation as a balance between attractive interactions between dipoles and the elastic deformation of the polymer chains. Moore and coworkers have more recently suggested that the transitions are associated with structural ordering within the microphases of Nafion [22, 27, 64–67]. They suggested increased crystallinity of teflon domains caused stiffening of the polymer, but they also suggested that ordering of sulfonate salts can contribute to the mechanical properties. Many other

models have been presented for clusters in Nafion [68–75]. These cluster models have generally assumed that the clusters exist at all conditions, and addition of water increases the sizes of the clusters. Gierke and Hsu proposed an elastic model for cluster growth by solvation shell [68, 71, 72, 76]. They also suggested that clusters could grow by ripening [77]. Other than the early papers by Eisenberg [25, 63] and Gierke, we have not seen any models relating changes in clustering to mechanical properties of Nafion, and those models do not account for the unusual effects that water absorption and temperature have on mechanical and transport properties reported above. We believe that formation and break up of hydrophilic clusters in Nafion can explain the unusual changes in mechanical properties of Nafion reported above.

Water sorption is a balance between the energy of solvation and the work done to swell the matrix to accommodate the solute. The number of hydrophilic clusters and their size is a balance between the entropy of dispersing the hydrophilic sulfonate salts throughout the hydrophobic matrix and the repulsive energy between the hydrophobic and hydrophilic domains. Increasing temperature favors dispersing smaller hydrophilic groups in the hydrophobic matrix (entropically driven). Solute (water) absorption increases the volume fraction of the hydrophilic domains. Clustering is analogous to micelle formation in surfactant solutions, the sulfonic acid are the hydrophilic head groups, and the perfluoroether and PTFE are the hydrophobic tails. Figure 14 is a model to illustrate the micellar structure of Nafion.

The clustering of sulfonate groups has several implications for properties of Nafion. Stress relaxation of Nafion shows two distinct behaviors. At higher temperatures and nearly dry conditions where singlets are favored, Nafion relaxes and approaches zero stress with a maximum relaxation time of ~10^3 s. In contrast, at conditions where clustering is preferred (low temperatures or in the presence of water vapor), stress relaxation occurs at a constant rate and there is no upper limit to the stress relaxation time. At conditions where clustering is not thermodynamically favorable, the lack of cross-links results in a polymer with a low viscosity which can flow to relax stress. When thermodynamics favor clustering, the cross-links increase the viscosity and slow down the stress relaxation. The formation of larger clusters is particularly slow as the smaller clusters must break apart and permit sulfonate groups to move and reform into new larger clusters.

5.4 Effects of Solute and Cation on Clustering

Solutes other than water can induce clustering. Figure 15 shows the tensile modulus of Nafion as a function of methanol activity at 25°C, 50°C, and 60°C [78]. The modulus shows a distinct maximum at a methanol activity of 0.1 at both 50°C and 60°C. This maximum in modulus is shifted to a higher solute activity with methanol than was observed with water. Because the solubility difference between the hydrophilic phase (sulfonate groups + methanol or water) and the hydrophobic phase (TFE + PFAE) is reduced for methanol compared to water, the driving force

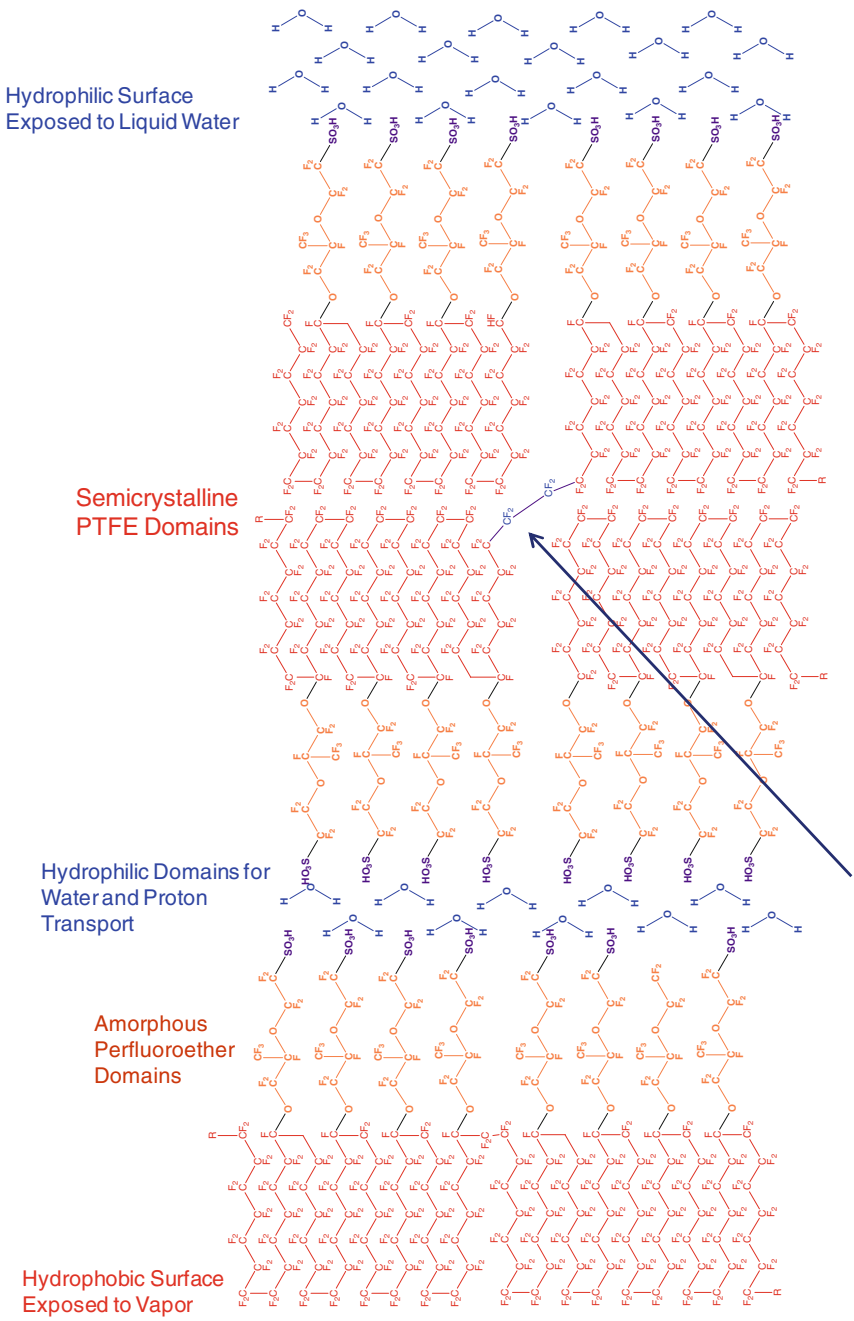

Fig. 14 A conceptual model of Nafion as a micellar structure. The PTFE groups segregate to the core with the perfluoroether groups forming a shell terminated with the sulfonic acid groups forming a hydrophilic channel for water and proton transport. The PTFE chains form cross-links between hydrophilic domains imparting mechanical strength. The surface of Nafion can rearrange when in contact with vapor or liquid water to be either hydrophilic or hydrophobic

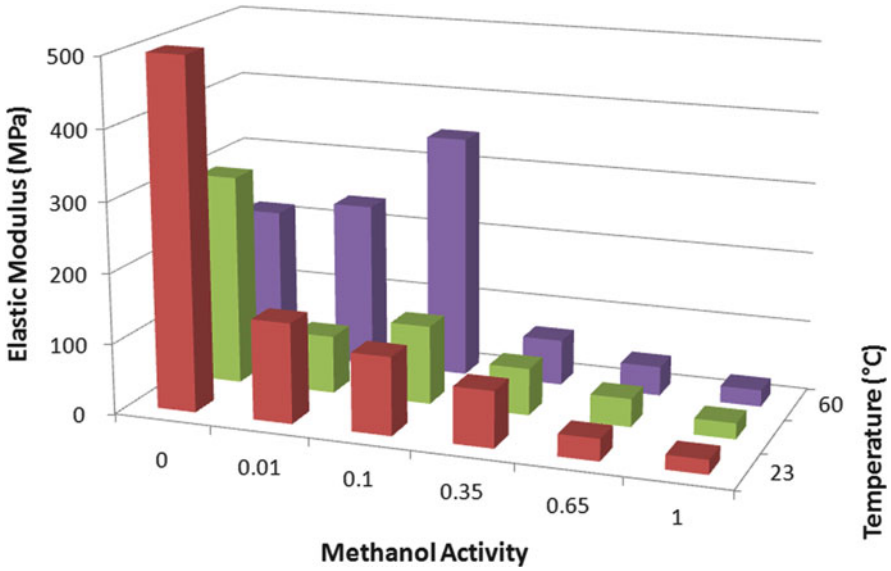

Fig. 15 Elastic modulus of Nafion as a function of temperature and methanol vapor activity

for cluster formation is reduced with methanol. It takes a higher concentration of methanol to induce clustering than it takes with water.

Clustering and the cluster transition temperature are affected by both the choice of the cation and the concentration of the sulfonates. The attractive polar interactions between sodium sulfonates is greater than between sulfonic acids, which shifts the clustering transition to higher temperatures for the Na^+-Nafion. Figure 16 compares the elastic modulus as a function of temperature for dry 1100 EW Nafion in the H^+ and Na^+ forms. The large decrease in elastic modulus with increasing temperature indicates the breakup of the cross-links associated with clustering. The clustering transition temperature is 100°C greater for Na^+-Nafion compared to H^+-Nafion. The results in Figure 16 also show that the transition temperature shifts to higher temperature as EW decreases. Lower EW corresponds to higher density of sulfonates.

6 Physical Properties Affected by Clustering of Hydrophilic Domains

The physical properties that are correlated with the clustering of hydrophilic domains in Nafion are summarized in Table 1. This list is not complete but it indicates the range of properties that clustering affects. We have also summarized the trends in property changes associated with clustering.

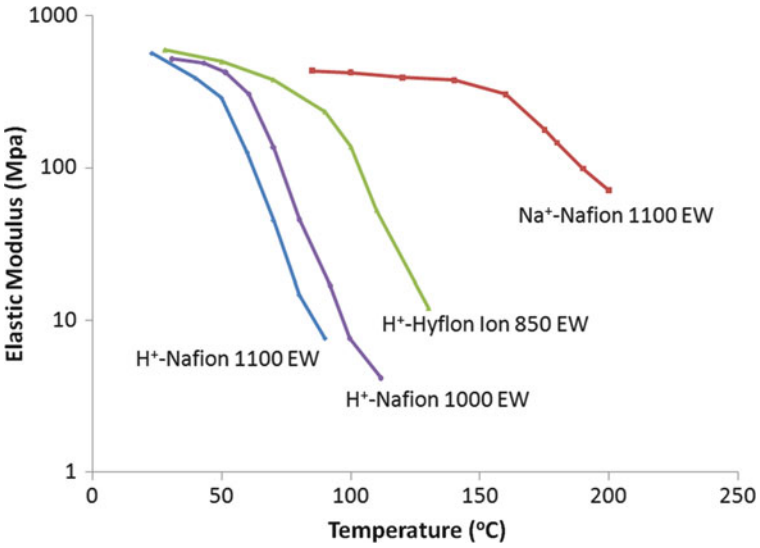

Fig. 16 Elastic modulus of perfluoro sulfonates at dry conditions ($a_w = 0$). The clustering transition temperature increases with decreasing equivalent weight for sulfonic acid forms, and the clustering temperature increases when substituting Na^+ cations for protons

Table 1 Physical properties correlated with sulfonate clustering in Nafion

Property	Effect of clustering
Elastic modulus	Clustering creates cross-links increasing the elastic modulus
Tensile creep rate	Clustering decreases the tensile creep
Proton conductivity	Clustering increases the proton conductivity
Stress relaxation rate	Clustering slows down stress relaxation
Water diffusion coefficient	Clustering increases the effective water diffusion coefficient
Tortuosity and water diffusion	Clustering increases hydrophilic domain connectivity, decreasing tortuosity, increasing water diffusion

7 Implications for Processing

One of the challenges in processing Nafion is the frequent lack of reproducibility of physical properties. We suggested that the key to reproducible processing of Nafion is to control the clustering transition. By proper processing, we have been able to prepare reproducible materials, extruded and recast films have been produced with identical properties, and there is no memory of machine direction from the extrusion process [33, 43–45, 47].

The key to reproducible processing is to take the material to a state where there is no order, i.e., a condition where clustering does not occur. The material should be kept in that state for a time longer than the relaxation time to erase memory of

built-in stresses. Because clustering depends on both temperature and solute activity, the ideal processing step is done in vacuum or in an inert atmosphere sufficiently above the clustering transition temperature so that the residual microstructure relaxes away. Based on the stress relaxation results shown in Fig. 12, we identified a minimum condition of 70°C in vacuum or dry nitrogen for 2 h to erase the memory of 1100 EW H^+-Nafion. Our experience has confirmed that any 1100 EW H^+-Nafion sample up to 250 μm thick shows identical mechanical and transport properties after the following sequence of processing:

1. Anneal at 80°C in vacuum for >2 h
2. Boil in 3% hydrogen peroxide solution for 1 h
3. Rinse with boiling deionized water
4. Ion exchange to H-Nafion by boiling in 1 M sulfuric acid for 1 h
5. Rinse with boiling deionized water
6. Heat the sample in a vacuum over or in flowing nitrogen at 70–80°C for 2 h

This procedure is robust for EW 1100 H^+-Nafion. It requires adjustments for samples with different solutes, cations, or equivalent weight as outlined below.

Vacuum annealing in steps 1 and 6 produce a homogeneous polymer without microphase separation. Step one was essential for solvent cast films. In polar solvents, such as alcohols and water, Nafion molecules will exist as a hydrophobic core surrounded by a shell of the hydrophilic sulfonate groups (like a micelle). After evaporation of the solvent, these micellar structures must be melted and allowed to form a homogeneous solution. The mixing will intertwine polymer chains making the hydrophobic PTFE phase continuous. Without annealing, the micelles will go back into solution when placed in water or other polar solvents. Moore and coworkers have also reported that annealing of solvent cast films is essential to provide mechanical stability to Nafion films [64, 67]. The temperature of the annealing is dependent on the presence of solute vapor (e.g., water or alcohols) and the cations present. This was discussed in greater detail in section 5.4. Steps 2–4 are to remove chemical impurities in the Nafion, such as alkali cations or organic impurities that can cause discoloration of Nafion. The final annealing is to remove the water from Nafion. Vacuum annealing >70°C for >2 h reduces the water content in Nafion to $\lambda < 0.1$ water/SO_3. It is essential to have vacuum or dry nitrogen during the annealing step. Results presented in Sect. 5.1 showed that small amounts of water vapor ($a_w > 0.01$, RH > 1%) is sufficient to induce clustering of hydrophilic clusters of sulfonic acid and water that dramatically alter the properties of Nafion.

The presence of small amounts of water vapor is sufficient to induce clustering. The clustering increases the viscosity of Nafion and slows down the relaxation processes as seen in Fig. 12. If the ambient air is 50% relative humidity ($a_w = 0.5$) at 25°C ($P_w^0 = 0.032$ bar), raising the temperature to 100°C ($P_w^0 = 1.0$ bar) reduces the water activity such that $a_w = 0.016$. However, even that small water activity is sufficient to induce clustering as demonstrated by the elastic modulus results shown in Fig. 11. The large effect of water activity on clustering is why it is so critical to work with vacuum or dry nitrogen. Processing Nafion out in the open air exposed to ambient relative humidity can make it almost impossible to control the state of

Nafion. Cascoila et al. had previously suggested that it was necessary to take Nafion to above 140°C to erase its memory [79]. We believe that they suggested a much higher temperature than we identified because they failed to recognize the importance of the presence of water in the atmosphere.

The processing and annealing procedure discussed above is sufficient to erase the memory of past processing of Nafion. However, the properties of Nafion do depend on the subsequent processing. The time–temperature–solute activity conditions will determine the state of clustering in Nafion. Rapid cooling after annealing will result in a material that is far removed from the equilibrium concentration of clustering at the final temperature. A slow annealing process near the clustering transition will produce Nafion with a high number of clusters leading to a stiffer material. The elastic modulus of H^+-Nafion samples after annealing at 80°C or 150°C in dry nitrogen and cooled to room temperature in 15 min was obtained at $T = 25$°C and $a_w = 0$, $T = 80$°C and $a_w = 0$, and $T = 25$°C and $a_w = 0.65$; the elastic moduli are summarized in Table 2.

The 80° annealing was near the clustering temperature and permitted a larger number of clusters to form than would form at 150°C. Annealing near the clustering temperature produced a greater clustering, which produced a material with a substantially greater elastic modulus as seen for the first two entries in Table 2. Some memory of the clustering was retained by the samples tested at 80°C. The elastic moduli of samples tested at 80°C were substantially less than at 25°C, but the sample annealed at 150°C had a lower modulus than annealing at 80°C. When the annealed samples were exposed to water vapor, the trend in the moduli was inverted as seen in the last two entries in Table 2. This resulted from water-induced clustering. Annealing at 150°C produced a material that had mostly isolated sulfonic acid groups. The initial cluster would produce dimers and lead to stiffening. In contrast, the sample annealed at 80°C started with multiplet clusters, and the addition of water led to growing of the clusters reducing the number of cross-links; hence, it now became the less stiff material.

The annealing at 150°C has a secondary effect on the structure of Nafion. At that temperature, the TFE domains are still below their melting point, while the material has a low viscosity. This permits increased crystalline growth of the TFE domains. That growth has been demonstrated by some elegant SAXS and DSC experiments by Moore and coworkers [22]. However, based on the results shown in Table 2, it appears that the ordering in the TFE domains has a smaller effect on the mechanical properties of Nafion than the clustering.

Table 2 Comparison of creep strain of 1100 EW H^+-Nafion for different annealing conditions

Annealing T (°C)	Annealing a_w	Testing T (°C)	Testing a_w	Elastic modulus (MPa)
80	0	25	0	580
150	0	25	0	300
80	0	80	0	26
150	0	80	0	9
80	0	25	0.65	120
150	0	25	0.65	145

There are a wide variety of methods to alter the final state of Nafion and the properties of the material. Nafion can be exposed to different solutes at different temperatures to induce clustering. Acids, gels, or particles can be added, which will alter the clustering. The combination of different solutes, temperatures, and times can result in materials with dramatically different properties that can be difficult to understand. Our findings suggest that the unique properties of Nafion are the result of clustering of the hydrophilic domains that is driven by temperature and solute activity. Control over the physical properties of Nafion is essential for processing membranes for fuel cells, and also for understanding the modes of membrane failure in fuel cells.

8 Conclusion

The mechanical and transport properties of Nafion correlate with clustering of hydrophilic domains in Nafion. Clustering is energetically driven by the dissimilarity of the hydrophilic sulfonate groups and the hydrophobic perfluorinated backbone and side chain. Increasing temperature causes the clusters to break apart due to entropy. Absorption of polar solutes such as water or methanol induces ordering by increasing the volume fraction of the hydrophilic domains.

Clustering of sulfonic acid groups and water helps elucidate the large and dramatic changes in proton conduction, water transport, elastic modulus, polymer creep, and stress relaxation that occur with Nafion at low water activity and high temperature. The identification of a clustering transition facilitates the choice of processing conditions to erase the memory of Nafion and better control the mechanical and transport properties.

Acknowledgment The authors thank the National Science Foundation (CBET–0754715 and DMR-0213707 through the Materials Research and Science Engineering Center at Princeton) for support of this work.

References

1. Mauritz KA, Moore RB (2004) State of understanding of Nafion. Chem Rev 104 (10):4535–4585
2. Yeo RS, Yeager HL (1985) Structural and transport properties of perfluorinated ion-exchange membrane. In: Conway BE, White RE, Bockris JOM (eds) Modern aspects of electrochemistry. Plenum, New York, pp 437–504
3. Kim J-S (2005) Ionomers. In: Kirk-Othmer encyclopedia of chemical technology. Wiley, New York, pp 1-32
4. Doyle M, Rajendaran G (2003) Perfluorinated membranes. In: Vielstich W, Gasteiger HA, Lamm A (eds) Fuel cell technology and applications. Wiley, New York
5. Berzins T (1978) Electrochemical relationships in chlor-alkali cells employing Nafion membranes. J Electrochem Soc 125(3):C163
6. Cise GE, Melnicki LS, Rudd EJ (1978) Evaluation and optimization of Nafion membranes in chlor-alkali cells. J Electrochem Soc 125(3):C162

7. Heitner-Wirguin C (1996) Recent advances in perfluorinated ionomer membranes: structure, properties and applications. J Memb Sci 120:1–33
8. Srinivasan S et al (1993) Overview of fuel cell technology. In: Blomen LJMJ, Mugerwa MN (eds) Fuel cell systems. Plenum, New York, pp 37–72
9. Du XZ et al (2001) Performances of proton exchange membrane fuel cells with alternate membranes. Phys Chem Chem Phys 3(15):3175–3179
10. Adjemian KT et al (2000) Novel Membranes for PEMFC Operation at 120 to 200 C. The Electrochemistry Society Meeting Abstracts, 2000. 2000-1: p Abstract 85
11. Costamagna P, Srinivasan S (2001) Quantum jumps in the PEMFC science and technology from the 1960s to the year 2000 Part II. Engineering, technology development and application aspects. J Power Sources 102(1–2):253–269
12. Yang C et al (2001) Approaches and technical challenges to high temperature operation of proton exchange membrane fuel cells. J Power Sources 103(1):1–9
13. Sato K, Nakao M, Ishii T (1986) Operational technology with Flemion for chloralkali electrolysis. J Electrochem Soc 133(3):C122
14. Yoshida N et al (1998) Characterization of Flemion (R) membranes for PEFC. Electrochim Acta 43(24):3749–3754
15. Moxley JF, Tulyani S, Benziger JB (2003) Steady-state multiplicity in the autohumidification polymer electrolyte membrane fuel cell. Chem Eng Sci 58(20):4705–4708
16. Benziger J et al (2004) The stirred tank reactor polymer electrolyte membrane fuel cell. AIChE J 50(8):1889–1900
17. Rama P, Chen R, Andrews J (2008) A review of performance degradation and failure modes for hydrogen-fuelled polymer electrolyte fuel cells. Proc Inst Mech Eng Part A J Power Energy 222(A5):421–441
18. Mittal VO, Kunz HR, Fenton JM (2007) Membrane degradation mechanisms in PEMFCs. J Electrochem Soc 154(7):B652–B656
19. Gebel G, Diat O (2005) Neutron and x-ray scattering: suitable tools for studying ionomer membranes. Fuel Cells 5(2):261–276
20. Loveday D et al (1997) Investigation of the structure and properties of polyisobutylene-based telechelic ionomers of narrow molecular weight distribution.2. Mechanical. J Appl Polym Sci 63(4):507–519
21. Pineri M (1986) Microstructure of organic ionic membranes. ACS Symp Ser 302:159–174
22. Page KA et al (2006) SAXS analysis of the thermal relaxation of anisotropic morphologies in oriented Nafion membranes. Macromolecules 39(11):3939–3946
23. Gierke TD, Munn GE, Wilson FC (1982) Morphology of perfluorosulfonated membrane products – wide-angle and small-angle X-ray studies. ACS Symp Ser 180:195–216
24. Yeo RS, Chan SF, Lee J (1981) Swelling behavior of Nafion and radiation-grafted cation-exchange membranes. J Memb Sci 9(3):273–283
25. Yeo SC, Eisenberg A (1977) Physical properties and supermolecular structure of perfluorinated ion-containing (Nafion) polymers. J Appl Polym Sci 21(4):875–898
26. Miura Y, Yoshida H (1990) Effects of water and alcohols on molecular-motion of perfluorinated ionomer membranes. Thermochim Acta 163:161–168
27. Page KA, Cable KM, Moore RB (2005) Molecular origins of the thermal transitions and dynamic mechanical relaxations in perfluorosulfonate ionomers. Macromolecules 38(15):6472–6484
28. Kreuer KD (2001) On the development of proton conducting polymer membranes for hydrogen and methanol fuel cells. J Memb Sci 185(1):29–39
29. Kreuer KD et al (2004) Transport in proton conductors for fuel-cell applications: simulations, elementary reactions, and phenomenology. Chem Rev 104(10):4637–4678
30. Weber AZ, Newman J (2003) Transport in polymer-electrolyte membranes - I. Physical model. J Electrochem Soc 150(7):A1008–A1015
31. Weber AZ, Newman J (2004) Modeling transport in polymer-electrolyte fuel cells. Chem Rev 104:4679–4726
32. Majsztrik PW et al (2007) Water sorption, desorption and transport in Nafion membranes. J Memb Sci 301:93–106

33. Majsztrik PW, Bocarsly AB, Benziger J (2008) Water permeation through Nafion. J Phys Chem B 112(51):16280–16289
34. Satterfield MB, Benziger JB (2008) Non-Fickian water sorption dynamics by Nafion membranes. J Phys Chem B 112(12):3693–3704
35. Zawodzinski TA et al (1991) Determination of water diffusion-coefficients in perfluorosulfonate ionomeric membranes. J Phys Chem 95(15):6040–6044
36. Zawodzinski TA et al (1993) Water-uptake by and transport through Nafion(R) 117 Membranes. J Electrochem Soc 140(4):1041–1047
37. Hinatsu JT, Mizuhata M, Takenaka H (1994) Water uptake of perfluorosulfonic acid membranes from liquid water and water vapor. J Electrochem Soc 141(6):1493–1498
38. Bass M, Freger V (2006) An experimental study of Schroeder's paradox in Nafion and Dowex polymer electrolytes. Desalination 199(1–3):277–279
39. Choi PH, Datta R (2003) Sorption in proton-exchange membranes – an explanation of Schroeder's paradox. J Electrochem Soc 150(12):E601–E607
40. Onishi LM, Prausnitz JM, Newman J (2007) Water-nafion equilibria. Absence of Schroeder's paradox. J Phys Chem B 111(34):10166–10173
41. Cornet N, Gebel G, de Geyer A (1998) Existence of the Schroeder paradox with a Nafion membrane? Small-angle x-ray scattering analysis. Journal De Physique IV 8(P5):63–68
42. Satterfield MB, Benziger JB (2009) Viscoelastic properties of Nafion at elevated temperature and humidity. J Polym Sci B Polym Phys 47(1):11–24
43. Satterfield MB et al (2006) Mechanical properties of Nafion and Titania/Nafion composite membranes for PEM fuel cells. Journal of Polymer Science B 44:2327–2345
44. Satterfield MB (2007) Mechanical and water sorption properties of Nafion and Nafion/Titanium dioxide membranes for polymer electrolyte membrane fuel cells. In: Chemical Engineering. Princeton University, Princeton, NJ, p 208
45. Majsztrik PW (2008) Mechanical and transport properties of Nafion for PEM fuel cells; temperature and hydration effects. In: Chemistry. Princeton University, Princeton, NJ, p 235
46. Majsztrik PW, Bocarsly AB, Benzigerv JB (2007) An instrument for environmental control of vapor pressure and temperature for tensile creep and other mechanical property measurements. Rev Sci Instrum 78(10):103904
47. Majsztrik PW, Bocarsly AB, Benziger JB (2008) Viscoelastic response of Nafion. Effects of temperature and hydration on tensile creep. Macromolecules 41(24):9849–9862
48. Yang C et al (2004) A comparison of physical properties and fuel cell performance of Nafion and zirconium phosphate/Nafion composite membranes. J Memb Sci 237(1–2):145–161
49. Zhao Q, Majsztrik P, Benziger J (2011) Diffusion and interfacial transport of water in Nafion. J Phys Chem B. dx.doi.org/10.1021/jp112125
50. Cheah MJ, Kevrekidis IG, Benziger J (2011) Effect of applied potential, water activity and temperature on proton and water transport in Nafion. J Phys Chem B (submitted)
51. Bass M et al (2010) Surface structure of Nafion in vapor and liquid. J Phys Chem B 114 (11):3784–3790
52. Kyu T, Eisenberg A (1982) Mechanical relaxations in perfluorosulfonate-ionomer membranes. ACS Symp Ser 180:79–110
53. Hodge IM, Eisenberg A (1978) Dielectric and mechanical relaxations in a Nafion precursor. Macromolecules 11(2):289–293
54. Choi P et al (2006) Consideration of thermodynamic, transport, and mechanical properties in the design of polymer electrolyte membranes for higher temperature fuel cell operation. J Polym Sci B Polym Phys 44(16):2183–2200
55. Escoubes M, Pineri M, Robens E (1984) Application Of coupled thermal-analysis techniques to thermodynamic studies of water interactions with a compressible ionic polymer matrix. Thermochim Acta 82(1):149–160
56. Jalani NH, Dunn K, Datta R (2005) Synthesis and characterization of Nafion$^{(R)}$-MO_2 (M = Zr, Si, Ti) nanocomposite membranes for higher temperature PEM fuel cells. Electrochim Acta 51(3):553–560

57. Kawano Y et al (2002) Stress-strain curves of Nafion membranes in acid and salt forms. Polimeros: Ciencia e Technologia 12(2):96–101
58. Khare VP, Greenberg AR, Krantz WB (2004) Investigation of the viscoelastic and transport properties of interfacially polymerized barrier layers using pendant drop mechanical analysis. J Appl Polym Sci 94(2):558–568
59. Laporta M, Pegoraro M, Zanderighi L (1999) Perfluorosulfonated membrane (Nafion): FT-IR study of the state of water with increasing humidity. Phys Chem Chem Phys 1(19):4619–4628
60. Taylor EP et al (2006) Counterion dependent crystallization kinetics in blends of a perfluorosulfonate ionomer with poly(vinylidene fluoride). Polymer 47(21):7425–7435
61. Osborn SJ et al (2007) Glass transition temperature of perfluorosulfonic acid ionomers. Macromolecules 40(10):3886–3890
62. Bauer F, Denneler S, Willert-Porada M (2005) Influence of temperature and humidity on the mechanical properties of Nafion (R) 117 polymer electrolyte membrane. J Polym Sci B Polym Phys 43(7):786–795
63. Eisenberg A (1970) Macromolecules 3:147
64. Moore RB et al (2005) Alteration of membrane properties of perfluorosulfonate ionomers using solution and melt processing procedures. Abstracts of Papers of the American Chemical Society. 230: p 756-POLY
65. Page KA, Jarrett W, Moore RB (2007) Variable temperature F-19 solid-state NMR study of the effect of electrostatic interactions on thermally-stimulated molecular motions in perfluorosulfonate lonomers. J Polym Sci B Polym Phys 45(16):2177–2186
66. Park JK, Moore RB (2009) Influence of ordered morphology on the anisotropic actuation in uniaxially oriented electroactive polymer systems. ACS Appl Mater Interfaces 1(3):697–702
67. Phillips AK, Moore RB (2006) Mechanical and transport property modifications of perfluorosulfonate ionomer membranes prepared with mixed organic and inorganic counterions. J Polym Sci B Polym Phys 44(16):2267–2277
68. Gierke TD, Hsu WY (1982) The cluster-network model of ion clustering in perfluorosulfonated membranes. ACS Symp Ser 180:283–307
69. Escoubes M et al (1984) Ion clustering in styrene-based ionomers – calorimetric and gravimetric hydration studies and effect of ion concentration and thermal history. J Appl Polym Sci 29(4):1249–1266
70. Hsu WY, Gierke TD (1982) Ion clustering and transport in Nafion perfluorinated membranes. J Electrochem Soc 129(3):C121
71. Hsu WY, Gierke TD (1982) Elastic theory for ionic clustering in perfluorinated ionomers. Macromolecules 15(1):101–105
72. Hsu WY, Gierke TD (1983) Ion-transport and clustering in Nafion perfluorinated membranes. J Memb Sci 13(3):307–326
73. Yoshida H, Miura Y (1992) Behavior of water in perfluorinated ionomer membranes containing various monovalent cations. J Memb Sci 68(1–2):1–10
74. Schmidt-Rohr K, Chen Q (2008) Parallel cylindrical water nanochannels in Nafion fuel-cell membranes. Nat Mater 7(1):75–83
75. Choi P, Jalani NH, Datta R (2005) Thermodynamics and proton transport in Nafion - II. Proton diffusion mechanisms and conductivity. J Electrochem Soc 152(3):E123–E130
76. Hsu WY, Gierke TD, Molnar CJ (1983) Morphological effects on the physical-properties of polymer composites. Macromolecules 16(12):1945–1947
77. Gierke TD, Munn GE, Wilson FC (1981) The morphology in Nafion perfluorinated membrane products, as determined by wide-angle and small-angle X-ray studies. J Polym Sci B Polym Phys 19(11):1687–1704
78. Ranney C (2008) Effects of temperature and solvent activity on the viscoelastic response of Nafion for PEM fuel cells. In: Chemical Engineering. Princeton University, Princeton, p 62
79. Casciola M et al (2006) On the decay of Nafion proton conductivity at high temperature and relative humidity. J Power Sources 162:141–145

Struct Bond (2011) 141: 115–168
DOI: 10.1007/430_2011_45

Published online: 17 June 2011

The Use of Heteropoly Acids in Proton Exchange Fuel Cells

Sonny Sachdeva, John A. Turner, James L. Horan, and Andrew M. Herring

Abstract In this chapter, we discuss the proton conductivity and use of heteropoly acids (HPAs) in proton exchange fuel cells. We first review the fundamental aspects of proton conduction in the HPAs and then review liquid HPA-based fuel cells. Four types of composite proton exchange membranes containing HPAs have been identified: HPAs imbibed perfluorosulfonic acid membranes, HPAs imbibed hydrocarbon membranes, sol–gel-based membranes, and polymer hybrid polyoxometalate (polypom)-based membranes.

Keywords Fuel cell · Heteropoly acid · Polyoxometalate · Proton exchange membrane · Proton transport

Contents

S. Sachdeva, J.L. Horan, and A.M. Herring (✉)
Department of Chemical Engineering, Colorado School of Mines, Golden, CO 80401, USA
e-mail: aherring@mines.edu

J.A. Turner
Energy Sciences, National Renewable Energy Laboratory, Golden, CO 80401, USA

Abbreviations

DMFC	Direct methanol fuel cell
FC	Fuel cell
HPA	Heteropoly acid
HPMo	12-Phosphomolybdic acid
HPW	12-Phosphotungstic acid
HSiW	12-Silicotungstic acid
MEA	Membrane electrode assembly
PEM	Proton exchange membrane
PFG	Pulsed field gradient
PFSA	Perfluoro sulfonic acid
POM	Polyoxometalate

1 Introduction

Current perfluorosulfonic acid (PFSA) membrane-based proton exchange membrane fuel cells (PEMFCs) must operate at temperatures at or below 100°C, (typically at 80°C) to maintain the saturated state of water hydration necessary to facilitate proton conduction. In order to prevent the membrane from drying out even at temperatures below 80°C, inlet gases must be humidified which in turn creates a parasitic loss of efficiency and can create operational complications such as reactant gas dilution and gas diffusion layer "flooding" at high current densities [1, 2]. It would also be desirable to operate PEMFCs at higher temperatures to alleviate CO poisoning on the Pt anode from impure H_2 reformate fuel streams. In this way, H_2 adsorption on Pt becomes competitive with CO adsorption [3]. A quantitative analysis of the free energy of H_2 and CO adsorption on platinum as a function of temperature indicates that raising the temperature to 145°C will increase the CO tolerance at the anode by a factor of ~20 times [4]. One approach to this problem is to form composite proton exchange membranes (PEMs) with inorganic components [5]. Of all the inorganic components considered, the heteropoly acids (HPAs) have the most potential.

The interest in HPAs for fuel cell applications began three decades ago with a report of extremely high room temperature proton conductivities, as high as 2×10^{-1} S/cm for 12-phosphotungstic acid (HPW) [6]. However, solid 12-HPW must be kept in its fully hydrated crystalline ($H_3PW_{12}O_{40} \cdot 29H_2O$) form to obtain this high proton conductivity (2.0×10^{-1} S/cm). Attempts [7–9] have been made to use HPAs as the solid electrolytes in their crystalline form for room temperature fuel cells but are unstable as they dissolve in the water formed during cell operation. Concentrated HPW exhibited even higher proton conductivity (3.0×10^{-1} S/cm at 295 K). Hence, Giordano et al. [10] used a concentrated (60%) solution of HPW

as the fuel cell electrolyte which showed comparable proton conductivity, chemical stability to a PEMFC overcoming the physical instability of the solid HPA electrolyte. However, at lower current densities, aqueous HPA fuel cells (HPAFCs) performance is below that of PEMFC due to voltage losses resulting from chemical crossover phenomena.

In order to increase the stability, HPAs were incorporated in sols of alumina [11] and silica [12]. HPAs immobilized on supports like silica, although stable in the presence of water, could not be used as electrolytes in fuel cells in the powdered form. For this reason, composite membranes [13, 14] have been developed, using a polymer as binder for the formation of thermally and mechanically resistant membranes with low gas permeability and silicotungstic acid or phosphotungstic acid immobilized on silica as the inorganic proton conductor.

Importantly, for elevated temperature PEM fuel cell operation, the HPAs may be structurally stable to $>600^{\circ}C$, although under anhydrous conditions their stability may be limited to $200^{\circ}C$, and they incorporate some water molecules and protons up to $>300^{\circ}C$ depending on the system [15]. Because of their structural diversity, these materials are particularly suitable for incorporation into a wide variety of membrane materials for which they can be specifically tailored. They have been studied in four composite systems: HPAs infused into perfluorinated sulfonic acid (PFSA) polymers such as Nafion® [16, 17], HPA cast in inert matrices such as poly (vinyl alcohol) (PVA) [18], HPA immobilized in polymer/silicate nanocomposites via sol–gel methods [19], and HPA directly incorporated into polymer films via functionalization to monomers [20]. Here after a discussion of fundamental studies, we review the various HPA-based materials used for fuel cells.

2 Fundamental Studies

The HPAs are a subset of the well-known inorganic metal oxides called polyoxometalates (POMs) [21, 22]. They are distinguished by a central heteroatom, which can be almost any atom in the periodic table that is surrounded by several metal oxygen octahedra; the metal is usually tungsten or molybdenum or less commonly vanadium or uranium. The heteropoly anions having metal-oxygen octahedral as the basic structural units make up the primary structure of the HPA as shown in the Keggin anion (Fig. 1), which has been fully characterized by X-ray crystallography [23], nuclear magnetic resonance (NMR) spectroscopy [24, 25], and infrared (IR) spectroscopy [26] studies. Many of the HPAs can exist as free acids and typically contain three to six lone pairs of electrons and are considered to be super acids in a Bronstead–Lowry context. The proton conduction is believed to occur in the space between the anions, often referred to as the secondary structure or pseudoliquid phase. They can incorporate a significant number of water molecules as part of their chemical structure. Two types of water of hydration have been identified: (a) those stable at low temperatures, that is, the waters of crystallization in which proton conduction can be described in terms of acidified water and has been

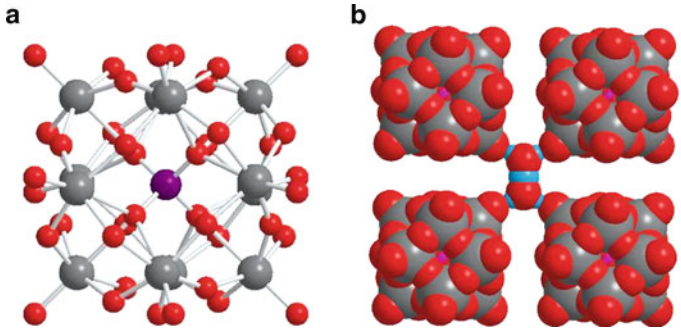

Fig. 1 Heteropoly acid structures (**a**) Ball and stick model of the silicotungstic Keggin anion ($SiW_{12}O_{40}^{-4}$). (**b**) Space filling model of the secondary crystalline structure of Keggin HPA with base-centered cubic arranged cavities containing $H_5O_2^+$ cations (*red* = O, *gray* = W, *blue* = H, *purple* = P or Si)

well understood [27], and (b) those stable at higher temperatures, that is, the water of hydration in the secondary structure.

The most thoroughly studied HPAs are $H_3PW_{12}O_{40}$ (HPW) and $H_3PMo_{12}O_{40}$ (HPMo) which consist of a centrally located, four-coordinate phosphorus linked via oxygen atoms to 12 tungsten–oxygen and molybdenum–oxygen octahedra, respectively. Before the discovery of the high proton conductivity of HPW, a number of studies had been conducted to determine its structure under various conditions, and it was found that a series of hydrated HPW phases exists, the stable form depending on temperature and relative humidity [28]. The HPAs crystallize with a large number of water molecules: 29 (HPW and HPMo) and 30 for HSiW, some of which can be lost very easily even at room temperature. In the process of dehydration/calcination, HPA hydrates lose water molecules continuously, transforming into lower hydrates. The basic structural unit of HPW·nH$_2$O is the $[PW_{12}O_{40}]^{3-}$ with different number of water molecules (n = 6, 14, 21, 29). Single-crystal X-ray and neutron diffraction studies had been conducted on HPW·29H_2O [29], HPW·21H_2O [30], HPW·14H_2O [31], and HPW·6H_2O [23], which showed that except for the lowest water content, the water molecules showed large thermal motion and the acid protons were not distinguishable. The HPW hexahydrate, HPW·6H_2O, (HPW in its high-temperature limited hydration state) had a anionic cubic structure of Keggin where all hydrogen atoms are present as $H_5O_2^+$ [23]. A stable form contains six water molecules of hydration per Keggin unit, forming a body-centered cubic (bcc) structure with Keggin units at the lattice points and $H_5O_2^+$ bridges along the faces. Each terminal oxygen atom is bound to a hydrogen atom of an $H_5O_2^+$ bridge. In this structure, the acidic protons are located in the $H_5O_2^+$ bridges between lattice points. A quasi-elastic neutron diffraction scattering study [32] of HPW·6H_2O has shown that the water molecules in the $H_5O_2^+$ complex undergo a twofold reorientation about the central hydrogen bond.

Nakamura et al. [6] found the proton conductivities of the 29-hydrates of HPW and HPMo to be 1.7×10^{-1} S/cm at 293 K and the observed activation energies to

be 15.5 kJ/mol for 12-HPMo and 17 kJ/mol for 12-HPW [33, 34]. Slade et al. [35] investigated the effect of temperature on the proton conductivities and ^{1}H self-diffusion coefficients (D) for the polycrystalline hydrates of 12-HPW·nH$_2$O (n = 6, 14, 21, and 29) using ac conductivity and pulse field gradient-nuclear magnetic resonance (PFG-NMR) techniques. They determined the ambient temperature conductivities to be 5×10^{-3} S/cm for HPW·21H$_2$O and 3.0×10^{-2} S/cm for HPMo·21H$_2$O, which are lower than the 29-hydrates but compare well with those of other solid-state proton conductors. The temperature dependences of the ac conductivities of pelletized 12-tungstophosphoric acid, HPW hydrates, show an Arrhenius form in the experimental temperature range, with E_A = 43 [35], 32 ± 4 [36], and 27 ± 2 kJ/mol for HPW·nH$_2$O with n = 21, 14, and 6, respectively. Ambient temperature conductivity increases with n (i.e., higher for a higher water-content phase). The temperature dependences of the self-diffusion coefficients, D, for the HPW hydrates also obey Arrhenius law, with E_A = 18 ± 2 and 16 ± 1 kJ/mol for HPW·nH$_2$O with n = 14 and 21, respectively. It was observed that the conductivity data obtained from Nernst–Einstein equation using the diffusion coefficient, D, for the higher hydrates was overestimated by a factor of 6, and also the activation energies obtained by conduction and diffusion measurements were different. From these observations, they concluded that, for higher hydrates, the mechanism of ^{1}H self diffusion differs from charge transport (H^+) and at lower temperatures (T < 280 K) a change in rate-determining step of the diffusion mechanism leads to much stronger temperature dependence for the diffusion coefficients, D. In the experimental temperature range conductivity for the HPW hydrates increases in the order 6H$_2$O < 14H$_2$O < 21H$_2$O < 29H$_2$O.

Slade et al. [37] used a combination of ac and dc techniques to fully characterize the origin of protonic conductivity in pelletized HPW hexahydrates. The studies definitely assigned a protonic conduction mechanism, with evidence for conduction via crystallite surfaces. They obtained ambient temperature ac conductivities measured using Ag electrodes for HPW·6H$_2$O and HSiW·6H$_2$O that varied in the range of 6×10^{-5} to 2×10^{-4} S/cm. The conductivity mechanism of a continuous, more or less random, structure of protonic species essentially requires low activation energy (as for the higher hydrates), while in the discontinuous and more ordered structure (like in hexahydrate) it appears to consist of mainly H_3O^+ and H$_2$O hopping demanding a high activation energy and therefore a drop in conductivity by three orders of magnitude.

These measurements had been conducted on pressed HPW powders, which being soft might decompose under pressure and exhibit high water partial pressures. Moreover, short-circuiting of the bulk conductivity by fast conduction paths could also occur. To obtain more reliable data on bulk transport, Kreuer et al. [38] prepared single crystals of a defined state of hydration. They measured the ac conductivity and PFNMR measurements and found that the Nernst–Einstein relationship was obeyed. They also concluded that the vehicle mechanism is the operating proton conduction mechanism instead of Grotthuss mechanism which had been believed until then. The conductivity and NMR studies showed that the water molecules to be linked in a 3D network. The high proton conductivity was

explained on the structural basis as all the waters of crystallization to be located in the interstice of big and globular (about 12 Å) anion $[Mo_{12}PO_{40}]^{-}$, and the acid protons to be hydrated. Furthermore, it was suggested that the proton may be transported through the hydrogen bond network as fast as liquid water, which accounted for the observed fast conduction of the proton. Moreover, differing water contents lead to static reorientation of the anions relative to one another.

Mioc et al. [39] studied different HPA hydrates of $H_3PMo_{12}O_{40}{\cdot}29–31H_2O$ (MoPA), $H_3PW_{12}O_{40}{\cdot}29H_2O$ (HPW), and $H_4SiW_{12}O_{40}{\cdot}28H_2O$ to understand the various protonic forms responsible for protonic conduction at various temperatures. Infrared and Raman spectra showed the existence of three proton species in the HPA hydrates at room and low temperatures: almost free OH groups attached to the skeleton of Keggin anions, oxonium ions (H_3O^{+}), and water molecules (H_2O); there being in a temperature-dependent equilibrium among these. They established that a highly disordered quasi-liquid state of different protonic species is likely to exist at room temperature, but a better-defined structure appears at liquid nitrogen temperature where OH. . .H_2O, H_2O. . .H_2O, and H_3O^{+}. . .H_2O interactions could be distinguished. Similar observations were made by the NMR studies of the Keggin ion where deuterium wide-line spectra of HPW with hydration levels less than six water molecules were rather featureless indicating a disordered secondary structure [40]. Measurements of the ^{31}P spin–lattice relaxation time as a function of hydration level suggested that the protons can either penetrate the Keggin anion or rapidly migrate among various Keggin anion surface sites [41].

In order to have a deeper understanding of the behavior of HPW hydrates at high temperatures, Mioc et al. [42] conducted thermogravimetric analysis (TGA), X-ray powder diffraction (XRD), and scanning electron microscopy (SEM) studies in the range of room temperature to 1,150°C. The existence of the various hydrates at different temperatures and the structural transformations that occur during the temperature change can be represented as follows:

$$\begin{aligned}&\mathrm{HPW}-29\,(\mathrm{Triclinic}) \xrightarrow{28-31^{\circ}\mathrm{C}} \mathrm{HPW}-21\,(\mathrm{Orthorhombic}) \xrightarrow{35-42^{\circ}} \\ &\mathrm{HPW}-14/6\,(\mathrm{Triclinic}) \xrightarrow{60^{\circ}\mathrm{C}} \mathrm{HPW}-6\,(\mathrm{Cubic}) \xrightarrow{175-230^{\circ}\mathrm{C}} 0-\mathrm{HPW}\,(\mathrm{Cubic}) \\ &\xrightarrow{410-440^{\circ}\mathrm{C}} \mathrm{D}-\mathrm{HPW}\,(\mathrm{Cubic}) \xrightarrow{580-602^{\circ}\mathrm{C}} \mathrm{bronze}\end{aligned}$$

A further detail of the above representation is described here in [42]. The starting HPA 29-HPW, which is triclinic in structure, underwent two symmetry transformations; from triclinic to orthorhombic (29-HPW to 21-HPW) and then to triclinic (21-HPW to 14-HPW) again, before the stable 6-HPW phase was formed. Corresponding to this in TGA, the doublet observed at 50°C (endothermic) was resolved in two components at about 30°C corresponding to 21-HPW formation and 40°C corresponding to 14-HPW formation The phase transformation of 14-HPW to 6-HPW hydrate is a fast process; while its formation finished at about 60°C, it remained stable up to 170°C. The phase structure of 6-HPW was stable up to 170°C until the exothermal structural phase transition of HPC to doped bronzes.

The sample loses 5.8–6 molecules of water in two steps between 170 and 240°C and becomes anhydrous (0-HPW). At this stage, there would not be any crystalline water present and only free protons. Heating of the 6-HPW above 170–250°C leads to considerable structural changes leading to a slight decrease in the unit cell dimensions, caused by dehydration of the 6-HPW phase forming 0-HPW phase with composition $H_3PW_{12}O_{40.}$ In the temperature range 250–400°C, there is an increase in the unit cell dimensions, which they proposed to be due to the mutual electrostatic repulsion of Keggin's anions which results in an elongation of the hydrogen bonds between them. The anhydrous phase is stable up to 410°C, at which they observe a T_g anomaly, corresponding to an exothermic transformation followed by the loss of mass of one water molecule. This confirmed the presence of only acid protons in the 0-HPW phase. This water molecule is formed from the protons and oxygen of the host lattice. It was revealed from XRD and SEM experiments that cubic symmetry and crystal forms of the 0-HPW phase were preserved. Further increase in temperature in the range of 400–450°C led to a new phase called the denuded Keggin's anion, D-HPW, stable up to 550°C. This phase was formed by the loss of one water molecule, but still the Keggin's framework remained stable till 550°C and also reversible to form 6-HPW on lowering of temperature. The peak at 602°C corresponds to a recrystallization of Keggin's anions to bronze formation.

Similar observations were made by Slade et al. [43] during the course of thermogravimetric dehydration of $HPW{\cdot}6H_2O$ – an initial loss of surface water (the surface is hygroscopic and this is the origin of bulk protonic conductivity in $HPW{\cdot}nH_2O$) occurred, followed by loss of crystal water which stopped at 250°C where Fournier et al. identified an anhydrous HPW with a tetragonal structure. This anhydride looses water with phase segregation at $T > 420$°C ($H_3PW_{12}O_{40} \rightarrow 3/2H_2O + 1/2\ P_2O_5 + 12WO_3$). The product is a pale green powder, consistent with the presence of WO_3 (oxygen deficient due to the reaction conditions).

Tjapkin et al. [44] confirmed the existence of different protonic species in HPAs by dielectric measurements from Cole–Cole diagrams. The bulk proton conductivity at room temperature obtained from impedance measurements on pelletized HPW-6 was found to be 3×10^{-11} S/cm. They observed an abrupt fall in conductivity of 6-HPW at about 140°C when the dehydration occurs at a metastable phase with $n \approx 2$, where the fast dehydration of the hexahydrate slows down. On lowering heating rates at this temperature, the evidence of dialometric changes similar to the contraction of dimensions of the hexahydrate cubic unit cell [42] was observed. The conductivity of anhydrous ($n \geq 0$) HPW is considerably lower than that of the hexahydrate, but at temperature around 143°C, a phase transition occurs causing an increase in the conductivity and lowering of the activation energy. Activation energies in anhydrous ($n \geq 0$) HPW are considerably lower than the activation energy of the hexahydrate, whereas in HPW heated to 400°C is even lower. The conductivity (1.4×10^{-6} S/cm) obtained for the anhydrous HPW was several orders of magnitude higher than the hexahydrate (3×10^{-11} S/cm) at room temperature. The high conductivity of anhydrous ($n = 0$) HPW can be understood to be the consequence of the calcination at 400°C, when a large number of protons are

released. The lower activation energies are a consequence of different bonding, greater disorder of the system, the influence of a different electronic enclosure. At this stage, the samples acquire a very dark color probably due to the transformation of W^{6+} into W^{5+}, and the electronic conductivity is drastically enhanced. The bronze-like structure is not formed at these temperatures, but a contribution of electronic conductivity is possible.

Slade et al. [43] also reported broadly similar results with little difference; conductivity in HPW·$6H_2O$ increases until ca. 180°C at which point dehydration begins to markedly decrease the conductivity of the pellet (which nonetheless remains intact throughout the measurements). Above 250°C, the protonic conductivity of the anhydride again increases with temperature, and at $T > 550$°C the form of the impedance spectrum changed irreversibly to that corresponding to reversible electrodes and the dominant electronic conduction within the pellet. They concluded from these observations that the conduction in dehydrated pellet was via particle surfaces. The equilibration of the highly hygroscopic surface of the anhydride with the cell atmosphere was slow but led to enhanced conductivity on soaking at a fixed temperature above 200°C.

Apart from the thermal and structural analysis, the proton dynamics needs to be described to explain the proton conductivity of HPW with different number of water molecules as well as anhydrous state. Mioc et al. [45] studied the effect of increase in temperature and found that the water loss is followed by an increase in H_3O^+ ion concentration and that the oxonium ion may form dioxonium ion ($H_5O_2{}^+$) with some of remaining water molecules. At higher temperature, the proposed equilibrium is displaced to the right, and when the dehydration is complete at about 250°C, only protons stabilize the Keggin ion structure. The dynamic equilibrium can be represented as below:

$$H_5O_2^+ \leftrightarrow H_3O^+ + H_2O \leftrightarrow H^+ + 2H_2O$$

The above conclusions from IR and Raman were also supported by inelastic incoherent neutron scattering (IINS) data [46], and it was concluded that the process of dehydration of HPW-6 passes through several dehydrated forms, to be the "proton-free" phase. This process is reversible up to 500°C. The crystal structure of HPW-6 determined by Brown et al. [23] was thought to be a body-centered cubic packing of $PW_{12}O_{40}{}^{3-}$ and $H_5O_2{}^+$. They suggested that the Keggin's anions in HPW-6 were stabilized by $H_5O_2{}^+$ ions, whereas Mioc et al. [45] proved that there existed a temperature-dependent dynamic equilibrium between various proton species confirmed by IR, Raman, and IINS studies. Moreover, with the increase in temperature, $H_5O_2{}^+$ ions reorganize forming various protonic species (H_3O^+, $H_7O_3{}^+$…, OH^-, or H^+) that may influence the oxidation level of heteroatoms and cause partial reduction of W^{6+} to W^{5+} confirmed by XRD and Raman studies. The change in the ratio of the protonic entities modifies the electron density around the Keggin anions. As a result of this, a reversible phase transition occurs in HPW-6 at 47°C (T_c). The XRD results showed that the Keggin's ion particularly PO_4 tetrahedra changes (shrink by approximately 10%) near T_c, and

the crystal structure space group preserves during the phase transition; therefore, the phase transition near 47°C is nonconvergent [47, 48].

Solid-state ^{31}P, ^{1}H (MAS) NMR spectra obtained as a function of hydration level and temperature have revealed distinct proton and phosphorous sites in HPW [49–52]. Essayem [51] has shown, by ^{1}H MAS NMR and IINS spectroscopy, that various protonic species and "free protons" are present in deutereted HPW-n and CsHHPW salt, and that the relative amount is a function of temperature. Uchida et al. [52] also investigated the states and dynamic behavior of acidic protons and water molecules in the solid $H_3PW_{12}O_{40}{\cdot}nH_2O$ ($0 < n < 6$), by comprehensive application of ^{31}P, ^{1}H, and ^{17}O magic-spinning (MAS) NMR. This was the first quantitative observation of the protons in hydrated HPAs by spectroscopic methods. They described the structure of $H_3PW_{12}O_{40}{\cdot}6H_2O$ as the polyanions ($PW_{12}O_{40}^{3-}$) to be packed in a cubic structure and all acidic protons to be present in the form of $H_5O_2^+$ cations where the two H_2O molecules in $H_5O_2^+$ are bound together by unusually short hydrogen bond (O. . .O distance: 0.24 nm). They called the acidic protons in anhydrous sample ($H_3PW_{12}O_{40}{\cdot}0H_2O$) as isolated acidic protons, as these protons have no hydrogen bonded with water molecules. In a previous work [53, 54], they observed four peaks in ^{31}P MAS NMR of $Cs_xH_{3-x}PW_{12}O_{40}$ ($0 < x < 3$) which they assigned to polyanions to different number of protons (0, 1, 2, or 3). They applied the same interpretation to $H_3PW_{12}O_{40}{\cdot}nH_2O$ ($0 < n < 6$) and found four major peaks at −10.6, −11.9, 13.7, and −14.8 ppm at 173 K corresponding to 3, 2, 1, and 0 number of isolated acidic protons that directly attach to the polyanion and the last peak at −15.6 ppm is at the same position as in the hexahydrate. On the basis of assignment, they calculated the average number of isolated acidic protons per anion from the observed relative intensities of ^{31}P MAS NMR. Accordingly, of the three acidic protons in $H_3PW_{12}O_{40}$, m_{av} is the number of isolated acidic protons; the rest protons are in the form of protonated water. In this way, they could differentiate experimentally the three acidic protons in $H_3PW_{12}O_{40}$ to isolated acidic protons and protons bonded to water molecules. Moreover, they also confirmed that the isolated acidic protons are randomly distributed among the polyanions in the HPA. They also retrieved information about the states of protonated water from the value of average number isolated acidic protons per anion. They stated that all the water molecules are protonated and exist in two states H_3O^+ or $H_5O_2^+$, the ratio between the two species following a random distribution. Figure 2 is the schematic illustration of the protonic species, i.e., isolated acidic proton, H_3O^+, and $H_5O_2^+$. As for the anhydrous sample ($H_3PW_{12}O_{40}{\cdot}0H_2O$), each polyanion interacts with three isolated acidic protons. When the water content increases, the water molecules are protonated in pseudoliquid phase to form H_3O^+ and $H_5O_2^+$and accompanied by decrease in the amount of isolated acidic protons.

The location of the isolated acidic proton in dehydrated $H_3PW_{12}O_{40}$ has been controversial in the literature. Kozhevnikov et al. [55, 56] determined from ^{17}O NMR that the most likely position of the proton is bonded to the terminal oxygen atom, whereas other groups (IR [57], LCAO-MO calculations [58], density functional quantum chemical calculation [59], and SEDOR NMR) suggested that the

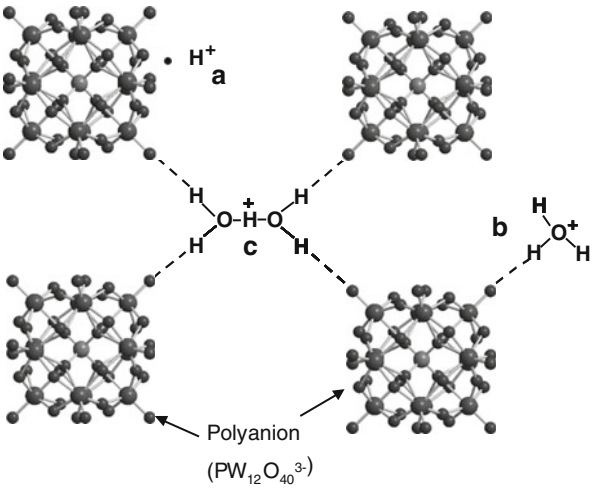

Fig. 2 Schematic illustration of the protonic species in $H_3PW_{12}O_{40}{\cdot}nH_2O$ ($0 < n < 6$); (**a**) isolated acidic proton, (**b**) H_3O^+, and (**c**) $H_5O_2^+$

isolated acidic proton is located on a bridging oxygen atom. Ganapathy et al. [60] reported the proton affinity of the bridging sites to be greater than the terminal site but concluded from DFT calculations combined with rotational echo double resonance NMR spectroscopy that the terminal position is favorable. Lopez et al. [61] used DFT calculations to show that the bridging sites are preferred for the addition of a single proton to mixed addenda Keggin and Wells-Dawson structured HPAs. Jainik et al. [62] performed quantum chemical calculations, which indicated that, in the absence of water molecules, protons are distributed among both bridging oxygen sites and the terminal oxygen sites. Prior calculations [59, 61] did not take into account the delocalization of the negative charge in the anion. Apart from these HPAs, Wu et al. [63–71] have reported the synthesis and characterization of a number of HPAs, and the proton conductivity for these HPAs has been reported in Table 1 [63–71].

It was concluded from the above discussion that the HPAs are very sensitive to environmental conditions and especially humidity and temperature. Moreover, the acid forms of HPAs are very soluble in water. Therefore, studies were extended to salts of HPAs (alkaline and alkaline earth elements) as the salts with large cations crystallize with fewer water molecules than acids and are more stable. HPAs can substitute Group I cations for some of the countercation protons which also have high proton conductivities, enhanced thermal stability, and a range of solubilities in water [72, 73]. Ukshe et al. [73] used alkaline salts and showed that their characteristics depend on the cation size. They distinguished two processes to show an influence of the cation on the protonic species. The first process is water dissociation that releases a free proton (which can cause the proton conductivity of the salt to be higher than the acid itself), and the second being the reduction of oxonium ion that generates OH groups. Another group [74–76] worked on similar salts but used alkaline earth metals. They have divided cations on the basis of their influence on

Table 1 Proton conductivity of various heteropoly acids

Heteropoly acid	Formula	Proton conductivity (S/cm)	References
Molybdotungstovanadogermanic	$H_5GeW_9Mo_2VO_{40}{\cdot}22H_2O$	2.79×10^{-4} (18°C)	[63]
Undecatungstocobaltoaluminic	$H_7[Al(H_2O)CoW_{11}O_{39}]{\cdot}14H_2O$	2.74×10^{-4} (18°C)	[64]
Molybdovanadogermanic	$H_5GeMo_{11}VO_{40}{\cdot}24H_2O$	2.03×10^{-4} (18°C)	[65]
Undecatungstochromoferrous	$H_6Fe(H_2O)CrW_{11}O_{39}{\cdot}14H_2O$	3.89×10^{-3} (20°C)	[66]
Undecatungstoferroaluminic	$H_6[Al(H_2O)FeW_{11}O_{39}]{\cdot}14H_2O$	4.07×10^{-4} (20°C)	[67]
Tungstovanadogermanic	$H_5GeW_{11}VO_{40}{\cdot}24H_2O$	3.09×10^{-3} (23°C)	[68]
Decatungstodivanaogermanic	$H_6GeW_{10}V_2O_{40}{\cdot}22H_2O$	1.20×10^{-2} (16°C)	[69]
Undecatungstochromoindic	$H_6In(H_2O)CrW_{11}O_{39}{\cdot}11H_2O$	1.15×10^{-3} (16°C)	[70]
Undecatungstocobaltoindic	$H_7[In(H_2O)CoW_{11}O_{39}]{\cdot}14H_2O$	6.64×10^{-3} (18°C)	[71]

protonic conductivity based on the cation radius which include weak and small cations with $r_i = 0.068$ to 0.1 nm (Li^+, Na^+, Be^{2+}, Mg^{2+}, and Ca^{2+}) called the A-class salts and strong large cations with $r_i = 0.133$–0.167 nm (K^+, Rb^+, Cs^+, Sr^{2+}, Ba^{2+}) called the B-class salts. A-class salts are soluble in water and tend to absorb small polar molecules because there is space available between the anions. The metal countercations and Keggin anions are more densely packed in B-class salts yielding much higher surface areas than the A-class salts, especially as the metal countercation substitution for H^+ countercations approaches 100%. A number of studies have been reported on the substitution of countercations like Cs [77–79], K [80], and Na [72, 81, 82]. In analogy to the categorizations based on water solubility, surface area, and the ability to absorb polar molecules, Dec and Herring [83] provided an additional classification scheme for highly substituted Group I salts of HPW, namely the presence of water molecules that have anisotropic or restricted rotational motion. They observed that the Li, Na, and Rb salts all have water molecules undergoing restricted rotational motion, while the K and Cs salts have highly mobile protons that are probably located in the surface sites. The ^{31}P MAS NMR and T_1 results indicate that the Li, Na, K, and Cs salts form one phase and the Rb salt two phases upon crystallization of the metal chloride from an aqueous solution of HPW.

The proton conductivity and stability of $Cs_2HPW_{12}O_{40}$ [77] above 100°C were investigated under various humidified conditions. The electrolyte showed the maximum conductivity at 100°C, but the conductivity continuously decreased with an increase in temperature, even under highly humidified conditions. In wet conditions, the samples were mechanically stable and showed the constant conductivity with no degradation for 20 h. These results suggested that the water absorbed into the electrolyte played an important role in the proton conduction mechanism. The fuel cell based on $Cs_2HPW_{12}O_{40}$ electrolyte (thickness; 1.25 mm) was fabricated, and the power generation in H_2/O_2 fuel cells using the $Cs_2HPW_{12}O_{40}$ electrolyte was first demonstrated at 120°C.

Davidovic et al. investigated magnesium and barium salts of HPW hydrate $MgHPW_{12}O_{40}{\cdot}14H_2O$ [74] and $BaHHPW{\cdot}7H_2O$ [75] in the microwave (X-band) and in lower frequency (5 Hz to 500 kHz) region. In the microwave region, dipolar relaxation was observed with the relaxation time of 1.6×10^{-11} s for the Mg salt and 1.7×10^{-11} s for the Ba salt; relaxation is attributed to the fast reorientation of H_2O molecules. Mioc et al. [84] investigated Mg and Ca salts of HPW (MgHHPW and CaHHPW, respectively) as superionic proton conductors. They identified protonic species as charge carriers in several hydration degrees of these salts by IR spectroscopy at low, room, and high temperatures. In the IR spectra, they have found the characteristic frequencies for H_3O^+, OH^-, H_2O, and $H_2O_5^+$, and the results showed that these salts had similarities with HPWs in terms of polarizability and size which gave them comparable proton conductivities. From these and more studies, Mioc et al. concluded that their characteristics also depend on other cation features such as hydration number, polarizing power, and coordination solvation number. These effects are simultaneous and it is difficult to analyze them separately. The HPAs were incorporated into gels of alumina [11], silica [12, 68] etc. to make them more resistant to dehydration which results in a better thermal stability.

The solid HPAs showed promising improvement in conductivity and fuel cell performance but dissolved in water formed by the electrochemical process of current generation [9]. This leaching of the acids led to decay in the performance of the fuel cells. To overcome the problem of electrolyte dissolution and the consequent short lifetime of the fuel cell, an approach was investigated in which the HPA was blocked inside a host material in such a way that it would maintain high proton conductivity of the original electrolyte. The immobilization of the HPA on a support could be attained by any of the three processes: physisorption, chemical attachment, and entrapment. Since weak forces are involved in physisorption, it is not an effective method to avoid the solubilization and leaching of the HPA from the support. The processes of immobilization by chemical attachment or entrapment are more effective as they form covalent or ionic bonds with the host material and very stable materials can be prepared.

We [85] have synthesized lacunary HPAs $[SiW_{11}O_{39}]^{8-}$ (SiW11) and $[SiW_{10}O_{36}]^{8-}$ (SiW10) and covalently bonded them to silica support using sol–gel chemistry. The lacunary HPA, SiW11 or SiW10, is suspended in a 1:1 H_2O/EtOH mixture, to which an appropriate amount of tetraethylorthosilicate (TEOS) at different molar ratios of TEOS to HPA. The reaction was catalyzed by adding excess HCl and a glassy solid obtained after solvent evaporation was ground into fine powder, and then further dried in air. IR spectroscopy, NMR, and XRD measurements confirm the formation of covalent bonds between the HPA and silica. The thermal analysis of the silica-supported HPA (SiW10/SiW11-SiO_2) shows that the thermal stability of the composite increases due to immobilization. The loss of crystal water for the supported SiW11-SiO_2 above 200°C is much less as compared to the SiW11-free acid which shows that the water retention increases on immobilizing the free acid on the silica support. Since the HPAs are covalently bonded to the silica and not entrapped in the silica matrix, the proton conduction is much higher and easier. The diffusion coefficients of the SiW10-SiO_2 hybrid under

100% relative humidity are an order of magnitude higher than the HPW-SiO_2 under similar conditions; maximum being 3.3×10^{-5} cm^2/s at 100°C and 100% RH.

3 Liquid HPA Fuel Cell

The solid HPAs as fuel cell electrolytes showed room temperature fuel cell performance similar to that of PEMFCs, but were unstable and would dissolve in the water formed during cell operation [9]. An alternative method of using HPAs as fuel cell electrolytes was explored by forming a concentrated (60 wt.%) solution of these [10]. Giordano et al. used phosphotungstic acid ($H_3PW_{12}O_{40}{\cdot}nH_2O$) as the liquid electrolyte. The fuel cell design was characterized by a continuous feed of electrolyte to the matrix sandwiched between two wet-proofed gas diffusion electrodes. The cell produced an output power density of about 700 mW/cm^2 at 1.5 A/cm^2. The observed fuel cell performance was due to the low resistance and promoting effect of the electrolyte to the oxygen reduction reaction ORR. In their previous work, they [86] had shown that the ORR on Pt was strongly promoted in concentrated phosphotungstic acid (60%) with respect to the other fuel cell liquid electrolytes like phosphoric acid. The aqueous form of the HPA electrolyte showed comparable proton conductivity, chemical stability to a PEMFC overcoming the physical instability of the solid HPA electrolyte, but at lower current densities HPAFC (aqueous HPAFCs) performance is below that of PEMFC due to voltage losses resulting from chemical crossover phenomena [87]. They realized that the utilization of a traditional cell with the electrolyte flow parallel to the electrodes was not suitable for this type of concentrated and viscous electrolyte, which hindered its own flow inside the porous matrix creating a high concentration difference between the inside and outside of the fuel cell. They made computational fluid dynamic studies of mass and heat transfer in the HPW electrolyte-based fuel cell to elucidate the cause of irregular failure at high current densities, which manifested through partial melting of the matrix and electrodes and crossover effect. It was established to be due to the bad construction of the reactant gas and liquid electrolyte distributors on the cathode and anode side of the HPWFC and lack of cooling system [88].

4 Heteropoly Acid Proton Exchange Membranes

4.1 HPA-Doped Membranes

Hybrid materials for use in fuel cell PEMs can be defined in terms of composition, structure, and properties. Hybrid organic–inorganic membranes are composites with the organic component and the inorganic component strongly interacting

with one another to form a homogeneous tightly bound mixture while at the same time acting independently to make unique contributions to the overall properties of the synthesized membrane [5]. On the compositional level, a hybrid membrane contains two materials, one inorganic and the other organic in nature. On the structural level, these materials are intimately and homogeneously mixed at the molecular or nanoscale level and strongly interacting through ionic or covalent bonding. The properties contributed by each component, either independent of one another or in conjunction, include:

(a) Super acidity for proton conduction
(b) Mechanical, thermal, and chemical stability
(c) Ability to fabricate into a thin, yet, robust membrane

Strong interactions can occur in several ways to form hybrid membranes.

- Hybrid membranes produced from strongly interacting super acid inorganic components and superacid polymer ionomers (PFSA polymer imbibed HPA)
- Polymer acid complexes (PAC) containing strong ionic interactions between a basic polymer ionomer and an inorganic acid (hydrocarbon imbibed HPA)
- Hybrid copolymer membranes with a homogeneously dispersed super acid component covalently bound to the organic polymer matrix (PolyPoms)

4.1.1 HPA Imbibed PFSA Membranes

PFSA polymer membranes such as Nafion® are commercially used in current PEMFC, and these membranes are composed of carbon–fluorine backbone chains with perfluoro side chains, containing sulfonic acid groups [1, 13]. The proton conductivity of the PFSA-based PEM increases essentially linearly with water content of the membrane, the highest conductivity corresponding to a fully hydrated membrane (due to the presence of hydrophilic sulfonic acid groups). In a fuel cell operating at a temperature above the boiling point of water, the membranes lose conductivity due to drying. Drying also results in membrane shrinkage and consequent poor contact and proton conduction between the membrane and the electrodes [89]. Comprehensive reviews of PFSA materials and structures are available [1, 2].

Four means of achieving PEMs that conduct under hotter and drier conditions have been proposed [14, 90]: (a) development of membranes made of new ionomers exhibiting the desired characteristics; (b) development of new membranes in which suitable oxygenated acids (e.g., phosphoric or sulfuric acids) are solubilized in a polymeric matrix bearing basic groups (e.g., polybenzimidazole); (c) improvement of the characteristics of known ionomeric membranes by dispersing inside their polymeric matrix acids with low solubility (e.g., HPAs) or particles of insoluble solids such as metal oxides, lamellar zirconium phosphates, or phosphonates; (d) development of membranes obtained by filling a nonproton conductive polymeric matrix with ionomers or inorganic particles of high proton conductivity. In this section, we discuss the third approach by impregnating HPAs in PFSAs to

alleviate the aforementioned problems. The role of the supported acid is to provide high concentrations of protons in the membrane pores by undergoing proton-transfer reactions, in much the same way as water does in the conventional membrane, but without its volatility problems.

Malhotra and Datta [89] impregnated Nafion® membranes with HPAs by imbibing them in solutions of a HPA, HPW in acetic acid or tetra-*n*-butylammonium chloride. Preliminary results showed a dramatic improvement in fuel cell output at elevated temperatures, e.g., at 110°C, the fuel cell provides a power density of 465 mW/cm^2 at 0.5 V which is comparable to the typical performance obtained with conventional PEM fuel cells at 80°C. Membranes have been cast from HPA impregnated Nafion® using long annealing times, 4 h, at 130–170°C to cross-link and immobilize the HPAs in the membrane [91].

Tazi and Savadogo [92] fabricated HSiW-doped recast Nafion® (volume of a commercial 5% Nafion® solution reduced by 50%) membranes with or without thiophene, named NASTATH and NASTA, respectively. To the HSiW-doped membranes (NASTA), liquid thiophene was added as plasticizer to produce the NASTATH membrane. The water uptake of the NASTA membrane (60%) was significantly better than that of Nafion® 117 (27%), while the water uptake of NASTATH (40%) was higher than that of Nafion® 117 (27%). The ionic conductivity of both the NASTA (1×10^{-1} S/cm) and the NASTATH (9.5×10^{-2} S/cm) was reported to be significantly higher than that of the Nafion® 117 (1.23×10^{-2} S/cm) at room temperature. Apart from silicotungstic acid, Nafion® solution was doped with other HPAs like HPW and HPMo called NaHPW and NaHPMo, respectively [93]. The ionic conductivity of these membranes increased in the order: Nafion® 117 (1.3×10^{-2} S/cm) < NaHPMo (1.5×10^{-2} S/cm) < NaHPW (2.5×10^{-2} S/cm) < NaHSiW (9.5×10^{-2} S/cm). Thus, HSiW insertion in Nafion® membranes increases the number of active sites in the membrane, as well as the number of water molecules by the addition of sulphonic groups, which results in the improvement of proton transport through the membrane and the electrochemical properties of the membrane. At 100°C and 100% RH, all the HPA-impregnated membranes show improved conductivity compared to the control with the greatest improvement being observed for HSiW as shown in Table 2.

Ramani et al. [94] prepared three types of organic/inorganic composite membranes with different HPA additives such as phosphotungstic acid, silicotungstic acid, phosphomolybdic acid, and silicomolybdic acid.

(a) Type I membranes prepared by casting additive (25 wt.%) doped 5% Nafion® 1100 solution and then heat treating 80°C for 1 h, and then at 120°C for 2 h.
(b) Type II membranes prepared by first ion exchanging the protons in the Nafion® with Na^+ followed by incorporation of the additive (25 wt.%) and the high boiling solvents.
(c) Type III membranes synthesized in a similar manner as type I membranes having additional equal volumes of high boiling solvents such as dimethyl formamide (DMF) one to five times of the Nafion® and the heat treatment included two additional hours at 145°C to maximize solvent (DMF) removal.

Table 2 Conductivity data for heteropoly acid/ionomer composite membranes, [ ] – control membrane data

Membrane polymer	Heteropoly acid	Loading	σ (S/cm) 80°C x% RH	σ (S/cm) 100°C x% RH	σ (S/cm) 120°C x% RH	References
Nafion® 1100 EW	$H_4SiW_{12}O_{40}$ $H_3PW_{12}O_{40}$ $H_3PMo_{12}O_{40}$			2.3×10^{-2} 1.5×10^{-2} 1.3×10^{-2} $[1.2 \times 10^{-2}]$ $x = 100$		[93]
Nafion® 1100 EW	$H_4SiW_{12}O_{40}$ $H_3PW_{12}O_{40}$ $H_3SiMo_{12}O_{40}$ 1–3 μm	25 wt.%	8.5×10^{-2} 6×10^{-2} 8×10^{-2} $[6 \times 10^{-2}]$ $x = 75$	4.5×10^{-2} 4×10^{-2} 3×10^{-2} $[4 \times 10^{-2}]$ $x = 70$	1.0×10^{-2} 1.5×10^{-2} 1.0×10^{-2} $[1.0 \times 10^{-2}]$ $x = 35$	[94]
Nafion® 1100 EW	$H_3PW_{12}O_{40}$ 30–40 nm	25 wt.%	1×10^{-1} $[6 \times 10^{-2}]$ $x = 75$	4.5×10^{-2} $[4.0 \times 10^{-2}]$ $x = 70$	$[1.5 \times 10^{-2}]$ $[1.0 \times 10^{-2}]$ $x = 35$	[94]
Nafion® 1100 EW	$H_3PMo_{12}O_{40}$	3.3 wt.% 6.7 wt.% 9.2 wt.%	2×10^{-1} 3×10^{-1} 3.5×10^{-1} $[1.2 \times 10^{-1}]$ $x = 100$			[95]
Recast Nafion® 115	$H_3PW_{12}O_{40}$/silica (TEOS) 120 μm			2.67×10^{-2} $x = 70\%$ (110 C) $[8.13 \times 10^{-3}]$		[96]
Nafion® 1100 EW	$H_3PW_{12}O_{40}$ 30 μm	10 wt.%		5×10^{-2} $[4.0 \times 10^{-2}]$ $x = 100\%$ 1.5×10^{-2} $[1 \times 10^{-3}]$ $x = 40$		[97]
Nafion® 115	$H_3PW_{12}O_{40}$/silica (TEOS)	10 wt.%		2.5×10^{-3} $[1.5 \times 10^{-3}]$ $x = 10$		[98]
3 M ionomer	$H_3PW_{12}O_{40}$ $H_4SiW_{12}O_{40}$	1 wt.%		83.7 75.6 [38.5] $x = 80\%$		[16]

Since the particle size of the HPA additive (1–10 μm) in the type I composite membranes was much larger than the cluster size, little improvement in conductivity was seen over pure Nafion® at low humidities. The conductivity of the composite membranes at 120°C and 35% relative humidity were of the order of 1.5×10^{-1} S/cm (see Table 2). Additives containing molybdenum were less stable in the membrane environment than those containing tungsten. Molybdates migrated into the catalyst layers, where they had a detrimental effect on performance by undergoing parasitic redox reactions on the surfaces of carbon and platinum, resulting in increased activation overpotential. Two major factors limiting the performance of Nafion®/HPA composite membranes were realized: (1) the high solubility of the HPA additive and (2) the large particle size of the inorganic additive within the membrane matrix. These two issues were addressed by Ramani et al. in synthesizing membranes using two different approaches, i.e., the synthesis of type II [99] and type III membranes [17, 100].

Type II membranes [99] stabilized the HPW additives within the Nafion® matrix to prevent additive loss due to leaching even after stringent treatment in aqueous environments for extended time periods at elevated temperatures. Ion exchanging the exchangeable protons of the HPA with large cations such as cesium, ammonium, rubidium, and thallium transforms the additives from a low surface area water soluble acid to a high surface area water insoluble acid salt. This could be due to the hydration enthalpy being less exothermic with increasing cation size (lowering of charge density) even as the lattice enthalpy remains nearly constant, given the large heteropoly anion size. Therefore, the enthalpy of solution, which is the difference between the hydration and lattice enthalpies, also becomes less exothermic, therefore lowering the solubility. The thermal stability of the composite membranes was improved by casting in the Na^+ form, using a high boiling solvent, which permitted a more stringent heat treatment process on the membrane electrode assembly (MEA). The membranes were robust and showed low crossover currents, and no internal shorting. The conductivities of Nafion®/HPW and Nafion®/modified HPW composite membranes with different number of protons substituted at 120°C and 35% relative humidity were very similar and had a value of about 1.6×10^{-2} S/cm as compared to the conductivity of a pure Nafion® membrane which was found to be 1.7×10^{-2} S/cm (see Table 2). The similarity in conductivities of the composite membranes to commercial Nafion® is attributed to the large particle size of the additive (which constitutes 25% by weight of the membrane), which results in blockage of channels.

Improving additive dispersion would facilitate improved conductivities by aiding proton hopping, and therefore, membranes with reduced additive particle size (type III) were evaluated [17, 100]. The additive particle size was reduced by nearly two orders of magnitude from 1 to 2 μm to 30 nm by appropriately modifying the casting procedure. The reduction of additive particle size results in an enhancement of the surface to volume ratio of the additive, which in turn permits more efficient proton hopping and hence larger proton conductivities by up to 35% in the composite membrane. The reduction in particle size attained using the adapted procedure was attributed to the minimization of the amount of high boiling solvent

present during the annealing step, which in turn minimized agglomeration of the additive [101]. The thermal analysis of these membranes yielded a higher decomposition onset point as compared to membranes synthesized previously [94] with large HPW particles.

Both the approaches were combined together to evaluate the performance of these HPA-loaded membranes with small particles [17] and MEA stabilization techniques to yield a stabilized MEA for operation at 120°C and 35% relative humidity (RH). MEAs were prepared using Nafion®/phosphotungstic acid composite membranes with phosphotungstic acid (HPW) particle size of 30–50 nm and the HPW additive stabilized by substituting its protons with cesium counter ions. The Nafion® in the membrane and electrodes were simultaneously converted to the Cs^+ form by an ion-exchange process. The melt processability of the Nafion® in the Cs^+ form permitted the MEA to be heat treated at 200°C and 30 atm, promoting the development of a durable membrane/electrode interface. The prior stabilization of the HPW permitted MEA reprotonation with minimal additive loss which was confirmed by FTIR, TGA, and in situ electrochemical impedance spectroscopy (EIS).

3 M ionomer membranes, PFSA polymer of 1,000 equivalent weight with pendant side chain $–O(CF_2)_4SO_3H$, were doped with the HPAs, HPW, and HSiW, having a strong interaction between themselves [16]. Under conditions of minimum hydration, the proton conductivity of the 5 wt.% HPW membrane had much higher proton diffusion coefficient as compared to the 1 wt.% doped sample. The maximum diffusion coefficient for 5 wt.% membrane HPW was around 100 and at 70°C for the 1 wt.% doped sample. Under dry conditions, the increase in HPA content decreased the E_a for the self-diffusion of water from 27 to 15 kJ/mol, while the reverse trend was seen below 100% RH conditions which proved that the HPA assists in proton diffusion in dry conditions. Moreover, the diffusion coefficient of the 5 wt.% doped membrane does not drop at temperatures higher than 130°C as opposed to the control membrane. Significantly, the E_a was 1/2 that of the undoped material at RHs of 40 and 60%. A practical proton conductivity of 0.113 S/cm was observed at 100°C and 80% RH. HPAs incorporated into cast membranes of 1,000 equivalent weight 3 M perfluorosulfonated ionomer by Haugen et al. [102] showed that using HPAs that do not rearrange or degrade in peroxide as dopants in perfluorinated ionomer membranes dramatically reduce the fluoride release rate and increase proton conductivity under slightly hotter and dried conditions (90°C and 70% RH). These improvements are expected to improve fuel cell performance and increase membrane lifetimes over nondoped perfluorosulfonated ionomer membranes.

Direct methanol fuel cells (DMFCs) face two major problems of methanol crossover and low proton conductivity. In order to overcome these problems, modified Nafion® membranes containing HPAs have been casted by sonicating the inorganic additives namely silicon dioxide particles and molybdophosphoric acid in commercially available Nafion® solution in high boiling point solvent (dimethylsulfoxide or 1-methyl-2-pyrrolidone) [95]. Additives were effectively immobilized in the cast membranes, which did not leach out on boiling in sulfuric

acid, by exposing them to solvent vapor at room temperature for 24 h and annealing at 150°C. The conductivity of the HPMo-impregnated membranes enhanced by a factor of three in comparison to the commercial Nafion® and pure recast Nafion®. The increase in conductivity of the composite membranes could not be explained on the basis of structural information as the crystallinity of the films was higher for lower loadings, 3 and 6 wt.% than for 9 wt.%. The ratio of the methanol permeation rate and the conductivity of the composite membrane was thus lower compared to Nafion® 117 and pure recast Nafion®, and the activation energy E_a for proton transport was approximately twice that of the recast Nafion® control. The conductivity data has been presented in Table 2 for comparison.

HPMo has high proton conductivity at room temperature and a high solubility in water and alcohols, but is insoluble in nonpolar solvents. Therefore, Sauk et al. [103] synthesized hybrid Nafion®/polyphenyleneoxide (PPO) membranes with HPMo, where HPMo is imbedded in polymer films using mixed solvents to immobilize it effectively and overcome this leakage problem from membrane. Since PPO and HPMo are insoluble in each other, HPMo is dissolved in methanol (HPMo–MC) and PPO is dissolved in chloroform (PPO–C). HPMo–MC was then dissolved well in PPO–C to form PPO–HPMo–MC which was cast on a glass plate. The composite Nafion® membranes were made by pouring Nafion® solution on these porous films. The membranes with a HPMo loading of 0.5 gave a comparable conductivity of 3.41×10^{-2} S/cm to that of Nafion® 115 membrane (3.85×10^{-2} S/cm) at room temperature. The permeability of methanol in the Nafion® 115 membrane was higher, with a value of 3.29×10^{-6} cm^2/s than those of composite membranes which varied from 2.01×10^{-6} (0.5 g HPMo) to 4.41×10^{-7} cm^2/s (1 g HPMo).

Recast Nafion®–silica composite membranes doped with HPW and HSiW for application in DMFCs at high temperature (145°C) have been synthesized by Staiti et al. [104]. The HPW-based membrane showed better electrochemical characteristics at high current densities with respect to both HSiW-modified membrane and silica–Nafion® membrane. A maximum power density of 400 mW/cm^2 was obtained at 145°C in the presence of oxygen feed, whereas the maximum power density in the presence of air feed was approaching 250 mW/cm^2. The results indicate that the addition of inorganic hygroscopic materials to recast Nafion® extends the operating range of a DMFC, which significantly enhances the kinetics of methanol oxidation. FTIR studies carried on these as well as basic and neutral alumina- and zirconia-impregnated Nafion® membranes [105] revealed that the surface acidity of the fillers influenced the bending and stretching vibrational frequencies of the water physically adsorbed on the filler surface. The conductivity of composite membranes and maximum power density of DMFCs at 145°C was related to the characteristics of the water adsorbed on the filler particles. Inorganic fillers characterized by acidic properties undergo a strong interaction with water and enhance the DMFC performance at high temperature. Various recast Nafion® composite membranes containing ceramic oxide fillers with different surface characteristics (SiO_2, SiO_2–HPW, Al_2O_3, ZrO_2) were also investigated for application in high-temperature DMFCs [106]. The cell resistance at 145°C increased as

a function of the pH of slurry of the inorganic filler indicating a strong influence of the acid–base characteristics on the electrolyte conductivity. This effect was attributed to the different water retention capabilities of the various membranes. Fuel cell performance at 145°C, expressed as both maximum power density and current density at 0.5 V cell potential, increases almost linearly as the pH of slurry of the oxide materials decreases.

Nafion®/silica/HPW membranes were fabricated by in situ sol–gel reaction in pretreated, initially hydrated, and alcohol-containing Nafion®117 [97]. X-ray diffraction (XRD) indicated that the crystallinity of Nafion® decreased with the increase in silica content and consequently methanol diffusion coefficients (D) decreased with the increase in silica content, at low silica content. The lowest methanol diffusion coefficient is 2.8×10^{-7} cm^2/s, while methanol diffusion coefficient for the commercial Nafion® without treatment is 5.2×10^{-7} cm^2/s possibly the incorporated silica particles tend to hold up methanol. The proton conductivities (σ) of these composite membranes are higher than those of commercial Nafion® 117, and the optimal silica content in composite membrane based on σ/D values is 38.2 μg/g. The data from single DMFC using these two membranes of commercial Nafion® without treatment and Nafion®/silica/HPW composite membranes with optimal silica content as polymer–electrolyte reveal that the cell with composite membrane has higher open circuit voltage (OCV = 0.75 V) and maximal power density ($P_{max} = 70$ mW/cm^2) than those of commercial Nafion® without treatment (OCV = 0.68 V, $P_{max} = 62$ mW/cm^2) at 80°C. Organic/inorganic hybrid Nafion®/silica/HPW membranes with well-dispersed HPW/silica particles generated by in situ microemulsion process in Nafion® 115 were fabricated [107]. A 50–80% reduction in methanol crossover was observed as compared to the Nafion® 115 membranes. The ionic conductivity of the membranes was increased with temperature and values higher than the Nafion® 115 (10^{-1} S/cm) at 50°C and 100% RH were obtained. In the various efforts to effectively immobilize the HPAs in the Nafion® matrix, Kim et al. [108] immobilized HPW on MCM-41 using two methods, namely impregnation and direct synthesis. In the case of impregnation method, XRD and SEM indicated that most of the HPA impregnated existed on the external surface, blocking the pores making it vulnerable to washing out, whereas direct synthesis method immobilized the HPW/MCM-41 more effectively making it very hard to wash out. The composite membranes fabricated with washed HPW-MCM-41 obtained by direct synthesis had better proton conductivity and proton selectivity, but higher methanol permeability as compared to the Nafion® 115 membrane.

Apart from DMFCs, Nafion®/silicon oxide (SiO_2)/phosphotungstic acid (HPW) and Nafion®/silicon oxide composite membranes were also used for the H_2/O_2 PEMFCs to be operated above 100°C [96]. The composite membranes were recast from Nafion® solution mixed with SiO_2 and HPW/SiO_2 mixtures, and the incorporation of the SiO_2 and HPW into the Nafion® membrane increased the crystallinity and improved the initial degradation temperature of the Nafion® membrane. The proton conductivity of the composite membranes appeared to be similar to that of the native Nafion® membrane at high temperatures at 100% relative humidity (RH);

however, it was much higher at low RH due to higher water uptake. When composite membranes, such as Nafion®/SiO_2/HPW and Nafion®/SiO_2, were used as an electrolyte in H_2/O_2 PEMFC, higher current density values (540 and 320 mA/cm^2 at 0.4 V, respectively) were obtained over Nafion® 115 membrane (95 mA/cm^2), under the operating condition of 110°C and at the humidified temperature of 100°C.

Self-humidifying composite membranes obtained by dispersing $Cs_{2.5}H_{0.5}PWO_{40}$/SiO_2 particles in Nafion® NRE 212 [109] were more steady as compared to HPW impregnated membranes, because the H^+ is substituted with Cs^+ which makes it insoluble in water and better immobilized on silica, reducing its leaching. These membranes exhibited improved fuel cell performance over Nafion® NRE-212 under both dry and wet conditions. On similar lines of work, $Cs_xH_{3-x}PWO_{40}$/CeO_2 nanoparticles, synthesized by solution-based hydrothermal method, were impregnated in Nafion® membrane to mitigate the free radical attack on the membranes in the fuel cell environment [110]. The resistance of $Cs_xH_{3-x}PWO_{40}$/CeO_2 membrane was much lower than CeO_2/Nafion® membrane (CeO_2 being nonconductive); thus the membrane conductivity was greatly improved by dispersing $Cs_xH_{3-x}PWO_{40}/CeO_2$ nanoparticles into the membrane. The durability of the composite membranes was evaluated via Fenton's test and OCV accelerated test which showed that $Cs_xH_{3-x}PWO_{40}$ particles can decompose H_2O_2 around the membrane bulk, and as a metal oxide with variable valence, CeO_2 can quench the free radicals effectively. In the durability tests, the fluoride emission rate (FER) reduced nearly one order of magnitude by adding $Cs_xH_{3-x}PWO_{40}/CeO_2$ nanoparticles into the Nafion® membrane.

PFSA membranes, made from the 3 M PFSA ionomer (825 EW), doped with silica immobilized lacunary HSiW, having particle size in the range of 35–50 nm, have been developed [111]. The HPA has been covalently bonded to the silica support by sol–gel method to effectively immobilize it in the membrane. Strong bonding between lacunary HSiW/silica and the ionomer matrix was confirmed by IR, XRD, and NMR data. Small angle X-ray scattering (SAXS) measurements show that the particles down to 3–4 nm in size were also present, and the sizes of the particles increased with increase in percent loading the HPA. The proton conductivity of the lacunary HSiW immobilized membranes increased with increase in percent loading of HSiW. Significant increase in the proton conductivity, nearly 1.7 times that of the control membrane, is obtained at 30% RH and 120°C for the 5 and 10 wt.% HSiW loading of membranes; the maximum proton conductivity obtained is nearly 3.0×10^{-2} S/cm at 120°C and 30% RH exhibiting high proton conductivity at high temperature and low relative humidity. Conductivity data have been presented in Table 2 for comparison.

4.1.2 HPA Imbibed Hydrocarbon Membranes

The disadvantages of PFSA membranes have stimulated many efforts to synthesize PEM based on fluorine-free hydrocarbon ionomer membranes as alternatives to

Nafion®. Moreover, the high cost of the perfluorinated polymers limits large-scale commercialization of the PEMFCs. PVA shows excellent insulation performance as a polymer material, and in a pure dry state its conductivity ranges between 10^{-10} and 10^{-14} S/cm [112], but in the hydrated form its proton conductivity can only reach 3.65×10^{-5} S/cm. Therefore, in these macromolecule materials, the doping impurity ions act as the primary proton carrier and the PVA-doped membrane becomes a conducting film. PVA membranes doped with HPAs such as 12-tungstogermanic acid ($H_4GeW_{12}O_{40}{\cdot}14H_2O$) [18], decatungstomolybdovanadogermanic acid $H_5GeW_{10}MoVO_{40}{\cdot}21H_2O$ ($GeW_{10}MoV$) [113], and HPW [114, 115] as proton conductors were cast by adding the HPAs in varying concentration to the aqueous solution of PVA. Spectroscopic studies confirmed the presence of the Keggin ion structure in the polymer matrix and also the existence of strong hydrogen bonds between the HPA, PVA, and water. Due to the large volume of the Keggin anion and the hydrogen bonds, it cannot move but its protons transfer along these hydrogen bonds. Thus, the addition of HPAs provides more protons and facilitates their transport due to the aggregation of Keggin anions which can form proton channels. The maximum room temperature proton conductivity obtained for 12-tungstogermanic, 10-tungstomolybdovanadogermanic, and HPW acid-doped PVA membranes was found to be 2.11×10^{-2} S/cm (80 wt.% loading), 1.22×10^{-2} S/cm (80 wt.% loading), and 6.27×10^{-3} S/cm (50 wt.% loading) as shown in Table 3, respectively. The proton conductivity of the composite HPW immobilized membranes increased with the increase in content of the HPA and along with that the methanol permeability also increased. This phenomenon was explained by percolation theory, which states that the terminal oxygen of the polyanion not only can link together the hydrated hydrogen ions but also can connect to a small polar molecule such as methanol. When HPAs are embedded with a higher weight fraction of PVA component, the PVA phase is a continuous network morphology and HPA phase dispersed through the PVA matrix phase, forming an "island" phase. Hence, the composite membranes had the lower proton conductivity and good methanol barrier capacity. On the contrary, with an increase in the HPW content, the probability of linking together the hydrated hydrogen ions and methanol would also increase, so that the conductivity and the methanol permeability would increase at the same time.

However, these HPA-doped PVA membranes swell too strongly to be used, and so Xu et al. [115] fabricated complex membranes of PVA doped with HPW supported on silica prepared by sol–gel procedure. The addition of silica into the PVA/HPW membrane improved its endurance and thermal stability. In the HPW-doped PVA complex membranes, where the weight ratio between PVA and HPW is 1.0, the proton conductivity decreased with an increase in silica content which was explained in accordance to the swelling behavior of the membranes at different SiO_2 content. At low SiO_2 content, the water in membrane was sufficient to dissociate HPW molecules, while, at higher silicate content, less water in the membrane was dramatically insufficient to dissolve HPW and produce free protons, which caused a decrease in the proton conductivity. The highest proton conductivity of 1.7×10^{-2} S/cm was obtained at the HPW content of 57 wt.%.

Table 3 Conductivity data for heteropoly acid/imbibed hydrocarbon composite membranes, [ ] – control membrane data

Membrane polymer	Heteropoly acid	Loading	σ (S/cm) 20°C x% RH	σ (S/cm) 80°C x% RH	σ (S/cm) 100°C x% RH	σ (S/cm) 120°C x% RH	References
SPEEK-70	$H_3PW_{12}O_{40}$	60 wt.%		1.2×10^{-2}	1.7×10^{-2}	2×10^{-2}	[116]
	$Na_2HPW_{12}O_{40}$			1.1×10^{-2}	1.3×10^{-2}	1.4×10^{-2}	
	$H_3PMo_{12}O_{40}$			9×10^{-3}	1.1×10^{-2}	1.0×10^{-2}	
				[3×10^{-3}]	[7×10^{-3}]	[5×10^{-3}]	
				$x = 80$	$x = 75$	$x = 55$	
SPEEK-80	$H_3PW_{12}O_{40}$	60 wt.%		6.5×10^{-2}	9.5×10^{-2}	1.1×10^{-1}	[116]
	$Na_2HPW_{12}O_{40}$			4.5×10^{-2}	6×10^{-2}	4×10^{-2}	
	$H_3PMo_{12}O_{40}$			1.5×10^{-3}	3×10^{-2}	1.0×10^{-2}	
				[4.5×10^{-2}]	[8×10^{-2}]	[2.8×10^{-2}]	
				$x = 80$	$x = 75$	$x = 55$	
SPEEK-65	γ-$[SiW_{10}O_{36}]^{8-}$	38 wt.%		2.2×10^{-2}			[117]
				[2.4×10^{-2}]			
				$x = 100$			
SPAENK-40	$H_3PW_{12}O_{40}$	20 wt.%		7×10^{-2}	8×10^{-2}	5×10^{-3}	[118]
		40 wt.%		1.1×10^{-1}	1.2×10^{-1}	4×10^{-2}	
		60 wt.%		1.5×10^{-1}	1.5×10^{-1}	7×10^{-2}	
				[4×10^{-2}]	[5×10^{-2}]	[$<4 \times 10^{-3}$]	
				$x = 100$	$x = 100$	$x = 100$	
SPSF	$H_3PW_{12}O_{40}$	60 wt.%		1.25×10^{-1}	1.3×10^{-1}	1.4×10^{-1}	[119]
PVA	$H_4GeW_{12}O_{40}$	80 wt.%	2.11×10^{-2}				[18]
PVA	$H_5GeW_{10}MoVO_{40}{\cdot}21H_2O$	80 wt.%	1.22×10^{-2}				[113]
PVA	$H_3PW_{12}O_{40}{\cdot}29H_2O$	50 wt.%	6.27×10^{-3}				[114]
PVA	$H_3PW_{12}O_{40}{\cdot}29H_2O$	57 wt.%	1.7×10^{-2}				[115]
PVA	Silica/$H_3PW_{12}O_{40}{\cdot}29H_2O$			4.13×10^{-3}	8.31×10^{-3}		[120]
				$x = 100\%$	$x = 100\%$		
PVA	$H_3PW_{12}O_{40}$	90 wt.%	5.176×10^{-4}				[121]

(*continued*)

Table 3 (continued)

Membrane polymer	Heteropoly acid	Loading	σ (S/cm) 20°C x% RH	σ (S/cm) 80°C x% RH	σ (S/cm) 100°C x% RH	σ (S/cm) 120°C x% RH	References
s-PEK	$ZrO2/H_3PW_{12}O_{40}$	s-PEK/ZrO2/TPA	[5.4×10^{-2}]				[122]
		100/0/0	8.2×10^{-2}				
		90/0/10	1.12×10^{-1}				
		40/0/60	1.1×10^{-1}				
		83/6/11	8.6×10^{-2}				
		64/8/28	3.0×10^{-4}				
		51/17/32	$x = 100$				
s-PEK	S66	62/38			2.4×10^{-2}		
	$S66/H_4$ [γ-Si(2)]	59/5/36			2.2×10^{-2}		
	$S66/RSiO_3a/H_4$ [γ-Si(2)]	54/8/38			6×10^{-3}		
	$S66/Aerosil-/H_4$ [γ-Si(2)]	62/38			2.0×10^{-2}		
	$S66/H_4$ [γ-Si(4)]	59/5/36			2.1×10^{-2}		
	$S66/RSiO_{3/2}/H_4$ [γ-Si(4)]	54/8/38			7×10^{-3}		
	$S66/Aerosil/H_4$ [γ-Si(4)]				1.2×10^{-2}		

Where H_4 [γ-Si(2)] is H_4 [γ-$SiW_{10}O_{36}$,(R-$SiO)_2O$], H_4[γ-Si(4)] is H_4[γ-$SiW_{10}O_{36}$(R-$SiO)_4$], and S66 is SPEEK with 66% sulfonation degree with R = 3-glycidoxypropyltrimethoxysilane

For $RSiO_{3/2}$, R = 3-aminopropyltrimethoxysilane

Aerosil is fumed silica Aerosil A380 containing amino groups on the surface

The lowest methanol crossover ($D = 0.35 \times 10^{-8}$ cm^2/s) was observed for the SiO_2 content of 33 wt.%. The optimal PVA/HPW/SiO_2 ratio in complex membrane obtained from the σ/D curves was obtained to be 0.40:0.40:0.20 wt. Similar membranes with silicotungstic acid immobilized on silica (using sol–gel method) were synthesized [120], where the silicotungstic acid perfectly preserved its Keggin structure after incorporation in PVA interacting with the polymer hydroxyl groups. The composite was stable at high temperature and stable conductivity values, $4.13–8.31 \times 10^{-3}$ S/cm, were obtained in the range of 80–100°C at 100% RH. The proton migration was dominant through Grotthuss mechanism, where the protons form hydrogen bond with water molecules and exists as H_3O^+ hopping from one active component to other through tunneling mechanism. Moreover, a low activation energy of 10 kJ/mol was obtained which is in the range of Grotthuss mechanism.

Lin et al. [121] prepared a series of hybrid membranes by incorporation of phosphotungstic acid into PVA polymer matrix using a modified solution-blending method. In order to obtain optimal values of water uptake and proton conductivity, a critical doping concentration of the HPA was defined where a sudden drop in water uptake was observed, in this case it was 40 wt.% loading of HPW. The proton conductivity of PVA/HPW hybrid membranes was in the order of 10^{-4} S/cm and increased with HPW content except for samples near the critical doping level. As in the case of water uptake, methanol permeability decreased beyond 20 wt.% HPW doping and a minimum permeability of 3.98×10^{-10} cm^2/s was obtained with PVA (10%)/HPW(90%) membrane. Similar trend in water uptake and methanol permeability, and the progressive shift in frequency of (W–O_c–W) band suggested the existence of intermolecular hydrogen bonding interaction between hydroxyl side chain of PVA and HPW which is responsible for continuous drop in water uptake and methanol permeability near and beyond the critical doping level. The selectivity of PVA20HPW80 hybrid membrane for DMFC use is even better than that of Nafion®115 at ambient temperature mainly due to lower methanol permeability of hybrid membranes which is particularly attractive for DMFC applications.

Composite membranes of PVA matrix doped with zirconium phosphate (10 wt.%) and phosphotungstic acid (10–30 wt.%) in water were fabricated [123] for which the highest proton conductivity of 1×10^{-2} S/cm at 60% RH and 333 K was obtained for 30 wt.% loading membrane with a low E_a of 3 kJ/mol. Anis et al. [124] synthesized cross-linked composite membranes consisting of poly(vinyl alcohol-*co*-vinyl acetate-*co*-itaconic acid) (PVACO) and polyphomolybdic acid (30 wt.%) using glutaraldehyde as the cross-linking agent. This loading of the HPA gives lower proton conductivity (2.03×10^{-3} S/cm) as compared to Nafion® 117 (6.2×10^{-2} S/cm) but a much lower methanol permeability of 1.54×10^{-6} cm^2/s than Nafion® 117 (6.5×10^{-6} cm^2/s).

Although the use of Nafion® membranes doped with phosphotungstic and silicotungstic acids has been considered for DMFC, the effective application of HPA/polymer hybrid membranes for DMFC face additional problems. The main inconvenience is the high methanol and water crossover. Furthermore, in many

cases, HPAs are partially soluble and washed out from the membrane during operation. In order to decrease the bleeding out of HPA from the composite membrane, two approaches have been adopted: the in situ generation of an oxide network by the sol/gel process from alkoxysilanes and the modification of the anion structure of the HPAs.

Composites membranes of sulfonated polyetherketone (s-PEK, 40–50% degree of sulfonation) with HPAs [HPW, HPMo, $H_5PNiMo_{11}O_{39}$ (aq) (NiMoPA) and $H_3(RSi)_2OPMo_{11}O_{39}$(aq) (SiMoPA)] immobilized on silica or zirconia support were synthesized by sol–gel method. *N*-(3-triethoxysilylpropyl)-4,5-dihydroimidazole and zirconium tetrapropylate in solution with dimethylformamide (DMF), *N*-methylpyrrolidone (NMP), or dimethylsulfoxide (DMSO) were used as precursors for the inorganic networks $RSiO_{3/2}$ (R = 3-2-imidazolin-1-yl) and ZrO_2, respectively, with addition of small amounts of water to promote the controlled hydrolysis of the inorganic precursor [122]. Membranes prepared just with HPW as the only inorganic component had a high proton conductivity along with water and methanol fluxes across the membranes. The permeability decreased considerably, when zirconium oxide was added in a range between 17 and 32 wt.% and an optimum balance was achieved with 8 wt.% ZrO_2 and 28 wt.% HPW such that the water and methanol fluxes were 1/6 and 1/10, respectively, of that of the unmodified membrane with similar thickness. The membranes on immersion in water for 24 h resulted in leaching of the HPAs reaching to nearly 100% in the case of phosphomolybdic acid. Hybrid membranes with s-PEK and ZrO_2-HPW had the highest conductivity values (0.110–0.086 S/cm). In order to decrease the bleeding out and to fix the HPMo in the polymeric matrix, two different strategies were followed: the synthesis of the HPA with a chemically modified anion structure (lacunary HPAs), and the use of silane as precursor for the oxide network, instead of zirconium propylate.

Lacunary HPAs, such as the organosilyl derivatives of the divacant tungstosilicate $[\gamma\text{-}SiW_{10}O_{36}]^{8-}$, having a modified anionic structure, are unsaturated Keggin ($SiW_{12}O_{40}{}^{4-}$) fragments, can form organic–inorganic materials due to nucleophilic surface oxygen atoms at the vacant site, which allow the covalent grafting of electrophilic groups. The introduction of 3-glycidoxypropyltrimethoxysilane (GPTMS) in the anion structure of lacunary HPA enables its attachment to a host material, by an epoxy ring opening reaction with appropriate functional groups present in the surface of the host material, without involving the protons and therefore without affecting the acidity of the HPA [125]. In each case, the organic functionality is linked to the polyanion surface by E–O–W bridges (E: Si (IV), P (V), Sn (IV), Ge (IV), or Ti (IV)), resulting in the saturation of the heteropoly anion surface. The inorganic phase in the polymer solution of sulfonated polyether ether ketone (SPEEK) with a sulfonation degree of 65–66% (EC: 1.66 meq/g) in *N*-methylpyrrolidone (NMP) (1) in situ generated by the sol–gel process from 3-aminopropyltrimethoxysilane (APTMS), or (2) obtained by dispersion of an amino-modified fumed silica. Membranes with an oxide phase, in situ generated by the sol–gel process or in the form of fumed-silica, had much lower proton conductivities than those of the plain membranes but were partially regained

with the incorporation of HPAs. For both inorganic-modified membranes, the methanol and water permeability was much lower than that of membranes prepared just with the lacunary species without any additional inorganic phase. This problem is effectively minimized by covalently binding the synthesized lacunary HPAs to the insoluble inorganic phase. Similar results were obtained with fumed silica and with in situ-generated silica, the bleeding out being slightly higher with the fumed silica.

Partially sulfonated poly(ether ether ketone) (SPEEK-70, 74, and 80% DS, degree of sulfonation) 150–300 μm thick, with homogeneously distributed 60 wt.% of the HPAs (phosphotungstic acid (HPW), its sodium salt (Na-HPW), and molybdophosphoric acid (HPMo)) in the size range of 0.05–0.15 μm have been fabricated by Zaidi et al. [116]. Incorporation of HPAs increased the membrane conductivity compared to the pure membrane, except in the case of the 80% sulfonated PEEK for which only the HPW/SPEEK membrane showed enhanced conductivity at temperatures higher than 80°C (Table 3). In all cases, the introduction of the HPAs improved the high temperature stability of the membranes. HPW, being a stronger acid, systematically yields a higher proton conductivity increase as well as a better water retention at high temperature, and showed a higher conductivity than Na-HPW and HPMo composites. Comparing these results with similar studies for sulfonated polysulfone membranes containing solid HPW, where the conductivity of 1.6×10^{-3} S/cm was registered, the proton conductivity displayed by HPA-SPEEK membranes proved to be much higher as can be seen in Table 3. These membranes even being fluorine-free polymeric materials have conductivities of the same order of magnitude. For all composite membranes, the activation energy for proton conduction was similar and close to 15 kJ/mol, which suggests a common charge transfer mechanism. The relatively low measured values of activation energy are suggestive of a liquid-like mechanism most probably based on the Grotthuss reorientational proton transfer scheme. The results showed that the composite membranes containing solid HPA are stable for the long term, with no change in their conductivity. They possessed good mechanical strength and flexibility except for those based on 80% sulfonated SPEEK that become weak because of excessive swelling. The best mechanical properties were found for the 70% DS SPEEK-based composites.

Ismail et al. [126] recently synthesized a composite polyether ether ketone (SPEEK with varying degree of sulfonation) containing HSiW (30–70 wt.%) loaded on silica–aluminum oxide (SiO_2–Al_2O_3, 25–75 wt.%) powders. NMR studies revealed that sulfonation modifies the chemical properties of PEEK, which reduces the crystallinity and affects the solubility of the polymer. At DS lower than 30%, SPEEK is soluble only in conc. H_2SO_4; above 30% DS SPEEK dissolves in hot dimethylformamide (DMF), DMAc (dimethylacetamide), and DMSO (dimethylsulfoxide) and above 70% they are soluble in methanol and at 100% DS in hot water. Thus, composite membranes were cast from 56 and 66% sulfonated PEEK. The SPEEK membranes with high DS, highest HSiW content, and highest SiO_2 content in SiO_2–Al_2O_3 composite show highest water uptake and a high proton conductivity 6.1×10^{-2} S/cm which is an order of magnitude higher

compared to Nafion® 112 (1.6×10^{-2} S/cm). However, with the increase in DS and silica content, the methanol permeability of the membranes also increases. Membrane DS66/70HSiW/25SiO_2/75Al_2O_3 possessed the highest overall factor (proton conductivity/methanol permeability) that is 58.9×10^3, while Nafion® possessed the lowest overall factor which is 1.065×10^4.

Bello et al. [127] embedded different proportions (10–30 wt.%) of inorganic conducting material (HPW/MCM-41) into SPEEK polymer matrix by solution casting method. The highest proton conductivity of value 2.75×10^{-2} S/cm was obtained for the composite membrane S70T2-M41 (70 wt.% SPEEK and 30 wt.% (50 wt.% HPW + 50 wt.% MCM-41)), which is four times higher than that of the control pure SPEEK membrane. The composite membranes showed nearly an eightfold decrease in methanol permeability for the membrane S90T1-M41 (90 wt.% SPEEK and 10 wt.% (60 wt.% HPW + 40 wt.% MCM-41)). Moreover, embedding HPW in MCM-41 prevented leaching of the HPA and also increased the thermal stability of the composite. Sulfonated poly(ether ether ketone)–silica–phosphotungstic acid membranes have been developed by Colicchio et al. [128] by mixing solutions of SPEEK, HPW, and polyethoxysiloxane (a liquid hyperbranched inorganic polymer used as the silica precursor instead of tetraethylorthosilicate) in two different ways, one in which the HPW was added in the beginning itself and the other in which it was added just before casting. However, the mixing procedure did not have any significant effect on the morphology of the membrane, but the former method favors the incorporation and anchoring of HPW to silica and hence reduces the chances of leaching from the membrane. The silica particles were generated in situ in two size ranges, 3–12 nm and 50–130 nm, and on their incorporation the proton conductivity of the SPEEK membranes at 100°C and 90% RH increased by two times. Among the three loading % of HPW that were tested, i.e., 5, 30, and 50 wt.% of the introduced PEOS, 5 wt.% leads to an increase in the proton conductivity by nearly three times than the pure SPEEK as the phosphotungstic acid catalyzes the hydrolysis of the ethoxy end-groups of PEOS and once incorporated enhances the proton conductivity.

Ion exchange membranes of polyether ether ketone (PEEK)/HPW and sulfonated block copolymer of polysulfone and poly(phenylene sulfide sulfone) (SPSf-*co*-PPSS)/HPW were synthesized [129]. The membranes prepared with SPEEK and SOSf-*co*-PPSS hydrolyzed above 80°C but those made after the addition of HPW did not hydrolyze exhibiting improved electrochemical, mechanical, and oxidative stability. The (SPSf-*co*-PPSS)/HPW membrane with 4.3% HPW showed the best properties; proton conductivity (6.2×10^{-2} S/cm, at 80°C), water content (23.9%), ion-exchange capacity (1.97 meq/g dry memb.), tensile strength (12.2 MPa), and elongation (147%).

Polymeric proton electrolytes based on the composite of silicotungstic (12-HSiW) and polyethylene oxide (PEO) form a new compound 12-HSiW-PEO, as the ether oxygens of the PEO get associated with H_3O^+ cations originated from 12-HSiW and show a substantial increase in proton conductivity [130]. The decrease in the crystallinity of the films at high relative humidities is conducive to the transfer of the hydroxoniums in the composite polymer films, and hence to the

enhancement of proton conductivity. The highest conductivity at room temperature has been found to be 6.3×10^{-2} S/cm for the composite with an $[H^+]/[EO]$ mole ratio of 0.025.

Polysulfone (PSF) and its sulfonated polymer, SPSF, were solution-blended with phosphotungstic to form composite HPW/(PSF), HPW/(SPSF) membranes. The IR spectrum of the composite showed band shifts with a possibility of intermolecular hydrogen bonding interaction between the HPA additive and the sulfonated polymer [119]. The composite membranes exhibited improved mechanical strength and low water uptake. The conductivity of the composite membrane, HPA–40/SPSF, consisting of 40 wt.% HPA and 60 wt.% SPSF [with a degree of sulfonation (DS) of 40%] 8.9×10^{-2} S/cm, at room temperature, linearly increased up to 1.4×10^{-1} S/cm at 120°C (see Table 3), whereas the widely used commercial membrane Nafion® 117 exhibited a room temperature conductivity of 10^{-1} S/cm that increased to only 1.2×10^{-1} S/cm at 120°C. In contrast, the composite of HPA–40/PSF exhibited a proton conductivity of 2.0×10^{-2} S/cm at room temperature that increased only to 7.0×10^{-2} S/cm at a temperature of 100°C. The incorporation of HPA into SPSF not only rendered the membranes suitable for elevated temperature operation of PEMFC but also provides an inexpensive alternative compared to Nafion®.

Kim et al. [117] fabricated composite membranes by solution casting the acid form of the sulfonated poly(arylene ether sulfone) copolymers (BPSH) and phosphotungstic acid in DMAc, where the weight ratio of HPA to BPSH copolymer was controlled from 0 to 60%. The composite membranes containing less than 40% of the disulfonation were tough, transparent, and had good retention of the HPA after exposure to water vapor, whereas HPA/Nafion® was opaque and easy extraction of HPA after immersion in liquid water is possible. Incorporation of HPA into the sulfonated copolymer significantly reduced the water-swelling behavior, without influencing the proton conductivity at room temperature. For fully hydrated membranes consisting of 30 wt.% HPA and 70 wt.% BPSH with 40 mol % disulfonation, the conductivity of 8.0×10^{-2} S/cm at room temperature linearly increased up to 1.5×10^{-1} S/cm at 130°C, whereas for the pure copolymer the proton conductivity of 7.0×10^{-2} S/cm at room temperature only reached a maximum conductivity of 9.0×10^{-2} S/cm, most probably due to dehydration at elevated temperatures (Table 3). The dehydration process of the composite membrane when compared with pure sulfonated copolymer showed that for the pure copolymer, dissociated and weakly hydrogen bonded water molecules were lost at temperatures less than 140°C, whereas the hydrogen bonding of the bridging water molecules between the tungstic oxide and sulfonic acid was stronger, increasing the dehydration process to the range of 100–220°C. This result suggests the attractive conductivity performance of the composite membrane at elevated (e.g., 130°C) temperatures with less than fully humidified conditions. These results indicate that the HPA/BPSH copolymers have promise as a composite PEM for elevated temperature (>100°C) operation in a fuel cell.

A series of sulfonated poly(arylene ether nitrile ketone) membranes, thermally stable up to 300°C, have been made by aromatic nucleophilic polycondensation of

6F-BPA with 2, 6-difluorobenzonitrile and sodium 5, 5′-carbonylbis(2-fluorobenzene-sulfonate) at various molar ratios [118]. The proton conductivity and water uptake of these membranes increased with the degree of sulfonation (SPAENK-50 and SPAENK-60 proton conductivity comparable to Nafion® 117), but their practical use has been limited due to increased swelling at higher temperature. SPAENK 40 (with limited swelling) membranes uniformly doped with HPA particles were tough and transparent and had a degradation temperature above 200°C, satisfying the requirement for use in PEMFC. The proton conductivities of the composite membranes were higher than that of SPAENK-40 and comparable with Nafion® 117 (Table 3). The composite membranes showed lower conductivity decrease with temperature than pure SPAENK and Nafion® 117 at temperatures above 100°C. It is expected that the aromatic nitrile groups might afford hydrogen-bonding sites for HPA particles; however, the FT-IR band shift only showed the interaction between HPA particles and sulfonic acid, and no further interaction between HPA and nitrile groups was found. The extraction of HPA particles from polymer matrix was a fatal problem for the practical use of HPA/sulfonated polymer composite membranes. Malers et al. synthesized [7] thin pellets as well as composite membranes of 1:1 (w/w) of HPA (HPW, $H_3P_2W_{18}O_{62}$, $H_6P_2W_{21}O_{71}$, and $H_6As_2W_{21}O_{69}$) and polyvinylidenedifluoride–hexafluoropropylene (PVDF–HFP). The high proton conductivities reported for HPAs at RT are demonstrated in fuel cells using HPA/PVDF–HFP composites with limiting current densities as high as 1.6 A/cm^2 using dry O_2 and H_2. Moderate fuel cell activity is demonstrated for $H_3P_2W_{18}O_{62}$ at 120°C and 25% RH. Unfortunately, all of the materials studied were somewhat porous and the open circuit potentials observed were low.

Polybenzimidazoles constitute a promising group of materials both for their low cost and high working temperature. It has been another potential membrane matrix explored in the literature for doping HPAs owing to its high thermal and chemical stability. PBI is a completely amorphous material with a reported glass transition temperature (T_g) of 420°C [131] and has been used in fuel cell [132] and sensor applications [133]. It has also been functionalized with acid groups using phosphoric acid and used as PEMs [134, 135]. However, preliminary conductivity tests of directly doped HPAs into PBI membranes led to very low proton conductivities of the order of 10^{-6} S/cm, which was explained in terms of low interaction between the HPW and polymer that does not allow the acid to remain fixed in the membrane [136].

PBI, synthesized from 3,3-diaminobenzidine tetrahydrochloride and isophthalic acid by polymerization in polyphosphoric acid (PPA) at 170–200°C, was doped with 30 wt.% HPW and HSiW to get high proton-conducting membranes (as thin as 10–50 μm) with very good homogeneity and mechanical strength [137]. At 200°C, the PBI composite membrane containing 30 wt.% HPW exhibits a conductivity of 5.8×10^{-2} S/cm, slightly lower than that of pure PBI membranes. The conductivity of the PBI composite membrane containing 30 wt.% HSiW is even lower. The activation energies were found to be 9.5 and 7.5 kJ/mol for the acid-doped membranes containing 30 wt.% HPW and 30 wt.% HSiW in PBI, respectively. At low temperature, the existence of water absorbed by the membrane led to an easy proton

transfer and the conductivity was found to be higher than that of the PBI membranes, but at high temperatures, the composite membranes seem more demanding for the humidity and a lower conductivity was observed than that for the PBI membranes. The conductivity data of the composite membranes have been presented in Table 4 for comparison.

PBI-based other derivatives such as poly(2,5-benzimidazole) (ABPBI) are equally promising as matrices for proton-conducting membranes as these are able to work at temperatures up to 200°C without humidification, and allow the use of H_2 with up to 3% of CO impurities with only a small power loss. Hybrid ABPBI–HPMo membranes were fabricated by dissolving desired amount of HPMo (up to 60 wt.%) in methanol sulfonic acid solution of poly(2,5-benzimidazole) (ABPBI), a product of condensation polymerization of 3,4-diaminobenzoic acid (DABA) monomers in polyphosphoric acid (PPA). Spectroscopic studies confirmed that even after immersing the ABPBI–HPMo membranes in H_3PO_4 acid 85%/H_2O 70:30 (in volume) for 3 days, HPMo still preserved its structure. ABPBI–HPMo hybrid membranes, with inorganic HPAs trapped within the organic polymer network, cast and impregnated with phosphoric acid, present high thermal stability [143] and proton conductivity as the benzimidazole membranes. The proton conductivities of ABPBI–HPMo membranes have reached values of 3.0×10^{-2} S/cm at 185°C. Thus, the HPMo anionic clusters are additives that increase the phosphoric acid uptake which is important not only to increase the conductivity, but also to avoid the leaching of the acid when the membranes operate as fuel cell electrolyte in PEMFC for long times [144].

Membranes were cast by incorporating, silica-supported phosphotungstic acid, prepared by sol–gel method and obtained in powdered form, to PBI mixed in *N*,*N*-dimethylacetamide at 150°C [138]. Thermally stable membranes up to 400°C were obtained, whose specific conductivity increased with relative humidity. At 100°C and 100% relative humidity, a specific conductivity of 3×10^{-3} S/cm was measured which was almost stable at temperatures up to 150°C (1.42×10^{-3} S/cm) due to the presence of silica as shown in Table. Similar mechanically stable PBI doped with silica immobilized HSiW membranes (80–100 μm) were cast containing 50% inorganic component having a maximum value of proton conductivity of 1.2×10^{-3} S/cm at 160°C [139] which is still low. The same membrane, after the phosphoric acid treatment, gives proton conductivity of 2.23×10^{-3} S/cm under the same test conditions, which were about five orders of magnitude higher than that of the membrane prepared with 50% of pure silicotungstic acid in polybenzimidazole (10^{-8} S/cm). The commonly observed poor proton conductivity of the PBI membranes doped with HPW or HSiW was due to the difficulty of the water to enter the hydrophobic PBI membrane. This was also shown by simple wettability tests that the membrane composed of pure HSiW and PBI was hydrophobic, while the membranes composed of HSiW, SiO_2, and PBI behaved as hydrophilic materials. The presence of silica in the composite membrane creates hydrophilic domains and helps the HPA to retain as much water as possible [138]. Thus, the silica improved the conductivity characteristics of the membranes probably increasing water absorption and creating an easier path for proton motion [139].

Table 4 Proton conductivity for inorganic acids and PBI composite membranes, [ ] – control membrane data

Membrane polymer	Heteropoly acid	Loading	σ (S/cm) 20°C x% RH	σ (S/cm) 80°C x% RH	σ (S/cm) 100°C x% RH	σ (S/cm) 120°C x% RH	References
PBI	H_3PO_4/$H_3PW_{12}O_{40}$	4.4/30	1.5×10^{-2}	3×10^{-2}	5.5×10^{-2}		[137]
	$H_4SiW_{12}O_{40}$	30	1.0×10^{-2}	3×10^{-2}	4.5×10^{-2}		
			[5×10^{-3}]	[4×10^{-2}]	[7×10^{-2}]		
			$x = 20$	$x = 10$	$x = 5$		
PBI	$H_3PW_{12}O_{40}$/Silica (TEOS)	40	1.0×10^{-3}	3.0×10^{-5}	3.0×10^{-3}		[138]
					$x = 100$		
		50	2.0×10^{-3}	3.0×10^{-5}			
		60	2.5×10^{-3}	6×10^{-4}			
		68	6×10^{-4}	1×10^{-5}			
			$x = 100$	$x = 100$			
PBI	45 wt.% $H_4SiW_{12}O_{40}$/Silica (TEOS)	30	2×10^{-4}	4×10^{-4}			[139, 140]
		50	4×10^{-4}	8×10^{-4}			
		70	1.5×10^{-3}	3×10^{-3}			
			$x = 100$	$x = 100$			
ABPBI	$H_3PW_{12}O_{40}$	45		1.4×10^{-2}			[141]
				8×10^{-3}			
				$x = 0$			
SEpoxy	$H_3PW_{12}O_{40}$		2.0×10^{-5}			4.0×10^{-5}	[142]
			[3.0×10^{-4}]			[0]	
			$x = 0$			$x = 0$	

Doping of PBI with HPAs has been attempted as reviewed above, but the conductivity of these materials was not high enough to be used in PEM fuel cells.

4.2 Sol–Gel-Based HPA Membranes

The solid HPAs showed promising improvement in conductivity and fuel cell performance but dissolved in water formed by the electrochemical process of current generation [9]. This leaching of the acids led to a decay in the performance of the fuel cells. To overcome the problem of electrolyte dissolution and the consequent short lifetime of the fuel cell, an approach was investigated in which the HPA was blocked inside a host material in such a way that it would maintain high proton conductivity of the original electrolyte. The immobilization of the HPA on a support could be attained by any of the three processes: physisorption, chemical attachment, and entrapment. Since weak forces are involved in physisorption because the HPA is just physically adsorbed on the support material, it is not an effective method to avoid the solubilization and leaching of the HPA from the support. The processes of immobilization by chemical attachment or entrapment are more effective as they form covalent or ionic bonds with the host material and very stable materials can be prepared.

Staiti et al. [12] synthesized silica-immobilized HPW and HSiW powders (containing 10% of crystallization water in their structure) by the sol–gel process using the acid-catalyzed condensation of TEOS (tetraethylorthosilicate). Since, it is difficult to operate fuel cells with powders silica-supported HPAs, these were immobilized in PBI membranes as discussed in the previous section. Sol–gel processing provides a versatile synthetic route to change hydrophobic/hydrophilic interfaces and synthesize organic/inorganic hybrid materials as realistic ion-conducting membranes for fuel cells. The structure of the hybrid has been designed to possess fast proton conduction through mostly manipulating organic ligand to inorganic surfaces. The polymerization of bridged trialkoxysilanes proceeds by a series of hydrolytic and condensation reactions by addition of HPAs such as HPW, which apart from being proton carrier also catalyze these reactions. The bridged polysilsesquioxanes have been synthesized by the three most commonly used approaches: (1) metallization of aryl, alkyl, or alkynyl precursors, followed by reaction with a tetrafunctional silane; (2) hydrosilyation of dienes (or polyenes) or less commonly dines; and (3) reaction of a bifunctional organic group with an organotrialkoxysilane bearing a reactive functional group (see Fig. 3).

Economic organic/inorganic high-temperature proton-conducting membranes consisting of SiO_2/PEO (polyethylene oxide) hybrids have been made through nano-sized interfusion among organics, inorganics, and acidic molecules by sol–gel processes. In various studies [19, 145–149], organic/inorganic proton-conducting nanohybrid membranes have been synthesized through sol–gel processing from organically modified alkoxysilane precursors, where methylene chain length $[(CH_2)_nO-]_m$ in the organic bridge have been systematically changed from $n = 2$

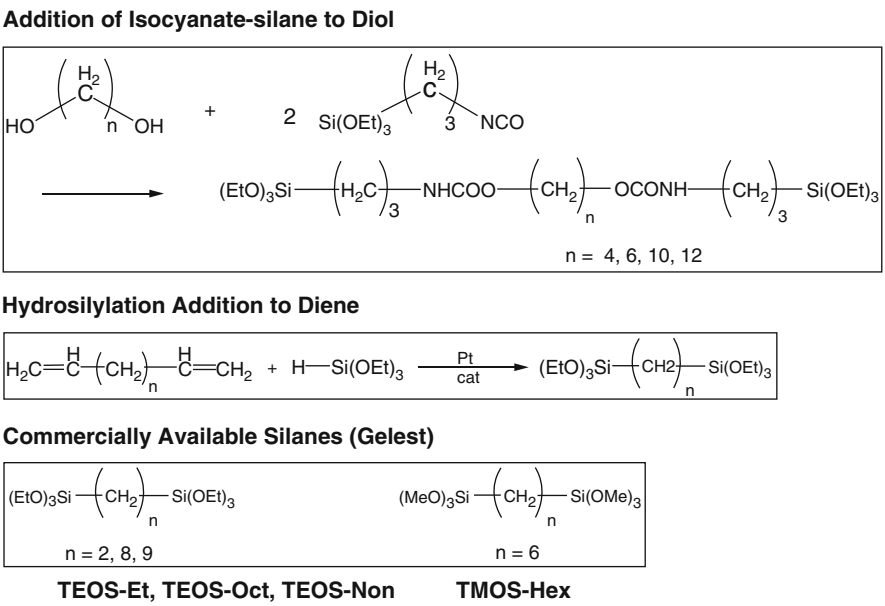

Fig. 3 Synthesis processes of bridged alkylenes polysilsesquioxanes from various kind of hydrocarbon monomers and reactive silicate species

(PEO) to $n = 4$ (PMTO) [145, 146]. When the organics and inorganics are hydrolyzed at nanoscale, the material properties of the composites become quite different from that expected from the linear combination of individual bulk properties. These membranes combine the flexibility of the organic polymer and stability of inorganic silicates to obtain beneficial properties, while doping the acidic molecules to provide proton-conducting pathways for the hybrid membrane. The general procedure of membrane casting was that the organoalkoxysilane of monophenyltriethoxysilane (MPH), used to increase the chemical as well as thermal stability and hydrophobicity of the membrane, was added to the solution of monododecylphosphate (MDP) or HPW (proton carrier) in THF along with alkoxysilane-endcapped PEO (prepared by mixing PEO of different molecular weights 200, 300, 400, 600, and 2,000 with alkoxysilane precursor of 3-isocyanatopropyltriethoxysilane at 70°C in N_2 atmosphere to form the urethane coupling between the two molecules which was completed after 5 days of aging). The reaction was catalyzed by HCl where the MPH also hydrolyzed and condensed simultaneously with hydrolyzing endcapped precursor to modify organic/inorganic hybrid precursors [145].

The thermal stability of polymer PEO phase in the composite was highly enhanced by the nanolevel confinement in the inorganic SiO_2 framework causing the decomposition of hybrid membrane to occur at a higher temperature of 350°C as it shifts the chemical as well as thermal stability of the polymer in the vicinity of the inorganic heterointerfaces. The proton conductivity of the hybrid membrane was

very small at low humidifier temperatures and increased with temperature and reached maximum conductivity of ~1 × 10^{-3} S/cm at higher than 80°C. The conductivity increased with the increase in MDP-doping concentration from 10 to 40% due to the increase in hydrated proton carrier concentration in the matrix, which indicates the mobile protonic carriers originate from MDP. The sample of 20% SiO_2/80% PEO membrane doped with 20% MDP was found to possess protonic conductivity of the order of 10^{-4} S/cm at a temperature range up to 160°C, indicating that the hybrid membrane can be a good protonic conductor at higher temperatures. The proton conductivity data of two loadings (10 and 40%) of HPW membranes was identical during the whole temperature scan from 60 to 150°C, while the conductivities gradually decrease with elevating temperature due to the loss of water. The conductivity of HPW-doped membrane was higher than the MDP-doped membranes in the whole temperature scan from 50 to 160°C [145, 146].

In order to control thermal stability and protonic conductivity of the hybrid electrolyte membranes, the molecular weight of PEO, PPO, and PTMO was systematically changed, and in particular, the starting materials like glycole polymers of PEG600 (molecular weight of 600), PPG700, PTMG250, PTMG650, and PTMG2000 were used [147]. Another modification was the addition of propylene carbonate (PC) with HPW (doping amount of each of PC and HPW varied from 0 to 100% by weight), which would dissolve protons from HPW clusters and play a role in hydrolyzing and condensing silicate precursors. The membranes cast were subjected to two steps of annealing, the first-step annealing temperature being 60°C for 12 h, at which all the hybrid membranes were formed successfully in a wide composition range of HPW (25–100% by wt.) and PC (0–100%). However, at elevated temperatures of annealing at 140°C, high concentration of HPW (>50%) and PC led to extremely high concentration of protons which attacked the polyether part of PEO $(-CH_2CH_2O-)_n$ and decomposed the PEO- and PPO-based hybrid membranes. On the contrary, membranes made from PTMO250 precursors were extremely temperature (even after annealing at 140°C) and acid tolerant in entire the HPW and PC composition range, due to an enhanced molecular stability of PTMO in the nanosized composite framework of silica. The proton conductivity of the membranes annealed at 60°C was higher than those annealed at 140°C probably, as the membrane annealed at 60°C involves more water molecules incorporated in the network, and have better proton dissociation from the HPW surfaces and mobility in the water nanophase sustained in a hybrid network through the Grotthuss mechanism. Since PC has a large molecular dielectric constant and can dissociate protons in a similar way to the water molecules in acidic solutions, it increased concentration of protonic carriers and had a positive effect on the proton conductivity of the hybrid membranes. Nafion® has almost identical protonic conductivity over a wide temperature range from ambient to 100°C with activation enthalpy of approximately 0.15 eV, when it is fully humidified. The hybrid membrane was more stable than Nafion® at elevated temperatures higher than 100°C [147]. Proton conductivities of 10^{-4}–10^{-3}S/cm at 160°C have been achieved at 100% RH as shown in Table 5.

Table 5 Conductivity data for sol–gel-based heteropoly acid composite membranes, [ ] – control membrane data

Membrane polymer	Heteropoly acid	Loading	σ (S/cm) 80°C x% RH	σ (S/cm) 100°C x% RH	σ (S/cm) 120°C x% RH	References
Hybrid PEO	$H_3PW_{12}O_{40}$/silica	10 wt.%	4×10^{-3} $x = 100$	3×10^{-3} $x = 100$	1×10^{-3} $x = 100$	[145, 146]
Hybrid PTMO/25% PC	$H_3PW_{12}O_{40}$/silica	50 wt.%	1×10^{-4} $x = 100$	2×10^{-4} $x = 100$	3×10^{-4} $x = 100$	[147]
Hybrid PTMO (1000)/PEO(600)	$H_3PW_{12}O_{40}$/silica	25 wt.%	8×10^{-3} $x = 100$	8×10^{-3} $x = 100$	7×10^{-3} $x = 100$	[148, 150]
Hybrid octamethylene glycol	$H_3PW_{12}O_{40}$/zirconia	40 wt.%	3×10^{-4} $x = 100$	8×10^{-4} $x = 100$	1×10^{-3} $x = 100$	[151]
Hybrid PEG (400)	$H_3PW_{12}O_{40}$/silica	30 wt.%	1×10^{-2} $x = 100$			[152]
Polydimethylsilane	$H_3PW_{12}O_{40}$/silica	40 wt.%	1×10^{-2} $x = 100$	1.5×10^{-2} $x = 100$	1×10^{-1} $x = 100$	[153]
Styrene/2-hydroxymethacrylate	$H_3PW_{12}O_{40}$/silica	15 wt.%	1.0 $x = 100$ 6×10^{-2} $x = 60$ 3×10^{-3} $x = 40$	1.0 $x = 100$	1.1 $x = 100$	[98]
GPTMS-H_3PO_4-APTES	$H_3PW_{12}O_{40}$ $H_3PMo_{12}O_{40}$	6 wt.% 3 wt.%			3×10^{-2} $x = 90\%$	[154]
GPTMS-H3PO4-APTES	$H_3PW_{12}O_{40}$ $H_3PMo_{12}O_{40}$	10 wt.% 10 wt.%	0.6×10^{-2} 0.4×10^{-2} (90°C) $x = 50\%$			[155]

The hybrid membranes made from endcapped PTMO of various molecular weights (250, 650, 1,000, and 2,000) mixed with HPW were condensed either by humid ca. at 60°C or dried conditions [148] to investigate the effect of synthesis conditions on the proton conductivity of the membranes. The membrane synthesized in the humidified condition did not change in size after the condensation of silicate species as the hybrid materials contain water inside a macromolecular network but the one synthesized in a dried condition shrunk after the condensation. The hybrid membrane synthesized with humidified condition had a larger conductivity at around 10^{-3} S/cm in a temperature range from 80 to 140°C (due to the retention of water while formation), while the membrane synthesized with a dry condition has smaller proton conductivity at around 10^{-5}–10^{-4} S/cm level in the same temperature range. The hybrid membrane was completely homogeneous at nanoscale with no discernible microstructure and could be understood as complete "nanohybrid" materials with no segregation of the HPW crystals.

Since the water content increases linearly with the polyether molecular weight of the hybrid and PTMO releases water molecules at much higher temperatures and has better water retention properties at higher temperatures than PEO, hybrid membranes with binary blends of PTMO1000 and PEO 200, 400, 600 polymers (with the identical PTMO/PEO weight ratio at 3/7) doped with HPW (25 wt.%) were cast [148, 150]. The nature of the binary blend polymer can be controlled by nanophase separation between hydrophobic PTMO (releases water at high temperatures) and hydrophilic PEO polymer, which are cross-linked by terminal inorganic silicate phases [150]. The binary hybrid membrane of PTMO1000/PEO600 had proton conductivity close to 10^{-2} S/cm in the temperature range from 80 to 120°C, while the conductivity level is dependent on the PEO polymer chain length (200–600). The conductivity is larger for higher PEO mixing ratio (PTMO/PEO = 1:9) at around 10^{-2} S/cm, which might be comparable to that of Nafion® membrane. The proton conductivity of the blend hybrid (10^{-2} S/cm) was higher than the conductivity of the membrane with just PTMO weight of 650, 1,000, 2,000 with a constant HPW/PTMO weight ratio ~40 wt.% HPW (10^{-3} S/cm). However, the conductivity is even smaller in the membrane with PTMO 250 at around 10^{-5}–10^{-4} S/cm level as shown in Table 5.

Bridged polysilsesquioxanes with various alkylenes based on ethane, hexane, octane, decane, etc. (methylene chain lengths of $(CH_2)_n$: n = 2–14) as precursors were hydrolyzed and condensed to form hybrid transparent, homogeneous, flexible gel membranes 100–300 μm thick, through a catalytic reaction by HPW (3–30 mole %). Protonic conductivities of the bridged alkylene hybrid membranes with various methylene chain $(CH_2)_n$: n = 2–14 measured at 60°C, 95% RH showed that among these hybrid membranes, octane (C8) hybrid as well as hexane hybrid (C6) were highly conductive having conductivity in excess of 10^{-2} S/cm but the other hybrids (C2, C10, C14) were not as conductive. Proton conductivity (at 60°C and 95% RH) of the octane hybrid with different HPW concentrations had a maximum value at 10 mol % HPW-doping concentration and decreased in excess of 10 mol % HPW. Similar tendency of the conductivity shift has been observed for hexane and decane hybrids, which suggests that the conductive channel structures are strongly affected

by the presence of HPW at the organic/inorganic interfaces. The heavy doping of HPW into the macromolecules might alter the amphiphilic polysilsesquioxane network involving the water phase interface, resulting in the less conductive channels.

The bridged polysilsesquioxane macromolecules processed from various organic bridging groups such as PEO, PTMO, Hex [$(CH_2)_6$], Oct [$(CH_2)_8$], and DEB are basically temperature-tolerant polymers, and their performance in terms of morphology, thermal properties, and proton conductivity has been compared. Organic/inorganic hybrid membrane synthesized from the bridged PTMO (650) hybrids shows that the hybrid polyether (PTMO) membrane has a random mixture structure approximately 3 nm in size, suggesting a homogeneous dispersion of HPW clusters which were isolated and did not form a bicontinuous network. However, the Oct hybrid membrane shows remarkable nanophase separation between the organic part at approximately 30 nm scale, and the inorganic phase forms bicontinuous pathways for ionic conduction because HPW clusters are self-assembled to form interconnected structures as shown in Fig. 4. The monomers are cross-linked by the silicate species; during the synthesis of the macromolecules, the organic bridging groups interconnect with the inorganic species at a molecular level. The HPW clusters are presumably supported on the silicate species by strong Coulombic interactions or structural trapping by silica skeletons. The organic/inorganic hybrid macromolecules possess many heterogeneous interfaces on a nanoscale due to the amphiphilic phase separation between the organic and inorganic domains, and the HPW clusters form conductive pathways. Because the

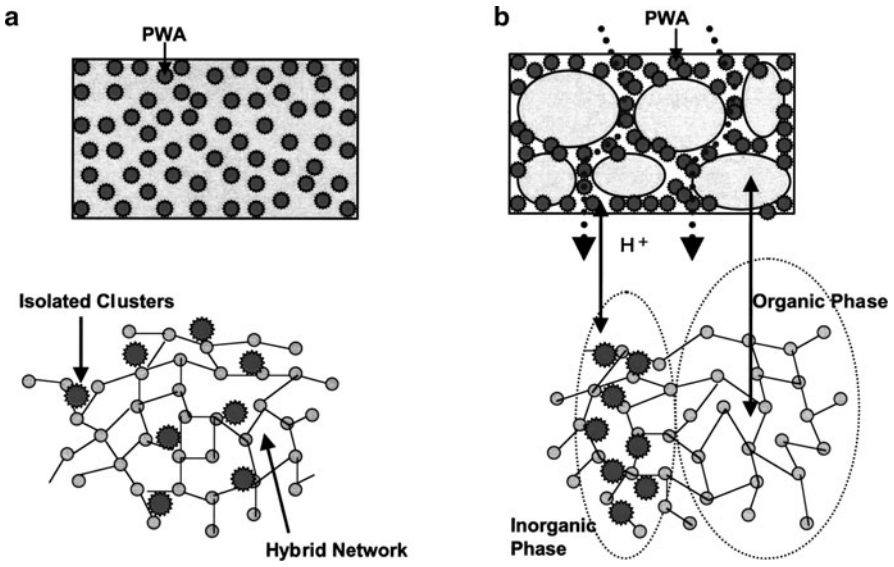

Fig. 4 Schematic structures of the organic/inorganic hybrid membranes synthesized through bridged polysilsesquioxanes macromolecules of the (**a**) PTMO and (**b**) Oct hybrid

PTMO hybrid has urethane bonds in the bridging structure, the degradation of the macromolecules is observed above 250°C. However, other hybrid membranes (DEB, Oct, Hex) show no degradation, indicating that the membranes are highly temperature tolerant even at 400°C [19] as these hybrids have no ether oxygen or urethane bonds in the bridging organic groups.

The proton conductivity of the hybrid membranes of PTMO mixed with PEO, Hex, Oct, and DEB were compared and the conductivity level of the bridged Oct hybrid is larger than the other hybrid membranes. The conductivities were measured in a temperature range from 80 to 160°C under fully saturated humidification conditions (100% RH). The Oct hybrid membranes (HPW doping ratio of 10 mol %) showed large proton conductivities of approximately 3×10^{-2} S/cm up to 160°C. The Hex and DEB hybrid membranes also possess large proton conductivities. Further, the proton conductivities of these membranes are stable at temperatures above 100°C; thus these membranes are apparently superior to Nafion®, which is well known to show irreversible structural and conductive changes at higher temperatures. The fast proton transport in the Oct hybrid membrane can be correlated with the nanophase separation of the macromolecules. The amphiphilic nature of the hybrid macromolecules promotes the self-assembly of the HPW clusters into a bicontinuous nanophase for fast proton transport; this may be the explanation for the higher proton conductivity of the Oct hybrid membrane than the PTMO hybrid membrane, while the former has interconnected conductive channels in the macromolecules. PTMO hybrid membranes possess more homogeneously dispersed HPW clusters in the macromolecules, which presumably results in the lower conductivity level compared to the Oct hybrid membrane. The conductivities of these bridged polysilsesquioxane families at higher temperatures are very high and may be used as organic/inorganic composite membranes in PEFCs.

The RH dependence of proton conductivity of the bridged Oct hybrid membrane at 120, 140, and 160°C was studied. The relative humidity was changed from 20 to 100% RH at 120°C. The decrease of the conductivity with a decrease of RH is relatively low because it has 10^{-3} S/cm level even at 20% RH. However, the RH dependence of the conductivity becomes more significant at 160°C; the conductivity decreases rapidly with a decrease of RH. The RH dependence of the conductivity is important primarily in particular for high temperature operation of PEFCs. The organic/inorganic hybrid membranes in work show remarkably larger proton conductivity at elevated temperatures and a relatively weak humidity dependence. The conductivity of the membrane was shifted by the structure of the organic bridging group in the hybrid macromolecules, which drastically change the nanophase structure of the macromolecules. The fast proton transport is attributed to the bicontinuous phase separation at the nanoscale, which provides conductive pathways for protonic species. The robust conductive channels with self-assembling HPW clusters may be strongly induced by the molecular nature of the amphiphilic organic/inorganic interfaces [149].

Since the gel structure plays a role in proton conductivity by controlling the conduction pathways in the organic/inorganic interfaces, Honma et al. [156]

modified the kinetics of hydrolysis and condensation by varying the ratio of processing water to ethoxy groups. They measured the proton conductivity of the bridged octane (C8) hybrid membranes at 60°C, and relative humidity 95%, where the hybrid membranes were prepared from the bridged octane polysilsesquioxanes, processed in (a) isopropanol solution (b) ethanol, and (c) 2-butanol. HPW doping ratio was changed from 0.05 to 0.15 meq/g in the macromolecules, while the role of water to ethoxy groups on the monomer (H_2O/OR: R = ethyl) in the sol solution was systematically changed in a range from 0.1 to 1.8. The hybrid membrane consists of nanophase-separated macromolecules doped with HPAs (HPW) exhibiting large proton conductivities ($>10^{-2}$ S/cm) at high temperatures up to 160°C. The conductivities were found to be dependent on the equivalent weight of HPW incorporated in the membranes and the amount of processing water in the sol solution [156]. In spite of the heavy doping, HPW never leaked out from the hybrid membrane, suggesting that all of the HPW was chemically incorporated in organic/inorganic hybrid network.

Groselj et al. [157] used organically modified electrolytes, called ORMOLYTES (a novel class of Li^+ or H^+ conductors in which the inorganic phase is formed by the hydrolysis and condensation of metal alkoxide precursors), (ICS-PPG) made from 3-isocyanatopropyltriethoxysilane (ICS) and poly(propylene glycol)*bis*-(2-amino-propylether) (2-APPG) hydrolyzed using varying amounts peroxopolytungstic acid (W-HPW). W-HPW spontaneously degrades at room temperature by releasing water and peroxo groups, but the addition of ICS-PPG stabilizes the W-HPW structure. The ICS-PPG increased the long-term and thermal stability (~70–80°C) of the W-HPW/ICS-PPG composites. The proton conductivity of the composite increases with the increasing percentage of W-HPW, but the amount of ICS-PPG does not alter the electronic conductivity of W-HPW. The proton conductivity of the ICS-PPG hydrolyzed by W-HPW gels increased with increasing temperature due to two opposing phenomena: temperature-activated proton mobility and the slow dehydration of the gels. ICS-PPG with the added W-HPW exhibits room temperature proton conductivities from 1.86×10^{-6} S/cm (10 mol % W-HPW) to 1.45×10^{-3} S/cm (99.18 mol % W-HPW), while the proton conductivity of W-HPW gels is 2.54×10^{-3} S/cm.

HPW and HSiW immobilized gels with varying polymer chain lengths of ICS-PPG (M_w = 4,000 [158], 2,000, and 230), where these HPAs themselves act as catalyst for the sol–gel reaction have been synthesized [159]. The HPW (HSiW): ICS-PPG ratio strongly influences the time of gelation from a few minutes to hours, and the amount of the incorporated HPA depends on its type and the length of the PPG chain. These gels or membranes were characterized by Thermal, XRD, IR, impedance, and fuel cell measurements. The thermal stability of the HPW and HSiW improves on incorporation to ICS-PPG, and IR confirmed the interactions between the modes of HPA (i.e., ν_{intra} W–O–W, ν_{inter} W–O–W, ν(W–O) terminal stretchings) and urea group modes in the range 1,500–1,700/cm (Amide I and II modes), which led to the formation of amidonium ions ($C(OH) = NH^+$). HSiW/ICS-PPG gels for high HSiW loading (70 and 75%) had a better conductivity compared to HPW/ICS-PPG, because of a higher proton concentration in the

material. However, for the low concentration (16%) of HPA in ICS-PPG, the opposite trend of proton conductivity was observed. In both cases, the increase in proton conductivity with HPA concentration from 10^{-6} S/cm (<10 wt.% of HPW or HSiW) to 10^{-3} S/cm (>70 wt.% of HPW or HSiW) in the ICS-PPG host is due to the high loading of HPAs and their uniform distribution in the sol–gel matrix, enabling the transport of protons through the gel (see Table 5). The amidonium ions play an important role in attaining the high proton conductivity of the synthesized hybrids. Due to the presence of urea groups and their ability to become protonated, high loadings of HPAs in the composites could be achieved. The most remarkable result is a high OCV for the HSiW/ORMOSIL membrane (878–790 mV) compared to the Nafion® 117 membrane (599–523 mV) as it indicates lower mixed potentials due to lower methanol crossover measured at room temperature. The HPW/ORMOSIL-coated Nafion® 117 shows a lower OCV (690–680 mV), but higher current densities compared to the performance of the pure HSiW/ORMOSIL membrane.

A series of novel fast proton conducting inorganic–organic nanocomposite hybrid membranes doped with a mixture of HPW and HPMo have been prepared by sol–gel process with GPTMS, 3-aminopropyltriethoxysilane (APTES), phosphoric acid (H_3PO_4), and tetraethoxysilane (TEOS) as precursors [154]. IR confirmed the good complexation of H_3PO_4 in the membrane matrix along with the presence of the Keggin anions of HPW and HPMo. Due to the incorporation of the inorganic SiO_2 framework, the membranes became thermally stable up to 300°C. High proton conductivity of 3×10^{-2} S/cm with composition of 50TEOS–25GPTMS–20H_3PO_4–5APTES–3HPMo–6HPW was obtained (6.35×10^{-3} S/cm at 150°C, 50% RH) at 120°C under 90% relative humidity. The high proton conductivity of the nanocomposite membranes is due to the proton-conducting path through the GPTMS-derived "pseudopolyethylene oxide" (pseudo-PEO) network in which the trapped solid acids (HPW and HPMo) as proton donors are contained. Similar membranes were prepared [155] using HPW and HPMo along with GPTMS, and tetraethoxysilane (TEOS) as precursors trimethylphosphate $PO(OCH_3)_3$. Thermal stability of membranes was significantly enhanced by the presence of SiO_2 framework. Proton conductivity of 1.59×10^{-2} S/cm with composition of 50TEOS–5$PO(OCH_3)_3$–35GPTMS–10HPW was obtained (1.15×10^{-2} S/cm for 10 mol % HPMo) at 90°C under 90% relative humidity.

Polydimethylsiloxane (PDMS)/zirconia/HPW hybrid membranes 80 and 500 μm thick were cast by modified sol–gel technique [160], where HPW (1.6–14 wt.%) was incorporated with Zr/PDMS hybrid matrix by Coulomb force and/or ionic bonding. Flexible, homogeneous, and transparent hybrid membranes were formed in the molar ratio of zirconium to PDMS from 2 to 8, while at higher zirconium concentration, the membrane became brittle and soft, and the hybrid membranes synthesized with HPW were heterogeneous. IR studies confirmed the formation of bond between Zirconium oxide moiety and PDMS via Zr–O–Si bonds. Zr/PDMS hybrid membranes, therefore, possess a good thermal stability at least up to 300°C and shows small proton conductivity of the order of 10^{-6} S/cm, and with increase in temperature, the conductivity increased from 4×10^{-7} S/cm at 30°C to 5×10^{-6} S/cm at 150°C. The conductivity of the membrane was improved on the

incorporation of HPAs like HPW, and for the membrane with 14 wt.% of HPW, the conductivity increased from 2×10^{-6} S/cm at 30°C to 5×10^{-5} S/cm at 150°C. The temperature dependence of the proton conductivity and low conductivity even at higher temperatures indicated that the protonic carriers such as H_3O^+ or $H_5O_2^+$ are bound in the hybrid matrix, and the continuous pathways for protonic conduction are not present in the organic/inorganic hybrid electrolytes. This fact was supported by the morphological characterization TEM, which shows the presence of HPW aggregates, which do not form bicontinuous channels. The maximum proton conductivity of the hybrid membrane with HPW 14 wt.% was 5×10^{-5} S/cm at saturated humidification condition of 150°C, which is too low for practical PEFC application. A slight modification in the synthesis procedure, that is the ultrasonic treatment on the membrane, increased the proton conductivity immensely and the maximum conductivity of 7.7×10^{-2} S/cm could be obtained under saturated humidification condition at 150°C [161]. The concentration of HPAs incorporated in the organic/inorganic hybrids can be increased from 14 to 35 wt.% by ultrasonic treatment. This can be due to the formation of ion-conductive channels in the organic/inorganic hybrid macromolecules. Hence, it could be inferred that not only carrier density (proton) but also the mobility of ions predominantly affects the conductivity where the conductive pathways are greatly influenced by the dispersion state of HPW either a homogeneous mixture or bicontinuous network.

Hybrid inorganic/organic membranes using a lacunary HPA proton conductor, $H_8SiW_{11}O_{39}$, in stable polymer matrices based on polyethylene glycol were prepared by a sol–gel method [162]. NMR and IR measurements indicate that this improved sol–gel membrane contains robust covalent bonds between the proton conductor and polymer backbone. However, the polymer in these model systems is not expected to be oxidatively stable. Diffusion coefficients measured for this material, 1.2 × 10–6 cm^2/s, are of the same order of magnitude as for to that of Nafion®, while ion exchange capacities, 2–2.5 meq/g, are twice that of Nafion® 117. The temperature dependence of the conductivity increases exponentially with temperature. However, fuel cell performance of this material is poor when compared to a Nafion® 117 MEA. One possible explanation is that there is a lack of organization of the proton-conducting elements in the hybrid material. In addition, ex situ membrane conductivity measurements compared to in situ MEA polarization measurements reveal large interfacial resistances in the hybrid membrane MEAs. Further, it appears that these membranes, as currently formulated, require quite stringent humidification requirements for maximum performance.

Proton-conducting high-temperature stable, hybrid electrolytes of zirconia/trimethylene glycol (TMG) or octamethylene glycol (OMG) molecules were developed [151]. Since the polymethylene monomers are known to be thermally stable, their hybrids to zirconia must be extremely stable, and therefore these precursors were used which on hydrolysis and condensation form hybrid macromolecules of robust, isotropic, and transparent polymeric materials. Zirconium alkoxide is very reactive and gets directly cross-linked to trimethylene glycol and octamethylene glycol hydrocarbon monomers by hydrolysis and condensation reactions. The hybrid material becomes proton-conducting electrolyte by incorporation of HPW

as a protogenic source where nanostructured macromolecules provide fast proton-conducting pathways by assembling HPW clusters at inorganic interfaces. The hybrids in the present work show high protonic conductivities at intermediate temperatures up to 150°C and were also found to be thermally stable due to the cross-linking of temperature-tolerant organic and inorganic species at molecular scale. HPW concentration in weight percent with respect to the zirconium alkoxide/methylene glycol materials was changed from 20 to 40 wt.%. The thermal analysis of pure TMG showed that it was stable in the range 150–200°C, but the thermal and chemical stabilities of the hybrids are increased up to 200 and 250°C, probably because the stability of organic fragments (TMG or OMG) increased by bridging those monomers with inorganic zirconia. Moreover, those with HPW addition are more improved up to 280°C than those without HPW. The enhancement of the thermal stability can be ascribed to the hybridization of inorganic zirconia moieties at molecular scale to the bridging organic monomers through retarding thermal decomposition of organic phases. The proton conductivities of the hybrid synthesized with the low molecular mass of methylene chains (TMG) are higher than those of the high molecular mass (OMG), which might be ascribed to the formation of ion-conductive channels in the organic/inorganic hybrid macromolecules. The maximum conductivities of 4×10^{-3} S/cm at 150°C are obtained for the zirconia/TMG hybrid sample with 40 wt.% HPW. The small conductivities of zirconia/OMG/20 wt.% HPW sample are possibly due to the hydrophobicity of the hybrid resulting in the low swelling capacities. The activation energy in the present hybrid is much larger than that of highly ionic conducting membrane such as Nafion®, suggesting restricted movement of protonic carriers in the conduction channels in the present organic/inorganic hybrid materials, in which temperature-tolerant hydrocarbons are used. The higher conductivity might be obtained by controlling conduction pathways in the hydrophilic/hydrophobic interfaces in the hybrid macromolecules.

Sol–gel-derived alkaline phosphate glasses have been developed as fast proton-conducting materials due to their large capacity for hydroxyl groups, mechanical, chemical, and thermal stability [163]. The glasses were prepared by partially hydrolyzing appropriate quantities of tetraethylorthosilicate, titanium isopropoxide, and trimethylphosphate with a solution of water and ethanol as reported in [163] and gelled for a month to completely hydrolyze the alkoxides. They observed that the proton conductivity increased with increase in temperature at a relative humidity and shows a maximum value of 3.6×10^{-2} S/cm at 90% RH. The power density of the fuel cell (20–88 $\mu W/cm^2$) increased with an increase in operating time in relative humidity and atmospheric pressure condition.

Similar membranes, P_2O_5–SiO_2–HPW, were fabricated using phosphotungstic acid (HPW) as the proton conductor [164]. The glasses have noncrystalline phases confirmed from structural studies but showed good mechanical and thermal stability. The maximum proton conductivity was found to be 9.1×10^{-2} S/cm at 90°C and 30% RH. A maximum power density value of 10.2 mW/cm^2 was obtained using 0.15 mg/cm^2 of Pt/C loaded on electrode and $5P_2O_5$–$87SiO_2$–8HPW. The performance of the membrane electrode assemblies was systematically studied as an effect

of SiO_2 and P_2O_5 concentrations, and the MEA (94 mol% SiO_2) was found to exhibit a maximum power density of 16.2 mW/cm^2 for an H_2/O_2 fuel cell at 30°C and 30% RH. Extending this work further, composite glass membranes of phosphosilicate gels doped with a mixture of HPW and HPMO were fabricated [165]. Proton conductivity of 1.34×10^{-1} S/cm was obtained at 90°C and 70% RH and 1.014 S/cm at 85°C and 85% RH and were thermally stable up to 400°C. The hydrogen permeability was found to decrease in the temperature range 30–110°C, going from 1.97×10^{-9} to 1.75×10^{-9} cm^2/s. A maximum output value of 35 mW/cm^2 and a current density of 137 mA/cm^2 were obtained at 28°C when using this novel glass composite membrane in fuel cell tests. A maximum performance was achieved for the HPW/HPMO: P_2O_5:SiO_2 glass composite membrane with a composition of 2/1:2:95 mol % and a Pt/C loaded of 0.1 mg/cm^2 on the electrodes. HPW-doped TiO_2–P_2O_5–SiO_2 glasses were synthesized for potentially low temperature applications [166]. These were thermally stable up to 500°C, and the fact that TiO_2 is more basic than SiO_2 could be responsible for the strong interaction between the HPAs and the titaniaphosphate surface. The new porous glass membranes have mechanical stability and low hydrogen permeability. A maximum conductivity of 7.2×10^{-2} S/cm was obtained for glass membranes containing 5 mol % of HPW and 1 mol % of TiO_2. A new type of proton-conducting glass composite membrane gave rise to a high power density of 46.3 mW/cm^2 for H_2/O_2 fuel cell at 28°C and 1 atm pressure, under hydrogen and oxygen feed conditions.

Homogeneous, transparent, and crack-free P_2O_5–ZrO_2 membranes have been synthesized by sol–gel process [167] following a similar procedure. Also phosphotungstic acid-doped membranes of molar composition 99.65 ($40P_2O_5$–$20ZrO_2$– $40SiO_2$)–0.35HPW were synthesized, where the doping to the sol with the phosphotungstic acid was done in the last step of the synthesis. The addition of SiO_2 improves the mechanical and chemical stability. On the other hand, compositions with higher content in P_2O_5 have demonstrated lower mechanical and chemical stability against water, but higher proton conductivity. The water retention and high porosity of inorganic membranes lead to high proton conductivity, 10^{-2} S/cm, at 140°C and 100% relative humidity. The incorporation of HPW in the sol–gel oxides provides an increase in the proton conductivity at low relative humidity. The most relevant behavior of this membrane consisted of an increase in conductivity by almost two orders of magnitude with increasing relative humidity from 24 to 84% at low temperatures.

4.3 Polypom Membranes

Although the HPAs have been immobilized in materials that conduct protons, reported proton conductivities achieved have been less than the state-of-the-art PFSA ionomers, such as Nafion® [5]. The main disadvantage of using HPAs in proton-conducting membranes is that most acidic forms are soluble in water and

easily leach out on washing with water. Therefore, the HPAs must be immobilized in the membrane in a unique way so that these remain bonded to the polymer matrix and do not leach out. One intriguing possibility for ionomer synthesis is to functionalize a lacunary HPA with an olefin, allowing the HPA moiety to be incorporated into a polymer backbone. The salts of selected HPAs have previously been immobilized by functionalization with Si-linked olefins, followed by polymerization, for example, with suitable comonomers to produce gels [168–171]. In previous work, we were able to synthesize films with lower wt.% immobilized HPA than in the present work, but these materials did not have significant proton conductivity at $<80°C$ and $<100\%$ RH [172]. We have reported [173], for the first time, the fabrication of membranes comprising the acid form of these compounds, with over 50 wt.% loadings of the HPA, as free-standing films and their high proton conductivity over a range of temperatures.

The hybrid materials synthesized by our group incorporate HPAs as the inorganic component and function as the only source of mobile protons, facilitating the movement of protons by nature of its unique structure and its interaction with bound waters of hydration in the secondary structure and with adsorbed free water present in the membrane. The organic components consist of an alkyl or phenyl moiety along with a vinyl group that can undergo radical polymerization to form a polymer. Along with the mechanism for polymerization, the organic components contribute the properties necessary for fashioning the polymer into a thin, flexible, and robust membrane. Hybrid monomers have been synthesized based on the Keggin structure of silicotungstic acid ($H_4SiW_{12}O_{40}{\cdot}nH_2O$) as mono- and dilacunary forms of this structure $H_8SiW_{11}O_{39}{\cdot}nH_2O$ (HSiW11) and $H_8SiW_{10}O_{34}{\cdot}nH_2O$ (HSiW10), respectively. The lacunary HPA is a nonsaturated form of silicotungstic acid ($H_4SiW_{12}O_{40}$), where a tungsten atom and an oxygen atom have been removed ($H_8SiW_{11}O_{39}$). Immobilization of the lacunary silicotungstic acid in these hybrid materials is achieved via covalent bonding between terminal oxygen of the lacunary HPA and silicon of functionalized silanes. Once the lacunary form of the HPA has been synthesized, it is reacted in a suitable solvent with a trialkoxy or trichloro silane, containing an organic functional group with carbon–carbon double bonds (which can be vinyl, styrl, or methacryl). The organic silanes include triethoxystyrylsilane, methacryloxypropyltrimethoxysilane (Gelest), or vinylethyltriethoxysilane (Gelest). The product is a hybrid monomer that consists of an inorganic HPA covalently bonded to an organic group through a O–Si–C bond [174]. The silanes contain organic functional groups (R) with carbon–carbon double bonds for subsequent radical polymerization processes. In this way, a lacunary HPA is functionalized with an olefin, allowing the HPA moiety to be incorporated into a polymer backbone. Once the hybrid monomer was synthesized in solution, the solvent was removed by evaporation or rotovapping to obtain the soluble acid form or the potassium or sodium salt of the monomer.

Triethoxystyrylsilane (TEOSS) was used as the organic component in the synthesis of HPA(styryl)2 monomers and was synthesized via Grignard reaction. A large variety of HPA(methacryl)2 monomers were synthesized based on several literature methods [175–178]. Both mono- and dilacunary silicotungstic acid were

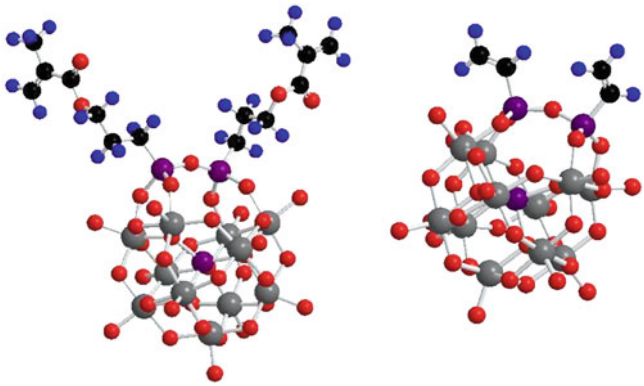

Fig. 5 Ball and stick models of HSiW11(methacryl)2 monomer (*left*) and HSiW11(vinyl)2 monomer (*right*) (*gray* = W, *red* = O, *black* = C, *blue* = H, *purple* = Si)

used for the inorganic component, which allowed for the synthesis of "bis" and "tetrakis" forms of the monomer. Methacryloxypropylsilane was used for the organic component. The cations associated with the inorganic component of the monomer include tetramethylammonium (TMA), tetrabutylammonium (TBA), potassium (K^+), and protons (H^+). The TMA and TBA salts were precipitated out of solution by the addition of tetramethylammonium chloride and tetrabutylammonium bromide, respectively. The potassium salt was prepared using the potassium salt of the lacunary silicotungstic acid and then obtained from solution by evaporation or rotovapping. The acid form of the monomer was obtained by cation exchange of the potassium salt of the monomer through a column of ion exchange resin. Only two types of HPA(vinyl)2 monomers were synthesized, KSiW11(vinyl)2 and HSiW11(vinyl)2. Figure 5 shows the structure of the HSiW11 (methacryl)2 monomer and the HSiW11(vinyl)2 monomer.

The synthesis of hybrid homopolymers by radical polymerization of the hybrid monomers was carried out according to literature methods [170, 171, 175]. Since 100 wt.% of the reactant was the hybrid monomer, the code for the polymer was PolyPOM-100*x*, with *x* represented by "s" for styryl, "m" for methacryl, or "v" for vinyl organic functionality. These materials were difficult to fabricate into membranes because of their brittle or "gel"-type nature. Dioelfins should be highly cross-linked and these polymers show the effects of this because they are brittle and not at all soluble in common solvents. Nonetheless, these materials were interesting to study in regard to their proton mobility. The hybrid organic–inorganic homopolymers were difficult to form into membrane materials for fuel cell applications because of their tendency to be brittle or to form gels. Blending these materials with organic comonomers and cross-linking agents was attempted in an effort to form membrane materials. The comonomers used were methyl methacrylate (MMA), butyl methacrylate (BMA), butyl acrylate (BA), and hexyl acrylate (HA).

Three general methods of copolymerization were attempted: (1) radical solution polymerization in an evacuated sealed glass tubes, (2) redox emulsion polymerization in water solution, and (3) radical polymerization (either in solution or neat) cast between mylar sheets to form a thin membrane film and initiated under a *uv* lamp. The third method proved to be the best for forming membrane materials that could easily be tested for proton conductivity in an in-plane conductivity cell. This method was used most extensively and produced a large number of viable membrane materials.

The process to synthesize an organic–inorganic hybrid membrane involves the following steps:

1. Synthesis of lacunary HPAs with vacant sites containing terminal oxygen atoms which can easily be bonded to silanes containing the desired organic functionality
2. Sol–gel reaction to attach silanes containing desired functionality to the lacunary HPA creating hybrid organic–inorganic monomers
3. Homo-polymerization of hybrid organic–inorganic monomers using radical polymerization
4. Copolymerization of hybrid organic–inorganic monomers with inert and proton-conducting comonomers by radical polymerization

Results from membrane fabrication and conductivity tests indicated that HSiW11 (vinyl)2 would be the best monomer to incorporate into PEMs which would be discussed here further. The vinyl functionalized $K_4[SiW_{11}O_{40}(Si(CH{=}CH_2))_2]$ [175] K4(SiW11v) was converted to the free acid over an ion exchange column, $H_4SiW11v$ (1–2 g, 75 wt.%) was dissolved in butyl acrylate (BA) with 1,6-hexanedioldiacrylate (HDDA) in the ratio 3:0.9:0.1 by weight [P(SiW11-75v-*co*-BA-*co*-HDDA)] and cast as polymer films by curing the suspension between two silicone-treated Mylar sheets under UV using Darocur 1173 (1 wt.%) as a photoinitiator (Fig. 6). The initially dark blue films bleached to transparent orange after exposure to air and had a typical thickness of 100–170 μm and a density of 2.58 g/cm^3. TGA indicated that the films included 67% inorganics (800°C), suggesting some of the hybrid monomer that remained undissolved in the comonomers may not have been included in the film.

The presence of the HPA moiety and the expected polymer backbone were confirmed by IR and NMR. Leaching studies also showed that it is predominantly

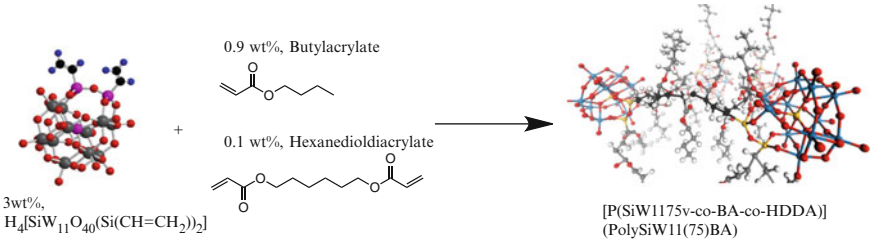

Fig. 6 Synthesis of copolymer (HDDA units omitted in the copolymer for clarity)

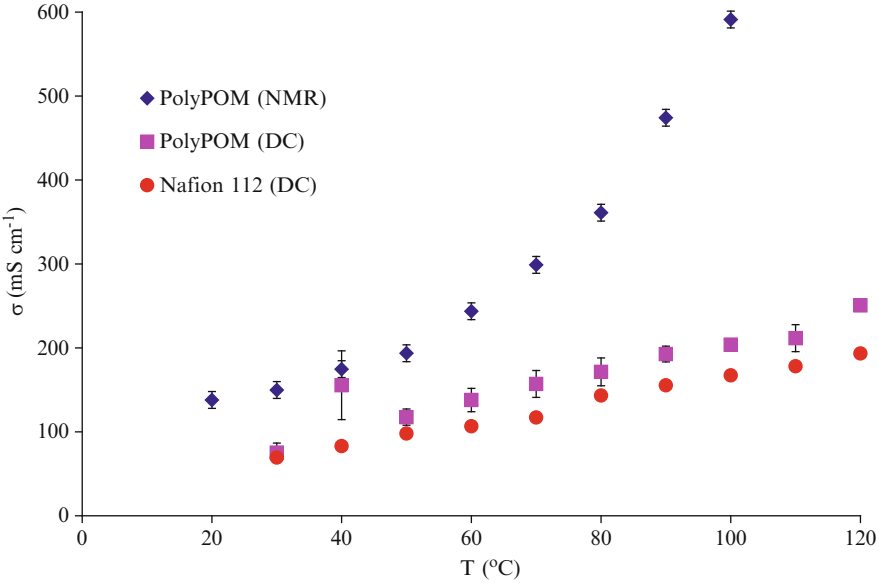

Fig. 7 In-plane proton conductivity for the P(SiW1175V-*co*-BA-*co*-HDDA) film and Nafion® 112 films measured by a DC method at 100% RH and the calculated proton conductivity for the P(SiW1175V-*co*-BA-*co*-HDDA) film from NMR measurements

small organic oligomers that are lost in liquid water and that the HPA [P(SiW11-75v-*co*-BA-HDDA)] was 81% immobilized. In water, the film swelled by 27% in thickness and 3% in-plane compared to 50% for a typical PFSA ionomer. Under the ambient conditions of the measurement, the high-modulus clusters exist in a range of 10–100 nm as confirmed by SAXS and AFM measurements.

The results for the DC measurement for the P(SiW11-75 V-*co*-BA-*co*-HDDA) film are compared to Nafion® 112 in Fig. 7. It can be seen that the P(SiW11-75 V-*co*-BA-*co*-HDDA) film outperforms the PFSA ionomer at all temperatures measured at 100% RH, achieving $\sigma = 1.70 \times 10^{-1}$ S/cm at 80°C, the standard operating conditions of a PEM fuel cell. Similar results were obtained for the resistance obtained from the EIS. The activation energy E_a, for proton conduction of this 75 wt.% HPA polymer, 10.0 kJ/mol, was slightly lower than that of Nafion®, 11.2 kJ/mol.

The proton transport was further probed by NMR using water as a standard, and the number of water molecules was determined by ^{1}H spin counting. It was determined that the number of waters per H^+, λ, varied between 6 and 8 from 20 to 100°C. This compares to a $\lambda = 22$ for Nafion® 117 [179] showing that this P(SiW11-75 V-*co*-BA-*co*-HDDA) film requires less water per H^+ to achieve a higher σ at 100% RH. However, on a functional group basis the film uptakes the same amount of water as a PFSA ionomer. Pulsed-field gradient spin echo (PGSE) NMR [180] was used to determine the self-diffusion coefficients, D, of protons in the polymer. For the P(SiW11-75 V-*co*-BA-*co*-HDDA) film at 100% RH and 20°C

$D = 4.0 \times 10^{-6}$ cm^2/s which is comparable to Nafion® 117 and as expected, due to tortuosity arguments, significantly less than water, 2.5×10^{-5} cm^2/s at 25°C. From 20 to 60°C, the data give $E_a = 9.2$ kJ/mol. Above 60°C a phase change is observed, D is as high as 2.5×10^{-5} cm^2/s at 100°C, and the calculated $E_a = 23.0$ kJ/mol. For sulfonic acid-based systems, the calculated σ from the Nernst–Einstein model typically under-predicts or is close to the measured σ. In our case, the calculated σ is much higher than the measured σ, suggesting that H^+ conduction is either by a different mechanism or more likely that in these first-generation HPA films that their morphology is far from ideal for H^+ conduction and that diffusion is severely restricted.

As a proof of concept and to show that the P(SiW11-75 V-*co*-BA-*co*-HDDA) film did actually conduct protons, a 50 cm^2 film was fabricated into a MEA using standard electrodes with Pt dispersed on carbon. The MEA was run as a H_2/air fuel cell at 70°C and 75% RH. On running successive polarization curves, the performance improved until an OCV of 0.86 V and 600 mA/cm^2 at 0.3 V with an area-specific resistance of 100 mΩ/cm^2 was achieved. The fuel cell survived for 4 days. Considering that this MEA was not optimized in any way, the fuel cell performance under these relatively dry conditions suggests that this new ionomer class has significant potential for application in PEM fuel cells.

In conclusion, we have fabricated polymers containing high wt.% of immobilized HPA into films and demonstrated high proton conduction at 100% RH for the first time. These materials are a new class of PEM ionomer and exhibit proton conductivities >0.1 S/cm at the temperatures of interest for operation of PEM fuel cells. While the full potential of this class of ionomers is still to be explored, this material represents a new tool for the development of PEMs for the operation of PEM fuel cells under hotter and drier conditions. Our recent work has been focussed to increase the loading of HPA in these systems, and we have been successful in making films with 85% loading of the HPA. Presently, these are being characterized well and the results look promising in terms of proton conductivity.

5 Conclusions and Future Directions

Current state of the art for membranes used in fuel cells are PFSA-based membranes which are limited to temperatures <80°C at fully humidified conditions. Hence, the ideal membranes needed for the fuel cell operation must be stable at higher temperatures, should have high proton conductivity at low humidity, be inexpensive, and durable. HPAs, which are super acids, have been used for H_2/O_2 and DMFCs in powdered as well as liquid form, but when used in their pure form have been found to give low performance and wash out easily with the water formed during the fuel cell operation. The HPA have been incorporated into various matrices both inert and ionomeric to be used at higher temperatures and drier conditions. Incorporation of HPAs into a membrane matrix can achieve all these properties, and so the key issue that remains is that the HPAs should be effectively

immobilized in the membranes and thereby keep their proton-conducting properties intact. The incorporation of HPAs in the PFSA and hydrocarbon-based membranes increased their proton conductivity and thermal stability, but the problem of leaching HPAs could not be effectively improved. The hydrocarbon imbibed membranes are inexpensive and have shown comparable properties to the PFSA-based membranes. Sol–gel chemistry seemed to work well in holding the HPAs in the membrane matrix, but with little compromise on the proton conductivity. The polypom-based membranes have a large potential to be used in fuel cells, if mechanically stable membranes could be made from them as they have high conductivity at elevated temperatures with minimal leaching problems. These novel hybrid polymers have demonstrated the ability to replace the sulfonic acid groups in fuel cell membranes with HPA proton conductors while still achieving similar levels of proton conductivity. We believe that with the optimum structural and morphological design, the strong interaction between the inorganic and organic component of the membrane will provide the thermal, mechanical, and oxidative stability along with the high levels of proton mobility necessary to operate under fuel cell conditions. The potential of the HPA proton conductors to maintain high levels of proton conductivity under dry conditions may eventually allow us to fabricate a membrane with the ability to operate under drier and hotter conditions than are currently possible with PFSA ionomer membranes.

Acknowledgment The authors would like to thank the NSF for financial support for the Renewable Energy MRSEC for this project under Grant DMR-0820518.

References

1. Hamrock SJ, Yandrasits MA (2006) Polym Rev 46:219
2. Mauritz KA, Moore RB (2004) Chem Rev 104:4535
3. Kartha S, Grimes P (1994) Phys Today 47:54
4. Adjemian KT, Lee SJ, Srinivasan S, Benziger J, Bocarsly AB (2002) J Electrochem Soc 149: A256
5. Herring AM (2006) Vol 46, Taylor & Francis, p 245
6. Nakamura O, Kodama T, Ogino I, Miyake Y (1979) Chem Lett 1:17
7. Malers JL, Sweikart M-A, Horan JL, Turner JA, Herring AM (2007) J Power Sources 172:83
8. Nakamura O (1982) Prog Batteries Sol Cells 4:230
9. Staiti P, Hocevar S, Giordano N (1997) Int J Hydrogen Energy 22:809
10. Giordano N, Staiti P, Hocevar S, Arico AS (1996) Electrochim Acta 41:397
11. Mioc UB, Milonjic SK, Stamenkovic V, Radojevic M, Colomban P, Mitrovic MM, Dimitrijevic R (1999) Solid State Ionics 125:417
12. Staiti P, Freni S, Hocevar S (1999) J Power Sources 79:250
13. Li Q, He R, Jensen JO, Bjerrum NJ (2003) Chem Mater 15:4896
14. Savadogo O (2004) J Power Sources 127:135
15. Mioc UB, Todorovic MR, Davidovic M, Colomban P, Holclajtner-Antunovic I (2005) Solid State Ionics 176:3005
16. Meng F, Aieta NV, Dec SF, Horan JL, Williamson D, Frey MH, Pham P, Turner JA, Yandrasits MA, Hamrock SJ, Herring AM (2007) Electrochim Acta 53:7

17. Ramani V, Kunz HR, Fenton JM (2005) J Membr Sci 266:110
18. Wu Q, Wang H, Yin C, Meng G (2001) Mater Lett 50:61
19. Honma I, Nakajima H, Nishikawa O, Sugimoto T, Nomura S (2002) J Electrochem Soc 149: A1389
20. James AG, Horan L, Ren H, Sikora BJ, Kuo M-C, Meng F, Dec SF, Haugen GM, Yandrasits MA, Hamrock SJ, Frey MH, Herring AM (2009) ChemSusChem 2
21. Pope MT (1983) Heteropoly and isopoly oxometalates. Springer, New York
22. Pope MT, Muller A (2001) Polyoxometalate chemistry: from topology via self-assembly to applications. Kluwer Academic, Dordtrecht
23. Brown GM, Noe-Spirlet M-R, Busing WR, Levy HA (1977) Acta Cryst B33:1038
24. Filowitz M, Klemperer WG, Messerle L, Shum W (1976) J Am Chem Soc 98:2345
25. Filowitz M, Ho RKC, Klemperer WG, Shum W (1979) Inorg Chem 18:93
26. Rocchiccioli-Deltcheff C, Fournier M, Franck R, Thouvenot R (1983) Inorg Chem 22:207
27. Kreuer K-D (1996) Chem Mater 8:610
28. Nakamura O, Ogino I, Kodama T (1981) Solid State Ionics 3–4:347
29. Spirlet M-R, Brown GM, Busing WR, Levy HA (1975) Acta Crystallogr A 31:S80
30. Spirlet M-R, Busing WR (1978) Acta Crystallogr B 34:907
31. d'Amour H, Allman R (1976) Z Krist 143:1
32. Pressman HA, Slade RCT (1988) Chem Phys Lett 151:354
33. Tell B, Wudl F (1979) J Appl Phys 50
34. Wada HT (1969) C R Acad Sci 259
35. Slade RCT, Barker J, Pressman HA, Strange JH (1988) Solid State Ionics 28–30:594
36. Hardwick A, Dickens PG, Slade RCT (1984) Solid State Ionics 13:345
37. Slade RCT, Pressman HA, Skou E (1990) Solid State Ionics 38:207
38. Kreuer KD, Hampele M, Dolde K, Rabenau A (1988) Solid State Ionics 28–30:589
39. Mioc U, Colomban P, Novak A (1990) J Mol Struct 218:123
40. Chidichimo G, Golemme A, Imbardelli D, Santoro E (1990) J Phys Chem 94:6826
41. Chidichimo G, Golemme A, Imbardelli D, Iannibello A (1992) J Chem Soc Faraday Trans 88:483
42. Mioc UB, Dimitrijevic RZ, Davidovic M, Nedic ZP, Mitrovic MM, Colomban P (1994) J Mater Sci 29:3705
43. Slade RCT, Omana MJ (1992) Solid State Ionics 58:195
44. Tjapkin N, Davidovic M, Colomban P, Mioc U (1993) Solid State Ionics 61:179
45. Mioc U, Davidovic M, Tjapkin N, Colomban P, Novak A (1991) Solid State Ionics 46:103
46. Mioc UB, Colomban P, Davidovic M, Tomkinson J (1994) J Mol Struct 326:99
47. Kremenovic A, Spasojevic-de Biré A, Dimitrijevic R, Sciau P, Mioc UB, Colomban P (2000) Solid State Ionics 132:39
48. Kremenovic A, Spasojevic-de Biré A, Bourée F, Colomban P, Dimitrijevic R, Davidovic M, Mioc UB (2002) Solid State Ionics 150:431
49. Kanda Y, Lee KY, Nakata S, Asaoka S, Misono M (1988) Chem Lett 17
50. Uchida S, Inumaru K, Dereppe JM, Misono M (1998) Chem Lett 27:643
51. Essayem N, Tong YY, Jobic H, Vedrine JC (2000) Appl Catal, A 194–195:109
52. Uchida S, Inumaru K, Misono M (2000) J Phys Chemistry B 104:8108
53. Okuhara T, Nishimura T, Watanabe H, Na K, Misono M (1994) Stud Surf Sci Catal 90:419
54. Okuhara T, Misono M (1992) J Mol Catal 74:247
55. Kozhevnikov IV (1987) Russ Chem Rev 56:811
56. Kozhevnikov IV, Sinnema A, van Bekkum H (1995) 34:213
57. Lee KYM, Okuhara T, Misono M (1989) Bull Chem Soc Jpn 62:1731
58. Taketa H, Katsuki S, Eguchi K, Seiyama T, Yamazoe N (1986) J Phys Chem 90:2959
59. Bardin BBB, Bordawekar SV, Neurock M, Davis RJ (1998) J Phys Chem B 102:10817
60. Ganapathy S, Fournier M, Paul JF, Delevoye L, Guelton M, Amoureux JP (2002) J Am Chem Soc 124:7821
61. Lopez X, Bo C, Poblet JM (2002) J Am Chem Soc 124:12574

62. Janik MJ, Campbell KA, Bardin BB, Davis RJ, Neurock M (2003) Appl Catal, A 256:51
63. Qingyin Wu HLGM (1999) Mater Lett 39:129
64. Wu Q (2000) Mater Lett 42:179
65. Wu Q, Meng G (2000) Mater Res Bull 35:85
66. Wu Q (2002) Mater Res Bull 37:2199
67. Wu Q, Xie X (2002) Mater Sci Eng, B 96:29
68. Jin H, Wu Q, Pang W (2004) Mater Lett 58:3657
69. Sang X, Wu Q (2004) Mater Res Bull 39:2329
70. Wu Q, Sang X, Liu B, Ponomareva VG (2005) Mater Lett 59:123
71. Wu Q, Sang X, Shao F, Pang W (2005) Mater Chem Phys 92:5
72. Okuhara T, Mizuno N, Misono M (1996) Adv Catal 41:113
73. Ukshe EA, Leonova LS, Korosteleva AI (1989) Solid State Ionics 36:219
74. Davidovic M, Cajkovskia T, Cajkovskia D, Likar-Smiljanic V, Biljic R, Mioc U, Nedic Z (1999) Solid State Ionics 125:411
75. Davidovic M, Cajkovskiajkovskia T, Likar-Smiljanic V, Biljic R, Mioc UB, Nedic Z (2002) Solid State Ionics 147:123
76. Todorovic MR, Mioc UB, Colomban Ph, Nedic ZP, Uskokovic SM, Borcic ID (1999) Solid State Ionics 125:425
77. Kukino T, Kikuchi R, Takeguchi T, Matsui T, Eguchi K (2005) Solid State Ionics 176:1845
78. Langpape M, Millet JMM, Ozkan US, Boudeulle M (1999) J Catal 181:80
79. Okuhara T, Watanabe H, Nishimura T, Inumaru K, Misono M (2000) Chem Mater 12:2230
80. Haber J, Matachowski L, Mucha D, Stoch J, Sarv P (2005) Inorg Chem 44:6695
81. Barton TJ, Bull LM, Klemperer WG, Loy DA, McEnaney B, Misono M, Monson PA, Pez G, Scherer GW, Vartuli JC, Yaghi OM (1999) Chem Mater 11:2633
82. Dec SF, Herring AM (2004) J Phys Chem B 108:12339
83. Dec SF, Jacobsen GM, Horan JL, Herring AM (2007) J Phys Chem C 111:7720
84. Mioc UB, Todorovic MR, Colomban P, Nedic ZP, Uskokovic SM, Borcic ID (1999) Solid State Ionics 125:425
85. Meng F, Dec SF, Sachdeva S, Turner JA, Herring AM (2011) Solid State Ionics, to be submitted
86. Giordano N, Arico AS, Hocevar S, Staiti P, Antonucci PL, Antonucci V (1993) Electrochim Acta 38:1733
87. Giordano N, Staiti P, Arico AS, Passalacqua E, Abate L, Hocevar S (1997) Electrochim Acta 42:1645
88. Lavric I, Staiti P, Novak P, Hocevar S (2001) J Power Sources 96:303
89. Malhotra S, Datta R (1997) J Electrochem Soc 144:L23
90. Alberti G, Casciola M (2003) Annu Rev Mater Res 33:129
91. Savadogo O (1998) J New Mater Electrochem Syst 1:47
92. Tazi B, Savadogo O (2000) Electrochim Acta 45:4329
93. Tazi B, Savadogo O (2001) J New Mater Electrochem Syst 4:187
94. Ramani V, Kunz HR, Fenton JM (2004) J Membr Sci 232:31
95. Dimitrova P, Friedrich KA, Stimming U, Vogt B (2002) Solid State Ionics 150:115
96. Shao Z-G, Joghee P, Hsing I-M (2004) J Membr Sci 229:43
97. Xu W, Lu T, Liu C, Xing W (2005) Electrochim Acta 50:3280
98. Aparicio M, Castro Y, Duran A (2005) Solid State Ionics 176:333
99. Ramani V, Kunz HR, Fenton JM (2005) Electrochim Acta 50:1181
100. Ramani V, Kunz HR, Fenton JM (2005) J Power Sources 152:182
101. Gebel G, Aldebert P, Pineri M (2002) Macromolecules 20:1425
102. Haugen GM, Meng F, Frey MH, Hamrock SJ, Aieta N, Horan J, Kuo MC, Herring AM (2007) Electrochem Solid-State Lett 10:B51
103. Sauk J, Byun J, Kim H (2005) J Power Sources 143:136

104. Staiti P, Arico AS, Baglio V, Lufrano F, Passalacqua E, Antonucci V (2001) Solid State Ionics 145:101
105. Arico AS, Baglio V, Blasi AD, Antonucci V (2003) Electrochem Commun 5:862
106. Arico AS, Baglio V, Di Blasi A, Creti' P, Antonucci PL, Antonucci V (2003) Solid State Ionics 161:251
107. Kim H, Chang H (2007) J Membr Sci 288:188
108. Kim YC, Jeong JY, Hwang JY, Kim SD, Yi SC, Kim WJ (2008) J Membr Sci 325:252
109. Wang L, Yi BL, Zhang HM, Xing DM (2007) Electrochim Acta 52:5479
110. Zhao D, Yi BL, Zhang HM, Yu HM, Wang L, Ma YW, Xing DM (2009) J Power Sources 190:301
111. Sachdeva S, James LH, Meng F, Herring AM (2011) Macromolecules, to be submitted
112. Zhu SS, Tang LH, Yue B, Lin BF (1999) Acta Chim Sin 57:533
113. Feng W, Wang J, Wu Q (2005) Mater Chem Phys 93:31
114. Li L, Xu L, Wang Y (2003) Mater Lett 57:1406
115. Xu W, Liu C, Xue X, Su Y, Lv Y, Xing W, Lu T (2004) Solid State Ionics 171:121
116. Zaidi SMJ, Mikhailenko SD, Robertson GP, Guiver MD, Kaliaguine S (2000) J Membr Sci 173:17
117. Kim YS, Wang F, Hickner M, Zawodzinski TA, McGrath JE (2003) J Membr Sci 212:263
118. Zhang H, Pang JH, Wang D, Li A, Li X, Jiang Z (2005) J Membr Sci 264:56
119. Smitha B, Sridhar S, Khan AA (2005) J Polym Sci, B: Polym Phys 43:1538
120. Shanmugam S, Viswanathan B, Varadarajan TK (2006) J Membr Sci 275:105
121. Lin CW, Thangamuthu R, Yang CJ (2005) J Membr Sci 253:23
122. Ponce ML, Prado L, Ruffmann B, Richau K, Mohr R, Nunes SP (2003) J Membr Sci 217:5
123. Helen M, Viswanathan B, Srinivasa Murthy S (2006) J Power Sources 163:433
124. Anis A, Banthia AK, Bandyopadhyay S (2008) J Power Sources 179:69
125. Ponce ML, de A Prado LAS, Silva V, Nunes SP (2004) Desalination 162:383
126. Ismail AF, Othman NH, Mustafa A (2009) J Membr Sci 329:18
127. Bello M, Zaidi SMJ, Rahman SU (2008) J Membr Sci 322:218
128. Colicchio I, Wen F, Keul H, Simon U, Moeller M (2009) J Membr Sci 326:45
129. Jang I-Y, Kweon O-H, Kim K-E, Hwang G-J, Moon S-B, Kang A-S (2008) J Membr Sci 322:154
130. Zhao X, Xiong H-M, Xu W, Chen J-S (2003) Mater Chem Phys 80:537
131. Musto P, Karasz FE, MacKnight WJ (1993) Polymer 34:2934
132. Samms SR, Wasmus S, Savinell RF (1996) J Electrochem Soc 143:1225
133. Bouchet R, Siebert E, Vitter G (1997) J Electrochem Soc 144:L95
134. Wainright JS, Wang JT, Weng D, Savinell RF, Litt M (1995) J Electrochem Soc 142:L121
135. Wang JT, Savinell RF, Wainright J, Litt M, Yu H (1996) Electrochim Acta 41:193
136. Xing B, Savadogo O (1999) J New Mater Electrochem Syst 2:95
137. He R, Li Q, Xiao G, Bjerrum NJ (2003) J Membr Sci 226:169
138. Staiti P, Minutoli M, Hocevar S (2000) J Power Sources 90:231
139. Staiti P (2001) Mater Lett 47:241
140. Staiti P (2001) J New Mater Mater Electrochem Syst 4:181
141. Gomez-Romero P, Asensio JA, Borros S (2005) Electrochim Acta 50:4715
142. Sweikart MA, Herring AM, Turner JA, Williamson DL, McCloskey BD, Boonrueng SR, Sanchez M (2005) J Electrochem Soc 152:A98
143. Asensio JA, Borros S, Gomez-Romero P (2003) Electrochem Commun 5:967
144. Asensio JA, Gómez-Romero P (2005) Fuel Cells 5:8
145. Honma I, Hirakawa S, Yamada K, Bae JM (1999) Solid State Ionics 118:29
146. Honma I, Takeda Y, Bae JM (1999) Solid State Ionics 120:255
147. Honma I, Nomura S, Nakajima H (2001) J Membr Sci 185:83
148. Honma I, Nakajima H, Nomura S (2002) Solid State Ionics 154–155:707
149. Honma I, Nakajima H, Nishikawa O, Sugimoto T, Nomura S (2003) J Electrochem Soc 150:A616

150. Nakajima H, Nomura S, Sugimoto T, Nishikawa S, Honma I (2002) J Electrochem Soc 149: A953
151. Kim J-D, Honma I (2004) Electrochim Acta 49:3179
152. Pern FJ, Turner JA, Herring AM (2004) In: Tarascon J-M, Leite ER, Chiang Y-M, Kelder EM (eds) Nanostructured materials in alternative energy devices, vol 822, p 159
153. Lavrencic Stangar U, Orel B, Vince J, Jovanovski V, Spreizer H, Surca Vuk A, Hocevar S (2005) J Solid State Electrochem 9:106
154. Lakshminarayana G, Nogami M (2009) J Phys Chem C 113:14540
155. Lakshminarayana G, Nogami M (2009) Electrochim Acta 54:4731
156. Honma I, Nakajima H, Nishikawa O, Sugimoto T, Nomura S (2003) Solid State Ionics 162–163:237
157. Grošelj N, Gaberščcek M, Opara Krašovec U, Orel B, Drazic G, Judeinstein P (1999) Solid State Ionics 125:125
158. Lavrencic Stangar U, Groselj N, Orel B, Colomban P (2000) Chem Mater 12:3745
159. Lavrencic Stangar U, Groselj N, Orel B, Schmitz A, Colomban P (2001) Solid State Ionics 145:109
160. Kim J-D, Honma I (2003) Electrochim Acta 48:3633
161. Kim J-D, Honma I (2004) Electrochim Acta 49:3429
162. Vernon DR, Meng F, Dec SF, Williamson DL, Turner JA, Herring AM (2005) J Power Sources 139:141
163. Uma T, Izuhara S, Nogami M (2006) J Eur Ceram Soc 26:2365
164. Uma T, Nogami M (2006) J Membr Sci 280:744
165. Uma T, Nogami M (2007) Chem Mater 19:3604
166. Uma T, Nogami M (2007) Chemphyschem 8:2227
167. Mosa J, Larramona G, Durán A, Aparicio M (2008) J Membr Sci 307:21
168. Hasegawa T, Murakami H, Shimizu K, Kasahara Y, Yoshida S, Kurashina T, Seki H, Nomiya K (2008) Inorg Chim Acta 361:1385
169. Hasegawa T, Kasahara Y, Yoshida S, Kurashina T, Aoki S, Yoza K, Nomiya K (2007) Inorg Chem Commun 10:1416
170. Mayer CR, Thouvenot R, Lalot T (2000) Macromolecules 33:4433
171. Mayer CR, Thouvenot R, Lalot T (2000) Chem Mater 12:257
172. Horan JL, Aieta NV, Leisch JE, Kuo M-C, Dec SF, Herring AM (2007) Electrochem Soc Trans 11:97
173. James LH, Anitha G, Hui R, Benjamin JS, Mei-Chen K, Fanqin M, Steven FD, Gregory MH, Michael AY, Steven JH, Matthew HF, Andrew MH (2009) 2:193
174. Knoth WH (1979) J Am Chem Soc 101
175. Judeinstein P (1992) Chem Mater 4:4
176. Mayers CR, Fournier I, Thouvenot R (2000) Chem Eur J 6
177. Judeinstein P, Deprum C, Nadjo L (1991) J Chem Soc Dalton Trans 1991
178. Weeks MS, Hill CL, Schinazi RF (1992) J Med Chem 35
179. Zawodzinski TA, Derouin SRC, Sherman RJ, Smith VT, Springer TE, Gottesfeld S (1993) J Electrochem Soc 140
180. Stejskal EO, Tanner JE (1965) J Chem Phys 42

Struct Bond (2011) 141: 169–201
DOI: 10.1007/430_2011_46

Published online: 17 June 2011

Perspective on the Storage of Hydrogen: Past and Future

Michael T. Kelly

Abstract There are clear advantages to using hydrogen as a fuel, but storage of hydrogen in a light-weight and compact form remains a challenge. This review highlights past breakthroughs that led to the current thinking in hydrogen storage methodology. Metal organic frameworks are discussed briefly, with greater attention to the storage of hydrogen in other molecules. Many molecular storage strategies rely on the thermal decomposition of hydrogen hetero atom bonds and formation of hydrogen to hydrogen bonds. An acid-base thought model is presented to explain observed behaviors and to guide future endeavors.

Keywords Ammonia borane · Hydrogen storage · Metal organic frameworks

Contents

M.T. Kelly
Department of Chemistry, Frick Laboratory, Princeton University, Princeton, NJ 08544, USA
e-mail: mtk2@princeton.edu

In recent years hydrogen gas has been promoted as a potential environment-friendly fuel. The growing body of data linking global warming with increasing amounts of carbon dioxide in the atmosphere, which has resulted from man's more widespread use of fossil fuels, has required the detailed consideration of alternatives. The replacement of fossil fuels by hydrogen would be accompanied by the formation of environmentally neutral water as the major oxidation product and thereby reduce the global emissions of carbon dioxide. Since dihydrogen gas does not occur in significant quantities on earth, it would be necessary to synthesize it using alternative energy sources. If fossil fuels are used to provide the energy source required for manufacturing dihydrogen, then it is necessary to calculate the quantities of carbon dioxide produced in the process relative to those which would have been emitted had the fossil fuel been used as the sole energy source. It will also be necessary to balance the energy and economic factors which would be involved in the mixed hydrogen/fossil fuel economy. There are therefore clear advantages in using solar energy directly to produce hydrogen from either water or other hydrogen sources if the economics and engineering problems can be overcome. This review summarizes the scientific and technical issues associated with storing hydrogen and addresses how the storage problems associated with hydrogen molecules may be overcome. While molecular hydrogen has the highest energy per unit weight of any known compound, it has a poor energy content per unit volume. Although the liquefaction of hydrogen results in a substantial volume reduction, it suffers from the disadvantages of using a fuel at 20 K in a 300 K environment. Therefore, dihydrogen production and storage present important scientific, engineering, and economic issues.

Elemental hydrogen gas has been a specialty fuel molecule for some time. It has the highest specific energy of any known compound and has been used in the US Space Program for launching vehicles into orbit. Hydrogen is not in general use as an energy storage molecule, but in recent years there has been a drive to change this. The momentum for change comes from a growing body of data indicating that oxidation of hydrocarbon fuel molecules in use globally is increasing the concentration of carbon dioxide in the Earth's atmosphere. There is strong evidence that this is already causing an increase in the average temperature of the Earth, which is likely to have significant future consequences for mankind [1].

The legitimacy of hydrogen as a replacement for hydrocarbons comes from two sources: first, the oxidation product of hydrogen is water, which does not have environmental consequences. The other potential benefit to hydrogen as a fuel molecule is that hydrogen gas is readily generated from inexpensive and abundant natural resources. In other words, though hydrogen does not occur in terrestrial nature, hydrogen can be synthesized if there is a desire to use it.

Unfortunately, there are difficulties with trying to implement hydrogen as an energy carrier. Since it does not occur in abundance terrestrially, hydrogen must be

synthesized in a process requiring energy. This energy must come from somewhere and currently most primary energy sources derive from fossil fuels. In fact, at present hydrogen is generated primarily from natural gas. It is difficult to prove that using fossil energy to make hydrogen to use as an energy carrier results in less atmospheric carbon dioxide than using the fossil energy as an energy carrier directly. Of course, nonfossil energy sources can also be used to make hydrogen from water, and widespread adoption of carbon-free generation of an energy carrier would be a significant contribution to the reduction of fossil fuel use [2].

Making hydrogen economically from nonfossil-based energy sources is certainly a key part of a sustainable energy strategy, but hydrogen presents certain technological problems as well. While hydrogen has the highest energy per unit weight of any known compound, it has poor energy per unit volume. Consider: hydrogen, H_2, contains about 120 MJ/kg (lower heating value) of energy. A liter of gasoline contains 44 MJ/kg (lower heating value) of energy. A kilogram of H_2, therefore, contains a little less than three times the amount of energy in a liter of gasoline. Also assume that 54 L of gasoline, a typical fill-up for a car, weighs approximately 40 kg. For the same amount of energy, hydrogen would weigh 15 kg. Treating hydrogen ideally at 150 atm, the typical pressure of a steel gas cylinder, 15 kg of H_2 will occupy 1,200 L. Even making some optimistic assumptions, such as increasing the storage pressure to 600 atm and using only 5 kg of H_2 to achieve useful energy equivalence with gasoline because electrochemical fuel cells extract energy more efficiently [3] than combustion engines, the result is still a volume several times that of a standard automobile gas tank. Utility is further constrained by requiring a cylindrical or spherical shape suitable for a pressure vessel, a significant inconvenience for vehicle design.

It is true that discussing the storage of energy for automobiles as the sole application of hydrogen is somewhat narrow minded, but it will be the main example for the immediate future. The reason for this is that a prime source of funding for hydrogen storage research is the United States Department of Energy (DOE), and DOE's focus is automobiles. Since transportation represents a third of the US oil consumption, any technology that successfully reduces carbon emission from this segment of the economy will have immense impact on both the economy and the environment. The major auto manufacturers throughout the world have also contributed significant resources to studying hydrogen storage. As the biggest prize, most of the benchmarking around hydrogen storage derives from transportation considerations. It should not be forgotten, however, that there are many other areas where a hydrogen energy carrier would be worthwhile, even though the thrust of the discussion herein will be on the needs of a transportation fuel.

It is difficult to solve the volume problem physically for hydrogen. Liquefaction of hydrogen results in substantial volume reduction but suffers from the practical difficulties associated with using a fuel at 20 K in a 300 K environment. Hydrogen is a well-studied element, and its behavior under pressure, volume, and temperature conditions (the phase diagram) is well known. These parameters define the required volumes of hydrogen. When storing the element in a container, there is no way to alter them.

Simple pressurization of hydrogen presents a volume issue. Hydrogen gas is nonideal, volume deviating in the positive direction from ideality at pressures not far above standard. Even at room temperature and standard pressure, hydrogen has a negative Joule–Thompson coefficient [4]. This means that the gas is already in a repulsive region with respect to intermolecular forces, and increasing pressure only moves farther into this disfavored condition. The reason is straight forward. Each hydrogen atom has a single 1s orbital associated with it which, in conjunction with another hydrogen atom, forms a bonding molecular orbital filled with two electrons. When two hydrogen molecules are close together, they experience Pauli-type repulsion. Bonding electrons cannot overlap with other bonding electrons, and the only alternative is to populate a high energy antibonding orbital. Thus, hydrogen gas shows significant deviation from ideal gas behavior with volume being higher than expected, with perhaps a 20% increase in volume at the 600–700 bars of pressure required to even consider storage in pressure containers.

Hydrogen molecules must interact with other atoms that provide additional orbitals, allowing hydrogen atoms to get closer together than they otherwise could. The answer is straightforward to state, if proven practically difficult to achieve. This introduces another part of the storage issue that whichever atoms are chosen for the interaction cannot too far outweigh hydrogen, so that the solution to the volume problem is to trade it for a weight problem. The last major factor is that after the hydrogen atoms are brought close together by some favorable electronic interaction with another atom, it must be convenient to regenerate free hydrogen for later use. The object of storage research has been to find this balance between volume, weight, and efficacy.

Two paths suggest themselves, illustrated in Scheme 1: the H–H bond in the gas could be broken, and the hydrogen atoms bound to some other molecule. Then, under the right set of conditions, the H-molecule bond is broken and the H–H bond is reformed. The other option is that the H–H bond could be left intact, but the molecule allowed to interact with another atom or molecule via a weak overlap of orbitals. This generally suggests a substrate or surface, and on the surface H atoms could be nearer to each other than Pauli repulsion would allow in the gas phase.

The remainder of this discussion will consider these other storage ideas.

The history of hydrogen storage is instructive, and a brief discussion is useful. First, physisorption ideas will be discussed. Then, what began as the absorption of hydrogen molecules into bulk materials underwent evolution into molecular

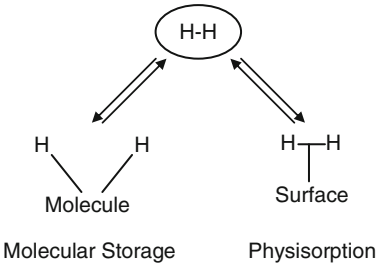

Scheme 1 Free H_2 molecules must interact with a surface, or dissociate into covalently bound H atoms

methods, wherein hydrogen atoms in discrete molecular species can be induced to combine and yield the gas. To gain a simple understanding of molecular storage behavior, the properties of binary compounds containing a light element and hydrogen are described. Molecular storage systems often exhibit hydrogen release behaviors related to those shown by the binary compounds of the atoms in the molecule with hydrogen. A few key advances in the molecular storage approach are particularly highlighted.

1 Brief History of Hydrogen Storage: Absorption

If simple compression of hydrogen is untenable as a broadly applicable storage method because the systems are overly large, other methods need to be found. Hydrogen makes bonds with nearly every element in the periodic table and, through bonding, hydrogen atoms can be pushed closer together than by physical compression. As such, there was considerable interest in a materials science solution to the volume problem outlined for the compressed gas. An approach was already known from a property of palladium metal. It was discovered in 1866 that palladium would absorb 900 times its own volume [5] in hydrogen gas at room temperature, forming PdH_x.

The palladium lattice has a face-centered cubic (fcc) structure. The fcc contains octahedral holes, a gap formed where six individual Pd atoms come together. There is one octahedral hole per Pd atom, and at standard pressures, up to 70% of the holes are occupied by hydrogen. At elevated pressures, further uptake will be observed until Pd and H exist in an approximately one-to-one ratio. Although retaining an fcc structure, the lattice does swell as hydrogen atoms enter. The metallic conductivity decreases with increasing hydrogen content, and eventually becoming a semiconductor. This indicates a disruption of the typical omnidirectional bonding of a metal, as the orbital contribution of hydrogen influences the structure. Diffusion of hydrogen atoms within the lattice is fast and the absorption is reversible. If heated, the hydrogen atoms will exit the metal and reform the gas [6]. Reversibility is a critical feature, as a system which stores hydrogen without convenient recovery will be of little utility.

With respect to the volume issue, palladium offers a solution. Consider the 5 kg of H_2 absorbed into Pd would yield a volume of 67 L and little different from the 54-L gasoline tank. Since the H_2 is not pressurized significantly, the cylindrical shape constraint is also removed. Of course, upon absorption of the gas, palladium swells and occupies greater volume, and the metal does not perform best as a monolithic block but as particles. These aspects increase the required volume, but clearly the volume and geometry issues facing compression technologies can be addressed via hydrogen absorption.

Realistically, as a precious metal palladium cannot be used to store hydrogen for economic reasons. In 1970, it was reported [7] that a far less expensive material would store even more hydrogen than palladium, and in a similar fashion. Lanthanum nickel ($LaNi_5$) was one of the first examples of an intermetallic compound that

absorbed hydrogen in a way similar to palladium at room temperature. In these compounds, like in the palladium example, hydrogen atoms reside in the interstices of the metal atom lattice and are thus called interstitial hydrides. On absorption of hydrogen, the compound stoichiometry is close to $LaNi_5H_6$ suggesting one hydrogen atom per metal atom, and ideally only 40 L of volume is required for 5 kg of H_2 storage.

The weight of $LaNi_5$ presents a problem. As noted above, addressing the volume issue merely by replacing it with a weight issue is not a solution. Lanthanum nickel is a reasonably dense material, and 360 kg of lanthanum nickel is required to store 5 kg of H_2. Conveniently, in many adsorption compounds the weight percent hydrogen is easily computed by taking the molecular weight of the hydrogen in the formula and dividing by the molecular weight of the hydrogenated compound.

$$\text{wt.\% H}_2 = \frac{\text{Mass H}_2}{\text{Mass Storage Media} + \text{Mass H}_2} \times 100\%$$

For $LaNi_5H_6$, the hydrogen is 1.4% of the molecular weight, and the storage capacity is thus reported as 1.4 wt.% H_2. This 360 kg is only for the hydrogen storage materials and is a troubling amount considering that it does not include the remainder of the systemic apparatus that is necessary to release the hydrogen.

Interstitial hydrides have an analogous issue with weight that compressed hydrogen has with volume. The problem is less obviously insoluble than the pressurized hydrogen case, wherein well establish elemental properties of hydrogen dictated what was available. In the three decades or so following the identification of $LaNi_5$, researchers discovered over two thousand additional interstitial hydrogen storage compounds [8] with the primary goal of using lighter elements to achieve the same results. A large number of compounds were found to be superior to $LaNi_5$ on a weight basis; however, very few exceeded 2 wt.% and did not adequately solve the weight issue. New ideas were needed.

2 Physisorption

In the late 1990s, a sea change in thinking was underway. Identifying an absorptive metal with adequately low weight had proven challenging, and a new approach was gaining traction. A gas in contact with a surface adheres to that surface. Perhaps large amounts of hydrogen could be adsorbed onto very high surface area carbon structures. Some very promising early results [9] stimulated interest in this area, but quickly became the topic of controversy as researchers tried to duplicate the reported storage capacities. Numerous carbon structures were tested: activated carbon, carbon nanotubes, multiwalled carbon nanotubes, graphites, and expanded graphites, among others [10]. Various catalyzing metals and approaches were also used to improve storage capacity and adsorption and desorption kinetics. In the end,

carbon structures appeared to work best at temperatures in the liquid nitrogen range, at which a few percent by weight hydrogen could be stored.

The failure of carbon to deliver sufficient storage capability can be understood by considering the binding energy of hydrogen to a graphite-like structure. The interaction between hydrogen and the graphite is an induced dipole-induced dipole. The energy of such interactions falls as the inverse of distance raised to the sixth power, and depends also on the polarizability of the interacting species. As such, the energy binding hydrogen to the carbon surface will be:

$$E_{\text{surf}} - \text{H}_2 \sim \frac{\alpha_{\text{H}_2}\alpha_{\text{surf}}}{R^6}.$$

At flat carbon, the energy of interaction will be about −5 kJ/mol [10]. At this strength, equilibrium would favor the gas at standard temperatures with limited physisorption on the surface, and only favor condensation on the surface at reduced temperatures. In 2006, Bhatia and Myers derived a thermodynamic relationship to predict the optimum binding energy for adsorptive storage of hydrogen at room temperature [11].

$$\Delta H_{\text{opt}} = T\Delta S^{\circ} + \frac{RT}{2}\ln\frac{P_1 P_2}{P_0^2}$$

In this equation, P_1 is the storage pressure, P_2 is the exhaust pressure, and P_0 is the standard pressure. If the temperature is to be 298 K, Bhatia and Myers predict that the optimal adsorption energy should be about −15 kJ/mol H_2. Subsequent work suggests that the entropy term might have been underestimated and the optimal binding energy for room temperature physisorption might be as high as −25 kJ/mol [12].

For carbon to succeed, the binding energy must be increased by a factor of about three to five. The polarizability, α_{H2}, of hydrogen gas molecules is not a variable parameter; so the only available lever to influence energy of the interaction would be the polarizability of the surface, α_{surf}. The pi-systems of a graphite layer are polarizable, and applying curvature to the surface would change the value of α_{surf}. Dopant molecules could also influence the polarizability. Unfortunately, none of these modifications has a sufficient impact on α_{surf} to make room temperature surface bound hydrogen a stable state, even at elevated pressures.

Many of the early reports of high storage capacity were the result of water or other impurities in the matrix rather than hydrogen gas [13]. The most recent considerations of carbon structures confirm that for storing significant amounts of hydrogen, carbon is not up to the task [14]. Fortunately, the idea of storing hydrogen on surfaces expanded to new high surface area structures. High surface area materials referred to as metal-organic frameworks, or MOFs, have emerged as a new physisorption material [15]. MOFs are coordination polymers, wherein metal centers are connected together by organic molecules. The structures formed are three dimensional, crystalline, and have high internal surface areas.

The prototypical MOF might be $Zn_4O(BDC)_3$ where BDC is the dianion 1,4-benzenedicarboxylate. This compound is referred to as MOF-5 [16]. MOFs in general have fascinating structures. MOF-5 forms open cubes, with the BDC ligands forming the edges. Each corner is a Zn_4O cluster. In such a structure, there is open space in the center of each cube. The surface area is very high, each ligand is essentially surface.

As a hydrogen storage option, the MOFs are attractive because in addition to the high surface area, and physisorptions of the type observed in the carbon structures, the framework can incorporate coordinatively unsaturated metal centers, and these metal centers can form sigma bonds with H_2 molecules. The molecule does not dissociate into a hydride at the metal, but remains a molecular ligand. Indeed, MOF-5 takes in 7.1 wt.% H2 at 77 K and 40 bar.

The promise of MOFs for improved storage performance over carbon is high. In contrast to carbon, there are many levers to pull in the design of an MOF structure. There is the choice of the ligand itself; it can be longer or shorter, which would change the size of the void spaces in the structure. It can be more or less polarizable, depending on its structure and the elements incorporated. It can coordinate to a metal differently or have more than two coordination sites. Either of these changes will have significant impact on the ultimate shape and stability of the framework. The choice of metal is another parameter, along with its oxidation state. Different metals will have differing degrees of unsaturation, influencing the strength and number of M–H_2 interactions. At the same time, the metal will affect the electronic structure of the ligand. It is also possible to use more than one metal or more than one ligand to further vary the structure.

With multiple methods of holding hydrogen, through physisorption and ligand formation, and the varied synthesis parameters, the number of possible structures seems infinite. In less than a decade since being first suggested as a storage medium, hundreds of different structures have been reported. A recent review [17] contains an extensive listing of MOFs, with information about surface area, pore volume, and H_2 storage properties.

MOFs are interesting because unlike the high surface area carbon, the energy of the interaction between hydrogen and unsaturated metal is tunable by changing the framework and changing the metal. A typical binding energy for an MOF is approximately -6 kJ/mol H_2 [18], and with the tools available might be modified to -15 to -25 kJ/mol range forecast as optimal. It does appear that cleverly designed MOFs can be brought near this optimal value. If the framework uses lightweight elements, a very high performance storage material might be found.

The binding energy in the typical MOF comparable to that of carbon suggests that hydrogen uptake will be best at reduced temperatures. Indeed, at liquid nitrogen temperatures, MOFs have shown hydrogen storage capacities of 10 wt.% H_2 [19]. These same MOFs at room temperature will hold only 1–2 wt.% hydrogen or less, so the ability to modify the binding energy in clearly of top importance in the field of hydrogen storage by adsorption. Excellent reviews of these topics has been written by Dincă and Long, leading researchers in this field [17, 18].

3 Binary Compounds of Hydrogen

At the start of the 1990s, it was clear that the traditionally studied metal hydrides could not be of low enough weight for practical H_2 storage. Using the simple formula for weight percent and the periodic table, one could deduce that no hydride based on a one-to-one atomic ratio between hydrogen and a transition metal could deliver the hydrogen storage potential needed for a practical system. Researchers could ask the simple question of which elements would be acceptable? Are there any compounds of light elements with hydrogen that might be used to supply the gas?

Looking at hydrogen content as a function of molecular weight finds hydrogen-rich molecules in the second row of the periodic table. All of the binary compounds with hydrogen LiH, BeH_2, B_2H_6, CH_4, NH_3, H_2O, and HF are worth considering, although some can be dismissed due to reasons associated with the properties of the compound, and not hydrogen storage utility.

3.1 Lithium Hydride

Across the row from left to right, the bonding between hydrogen and the element changes character from ionic to covalent and back to ionic. The first case, lithium hydride, the hydrogen is the anion of the salt. The molecular weight of LiH is 7.95 g/mol and has a density of 0.82 g/mL [4]. As such it stores 12.7 wt.% H_2 and 0.1 kg H_2/L. Lithium hydride is stable, and under proper conditions can be stored for long period of time without decomposition. This is the good news. The difficulty is that the stability of lithium hydride suggests a very strong interaction between lithium and hydrogen. For carbon structures and MOFs, the binding interaction was too weak, and at standard temperature hydrogen favors the gas. Lithium hydride has the opposite problem. The interaction is much too strong, and the decomposition of the compound into the elements takes place at about 850°C [20]; so hydrogen cannot be conveniently accessed in this way. The compound is synthesized by direct reaction of the elements. If a molecular solution to hydrogen storage is found, it is likely that lithium will be a part of that solution. As will be discussed later, lithium plays a key role in some of the important developments of the last few years in molecular hydrogen storage. LiH is the only binary compound that lithium and hydrogen form.

3.2 Beryllium Hydride

The bonding between beryllium and hydrogen is covalent, although it is reasonable to consider the compound salt-like and the hydrogen atoms as hydrides, although less so than in lithium hydride. The molecular weight of beryllium hydride, BeH_2, is

11.03 g/mol. Beryllium hydride contains significant amounts of hydrogen, 18.3 wt. % H_2, and 0.12 kg H_2/L. Beryllium hydride decomposes at an intermediate temperature of about 250°C [21]. Despite the favorable properties with respect to hydrogen, beryllium is not generally considered for hydrogen storage. The reluctance is twofold: Beryllium is a rare element, suggesting that it would be costly to use, and it is toxic, particularly by ingestion. Since it is easy to imagine that a solid-state hydrogen storage system will use powders to enhance surface area and improve kinetics, beryllium dust would be a legitimate concern.

3.3 Boron Hydride

Traveling across the second period beyond beryllium leads to boron. Diborane, B_2H_6, is a dimer of the BH_3 monomer. The isolated monomer is not observed. The bonding is covalent and contains hydrogen "bridges," wherein the pair of electrons bonding the hydrogen is shared between more than one boron center. Hydrogen is more electronegative than boron; so the hydrogen atoms in boron–hydrogen compounds are hydridic in nature. Diborane is 22% hydrogen by weight, making it nearly the equivalent of methane in terms of hydrogen storage capacity. Diborane is a gas, so the volume of storage would be a problem. The compound is highly toxic and also pyrophoric in air. These two issues rule out diborane as a storage material but not all boron hydride-containing compounds. Boron and hydrogen form many compounds, having a wide variety of structures [22, 23]. Even when using boron hydrides and not diborane, the possibility of forming diborane must be addressed when considering boron hydride compounds in hydrogen storage systems. Diborane has a positive heat of formation [4], indicating that it is favored thermodynamically to decompose into the elements. In practice, thermal decomposition does not result in the elements, but rather yields higher boron hydrides that are more stable than either diborane or the element [22].

Boron hydrides provide rich chemistry. The diborane molecule itself shows interesting bonding characteristics. The monomer is electron deficient, meaning that it does not fulfill the octet rule that dominates second period chemistry. To make up for the deficiency, the borane monomer dimerizes by sharing bonding electrons in B–H bonds and forming hydrogen bridges. These bridges and multicenter bonds dominate boron chemistry. Many boron hydride compounds are far safer than diborane with respect to both toxicity and reactivity. Of particular importance are the boron clusters. The willingness of boron hydrides to form structures where there can be a boron–boron bonds, boron–boron bonds bridged by a hydrogen atom, boron atoms bridged by hydrogen but not bound to each other as in diborane, and boron–hydrogen covalent bonds (illustrated in Scheme 2) is now a key part of molecular style hydrogen storage research. Boron hydride compounds are among the most promising of materials for hydrogen storage under consideration today.

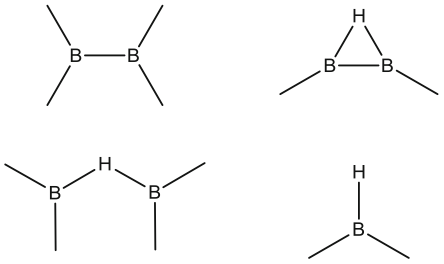

Scheme 2 Boron hydride structures. B–B covalent bond, hydrogen bridges with and without a B–B bond, and B–H covalent bond

3.4 Hydrocarbons

Methane is covalently bound and the most hydrogen-rich compound of the group. Technology for removing H_2 from CH_4 is well established, but does not address the basic question of reducing or eliminating hydrocarbon energy carriers from the world economy. Methane, CH_4, or natural gas is 25% hydrogen by weight, and the hydrogen can be extracted by steam reformation. It is a primary energy source and carrier and occurs abundantly in nature. Combining methane and steam is the standard economic approach to hydrogen generation. The side product of CO_2 being generated on a global scale now shows changes to Earth's environment. This is the motivation for trying to solve the hydrogen storage problem and replace natural gas and other fossil fuels as energy carriers.

This does not mean that hydrocarbon compounds cannot be part of an elegant energy solution or an approach to storing hydrogen. An older storage idea involving hydrocarbons is exemplified by the thermal decomposition of the methyl cyclohexane molecule, C_7H_{14}, to toluene, C_7H_8 [24]. The methyl cyclohexane molecule has a molecular weight of 98.19 g/mole and yields 3 mol of H_2 per mole of methyl cyclohexane. Thus hydrogen storage capacity is 6.2 wt.%. This particular carbon hydrogen system is complicated by volatility of the reactants and products and the need for catalysis, but is a good example of an approach to hydrogen storage using hydrogen–carbon bonds. Cooper, Pez et al. [25] have found that many carbon rings and heterocyclic compounds can be reversibly hydrogenated and dehydrogenated through a mild endotherm. At present, a precious metal catalyst is required. By changing the number and arrangement of the rings, and incorporating hetero atoms, properties like the size of the endotherm, the boiling point of the products and reactants, and the amount of hydrogen that can be stored are tunable.

3.5 Ammonia

Ammonia, like borane, is very promising for hydrogen storage, and nitrogen–hydrogen bonding is at center stage in current research for molecular hydrogen storage solutions. Concentrating on the ammonia molecule specifically for a

moment, ammonia as a storage molecule can be assessed. Among the positives, ammonia is produced at a commodity scale and is inexpensive. Ammonia is a gas but liquefies easily under modest pressure. It is nearly 18% hydrogen, and made by reaction of the elements over an iron catalyst in the Haber–Bosch process. Decomposition back to the elements over a catalyst is possible, and if a high performance "ammonia cracker" can be engineered ammonia could potentially be a solution to hydrogen storage. Unfortunately, the decomposition reaction is not complete, and fuel cells have proven very sensitive to ammonia in the hydrogen [26]. Sufficient removal of ammonia (below 1 ppm) from the hydrogen has been difficult to achieve outside of an industrial processing environment. Thus far, the effective separation of hydrogen from ammonia and nitrogen in the product stream has been the downfall of ammonia as a storage option.

Nitrogen and hydrogen do not exhibit the rich variety of chemistry that boron and hydrogen do. The only other relevant molecule is hydrazine, N_2H_4, which can be decomposed to the elements like ammonia. Hydrazine is also toxic and can be shock sensitive. Looking more widely at nitrogen–hydrogen-containing compounds, the bonding between hydrogen and nitrogen is covalent, but the electronegativity of nitrogen is sufficient that the hydrogen is protic. Having protic hydrogen in one molecule and hydridic hydrogen in another allows researchers to take advantage of acid–base type reactions that make hydrogen as a product. Following this simple logic leads to combining ammonia and borane, one of the most active areas of hydrogen storage research today, to be discussed below.

3.6 Water

Water contains 11% hydrogen, which can be extracted using electricity, but is challenging to accomplish thermally or catalytically. The bonding in water is such that hydrogen is protic, and in the liquid the hydrogen is networked through hydrogen-bonding interactions. By itself, there is no expectation that water will be a hydrogen storage option, but it can be a hydrogen-rich source of protons for reaction with hydrides. Water plus hydride reactions are the basis of the highest weight percent storage *systems* that have been designed for vehicular scale to date. This idea will also be discussed in some detail later.

3.7 Hydrofluoric Acid

Hydrogen fluoride, HF, contains the least hydrogen of the second row elements. Skin contact with HF is very painful and can cause significant injury, or even death. Bluntly stated, HF is a dangerous compound and should only be used in carefully controlled environments, and not in consumer-accessible products like fuels. The salts of fluorine are safer, but the acid is generally not worth working with for hydrogen storage applications.

3.8 Heavier Elements

The third period of the table also contains elements light enough to satisfy the weight requirements. From left to right, we first find sodium hydride, NaH. Hydrogen can be liberated from the compound thermally, but like lithium only at high temperatures [4]. Hydrolysis methods have been proposed for hydrogen release from sodium hydride [27], but the amount of hydrogen stored in NaH is below 5 wt.%, so it is unlikely to be a workable hydrogen storage solution on its own. Combined with other lighter elements, sodium might be part of a solution.

After sodium hydride comes magnesium hydride, MgH_2. This is a promising component for a hydrogen storage system at 7.66 wt.% hydrogen, but thermal stability of the compound makes it unsuitable by itself. Magnesium was perhaps the first light element to be considered during the period in which interstitial hydrides were of interest. Under 200 atm of pressure, magnesium will take up hydrogen to form MgH_2, having a storage capacity of 7.66 wt.% [28]. Weight (60 kg of Mg to hold 5 kg of H_2) and volume (45 L) parameters are respectable. Like lithium it is too stable, it can release hydrogen only if heated to 300°C. This is an inconveniently high temperature for any application where the magnesium hydride is expected to act as energy storage. A proton exchange membrane fuel cell operates at 80°C [3], significantly below the temperature required to release hydrogen. The fuel cell could supply electrical heat to make up the difference, but the endotherm of dissociation of MgH_2 into the elements (71 kJ/mol H_2) is 30% of the energy contained in the hydrogen (237 kJ/mol H_2). Including the inefficiency of the fuel cell (e.g., 50%) the majority of energy stored is used up just to release the hydrogen. Alloying the magnesium with other metals has not substantially lowered the reaction temperature [8].

Like sodium, magnesium may find use as a cation in another system. Both sodium and magnesium are interesting as stable hydrides, capable of acting as hydride donors to other materials. A reversible system that is rich in hydrogen may find sodium hydride or magnesium hydride as a product material, thermodynamically capable of rehydrogenating the other atoms under elevated temperature and/or pressure. This will be addressed further below.

AlH_3 is an interesting material for hydrogen storage from a weight and volume point of view. It contains 10 wt.% hydrogen and exists as a polymeric solid with a density of nearly 1.5 g/mL [29]. Hydrogen can be liberated thermally. The difficulty is the regeneration of the AlH_3, for which there is no practical industrial synthesis. It is generally made in small batches and used for organic transformation. Aluminum hydrides have excellent potential to be a part of the solution to hydrogen storage and remain a key topic of research, as AlH_3 specifically but also a promising component of more complex systems [30–34].

Silicon hydride (SiH_4), or silane, is isostructural with methane. It contains 12.5 wt.% hydrogen and exists as a gas. As a gas, silane is unlikely to have sufficient density to store hydrogen in a reasonable volume, but like other third period elements the number of hydrogen atoms that can bond to a single silicon

atom is sufficiently high that in conjunction with other elements silicon may be part of the solution. Phosphorus combines with hydrogen to make phosphine, PH_3. Phosphine stores a respectable 8.8 wt.% hydrogen. It is a gas at room temperature, and as in period two, it is sufficiently to the right side of the period table that the hydrogen atoms in phosphine are protic. Phosphines are like the other period three elements that bond multiple hydrogen atoms, a potential part of a solution, but are less widely considered than nitrogen, for example.

The only other elements storing capable of contributing nearly 5 wt.% or more to hydrogen storage capacity that might also be reasonably considered are sulfur, calcium, and titanium. This is not to say that other elements should be discarded automatically, but they should best be considered minor components or catalytic materials to facilitate hydrogen storage by lighter elements.

As the brief survey indicates, there is no single element whose hydride is an appropriate material for hydrogen storage, with boron and nitrogen perhaps being the closest. Interestingly, despite the high hydrogen weight percentage and good densities, compounds made up of only light elements and hydrogen were not under strong consideration in the early 1990s, and research focused tightly on finding lighter weight interstitial hydrides. Perhaps this was because storage capacity benchmarking by funding agencies had not yet gained traction, and DOE requirements that storage capacity be 6 wt.% (or 5 kg H_2 in 83 kg of storage, established as a target in 2003) and later on 9 wt.% (5 kg in 56 kg, established in 2006) [35], were not as firmly entrenched as they are at present. The well-known examples of light element, multimetal hydride compounds are the alanates ($LiAlH_4$, $NaAlH_4$, $Mg(AlH_4)_2$, etc.) and tetrahydridoborates (also called borohydrides, $LiBH_4$, $NaBH_4$, $Mg(BH_4)_2$, etc.). Differing substantially from the interstitial hydrides and generally thought to behave similarly to magnesium hydride, these molecules are salts where the anion is aluminum or boron in the +3 oxidation state covalently bound to four hydrogen atoms formally in the -1 oxidation state. As shown, the cations are generally alkali metals or alkaline-earth metals. Other metal cations are possible. The compounds are referred to as complex hydrides or chemical hydrides.

4 The Storage of Hydrogen in Molecules

In 1990, the focus was primarily on interstitial hydrides and the complex hydrides were not known to function as interstitial hydrides did, i.e., releasing hydrogen under heating and taking up hydrogen under pressure. As molecular entities, it was far from obvious that they should behave this way, and in fact most do not. Most of the complex hydrides were known to react readily with water however, and this was considered a potential hydrogen storage option. An unfortunate incident involving the reaction of sodium borohydride and water led to injuries at a plant in Massachusetts [36], and hydrolysis methods were apparently out of consideration.

Interestingly, concurrent with the new focus on high surface area structures for physisorption of hydrogen, three key observations changed the thinking on complex

hydrides for hydrogen storage. The 1997 disclosure by Bogdanovic and Schwickardi [37] that at least one complex hydride, $NaAlH_4$, would behave like an interstitial hydride if properly catalyzed brought alanates to the consciousness of the hydrogen storage community primarily focused on interstitials. This report was essentially the beginning for molecular hydrogen storage approach over hydrogen absorption. In 1998, Amendola reconsidered the hydrolysis of sodium borohydride with the formation of Millennium Cell Inc., and demonstrated that proper methodology resulted in a far safer hydrogen generation system [38, 39]. Progress in the systemization of borohydride plus water reactions solved both the toxicity and pyrophoricity problems of borane, restored boron to the forefront of thought. In 2002, Chen introduced a new player to the hydrogen storage field, the lithium amide/imide system [40]. Chen's work was unique, as the hydrogen atoms on the central nitrogen atom are protic, whereas nearly everything prior was a hydride. Each will be considered in turn.

4.1 Catalyzed Molecular Decomposition, and the Importance of Aluminum

Bogdanovic describes in the introduction of his paper introducing reversible hydrogen storage in Ti-catalyzed $NaAlH_4$, how it was known that the complex hydride could be synthesized from the elements and also that $NaAlH_4$ will decompose to NaH, Al, and H_2 according to a two-step reaction scheme.

$$3NaAlH_4 \rightarrow Na_3AlH_6 + 2Al + 3H_2 \quad (1)$$

$$Na_3AlH_6 \rightarrow 3NaH + Al + 1\,1/2H_2 \quad (2)$$

He rationalized correctly that it ought to be possible to accomplish both desorption of hydrogen and rehydrogenation in the same system, and discovered an effective catalyst for doing so. It is somewhat disappointing that of the four hydrogen atoms associated with $NaAlH_4$, only three are released at reasonably low temperatures, reducing the actual hydrogen storage capacity from 7.5 to 5.6 wt.%. Even considering the reduced storage capacity, the fact that the dehydrogenation took place at 200°C with three times the hydrogen capacity of a typical interstitial was a considerable breakthrough. Sodium aluminum hydride was performing essentially as previous researchers had hoped that MgH_2 would. A substantial body of literature would follow Bogdanovic's report, analyzing sodium aluminum hydride, other alanates, and related compounds like the borohydrides [41]. Later research would eventually show that for $NaAlH_4$, dehydrogenation could be accomplished at temperatures as low as 80°C [42]. Dehydrogenation at fuel cell temperature represented a major milestone in molecular hydrogen storage research.

From the consideration of the elemental behavior of sodium and aluminum with hydrogen, one can get a simplified view of the behavior of sodium aluminum hydride. Sodium aluminum hydride is often thought of as a salt of sodium cations and $[AlH_4]^-$ anions. It is worthwhile though to reconsider sodium alanate an acid–base adduct, where aluminum hydride is the acid, and sodium hydride is the base. This idea of considering hydrides as acid–base adducts is not new. Indeed, it was the guiding principle of the original research on boron hydride and aluminum hydride chemistry [43]. It does not explain all things, but provides a very useful conceptual picture of light metal-hydride chemistry.

X-ray crystallography performed on sodium alanate systems shows a distortion of the lattice as the temperature is raised [44]. Hydrogen is not well resolved in this technique, but one might imagine the driving force to be the formation of NaH and AlH_3. Using aluminum NMR techniques, Balema actually observed the formation of NaH [45]. The formation of a stable product, NaH, is likely a key factor in the overall behavior of $NaAlH_4$. From this viewpoint, that the dehydrogenation of $NaAlH_4$ stops after liberating three hydrogen atoms is to be expected. NaH is stable to significantly higher temperatures, so it remains while AlH_3 is easily decomposed to the elements. Rehydrogenation takes place because NaH has the reducing power to hydrogenate Al, with which it is already intimately mixed, and Na metal is readily hydrogenated to the hydride by direct reaction of the elements. Under hydrogen pressure and at elevated temperature, it is found that rehydrogenation occurs, and restoration of the starting compounds is observed. Catalysis obviously plays a crucial role, but the simplest ideas can be understood from the behavior of the elemental hydrides.

A key question regarding the progress of thermal decomposition of complex hydrides is the differences in the behavior of sodium aluminum hydride, lithium aluminum hydride, sodium borohydride, and lithium borohydride. The latter three compounds all contain more hydrogen per unit weight by virtue of having lower molecular weight, but none of the three reversibly dehydrogenates and rehydrogenates the way sodium alanate does. The structures of all four molecules are superficially similar, having an alkali cation and an anion comprised of a central atom and four hydrogen atoms in a nominal tetrahedron arranged about the center. Similarities end there with each having a different crystal structure [41, 46, 47].

When the sodium atom in sodium aluminum hydride is replaced with a lithium atom, it is found that lithium aluminum hydride readily dehydrogenates, with faster kinetics and at lower temperatures than the sodium species [48, 49]. One might conclude that the decomposition is related to the aluminum component of the anion, especially because structural analysis of the decompositions shows that there is a stable intermediate of AlH_6^{3-} in both the lithium and sodium cases. The faster kinetics and lower decomposition temperature are also expected, as lithium hydride is substantially more stable that sodium hydride, with stability measured by the heat of formation of each molecule [50].

At this point, one might also conclude that rehydrogenation is dependent on the cation, as this is where the behavior of the molecules differ. As before, consider the rehydrogenation in light of the behavior of the elements with hydrogen. Lithium hydride can reduce aluminum metal but rehydrogenation does not occur easily.

Returning again to the acid–base adduct thought model, the intermediate of the dehydrogenation and rehydrogenation Li_3AlH_6 can be loosely considered a coordination compound between three basic LiH molecules and an acidic AlH_3. It is found that for the reaction:

$$Li_3AlH_6 + 2Al + 3H_2 \rightarrow 3LiAlH_4 \quad (3)$$

the enthalpy change is positive and entropy change negative, and it cannot be expected that the reaction will take place [51]. The greater stability of LiH over NaH might be the difference, as eventually two of the three Li–H bonds would have to decompose to yield $LiAlH_4$.

Looking again at $NaAlH_4$, another interesting atomic substitution can be made. Replacing aluminum with boron to give sodium borohydride gives almost the same improvement in hydrogen storage capacity measured by weight percentage as replacing sodium with lithium. Sodium borohydride, however, does not behave the same way as sodium aluminum hydride when it comes to decomposition. Earlier, it was speculated that aluminum chemistry might be the controlling factor for dehydrogenation, and boron chemistry is significantly different from aluminum chemistry. Aluminum is a metal, and after the release of hydrogen, the covalent bonds between hydrogen and aluminum are replaced with metallic bonding as the metal is formed. Boron is a nonmetal, and elemental boron is covalently bound, with bonds between atoms highly directionalized. The strength of a B–H bond (−389 kJ/mol) is greater than an Al–H bond (−272 kJ/mol); so greater stability for the borohydrides is expected [52]. As a second period element, boron also lacks d-orbitals. The intermediate of the alanate decomposition is the AlH_6^{3-} moiety, and as a six-coordinate species, the bonding must involve contribution from d-orbitals. Having no d-orbitals, boron cannot go through an analogous BH_6^{3-} intermediate and one imagines a higher energy barrier to molecular rearrangement, accompanied by slower kinetics due to the higher energy barrier, than in the aluminum case. Boron hydrogen chemistry is much richer than aluminum hydrogen chemistry, with many known boron hydrogen compounds which might be preferred products over the elements, just as in the case of diborane.

Unlike aluminum, boron hydrides turn out to be quite stable, with sodium borohydride stable up until about 400°C, and requiring another 100°C of additional temperature before decomposition becomes rapid. The thermodynamic stability of boron cage compounds is well known, and these are likely products for decomposition of sodium borohydride rather than complete elimination of hydrogen to yield the elements. When diborane thermally decomposes, a spontaneous process at room temperature, the products are higher boranes and hydrogen, and not elemental boron [53]. Recalling the behavior of the elemental hydrides one finds the propensity of boron hydrides to form cages and the instability of NaH at the temperatures that boron hydrides undergo rearrangement. Thus, the expectation that sodium borohydride would decompose as sodium aluminum hydride does is rather low. If thermal dehydrogenation of borohydride is the goal, it would appear that a catalyst is desirable. The function of the catalyst might be to facilitate breakage of the

boron–hydrogen bond (lowering the activation barrier) or disruption of the formation of boron hydrogen cage compounds, or prevention of the closure of such compounds reducing the stability of the product (a pseudocatalytic process, as this change is thermodynamic and not kinetic). If closure of the cage can be prevented through a catalyst or additive, then the compound to be rehydrogenated would have lower symmetry, be less stable, and perhaps possess a lower barrier of activation to the rehydrogenation reaction.

Clearly, of the four lightweight alanate and borohydride choices, lithium borohydride is the most desirable starting material, containing the most hydrogen as a function of weight. Expectations for lithium borohydride thermally decomposing to make hydrogen might be higher than for sodium borohydride, simply based on the stability of LiH giving a thermodynamically favorable product. In fact, lithium borohydride does decompose to form hydrogen but does not decompose all the way to elemental boron, instead landing at $B_{12}H_{12}^{2-}$, the thermodynamically stable closed cage anion [54]. Considering previous discussion, rehydrogenation of lithium and boron compounds to make lithium borohydride would be surprising. In the German patent literature, there is a claim that lithium borohydride can be synthesized from the elements [55], but this has not been readily reproducible [56]. It has been shown recently, however, that pretreatment of the crystalline boron and lithium metal to make Li_xB_y compounds rich in lithium metal and defective boron structures can be hydrogenated, at least partially, to lithium borohydride [57]. The reaction is very slow, taking place on a timescale of days, and does not necessarily result in complete conversion to the borohydride. Lithium borohydride can be synthesized from lithium hydride and certain borates, but not with high yields under conditions amenable to reversible hydrogenation using the gas [58]. As results, these observations are valuable if not immediately applicable, and they are steps in the right direction. The appeal of $LiBH_4$ with 18.5 wt.% hydrogen keeps it an active area of study. The important realization is that it would not be necessary to withdraw all of the hydrogen to have an effective system. Partial dehydrogenation might simplify rehydrogenation, by starting from a less thermodynamically stable dehydrogenated state. It would also be possible to include significant amounts of catalytic, destabilizing, or cogenerating materials without sacrificing so much weight that the system is untenable [59, 60].

Perhaps, the culmination of sodium alanate research was the construction of a kilogram scale system for storage of hydrogen [61]. Including all components, the system stored approximately 1.5 wt.% hydrogen. Note that this actual system stores more hydrogen than the theoretical maximum in $LaNi_5$. The biggest penalties to the weight of the system was that a pressure vessel was still required, as the $NaAlH_4$ does not rehydrogenate until 150 bar, and heat exchangers have to be incorporated into the system to supply heat for dehydrogenation and remove heat during regeneration. A great deal was learned about what it would take to make a reversible hydrogen storage system operate, and overall, the engineering will help guide the future science. In the event that there is a breakthrough using lithium borohydride, the necessary system engineering research will be well underway.

4.2 Hydrolysis Methods, and the Importance of Boron

The other step forward occurring in the 1990s was the catalyzed sodium borohydride hydrolysis system, first put forward by Amendola et al. [39]. Sodium borohydride does have a unique property among the complex hydrides because it can be dissolved in water to make an aqueous solution. If the solution pH is high enough (pH ~ 14), the borohydride will remain in solution, for weeks to months [62]. On contact with a supported, heterogeneous catalyst, the solution undergoes a hydrolysis reaction (4) to yield hydrogen and sodium borate. The hydrolysis reaction is straightforward.

$$NaBH_4 + 2H_2O \rightarrow NaBO_2 + 4H_2 \tag{4}$$

The product shown here is anhydrous sodium metaborate, but in an aqueous system, the product is hydrated. At room temperature, the stable hydrate is $NaBO_2{\cdot}4H_2O$, but a phase change occurs at about 35°C, wherein the stable hydrate becomes $NaBO_2{\cdot}2H_2O$. This species is not a true "hydrate," in which water molecules do not surround an $NaBO_2$ salt, but is better described as $NaB(OH)_4$ [63]. This is also true of the room temperature species, which would be a dihydrate of the tetrahydroxy borate: $NaB(OH)_4{\cdot}2H_2O$. $NaBO_2{\cdot}4H_2O$ melts above 57°C [4]. The exothermic hydrolysis (4) is self-heating and the reaction runs hotter than 57°C, usually at the boiling point of the borohydride/water solution, a temperature that varies with the pressure at which the system operates. The products of the hydrolysis are molten borate hydrates of nonspecific stoichiometry. On cooling, the average amount of water per mole borate is about 2.5–3 moles (Millennium Cell, unpublished results, 2004–2007).

At first glance, lithium borohydride would be a more attractive molecule for hydrolysis because it holds much more hydrogen than sodium borohydride and undergoes reaction (4) just as sodium analog. The methodology cannot be applied to the lithium salt, however. Lithium borohydride does not stabilize in aqueous solutions the way sodium borohydride does even under very basic conditions, and is far less soluble (7% $LiBH_4$ by weight, compared with 35% for $NaBH_4$) [4] in water. These two features prevent lithium borohydride from being conveniently and controllably hydrolyzed in aqueous solutions at a supported catalyst.

The mechanism of hydrolysis is generally thought to involve H^+ and thus the stability of the basic solution [64]. Unfortunately, a second hydrolysis mechanism that is much slower kinetically includes direct reaction between water and borohydride precludes the indefinite storage of sodium borohydride in liquid solution.

Before Amendola's approach, hydrolysis of borohydride was generally accomplished by addition of water to the solid powder. Addition of powder to water has also been considered but it is generally accepted that solids handling is a more difficult engineering task and more prone to failure than liquid handling. During the process of water addition to the solid, the hydrolysis reaction rate is very difficult to control. Rapid at first and then slowing as the conversion of borohydride generated

the very basic sodium borate salts. The borates are also quite hygroscopic and tend to draw water away from the reaction with borohydride. The borate salts form protective layers over the unreacted borohydride. Yield is poor without large excess of water, and adding large excesses of water surrenders control over hydrolysis rate.

The aqueous solution of borohydride solved most of these problems by releasing the hydrogen catalytically. A number of different materials would catalyze spontaneous release of hydrogen from a solution of borohydride. The most effective catalysts for hydrogen release were found to be ruthenium and rhodium. Ruthenium metal is known to dissociate water into H^+ and OH^- at its surface [65], and it is surmised that the formation of H^+ on the metal surface, even in the basic solutions, is key to the observed catalytic activity. Base metal catalysts containing cobalt and nickel and other metals are also effective catalysts, and this body of literature has been recently reviewed [66] and remains an active area of research. Since a number of surfaces effectively catalyze the hydrolysis, other mechanisms involving interaction of the borohydride (rather than water) have also been discussed [67, 68].

One kilogram of aqueous solution that is 30 wt.% in $NaBH_4$ yields 64 g of H_2, or contains 6.4 wt.% H_2. Millennium Cell Inc. demonstrated that such a solution could be used effectively in a continuous operation catalytic reactor and logged a number of hours of testing. In 2007, that company submitted a system design to the United States DOE describing the components needed to construct a hydrogen generator that stored 10 kg of H_2 in 222 kg of system weight [69]. This translates to 4.5 wt.% hydrogen for the system. However, the system was never built. Given the 2001 effort between Millennium Cell and Chrysler Corporation which succeeded in building a 2.2 wt.% system that actually powered a minivan [70], it is reasonable to expect that the system would operate as described. A key difference between older 2001 system and the 2007 system is the inclusion of both a volume replacement scheme, wherein the volume occupied by the fuel is reused to store spent material, and a water recycling scheme, wherein steam generated at the catalyst could be recycled back into fuel storage. These capabilities were demonstrated on smaller scale [71, 72].

One of the reasons it was possible to make an actual vehicle powered by hydrogen produced by sodium borohydride was that the exothermic catalytic approach to hydrogen generation could operate at high rates. The system in the minivan was capable of liberating hydrogen at over 75 g H_2/min, a rate necessary to supply hydrogen to a 75 kW (100 hp) fuel cell under full electrical load. Like the sodium alanate case, there are significant penalties associated with systemization. At the end, sodium borohydride is not being considered for vehicle use [69], even though the 2.2 wt.% system is the highest that has actually been built on the proper scale for automotive use, and the proposed 4.5 wt.% system appears feasible. The hydrolysis products are supersaturated and solidify slowly; so although they do not pose a performance issue, the practical aspects of eventually removing a solid block of dehydrogenated material from a vehicle are a problem. Because the hydrolysis reaction yields B–O bonds as products, among the strongest known covalent single bonds, the hydrolysis reaction is not reversible by applying hydrogen pressure and increasing temperature. The energy intensive process required to break the borate

leaves the economic viability of synthesizing sodium borohydride for use in vehicles open to debate. Implementation of the recycling infrastructure required to reuse the boron products would also be difficult. It should not be forgotten, however, that while transportation is a main focus, there are other applications for hydrogen storage where these issues are not paramount, and hydrolysis methods could be readily used [72, 73].

The alanate system and the hydrolysis systems are the only two molecular hydrogen storage systems to have been scaled up to the kilograms of hydrogen level, and only a hydrolysis system has powered a standard vehicle [74]. It is thought provoking that despite being radically different in mechanism and design, both the sodium borohydride and sodium alanate operational systems actually constructed resulted in system storage capacities of about 30% of the theoretical storage capacity of the starting materials. The proposed 4.5 wt.% system would be 70% of the theoretical value, and it is unfortunate that it has not been built and tested. In battery research, another important energy storage field, it has been found that systemizing a battery chemistry results in about 30% of the theoretical energy stored in the chemical components, independent of the type of battery [75]. If a similar factor of three is the approximate penalty for hydrogen storage, it is a sobering realization that to achieve 5–6 wt.% storage system will require 15–18 wt.%-H_2 starting materials. A >4 wt.% H_2 system containing 5–10 kg of H_2 based on theoretical 6.4 wt.% H_2 borohydride solutions would show that the general limitation seen in energy storage via battery does not translate to energy storage via H_2.

4.3 Electronegative Elements and the Importance of Nitrogen

The third important discovery in molecular hydrogen storage was the reversible uptake of hydrogen by lithium nitride Li_3N by Chen in 2002 [40]. Chen points out in her initial paper that LiN_3 and H_2 were known to generate a ternary Li–N–H species for nearly a century, but the reverse reaction had not been considered earlier. A simple series of chemical equilibrium expressions account for the behavior of the system:

$$Li_3N + 3H_2 \rightarrow LiH + Li_2NH + 2H_2 \tag{5}$$

$$LiH + Li_2NH + 2H_2 \rightarrow 2LiH + LiNH_2 + H_2 \tag{6}$$

$$2LiH + LiNH_2 + H_2 \rightarrow 3LiH + NH_3 \tag{7}$$

Equilibrium favors the products of (5) and the reactants of (7). This means that lithium nitride will react with hydrogen to make lithium imide (Chen's starting point), and that LiH will react with ammonia to make the lithium amide. Reaction (6) can be reversibly pushed back and forth by temperature and pressure swings [40].

The release of hydrogen from lithium amide to make lithium imide via reaction (6) is a reasonably rich hydrogen storage system, storing about 6.4% wt-H_2. As stated before, the system also has the rather unique aspect of having protic hydrogen attached to the nitrogen center. Compare this with the alanate and borohydride systems and many other proposed systems where the hydrogen is primarily hydridic in nature. The lithium amide–imide system is amenable to acid–base analysis. Lithium hydride is the base and lithium amide is the acid, the key components being the hydridic hydrogen atom in LiH and the protic one in $LiNH_2$. Heat activates the reaction between the two to generate hydrogen. The elimination of hydrogen is a neutralization reaction, and the imide product (lithium imide, Li_2NH) is the salt of the conjugate acid (Li^+) and base ($[LiNH]^-$). Similar analogies can be drawn for all three reactions.

Significantly, Chen also demonstrated that the system was not specific to lithium. In the same paper as the initial disclosure, similar behavior was seen using calcium hydride as the base. It would be reported a short time later that the magnesium hydride also performed well [76].

From Bogdanovic's work, the sequel to interstitial hydrides was found using only light, metallic elements in the form of salts and giving several times the hydrogen storage of prior work. This was really the first attempt at molecular hydrogen storage. Amendola's work focused on boron, the noncarbon element with the best capacity per unit weight to make bonds with hydrogen, and resulted in the best systemized hydrogen storage performance to date. Chen's work introduced an electronegative central element and reversible storage of hydrogen using protic species. By themselves, none of these systems was enough to build a generally applicable energy storage unit for transportation, but much recent work in reversible hydrogen storage tries to make use of the best aspects of these systems.

5 Continuing Advances

There is a common lesson to be learned from alanate decomposition, the amide/imide system, and hydrolysis approaches. Sodium aluminum hydride thermal decomposition is reversible as the sodium component remains in place to rehydrogenate aluminum and react directly with hydrogen to form new hydrides. Success was not duplicated in either lithium aluminum hydride or borohydrides because the final dehydrogenated products were too stable for convenient rehydrogenation. It is not reasonable to expect that enough hydrogen pressure can be applied to drive such a favorable reaction in reverse. The approach also does not work with hydrolysis products because they too are stable. Further, it is inconvenient to completely dehydrogenate lithium imide to the nitride because LiH is too stable. Just as the MOF community learned that the hydrogenated frameworks must be stabilized by strengthening the binding with hydrogen, the molecular storage community learned that the hydrogenated state must be of higher energy, or destabilized to provide reversibility, as shown in Scheme 3. This idea actually existed long before

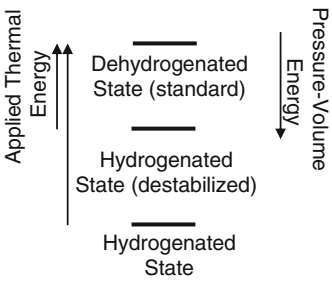

Scheme 3 The destabilized hydrogenated state requires less thermal energy to undergo dehydrogenation. The reverse reaction requires less PV energy in the form of hydrogen pressure to restore the system to the destabilized state

molecular and hydrolysis approaches came into vogue. Reilly and Wiswall outlined the destabilization of hydrogenation products in the late 1960s, while attempting to improve the reversibility of MgH_2 by alloying it with copper and nickel [77, 78]. The idea was revived in 2004 by Vajo and colleagues [79], and elegantly and explicitly codified by Seigal [80]. Management of the energy difference between the dehydrogenated and hydrogenated states is now a guiding principle of contemporary research in molecular methods.

The other important lesson from Bogdanovic, Amendola, and Chen is that the key elements for lightweight, reversible systems appear to be lithium, boron, nitrogen, and aluminum. Boron–nitrogen–hydrogen compounds store significant amounts of hydrogen, so that even incomplete hydrogenation or dehydrogenation will yield significant hydrogen carrying capacity while still allowing control of the stability of the dehydrogenated state. Since 2000, there has been significant interest in the simplest nitrogen boron hydrogen compound ammonia borane, BH_3NH_3. In terms of hydrogen content, few molecules are as rich in hydrogen as ammonia borane, each equivalent yielding up to three equivalents of hydrogen or 19.6 wt.% H_2. It is this richness that led researchers to consider ammonia borane, which had been known as a compound since 1955 [81]. One important feature of ammonia borane that should not be forgotten is that there are two known structures for BNH_6, shown in Scheme 4, even though discussion commonly begins with the assumption of the ethane structural analog. The second structure is a borohydride salt, $[H_2B(NH_3)_2]^+[BH_4]^-$, referred to as DADB for the diammonate of diborane [82].

The formation of the DADB salt comes from the reaction of small, hard bases (like ammonia) with a borane species. Considering B_2H_6, the base induces an asymmetric cleavage of borane into a BH_2^+ fragment, and a BH_4^- fragment [53]. The borohydride is stable, and BH_2^+ coordinates two bases. In the thermal decomposition of amine borane, researchers often see induction periods wherein reactions are slow to begin, and then accelerate later. These induction periods are potentially isomerization of BH_3NH_3 into the DADB salt, followed by further reaction [83].

Softer bases will also react with diborane and cause symmetric cleavage. A typical preparation for ammonia borane from diborane that seeks to avoid the salt structure would be to cleave the diborane symmetrically with a soft base, forming a BH_3:Soft Base adduct. The soft base is then displaced by ammonia to yield the product, in the desired BH_3NH_3 form [53].

Scheme 4 Isomers of BNH_6

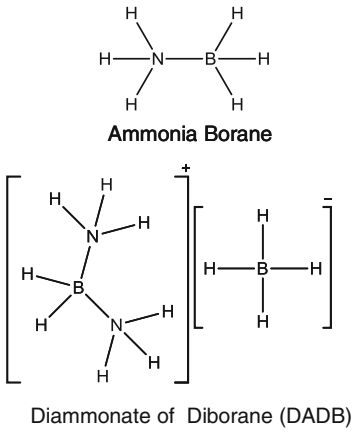

Scheme 5 Thermal decomposition of ammonia borane leads to volatile borazine. The polyiminoborane would be the preferred product

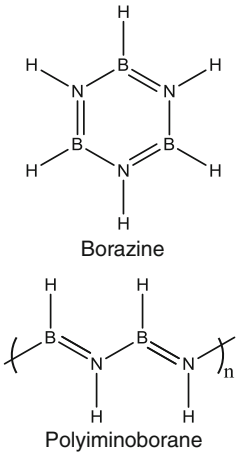

For a reversible system, it is generally considered infeasible to get all of the hydrogen out of amine borane, because the product would be boron nitride (BN). Boron nitride is isostructural with diamond, and the rehydrogenation of boron nitride is about as easy as the hydrogenation of diamond to ethane, an obvious violation of the principle of retaining destabilized products. Thus, the target for ammonia borane is to eliminate two equivalents of hydrogen. The hydrogen evolution reaction is similar to Chen's lithium amide/lithium hydride reactions. It is intermolecular, rather than intramolecular, where the hydridic species on boron in one molecule reacts with the protic species on nitrogen in a neighboring molecule [84]. Ideally, the first dehydrogenation gives polyaminoborane ($[BH_2NH_2]_n$), and the second polyiminoborane ($[BHNH]_n$), shown in Scheme 5. This would be

hydrogen storage of 13 wt.%, adequate for any application. In practice, the thermal decomposition of ammonia borane is not so clean. Side products of the reaction appear to be monomeric aminoborane, BH_2NH_2, borazine $(BHNH)_3$, ammonia, and diborane [85, 86]. Borazine is isoelectronic with benzene and volatile. The volatile product contaminates the hydrogen stream. The rings are toxic to humans and poisonous to fuel cells. The linear polymers, by contrast, are isoelectronic with polyacetylene. The long chains are not volatile, and are thus the goal of researchers in the field.

Simple thermal decomposition of ammonia borane does not perform as required to be a hydrogen storage material, but like $LiBH_4$ the hydrogen content of the molecule is too high to ignore. Even partial H_2 release would be satisfactory for many applications and will probably facilitate the goal of having a reversible system. In the solid state, catalytic decomposition can help reduce the temperature of reaction (the reaction is exothermic, so the molecule is only kinetically stable), and also influence the distribution of products to favor H_2 over the side products listed above.

Research to control the products of ammonia borane decomposition is being carried out using porous superstructures impregnated with the compound. The scaffold seems to provide a respectable catalyst for dehydrogenation of ammonia borane, and the pores are too small to allow for cyclization to borazine. This enforces the linear form and the hydrogen release is very clean [87]. At present, the approach is storing substantially below what is possible; the scaffold contributes 50% of the weight of the storage without contributing any hydrogen storage capacity. The 19.6 wt.% material is thus reduced to 9.8 wt.%. Two of the three equivalents of hydrogen are released from the ammonia borane at moderate temperature, lowering the storage to 6.5 wt.%. Although recent progress has been made on polymeric amino-boranes in general [88, 89], rehydrogenation remains an issue; but the demonstration of controlling hydrogen release through a confining structure spurred additional research on this approach, using a number of high hydrogen content species [90].

Also possible is the solution phase catalysis of ammonia borane into hydrogen and the standard products [91]. As always, the function of the catalyst is to improve reaction kinetics and reduce reaction temperature, and also to promote formation of linear chain products over cyclic products. Organic solvents are somewhat problematic, as the exothermic decomposition leads to evaporation of the solvent and contamination of the H_2 product. Using ionic liquids as solvents is a potential solution to this difficulty [92].

The influence of Amendola and Chen becomes apparent as research on ammonia borane continues. Ammonia borane can be catalytically hydrolyzed in water, much the way Amendola's sodium borohydride can, ideally according to reaction (8):

$$NH_3BH_3 + 2H_2O \rightarrow NH_4BO_2 + 3H_2 \tag{8}$$

Both heterogeneous and homogeneous phase catalysts have been identified [93, 94]. Only half of the hydrogen atoms contained in the molecule, the hydrides

bound to boron, are available for hydrolysis. The hydrogens from water also make a contribution, and in theory the reaction could deliver 9 wt.% H_2. The difficulty of recycling borate to a boron hydride still remains.

Chen taught that acid–base chemistry between LiH and $LiNH_2$ could be used to generate hydrogen. It follows that other hydrides would also act as bases, with properties superior than LiH. For example, lithium hydride certainly performs well with amides, and other simple hydrides such as NaH, MgH_2, and CaH_2 also react with amides to yield hydrogen. It is reasonable then to try complex hydrides with amides to see whether higher yields and better kinetics can be obtained. An explosion of work on precisely this idea followed Chen's disclosure, and she has recently reviewed [95] the progress in this direction while work continues unabated [96]. Instead of simple ammonia borane with ammonia and borane monomer, the borane monomer can be combined with $LiNH_2$ or other amides to make light-weight, hydrogen-rich compounds having different thermodynamics and kinetics from the ammonia borane parent. The simple lithium amide borane acid–base adduct $LiNH_2$:BH_3 will release 10 wt.% H_2 at less than 100°C in 5 h [97]. The hydrogen release is less exothermic, as an overall process, than hydrogen from amine borane. If the lowered exothermicity is shown to be associated with primary reaction step, this could help with rehydrogenation. Sodium and calcium cations have also been shown to make compounds releasing hydrogen, with different thermodynamic properties than either ammonia borane or $LiNH_2$:BH_3 [98, 99]. There is great potential in this approach. Ammonia borane research has been reviewed in the context of a larger review of boron hydride compounds for hydrogen storage [100], and of course by Chen.

6 Theoretical Studies

The total efforts in the field of hydrogen storage resulted in valuable narrowing of the possibilities. Studying the thermal decomposition of compounds such as ammonia borane, lithium borohydride, and more complex Li–B–N systems makes a great deal of sense. It is very good strategy to consider destabilization of product states to lower the energy differences between the reagents and products, enhancing the probability of reversibility. Manipulation of the thermodynamic parameters is a powerful tool, both for screening out losers and identifying promising leads. Simple acid–base thinking outlined here describes why some compounds behave the way they do, starting from the behavior of the binary compounds with hydrogen. Knowledge of the stable states and structures, particularly for boron compounds, allows experimentalists to make reliable guesses about the mechanisms and final products of thermal decompositions. Unfortunately, intuitive thinking and thermodynamic considerations only go so far.

New research needs to consider kinetics and mechanistic pathways. Much of the recent work on storage material outlines compounds that release 7–9 wt.% H_2, but will take hours to do so. The slow kinetics are not a new observation to researchers

in this field. The key question centers on the slowness of the kinetics. If it can be shown, or even rationally speculated, what movements the atoms have to make to perform the transition from the hydrogenated to dehydrogenated species and back, then perhaps the current crop of hydrogen-rich storage systems can be further pared down to those whose reaction pathways might be influenced with clever choices of catalysts or lightweight additives.

From the work performed thus far, the desirable traits of a successful system are known, and the elements to be used have been identified. Still, there are a great many potential compounds to explore. Testing all of them is an untenable proposition, so it falls to theory and modeling to confine the field. Theoretical calculations are becoming an increasingly important and useful guide in both molecular storage systems and MOF systems. With respect to MOFs, similar types of contributions appear in new studies. For example, theoretical calculations suggest that incorporating boron into the pi-systems of the linkers and unsaturated calcium into the structure could result in a framework possessing a binding energy of −20 kJ/mol [101]. This would be quite close to the optimal result suggested by the earlier theoretical work. In the near future, theory will begin to lead experiment, as computation begins to show what should be possible [102].

In molecular storage, recent work predicts a solid boron hydride material, wherein boron chains are held together by hydrogen atoms bound to multiple boron centers on different chains [103]. Bonds of this type are well known in higher boranes, and exploiting them to make network solids instead of compounds appears a worthwhile experimental endeavor.

For molecular systems, Wolverton et al. describe a worthy "must" list for successful modeling work [104]. Models need to:

(1) Accurately predict decomposition thermodynamics
(2) Predict structures for previously unknown molecular hydrogen storage species
(3) Predict preferred decomposition pathways

Any model that can accomplish these tasks will substantially reduce the amount of experimental trial and error researchers must undertake in finding a molecular solution to the hydrogen storage problem. In the work defining this list, successes in each of the three predictions lead to significant revelations about Li–B–N systems, and M–B–N in general [104].

Even with good models, development of effective catalysts, if necessary, will require significant resources. Kinetic issues will also need to be addressed by experimental work, and hopefully by continuing theoretical development. Theory will be a vital part of finding a working solution to hydrogen storage, via any means, molecular or not. It should be also kept in mind that theory is only as good as the model, and the developments by Bogdanovic, Amendola, and Chen came from thinking that differed from their contemporary conventions with a dose of serendipity. In this field, as in many others, theory and experiment exist symbiotically.

7 Toward a Solution

From Bogdanovic, Amendola, and Chen came the ideas of molecular hydrogen storage, aluminum, aminoborane, and Li–B–N systems. The elements Li–B–N represent the limit of the periodic table. A few other elements such as C, Mg, and Al also appear. There are no more elements left to explore, only smarter combinations of those above, sprinkled with a few of the other elements to adjust energies and promote faster reactions. Fortunately, researchers have not reached the end of inquiry. It is more true to say that at this point, having narrowed down to just a few elements, there are more questions than before, but progress will be faster and the answers will be more promising than at any time in the past. All materials under active consideration are very rich in hydrogen, and there is no requirement that a storage material start in fully hydrogen saturated state and/or desorb to fully dehydrogenated elements or alloys. Thus, there is flexibility in the starting point and the endpoint, and finding the right combination will lead to success. Previous experimental discoveries and recent theoretical support will be the guides.

To illustrate, consider lithium and boron. Generally, the first thought is of lithium borohydride, an 18.5 wt.% material. It has been discovered that even within the limit of two elements, one can think more broadly. For example, one could also consider LiB_2H_7 without departing from lithium and boron. LiB_2H_7 actually stores more hydrogen than lithium borohydride, on par with ammonia borane at 19.8 wt.% H_2. The structure is less symmetric and more open, containing a hydrogen bridge between two monoboranes [105]. Perhaps, these features will lead to greater willingness to release hydrogen. LiB_3H_8 stores less hydrogen than lithium borohydride, at 17.0 wt.%, but has a significantly different structure, containing a boron–hydrogen ring (Scheme 6) [106]. The sodium form of this triborohydride species is more resistant to hydrolysis in water than even $NaBH_4$ [107]. This property might ultimately prove useful in systemizing the generation of hydrogen [108].

A similar point can be made for the products of boron hydride dehydrogenations. The most desirable case weight-wise is dehydrogenation to elemental boron, but

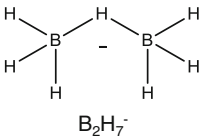

$B_2H_7^-$

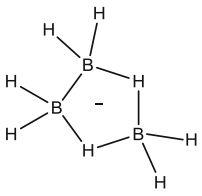

$B_3H_8^-$

Scheme 6 The $B_2H_7^-$ and $B_3H_8^-$ (triborohydride) anions. The bridging and covalent hydrogen species can interchange, the B–B bond moving about the ring

experiment and theory have both suggested that this is an unrealistic expectation. Instead, boron hydride clusters often form the most stable thermodynamically of which is the dodecahedral $B_{12}H_{12}^{2-}$. This might be difficult to rehydrogenate, but there are many other possible intermediates of varying stability and symmetry. Well-known examples are B_4H_{10} and $B_{10}H_{14}$, both neutral species, and neither a fully closed structure.

Systemically, still considering only Li–B one imaginable scheme might be:

$$5LiB_2H_7 \rightarrow 5LiH + B_{10}H_{14} + 8H_2 \tag{9}$$

storing 9 wt.% without either saturated hydrogenation or complete dehydrogenation. This scheme is easily criticized, as it is difficult to isolate LiB_2H_7 as a solid, and there is no guarantee that the decomposition will stop at $B_{10}H_{14}$ rather than $B_{12}H_{12}^{2-}$ or something else. The objective of this example is not to introduce a new system, but rather to show that even though it is known that very few elements can be a part of an effective hydrogen storage system, there is potential within the available chemistry to meet hydrogen storage needs because of the richness of that chemistry.

Adding N, Al, Mg, and C to the Li–B–H systems increase the number of molecular options exponentially. Useful theoretical tools have emerged and improve continuously with both experience and computational power. From the breakthroughs of a few and the clever effort of many more, the families of countless molecular storage species and physisorption structures have been identified. Catalytic discoveries and systemization technology have made good progress in the last 10 years, and this knowledge will be exported for use in superior chemical systems. The problem of hydrogen storage in molecular species still appears daunting, but the solutions to the problem may now be within reach.

References

1. Parry ML et al (eds) (2007) Contribution of working group II to the fourth assessment report of the intergovernmental panel on climate change, 2007. Cambridge University Press, Cambridge
2. Ball M, Wietschel M (eds) (2009) The hydrogen economy: opportunities and challenges. Cambridge University Press, Cambridge
3. Larminie J, Dicks A (2003) Fuel cell systems explained, 2nd edn. Wiley, West Sussex
4. (1988) CRC handbook of chemistry and physics, 69th ed. CRC, Boca Raton, FL
5. Graham T. Brittanica online encyclopedia. Available at: http://www.britannica.com/EBchecked/topic/240743/Thomas-Graham#ref=ref94045. Accessed 30 Jan 2009
6. Palladium hydride. Wikipedia. Available at: http://en.wikipedia.org/wiki/Palladium_hydride. Accessed 5 Mar 2011
7. Van Vucht JHN et al (1970) Reversible room-temperature absorption of large quantities of hydrogen by intermetallic compounds. Philips Res Rep 25:133–140
8. Hydride-Metal Related Databases. Sandia National Laboratory. Available at: http://hydpark.ca.sandia.gov/DBFrame.html. Accessed Jan 2009

9. Chambers A et al (1998) Hydrogen storage in graphite nanofibers. J Phys Chem B 102:4253–4256
10. Strobel R et al (2006) Hydrogen storage by carbon materials. J Power Sources 159:781–801
11. Bhatia SK, Myers AL (2006) Optimum conditions for adsorptive storage. Langmuir 22:1688
12. Garrone E et al (2008) Enthalpy–entropy correlation for hydrogen adsorption on zeolites. Chem Phys Lett 456:68–70
13. Yang R (2000) Hydrogen storage by alkali-doped carbon nanotubes revisited. Carbon 38:623–641
14. Liu C et al (2010) Hydrogen storage in carbon nanotubes revisited. Carbon 48:452–455
15. Zhao X et al (2004) Hysteretic adsorption and desorption of hydrogen by nanoporous metal-organic frameworks. Science 306:1012–1015
16. Li H et al (1999) Design and synthesis of an exceptionally stable and highly porous metal-organic framework. Nature 402:276–279
17. Murray LJ et al (2009) Hydrogen storage in metal-organic frameworks. Chem Soc Rev 38: 1294–1314
18. Dinca M, Long JR (2008) Hydrogen storage in microporous metal-organic frameworks with exposed metal sites. Angew Chem Int Ed 47:6766–6779
19. Kaye SS et al (2007) Impact of preparation and handling on the hydrogen storage properties of Zn_4O (1,4-benzenedicarboxylate)$_3$ (MOF-5). J Am Chem Soc 129:14176–14177
20. Messer CE (1960) United States of America. Office of Scientific and Technical Information. A Survey Report on Lithium Hydride
21. Beryllium hydride. Wikipedia. Available at: http://en.wikipedia.org/wiki/Beryllium_hydride. Accessed 17 Mar 2009
22. Huheey JE et al (1993) Inorganic chemistry: principles of structure and reactivity, 4th edn. Addison-Wesley, New York
23. Adams RM (ed) (1964) Boron, metallo-boron compounds, and boranes, 1st edn. Interscience, New York
24. Newson E et al (1998) Seasonal storage of hydrogen stationary systems with liquid organic hydrides. Int J Hydrogen Energy 23:905–909
25. Pez GP et al (2006) Hydrogen storage by reversible hydrogenation of pi-conjugated substrates. US Patent 7101530 B2
26. Uribe FA et al (2002) Effect of ammonia as potential fuel impurity on proton. J Electrochem Soc 149:A293–A296
27. Checketts JH (1998) Hydrogen generation system and pelletized fuel. US Patent 5817157
28. Magnesium hydride. Wikipedia. Available at: http://en.wikipedia.org/wiki/Magnesium_hydride. Accessed Feb 2011
29. Aluminum hydride. Wikipedia. Available at: http://en.wikipedia.org/wiki/Aluminium_hydride. Accessed Feb 2011
30. Zidan R et al (2009) Aluminum hydride: a reversible storage material for hydrogen storage. Available at: http://sti.srs.gov/fulltext/SRNS-STI-2008-00068.pdf
31. Ahluwalia RK et al (2009) Automotive storage of hydrogen in alane. Int J Hydrogen Energy 34:7731–7740
32. Lacina D et al (2011) The reversible synthesis of bis(quinuclidine) alane. J Alloys Compd (in press) doi:10.1016/j.jallcom.2010.10.010
33. Graetz J et al (2011) Aluminum hydride as a hydrogen and energy storage material: past, present and future. J Alloys Compd (in press) doi:10.1016/j.jallcom.2010.11.115
34. Li H et al (2010) Preparation and characterization of alane complexes for energy applications. J Phys Chem C 114:3318–3322
35. US Department of Energy. Targets for on-board hydrogen storage systems: Current R&D focus is on 2010 Targets. Available at: http://www1.eere.energy.gov. Accessed 31 Jan 2009
36. Dowdy ZR (1995) Chemical explosion burns 2 lab technicians; building evacuated after S. Boston blast. The Boston Globe, City Edition ed., Metro/Region sec: 24

37. Bogdanovic B, Schwickardi M (1997) Ti-doped alkali metal aluminum hydrides as potential novel reversible hydrogen storage materials. J Alloys Compd 253–254:1–9
38. Amendola SC et al (1999) A novel high power density borohydride-air cell. J Power Sources 84:130–133
39. Amendola SC et al (2000) A safe, portable, hydrogen gas generator using aqueous borohydride solution and Ru catalyst. Int J Hydrogen Energy 25:969–975
40. Chen P et al (2002) Interaction of hydrogen with metal nitrides and imides. Nature 420:302–304
41. Orimo S-i et al (2007) Complex hydrides for hydrogen storage. Chem Rev 107:4111–4132
42. Jensen CM, Gross KJ (2001) Development of catalytically enhanced sodium aluminum hydride as a hydrogen-storage material. Appl Phys A 72:213–219
43. Schlesinger HI et al (1953) New developments in the chemistry of diborane and the borohydrides. I. General summary. J Am Chem Soc 75:186–190
44. Gross K et al (2000) In situ X-ray diffraction study of the decomposition of $NaAlH_4$. J Alloys Compd 297:270–281
45. Balema VP, Balema L (2005) Missing pieces of the puzzle or about some unresolved issues in solid state chemistry of alkali metal aluminohydrides. Phys Chem Chem Phys 7:1310–1314
46. Zuttel A et al (2007) Tetrahydroborates as new hydrogen storage materials. Scr Mater 56:823–828
47. Soldate AM (1947) Crystal structure of sodium borohydride. J Am Chem Soc 69:987–988
48. Chen J et al (2001) Reversible hydrogen storage via titanium-catalyzed $LiAlH_4$ and Li_3AlH_6. J Phys Chem B 105:11214–11220
49. Balema VP et al (2000) Rapid solid-state transformation of tetrahedral $[AlH_4]^-$ into octahedral $[AlH_6]^{3-}$ in lithium aluminohydride. Chem. Commun 1665–666
50. Heats of formation and chemical compositions. Purdue School AAE Propulsion Web Page. Available at: http://cobweb.ecn.purdue.edu/~propulsi/propulsion/comb/propellants.html. Purdue School of Aeronautics and Astronautics. Accessed 7 Feb 2009
51. Block J, Gray AP (1965) The thermal decomposition of lithium aluminum hydride. Inorg Chem 4:304–305
52. Engel T, Reid P (2010) Thermodynamics, statistical thermodynamics, and kinetics, 2nd edn. Prentice Hall, Upper saddle River, p 69
53. Shriver DF et al (1990) Inorganic chemistry. Oxford UP
54. Orimo S et al (2006) Experimental studies on intermediate compound of LiBH4. Appl Phys Lett 89:021920
55. Dieter G (1958) Verfahren zur Herstellung von Boranaten. German Patent 1077644
56. Au M, Walters RT (2010) Reversibility aspect of lithium borohydrides. Int J Hydrogen Energy 35:10311–10316
57. Friedrichs O et al (2008) Direct synthesis of $LiBH_4$ and $LiBD_4$ from the elements. Acta Mater 56:949–954
58. Wade RC (1981) Specialty inorganic chemicals. In: Thompson R (ed) Royal Society of Chemistry, London, pp 25–57
59. Shim J-H et al (2010) Effect of hydrogen back pressure on dehydrogenation behavior of LiBH4-based reactive hydride composites. J Phys Chem Lett 1:59–63
60. Pendolino F et al (2009) Effect of boron on the activation energy of the decomposition of $LiBH_4$. J Phys Chem C 113:17231–17234
61. Anton DL, Mosher DA (2005) High density hydrogen storage system demonstration using $NaAlH_4$ based complex compound hydrides. Department of Energy Hydrogen Program. Available at: http://www.hydrogen.energy.gov/pdfs/progress05/vi_a_2_anton.pdf. Accessed 31 Jan 2009
62. Venpure™ Solution. Rohm and Haas Corp
63. Garrett DE (1998) Borates: handbook of deposits, processing, properties, and use. Academic, Sand Diego

64. Kreevoy MM, Hutchins JEC (1972) H_2BH_3 as an intermediate in tetrahydridoborate hydrolysis. J Am Chem Soc 94:6371–6376
65. Michaelides A et al (2003) Different surface chemistries of water on Ru{0001}: from monomer adsorption to partially dissociated bilayers. J Am Chem Soc 125:2746–2755
66. Liu BH, Li ZP (2009) A review: hydrogen generation from borohydride hydrolysis reaction. J Power Sources 187:527–534
67. Holbrook KA, Twist PJ (1971) Hydrolysis of the borohydride ion catalyzed by metal-boron alloys. J Chem Soc A 890–894
68. Pena-Alonso R (2007) A picoscale catalyst for hydrogen generation from $NaBH_4$ for fuel cells. J Power Sources 165:315–323
69. Go/No-Go Recommendation for Sodium Borohydride for On-Board Vehicular Hydrogen Storage. Rep. no. NREL/MP-150-42220. Nov 2007. National Renewable Energy Laboratory. Available at: http://www1.eere.energy.gov/hydrogenandfuelcells/pdfs/42220.pdf. Accessed 7 Feb 2009
70. Hovland V et al (2003) Water and heat balance in a fuel cell vehicle with a sodium borohydride hydrogen fuel processor. Presented at the future transportation technology conference & exhibition, Costa Mesa, CA. SAE 2003-01-2271
71. Strizki M, Mohring RM (2004) Hydrogen gas generation system. US Patent 7105033
72. Millennium Cell and Horizon poised to unveil HydroPak. Fuel Cell Today. Available at: http://www.fuelcelltoday.com/online/news/articles/2008-01/Millennium-Cell-and-Horizon-pois. Accessed 17 Mar 2009
73. Demirci UB, Adkim PM (2009) Ten-year efforts and a no-go recommendation for sodium borohydride for on-board automotive hydrogen storage. Int J Hydrogen Energy 34:2638–2645
74. Aardahl CL, Rassat SD (2009) Overview of systems considerations for on-board chemical hydrogen storage. Int J Hydrogen Energy 34:6676–6683
75. Linden D, Reddy T (2001) Handbook of batteries. McGraw-Hill Professional, New York
76. Xiong Z et al (2004) Ternary imides for hydrogen storage. Adv Mater 16:1522–1525
77. Reilly JJ, Wiswall RH (1967) The reaction of hydrogen with alloys of magnesium and copper. Inorg Chem 6:2220–2223
78. Reilly JJ, Wiswall RH (1968) Reaction of hydrogen with alloys of magnesium and nickel and the formation of Mg_2NiH_4. Inorg Chem 7:2254–2256
79. Vajo JJ et al (2004) Altering hydrogen storage properties by hydride destabilization. J Phys Chem B 108:13977–13983
80. Siegel DJ (2007) Thermodynamic guidelines for the prediction of hydrogen storage reactions and their application to destabilized hydride mixtures. Phys Rev B 76:134102
81. Shore SG, Parry RW (1955) The crystalline compound ammonia-borane, HNBH. J Am Chem Soc 77:6084–6085
82. Wahl WA (1925) Probleme der Borchemie. Z Anorg Allgem Chem 146:230
83. Stowe AC et al (2007) In situ solid state 11B MAS-NMR studies of the thermal decomposition of ammonia borane: mechanistic studies of the hydrogen release pathways from a solid state hydrogen storage material. Phys Chem Chem Phys 9:1831–1836
84. Smith S et al (2005) Prepr Symp Am Chem Soc Div Fuel Chem 50:112–113
85. Sit V et al (1987) The thermal dissociation of NH_3BH_3. Thermochim Acta 113:379–382
86. Baumann J (2005) Thermal decomposition of polymeric aminoborane $(H_2BNH_2)_x$. Thermochim Acta 430:9–14
87. Gutowska A et al (2005) Nanoscaffold mediates hydrogen release and the reactivity of ammonia borane. Angew Chem Int Ed 44:3578
88. Davis BL et al (2009) Efficient regeneration of partially spent ammonia borane fuel. Angew Chem Int Ed 48:6812–6816
89. Campbell PG et al (2010) Hydrogen storage by boron-nitrogen heterocycles: a simple route for spent fuel regeneration. J Am Chem Soc 132:3289–3291

90. de Jongh PE, Adelhelm P (2010) Nanosizing and nanoconfinement: new strategies towards meeting hydrogen storage goals. ChemSusChem 3:1332–1348
91. Keaton RJ (2007) Base metal catalyzed dehydrogenation of ammonia-borane for chemical hydrogen storage. J Am Chem Soc 129:1844–1845
92. Bluhm ME et al (2006) Amineborane-based chemical hydrogen storage: enhanced ammonia borane dehydrogenation in ionic liquids. J Am Chem Soc 128:7748–7749
93. Chandra M, Xu Q (2007) Room temperature hydrogen generation from aqueous ammonia borane using noble metal nanoclusters as highly active catalysts. J Power Sources 168:135–142
94. Clark TJ et al (2007) Highly efficient colloidal cobalt- and rhodium-catalyzed hydrolysis of H_3N-BH_3 in air. Inorg Chem 46:7522–7527
95. Chen P, Zhu M (2008) Recent progress in hydrogen storage. Mater Today 11:36–43
96. Wu H et al (2010) A new family of metal borohydride ammonia borane complexes: synthesis, structures, and hydrogen storage properties. J Mater Chem 20:6550–6556
97. Kang X et al (2008) Ammonia borane destabilized by lithium hydride: an advanced on-board hydrogen storage material. Adv Mater 20:2756–2759
98. Diyabalange HV et al (2007) Calcium amidotrihydroborate: a hydrogen storage material. Angew Chem Int Ed 46:8995–8997
99. Xiong Z et al (2008) High-capacity hydrogen storage in lithium and sodium amidoboranes. Nat Mater 7:138–141
100. Wang P, Kang X (2008) Hydrogen-rich boron-containing materials for hydrogen storage. Dalton Trans 40:5400–5413
101. Zou X et al (2010) Hydrogen storage in a Ca-decorated, B-substituted metal organic framework. Int J Hydrogen Energy 35:198–203
102. Fahra OK (2010) De novo synthesis of a metal organic framework featuring ultra high surface areas and gas storage capacities. Nat Chem 2:944–948
103. Tesfaye AA et al. Prediction of a multi-center bonded solid boron hydride for hydrogen storage. Accepted PRB available at: http://arxiv.org/PS_cache/arxiv/pdf/1003/1003.0492v1.pdf. Accessed 3 Mar. 2011
104. Wolverton C et al (2008) Discovery of novel hydrogen storage materials: an atomic scale computational approach. J Phys Condens Matter 20:064228, 14pp
105. Shore SG et al (1982) Structure of the $[B_2H_7]^-$ anion. J Am Chem Soc 104:7669–7670
106. Beall H, Gaines DF (1999) Mechanistic aspects of boron hydride reactions. Inorg Chim Acta 289:1–10
107. Hough WV et al (1956) The sodium-diborane reaction. J Am Chem Soc 78:689
108. Ortega JV et al (2005) Triborohydride salts as hydrogen storage materials and preparation thereof. Patent US 2005/0135996 A1

Index